Low Field dc SQUID NMR on Room Temperature Samples and Single Crystal UPt_3

by

Aya Shibahara

Department of Physics

Royal Holloway University of London

This thesis is submitted for the degree of

Doctor of Philosophy

September 2010

I, Aya Shibahara confirm that the work presented in this thesis is my own. Where information has been derived from other sources, I confirm that this has been indicated in the thesis.

Signature: .....

Date: .....

Abstract

This thesis is an account of two distinct experiments with a common theme, which is the technique of dc SQUID NMR. Firstly the application of the technique for broadband spectroscopy on room temperature samples is described. The motivation behind this work was to try to obtain SQUID NMR signals from liquid samples such as water and the amino acid glycine in order to demonstrate a few of the potential applications of this technique in the low field regime. These include increased frequency resolution, the possible detection of relatively small amounts of oil contamination in water samples and low field J-spectroscopy as a chemical bond detector. Measurements were performed on samples of water and oil-water mixtures on a dipper probe that provided a simple, compact shielding arrangement that uses a two-stage SQUID sensor as the front end amplifier. With the introduction of a low frequency amplifier and modifications to the setup the SNR was increased by a factor of 4. However, the SNR became limited by flux trapping in the superconducting materials surrounding the sample, leading to the investigation of alternative materials and methods to maintain low field homogeneity at higher polarising fields.

The second part describes SQUID NMR measurements on a single crystal of the heavy fermion superconductor UPt_3. Despite serious experimental and theoretical efforts, the symmetry and nature of the unconventional superconducting order parameter has not been resolved due to contradicting experiments, in particular that of the Knight shift into the superconducting state. Measurements were performed on a dilution refrigerator. A two-stage SQUID was mounted onto the fridge, a ^{3}He marker was implemented for accurate local field determination and an overlapping superconducting shield was made to decrease the spectrometer deadtime. NMR measurements are presented for the static field parallel to the c-axis of the crystal from 600 mK down to 400 mK in a static field of 71.5 mT. The Knight shift is measured to decrease from -1.7 % in the normal state to -1.35 % at 400 mK. Together with the results from a Knight shift experiment at 30° to the c-axis, it is argued that these results may provide evidence for the E_{2u} model. Strategies for future measurements are addressed.

Acknowledgements

I feel honoured to have the opportunity to thank all the people that have together made every day an enjoyable one during my time here at Royal Holloway. In particular, I would like to thank my supervisor John Saunders, who without realising it has given me a lot of inspiration over the years. His enthusiasm and sharpness has been a great motivator. My advisor Chris Lusher and Brian Cowan for passing down their invaluable knowledge of SQUIDs and NMR. Rainer Körber, Andrew Casey, Jan Nyéki, Michael Neumann and Malcolm Poole for all their advice on experimental physics, as well as emergency help on the dilution fridge. Priya Sharma, for her clear explanations on spin matrices.

I greatly appreciate the excellent work that has been carried out on my behalf by the technical staff. In particular, I thank Dave Bosworth, John Taylor and Alan Betts. Andy Alway and Leon Ellison for always being concerned about my safety, and Ian Murray for always being the friendliest person up in the teaching lab. Howard Moore and Francis Greenough, for always enabling me to keep my cryostat topped up with helium. Tom Crane, who managed to rescue my corrupted data hard drive with his unrivalled computer expertise. Last but not least, Massimo Venti, for giving me advice on life, cars and encouraging me to bake.

A big thank you to fellow student Michèle Piscitelli for being my lab partner and for being an amazing housemate. She can always be relied upon and is the most meticulous person I know when it comes to experimental work. Also for enjoyable times and good advice in and out of the giraffe house, thanks to Ben, Rob, Lev and George. Chris, thank you so much for letting me write up in your lab and for proofreading and making me decent tea. Stephen, for all your jokes, keeping me fed and teaching me Corel Draw. Giovanna, for her frequent motivating visits and Simon, for not eating all of my sweets. A big mention goes to Richard with glitter and stars, for looking out for me and being truly inspirational!

Thank you to my parents for always being there to talk to and for making me happy. To Oli, for your constant patience, support and puns. To my three little brothers, Sei, Josh and Kai, I'm proud of you all and to you, I dedicate my thesis.

Contents

List of Figures

List of Tables

Chapter 1

Introduction

The ultimate aim of physics is to try to understand how the universe behaves. Much research is labelled *fundamental* - undertaken out of curiosity, with no immediate or direct commercial benefit. However, it is a fact that through better understanding, more and more novel applications are found, which naturally benefit society. In this thesis both avenues are explored: the fundamental research into the order parameter of the heavy fermion superconductor UPt_3, and the applied research into low field nuclear magnetic resonance (NMR) spectroscopy of biological samples. This thesis is divided into two distinct experimental areas with a common theme, which is the technique of dc SQUID NMR. The theory behind this technique is given in Chapter 2 as an introduction to both experiments.

In Chapter 3, I apply the technique to room temperature samples. Here, the SQUID spectrometer was essentially mounted onto a simple dipping probe for initial testing with the aim to extend the setup to a low field MRI system in the future. The motivation behind low field NMR on room temperature samples is plentiful and includes lower cost medical equipment, better frequency resolution and a potential increase in image contrast compared to high field NMR, to name but a few. For this project, my ambition was to develop a spectrometer to demonstrate the sensitivity of state of the art two-stage SQUID detection of low field NMR signals on biological substances (which must necessarily be at room temperature), specifically by obtaining a J-resolved spectrum of the amino acid glycine. Water and oil-water samples were studied successfully as pilots and are

documented here. However, limitations of the dipper probe setup were reached and due to project delays in setting up a new experiment to remedy this that were out of my control, it was decided in the meantime to start a second experiment - that of measuring the Knight shift of the heavy fermion superconductor UPt_3. This forms the larger part of my thesis and is reported from Chapter 4 onwards.

UPt_3 is a very unique and interesting compound. Discovered in 1983 by Stewart *et al.* [1], it is the first compelling example of a superconductor with an order parameter of unconventional symmetry, following the discovery of unconventional superfluidity in liquid ^{3}He. This means that it does not follow the traditional s-wave pairing suggested by BCS theory; moreover, the superconducting state has an order parameter with a smaller rotational symmetry group than that of the normal metallic crystal. UPt_3 belongs to the family of heavy fermion superconductors. These are a subset of the intermetallic compounds containing f-electron elements. These compounds are distinguished at low temperatures by an anomalously large electronic specific heat coefficient (γ), with a correspondingly large Pauli paramagnetic susceptibility (χ). The coexistence of strong local moments and superconductivity was the enigma that led to the study of the first heavy fermion superconductor $CeCu_2Si_2$ and still remains a central challenge for the understanding of these materials today. As UPt_3 was the first known instance in nature of a superconductor with multiple phases, it has been extensively studied and there is hope that with continued collaboration between theorists and experimentalists, further study will eventually lead to a possible microscopic theory of heavy fermion superconductivity.

Despite many efforts in the last couple of decades, the symmetry of the order parameter, the precise shape of the gap function and the nature of its coupling to magnetism for UPt_3 have progressed but still not been fully resolved. The determination of the NMR Knight shift can probe the electronic spin susceptibility into the superconducting state, as the electronic susceptibility cannot be measured directly with conventional methods because of the Meissner effect. The Knight shift gives us information which contributes to the determination of the spin structure of the Cooper pair. The most recent experiment on measuring the low field Knight

shift of UPt_3 into the superconducting state was performed by Körber [2]. However, due to the unfortunate misalignment of the c-axis of the crystal by 30° with respect to the applied magnetic field, it has been necessary to repeat these measurements using a different crystal, using the benefit of a new two-stage SQUID sensor with lower intrinsic noise.

Chapter 4 introduces the reader to NMR on type II superconductors, including the origin of the Knight shift and its temperature dependence for singlet and triplet superconductors. It also contains a literature review on UPt_3 including an overview of its normal state and superconducting state properties. An introduction to the symmetry framework used in describing unconventional superconductivity is given as well as the predictions of the three most prominent theories on the Knight shift of UPt_3 into the superconducting state. Previous measurements on the Knight shift of UPt_3 are discussed, leading to the justification of the measurements performed in this thesis.

Chapter 5 describes the experimental setup used to perform low field NMR measurements of UPt_3 at milliKelvin temperatures, including a description of the cryostat and the dilution fridge. An account of the improvements that were made to the instrumentation is given. This includes the latest in the series of two-stage SQUID sensors being mounted onto the cryostat, decreasing the white noise level by an order of magnitude and a new superconducting inner shield, constructed using results obtained from tests on the room temperature probe. Most notably, a liquid ^{3}He marker replaced the existing platinum bundle used for measuring the static magnetic field at the sample, essential for the accurate determination of the Knight shift.

Chapter 6 is the main results chapter. The sample characterisation of the UPt_3 single crystals is included. NMR signals from Sample 1 with B_0 parallel to the c-axis are shown, including measurements that show the Knight shift decreasing into the superconducting state for signals taken at a resonance frequency of 640 kHz. Despite much effort, the small signal size and increasing noise was the limiting factor for the lowest temperatures and fields, and so NMR signals were obtained only down to 400 mK. Unfortunately, time constraints meant that NMR signals for

the other crystal orientations could not be measured. However, together with the previous result for the field at 30° to the c-axis by Körber, a possible conclusion is drawn that supports the E_{2u} model. Finally, rigorous signal to noise calculations make a direct comparison with the previous UPt_3 experiment on this cryostat which measured a different UPt_3 crystal and show that it still possible to obtain a very good signal to noise ratio given larger crystals, or more significantly, with a sample such as the previous wafer with a sharper NMR linewidth. The technique of low field dc SQUID NMR continues to be an excellent technique for studying a wide range of materials and systems.

Chapter 2

Dc SQUID Nuclear Magnetic Resonance

Nuclear magnetic resonance (NMR) is a phenomenon which has been exploited in many areas of science, from medical imaging and chemical spectroscopy to petroleum and natural gas exploration and recovery. In condensed matter, NMR is used to probe the local electronic environment of the nucleus as well as provide information about molecular motion. Much experience has been gained by the use of dc SQUIDs (Superconducting QUantum Interference Devices) as low noise preamplifiers for NMR, here at Royal Holloway on studies of confined helium. They are detectors of magnetic flux with unparalleled sensitivity, making it the sensor of choice for low field NMR experiments.

In this thesis, two separate SQUID NMR spectrometers were used. The UPt_3 experiment was mounted onto a dilution refrigerator and an rf tipping field was applied to excite the sample. The room temperature experiment was mounted on a dipper probe and liquid samples were excited by application of a prepolarising field (described in Section 3.3). In both experiments, a broadband input configuration using dc SQUIDs was used to detect the NMR signal. This chapter provides a description of the aspects of dc SQUID NMR that are common to both experiments. Details of the specific spectrometers are given in Section 3.4 for the room temperature experiment and Section 5.2 for the UPt_3 experiment.

2.1 Nuclear Magnetic Resonance

Nuclear magnetic resonance has developed to become one of the most important experimental techniques in modern science. In this section I explain the microscopic origin of the NMR signal, the time constants associated with its relaxation to equilibrium and what these tell us about the sample measured. An explanation of pulsed NMR is also given with a recap of Fourier transform NMR. A more comprehensive discussion of NMR is given by Cowan [3].

2.1.1 Nuclear Paramagnetism

Nuclei of certain isotopes possess intrinsic angular momentum or spin and are characterised by the nuclear spin quantum number I. NMR can only be observed in nuclei with non-zero I, which can take integer or half integer values, depending on the isotope. The nuclei of ^{1}H, ^{13}C, ^{3}He and ^{195}Pt, all have $I = \frac{1}{2}$. The non-zero spin gives rise to a nuclear total angular momentum $\mathbf{L}$, giving the nucleus a net magnetic moment of

$$\boldsymbol{\mu} = \gamma \mathbf{L},$$

where γ is the gyromagnetic ratio, a constant characteristic to each nuclear species with units Hz T^{-1}. When placed in a static magnetic field, $\mathbf{B_0}$, the nuclear spins orient themselves to give a net magnetic moment parallel to $\mathbf{B_0}$, hence it is called nuclear paramagnetism. The magnitude of the total angular momentum is given by

$$L = \sqrt{I(I+1)}\hbar$$

and in the z direction, defined as the direction of the applied static field, it is quantised by the magnetic quantum number m due to Zeeman splitting of energy levels:

$$L_z = m\hbar,$$

where $m = -I, (-I+1)...I$. The energy associated with each nuclear spin in these states is

$$E = -\boldsymbol{\mu}.\mathbf{B_0} = -\gamma m \hbar B_0$$

so that resonant transitions between adjacent states can be induced by the application of an energy:

$$\Delta E = \hbar\gamma B_0 = \hbar\omega_0,$$

where ω_0 is the resonant Larmor frequency. This relation leads to the often used relation between magnetic field and resonance frequency:

$$\omega_0 = \gamma B_0. \tag{2.1}$$

The energy difference between these states is on the order of radio frequency (rf) and depends upon the strength of the field.

We now restrict ourselves to nuclei with spin $I = \frac{1}{2}$, which gives rise to two energy states separated by $\hbar\omega_0$ when placed in a magnetic field (Figure 2.1). Traditionally, these are called the spin up $\uparrow$ ($m = +\frac{1}{2}$) and spin down $\downarrow$ ($m = -\frac{1}{2}$) states.

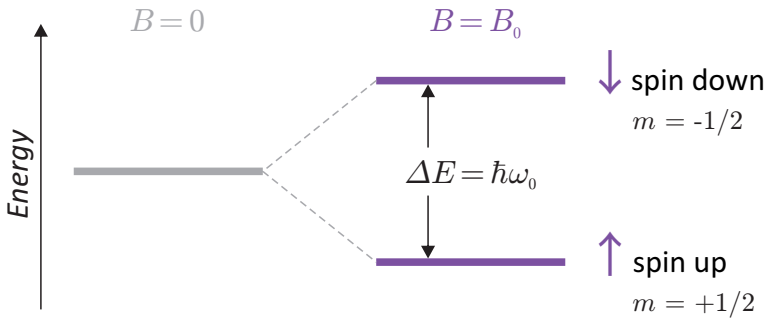

Figure 2.1: Energy level splitting of a spin 1/2 nucleus in the presence of a magnetic field B_0.

In thermal equilibrium, the ratio of occupation of the spin up and spin down states is given by the Boltzmann distribution, and it is the small fraction ($\sim 10^{-8}$) of excess spins in the low energy spin up state that is detected. This physical quantity is the magnetisation M in the static field direction:

$$M = (N_\uparrow - N_\downarrow)\mu,$$

where $N_\uparrow$ is the number of nuclei in the spin-up state, $N_\downarrow$ is the number of nuclei in the spin-down state and μ is the nuclear magnetic moment of a single nucleus. When the magnetic field is sufficiently small or the temperature is sufficiently high, such that $\hbar\gamma B_0 \ll 2k_BT$, the magnetisation is proportional to the applied field and inversely proportional to temperature. This is given in Equation 2.2 for a nucleus of spin I and is known as Curie's law. We are in this linear regime for the experiments in this thesis.

$$M_0 = \frac{N_v\hbar^2\gamma^2 I(I+1)}{3k_BT}B_0 \tag{2.2}$$

Here, N_v is the spin density in m^{-3} and k_B is the Boltzmann constant. For nuclei with spin $\frac{1}{2}$, this expression reduces to Equation 2.3.

$$M_0 = \frac{N_v\hbar^2\gamma^2}{4k_BT}B_0 \tag{2.3}$$

2.1.2 Precession and relaxation

The above picture is a static picture of the magnetisation in a magnetic field. Using microscopic first principles to describe the forces on a magnetic moment in a magnetic field, we obtain an equation of motion for the magnetisation:

$$\dot{\mathbf{M}} = \gamma|\mathbf{M}\times\mathbf{B}|. \tag{2.4}$$

Solving this for a static field in the z-direction gives circular motion in the x-y plane and a constant magnetisation in the z direction. The magnetisation vector therefore precesses about the static field with frequency equal to the Larmor frequency, ω_0 as depicted in Figure 2.2.

In reality however, when such a system is perturbed out of equilibrium, it will return to equilibrium in a characteristic time. This relaxation was included in the equations of motion in a phenomenological approach to give the Bloch equations:

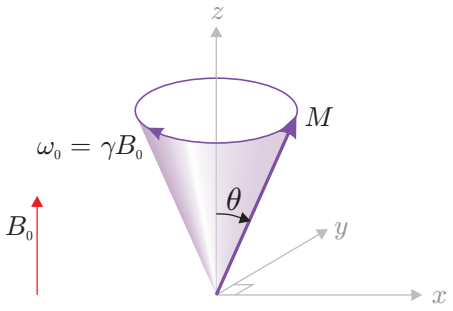

Figure 2.2: Larmor precession of the magnetisation vector **M** about $\mathbf{B_0}$.

$$\dot{M}_x = \gamma|\mathbf{M} \times \mathbf{B}|_x - \frac{M_x}{T_2} \tag{2.5a}$$

$$\dot{M}_y = \gamma|\mathbf{M} \times \mathbf{B}|_y - \frac{M_y}{T_2} \tag{2.5b}$$

$$\dot{M}_z = \gamma|\mathbf{M} \times \mathbf{B}|_z + \frac{(M_0 - M_z)}{T_1}, \tag{2.5c}$$

which have the following solutions:

$$M_x(t) = M_x(0)\cos(\omega_0 t)\exp(-t/T_2) \tag{2.6a}$$

$$M_y(t) = -M_y(0)\sin(\omega_0 t)\exp(-t/T_2) \tag{2.6b}$$

$$M_z(t) = M_0 - [M_0 - M(0)]\exp(-t/T_1), \tag{2.6c}$$

where T_1 is the longitudinal or spin-lattice relaxation time and T_2 is the transverse or spin-spin relaxation time.

2.1.3 Longitudinal relaxation time

When an unmagnetised sample is placed in a constant magnetic field, its magnetisation in the z-direction M_z builds up to M_0 exponentially with time constant T_1 as described by Equation 2.6c. M_0 is the thermal equilibrium magnetisation in the z-direction (after $t = \infty$) given by Equation 2.3 and the initial magnetisation of the sample is $M(0)$. This is an energy exchanging process - energy is lost from the spins to the lattice by the hyperfine interaction as the occupation of the energy levels change. Different substances have different values for T_1. A short T_1 means there is good thermal contact between the spin-system and the lattice.

2.1.4 Transverse relaxation time

A non-equilibrium magnetisation in the transverse plane will relax to zero through dephasing of spins. This relaxation occurs as the local magnetic field that each spin experiences is not the same for every nucleus in the sample. This is due to two factors: (a) the magnet inhomogeneity $\alpha = \Delta B/B$ and (b) dipole-dipole interactions between neighbouring nuclear spins. As the different local fields cause the spins to precess at different rates, destructive interference of spins occurs after the initial coherent excitation. The measured relaxation time due to both of these factors has a time constant T_2^* and the true relaxation time intrinsic to the sample and not due to the magnet is T_2 (the time constant given in Equations 2.6a and 2.6b). These are related by the following equation:

$$\frac{1}{T_2^*} = \frac{1}{T_2} + \gamma \Delta B, \tag{2.7}$$

where ΔB is the spread in field of the NMR magnet and the relative magnet homogeneity is denoted by $\alpha = \Delta B/B$. As the NMR linewidth in the frequency domain is inversely proportional to T_2^* as we shall see in Section 2.1.7, we can see that the broadening of the NMR line scales linearly with the strength of the measurement field. The mechanism for spin-spin relaxation involves mutual spin flips and does not involve energy exchange.

By measuring T_2^* as a function of magnetic field, it is possible to determine the intrinsic T_2 as well as the magnet homogeneity α as demonstrated in Section 3.5.5. The measured relaxation of magnetisation in the transverse plane is known as a free induction decay (FID) and has the form of an exponentially decaying cosine wave as shown in Figure 2.3. The measurement of T_2 gives us information about the local magnetic field at the nuclei of the sample, determined by the electron distribution at the nucleus. This is explained with reference to UPt_3 in Section 4.1.5. T_2 also gives information about the motion of nuclei in liquid samples, as we shall see in the following section. This is therefore most applicable to the room temperature measurements performed on liquid samples in Chapter 3.

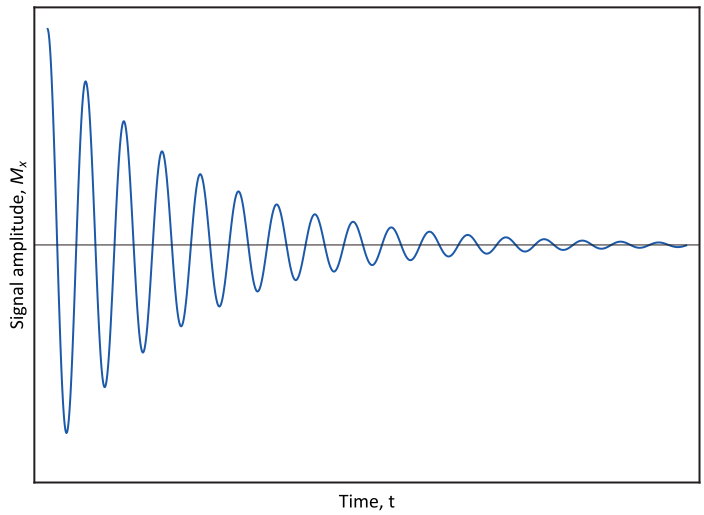

Figure 2.3: Free induction decay $M_x(t)$ showing transverse relaxation, as would be measured in the time domain.

2.1.5 Relaxation in liquid samples

In a liquid sample such as water, the spins are mobile, such that the local magnetic field experienced due to neighbouring spins is fluctuating through time. Here, the expression for T_2 for liquid samples is obtained by calculating the shape of the FID envelope when taking into account this motion.

We can use the mean field approximation and treat each spin as independent, seeing the composite field $\mathbf{b}_i$. Only the component b_z parallel to B_0 causes frequency variations about B_0 so we consider these only and write for a fluctuating b_z:

$$b_z = B_0 + b(t).$$

Also, we need only consider the transverse components of magnetisation for T_2 relaxation, and can write these components as an imaginary number: $\mu_t = \mu_x + i\mu_y$. By substituting these into the equation of motion for the magnetic moment (Equation 2.4) we obtain the following solution for an average over all spins:

$$M(t) = \exp(-i\gamma B_0 t) \left\langle \exp\left(-i\gamma \int_0^t b(\tau)\, d\tau\right) \right\rangle M(0). \tag{2.8}$$

Here, Larmor precession is contained in the first term, the initial transverse magnetisation is the last term and the relaxation term is in chevrons. The latter is the envelope of the FID, $F(t)$, which can be simplified by writing it in terms of $\phi(t)$, the phase accumulated by a spin in time t:

$$F(t) = \left\langle \exp(i\phi(t)) \right\rangle,$$

where $\phi(t) = -\gamma \int_0^t b(\tau)\, d\tau = \int_0^t \omega(\tau)\, d\tau$ and $\phi(t)$ is a fluctuating random variable with an average of zero. It is shown in Cowan [3] that by assuming a normal probability distribution for $\phi(t)$ and with a change of variables, the expression for the FID envelope is given by Equation 2.9.

$$F(t) = \exp\left(- \int_0^t (t - \tau) G(\tau)\, d\tau \right) \tag{2.9}$$

Here, $G(\tau)$ is the local frequency autocorrelation function, which is a useful function for describing random functions of time. It is usually expressed in the form $G(\tau_2 - \tau_1) = \left\langle \omega(\tau_1)\omega(\tau_2) \right\rangle$ where ω is the local frequency. Its general form is given in Figure 2.4. The correlation time, τ_c, relates to the time variation of local fields such that $|b|$ does not change much for $\tau \ll \tau_c$ but changes significantly for $\tau \gg \tau_c$.

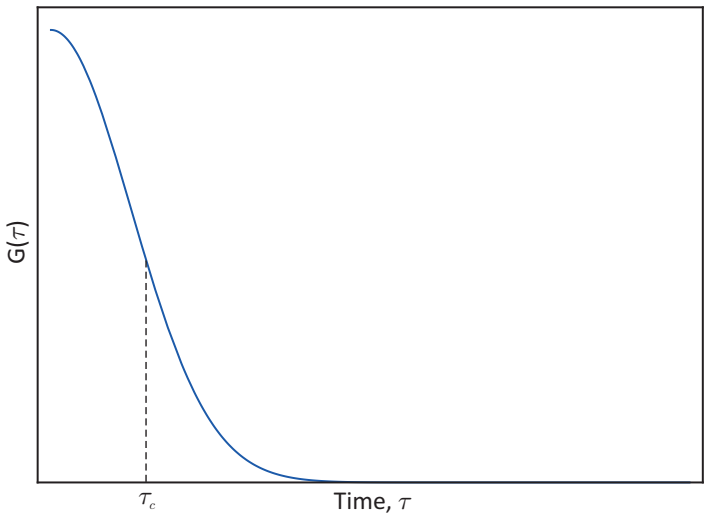

Figure 2.4: Autocorrelation function for a random variable.

The correlation time is therefore a measure of motion of spins, being short for fast motion. This behaviour is embodied in the autocorrelation function for $\omega(\tau)$:

$$\begin{aligned} \text{For} \qquad & t \ll \tau_c \qquad G(\tau) = G(0) \\ & t \gg \tau_c \qquad G(\tau) = 0. \end{aligned}$$

When we measure the system, we are interested in times much greater than τ_c, which results in an exponential FID envelope that can be related to the relaxation time T_2:

$$\begin{aligned} F(t) &= \exp\left(-t \int_0^\infty G(\tau)\, d\tau\right) \\ &= \exp\left(-t/T_2\right), \end{aligned} \tag{2.10}$$

where

$$1/T_2 = \int_0^\infty G(\tau)\, d\tau, \tag{2.11}$$

which is simply the area under the autocorrelation function. This area can be approximated by the initial height $G(0)$ multiplied by τ_c, which leads to the expression for T_2 for a liquid sample:

$$\frac{1}{T_2} = \left\langle \omega_{loc}^2 \right\rangle \tau_c. \tag{2.12}$$

The transverse relaxation rate is therefore determined by the mean square strength of the local fields and, the motion now influences the relaxation through the dependence on the correlation time τ_c. This effect of motion enhancing coherence is called 'motional averaging'. It can be understood by considering that as the nuclei move faster, the field they experience due to their surroundings is better averaged, resulting in a more homogeneous field experienced by all spins. This means the spins can remain in phase for longer in the transverse plane, leading to a longer T_2. This corresponds to a narrowing of the linewidth of the NMR signal in the frequency domain, as will be shown in Section 2.1.7.

Low field relaxation

So far we have considered NMR relaxation in applied magnetic fields B_0 that are seen by the spins to have a well defined orientation. However, when the motion is more rapid than the Larmor period, when $\omega_0\tau_c \ll 1$, the orientation of B_0 becomes difficult to distinguish. For the lowest fields used in the room temperature experiment in Chapter 3, this is the case.

Expressions for T_1 and T_2 relaxation can be written in terms of the spectral density function, $J(\omega)$, which is the Fourier transform of the autocorrelation function and gives the spread of precession frequencies. In the low field, fast motion regime, these are given by Equations 2.13 [3].

$$\frac{1}{T_1} = J(\omega_0) + 4J(2\omega_0) \tag{2.13a}$$

$$\frac{1}{T_2} = \frac{3}{2}J(0) + \frac{5}{2}J(\omega_0) + J(2\omega_0) \tag{2.13b}$$

This shows that T_1 relaxation needs an rf field oscillating at ω_0 and net spin flips are needed for relaxation. This is not needed for T_2 relaxation but there is still a T_1 contribution. $J(\omega)$ has the general form

$$J(\omega) = \frac{2}{3}\frac{M_2\tau_c}{1+\omega^2\tau_c^2}, \tag{2.14}$$

where $M_2 = \left\langle \omega_{loc}^2 \right\rangle$.

The behaviour of T_1 and T_2 relaxation can now be deduced for the low field limit as $\omega \to 0$ and the rapid motion limit, as $\tau_c \to 0$. For both cases, summarised as when $\omega_0\tau_c \ll 1$, the result is

$$\frac{1}{T_1} = \frac{1}{T_2} = \frac{10}{3}M_2\tau_c. \tag{2.15}$$

The physical explanation of this is when motion is rapid and the magnetic field is low, it is difficult for the spins to tell the direction of the static field. Its frequency changes many times in one Larmor period, so it no longer makes sense to describe the system in terms of a precession frequency.

2.1.6 Pulsed NMR

For a sample in thermal equilibrium in the static field B_0, there is a net magnetisation in the z-direction but not in the transverse plane as the spins have random phases. In the experimental setup, the three NMR coils (magnet, transmitter and receiver) are mounted orthogonal to each other. It is thus necessary to create a transverse magnetisation in order to measure it. In pulsed NMR, there are two ways of doing this: (a) Applying a burst of rf at the resonance frequency or (b) Applying a dc prepolarising pulse for a given time, both through the transmitter coil in the x-direction. Measurement of the precessing signal is then carried out after the pulse, by a receiver coil with its axis in the y-direction. The experimental aspects of the rf tipping technique are discussed in this section. This is the excitation technique used in the experiment on UPt_3 and is also used for some measurements in the room temperature experiment. The prepolarising excitation method is used only in the room temperature experiment and is described in Section 3.3.

For rf tipping, the excitation pulse, $B(t) = B_{rf}\cos(\omega_0 t) = 2B_1\cos(\omega_0 t)$ is a burst of ac current at the resonance frequency ω_0 that is applied through the transmitter coil for a time τ. This creates a linearly polarised field along the x-axis that can be thought of as a rotating and counter-rotating component in the xy plane about z (Figure 2.5). Only the rotating component with frequency ω_0 needs to be considered as the other component is far from resonance and has a negligible effect.

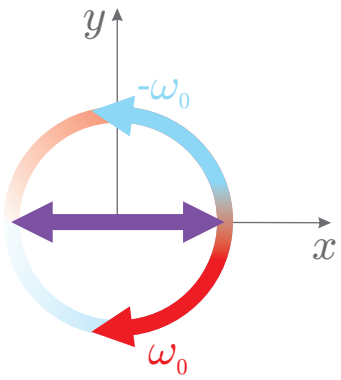

Figure 2.5: A linearly polarised field along x (purple) can be thought of as a rotating and counter-rotating component in the xy plane (red and blue respectively), rotating around z.

The situation is easily visualised by considering the system in a frame of reference that is rotating with the spins about z at the Larmor frequency. The axes in the rotating frame are now x', y' and z', where $z' = z$. In this frame of reference, the magnetic moment vector is static, and so the static field B_0 no longer exists. As the rf excitation field is rotating around z at the Larmor frequency, the effective field seen by the spin is just a static field in the x'-direction, B_1. The spin, thus, precesses around B_1 with angular velocity $\omega_1 = \gamma B_1$. In both frames of reference, this has the effect of tipping the spin away from the z-direction, by an angle θ given by:

$$\theta = \gamma B_1 \tau, \tag{2.16}$$

where τ is the length of the rf pulse. The duration of this applied rotating magnetic field therefore determines the orientation of the sample's net magnetisation. A 90 ° pulse is just long enough for the equilibrium magnetisation M_0 to be rotated 90 ° into the transverse plane. Similarly, a 180 ° pulse reverses the directions of the spins. After the rf pulse is switched off, the magnetisation again precesses about the static field B_0; T_1 and T_2 relaxation continue.

2.1.7 Fourier transform NMR

In order to extract information about the NMR signal such as the relaxation time T_2^* and the resonance frequency f_0, the captured FID (Figure 2.3) needs to undergo a Fourier transformation (FT) into the frequency domain. The standard Fourier transform and the inverse transform equations are given by Equations 2.17 and 2.18 respectively, below.

$$F(\omega) = \int_{-\infty}^{\infty} f(t) \exp(-i\omega t)\, dt \tag{2.17}$$

$$f(t) = \frac{1}{2\pi} \int_{-\infty}^{\infty} F(\omega) \exp(i\omega t)\, d\omega \tag{2.18}$$

The captured FID in the time domain will have an associated phase, ϕ and is defined by:

$$f(t) = A \cos(\omega_0 t + \phi) \exp(-t/T_2^*), \tag{2.19}$$

which has the form of Equation 2.6a with an incorporated phase. Here, A is the initial amplitude of the FID in the time domain. The Fourier transform of this signal for $t \geqslant 0$ is a complex function. The peak at resonance is given by:

$$F(\omega) = \frac{\frac{1}{2}AT_2^* \exp(i\phi)}{1 + i(\omega - \omega_0)T_2^*},$$

which, in terms of frequency f, is

$$F(f) = \frac{\frac{1}{2}AT_2^* \exp(i\phi)}{1 + 2\pi i(f - f_0)T_2^*}. \tag{2.20}$$

The real and imaginary components of Equation 2.20 along with the magnitude are plotted in Figure 2.6a for an arbitrary signal. The square of the magnitude, $|F(f)|^2$, is shown in Figure 2.6b, for which a Lorentzian can be fitted to give the NMR signal parameters $f_0, \Delta\nu_{meas}$ and A. From the measured linewidth, $\Delta\nu_{meas}$, the relaxation time T_2^* can be calculated using:

$$T_2^* = \frac{1}{\pi\Delta\nu_{meas}}. \tag{2.21}$$

As Figure 2.6a shows, the peak height of the magnitude of the Fourier transform, H_0, is equal to that of the real component for phase $\phi = 0$. This is given by the $f = f_0$ value, which is simply

$$H_0 = \frac{AT_2^*}{2}. \tag{2.22}$$

However, when performing a discrete Fourier transform (as in the LabVIEW FFT routine), we obtain

$$H_0 = \frac{AT_2^*}{2\Delta}, \tag{2.23}$$

where Δ is the time between data points, as $F(f) \approx \Delta F_n$ where F_n denotes the discrete Fourier transform. As A can be calculated for a given sample and setup, this enables the signal size to be estimated in the frequency domain. Sections 3.5.4 and 6.4.1 carry out signal size calculations for water and UPt_3 respectively.

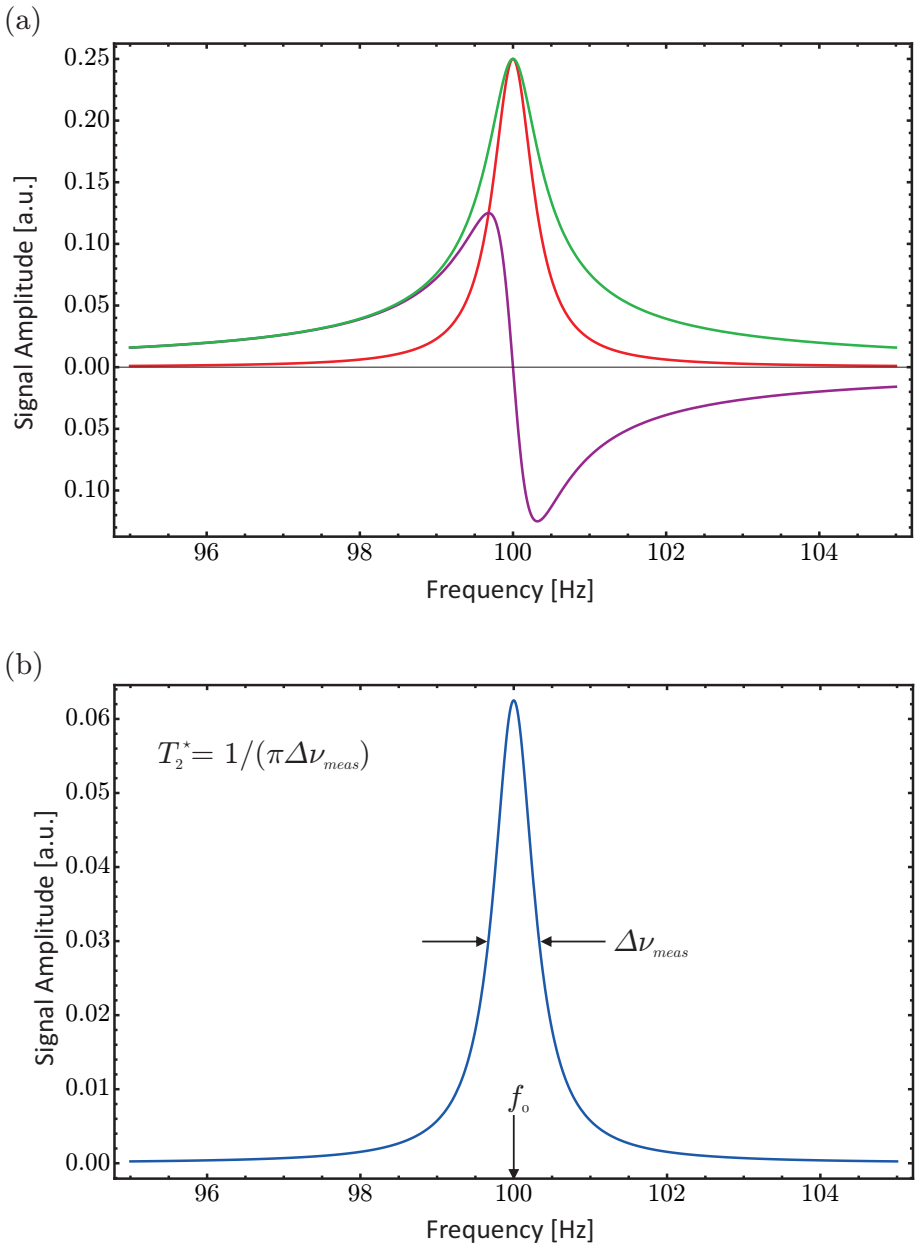

Figure 2.6: (a) The real (red), imaginary (purple) and magnitude (green) parts of the Fourier transform of an FID as given by Equation 2.19. This FT is for $A = 1$, $f_0 = 100$ Hz, $\phi = 0$ and $T_2^* = 0.5$ s. (b) The square of the magnitude of the Fourier transform is a Lorentzian centred at the resonance frequency f_0, with linewidth $\Delta\nu_{meas}$ at half maximum.

We now focus on the detection of this NMR signal using dc SQUIDs as low noise preamplifiers.

2.2 Dc SQUIDs

There are several reasons for using a dc SQUID as the front end amplifier in the experiments in this thesis. With conventional Faraday detection, the signal size is proportional to ${\omega_0}^2$ as it is the rate of change of flux that is measured whereas dc SQUID detection measures the flux directly. In our coupling scheme the signal size is proportional to ω_0, from the magnetisation, thus the SQUID detection is therefore advantageous for the low magnetic fields used in the experiments in this thesis. The signal sizes that would be measured are also inherently small at low magnetic fields (the ^{13}C signal in the room temperature experiment and the UPt_3 signal on the dilution fridge). Only a low noise dc SQUID amplifier has the sensitivity to observe these signals above the noise in a reasonable amount of time.

Finally, the untuned input coupling scheme used for coupling the flux into the SQUID enables the detection of signals to be broadband from dc up to the bandwidth of the spectrometer. This enables NMR measurements as a function of frequency to be performed. Low field pure J-spectroscopy becomes an exciting possibility especially if we are able to detect signals from more than one chemical species simultaneously. Measuring NMR signals from UPt_3 at different fields also enables the separation of the diamagnetic shift associated with the formation of the Abrikosov lattice from the true Knight shift. The second advantage of broadband input coupling is that the time constant characterising the decay of the transmitter pulse is short compared to tuned systems. This enables the NMR signal to be captured relatively quickly after the end of the tipping pulse, important for capturing NMR signals from metals, which typically have short T_2 relaxation times ~ 50 μs. We now look at the dc SQUID in more detail.

2.2.1 Characteristics of the dc SQUID

Here I briefly describe the characteristics of the dc SQUID. Detailed accounts can be found in [4–6].

The dc SQUID is a device consisting of a superconducting ring of inductance L interrupted by two Josephson junctions connected in parallel, each with a sim-

ilar critical current i_c. Fundamentally they are sensitive detectors of magnetic flux change, able to detect changes in flux of much less than a flux quantum, $\Phi_0 = 2.067 \times 10^{-15}$ Wb with typical noise levels of $\sim 10^{-6}\Phi_0$ Hz$^{-1/2}$ for commercial devices. For zero bias current through the SQUID, the circulating supercurrent i_s increases in step with the externally applied flux Φ_{ext} so that the total flux linking the ring maintains its original quantised value

$$\Phi_{ext} + Li_s = \frac{nh}{2e} = n\Phi_0, \tag{2.24}$$

where n is a positive integer or zero. When a bias current I is applied, the maximum supercurrent that the ring can support is given by:

$$I_c = 2i_c \left| \cos\left(\frac{\pi\Phi_{ext}}{\Phi_0}\right) \right|, \tag{2.25}$$

which varies periodically with external applied flux, the maximum value occuring when $\Phi_{ext} = n\Phi_0$ (constructive interference) and the minimum value occuring when $\Phi_{ext} = (n + \frac{1}{2})\Phi_0$ (destructive interference). If the SQUID is biased with a current exceeding the critical current of the double junction, then a direct voltage appears across the junctions that is a periodic function of the applied external flux. This property forms the basic mode of operation of a dc SQUID. Figure 2.7 shows a schematic of the dc SQUID, the I-V curves and the V-Φ characteristic

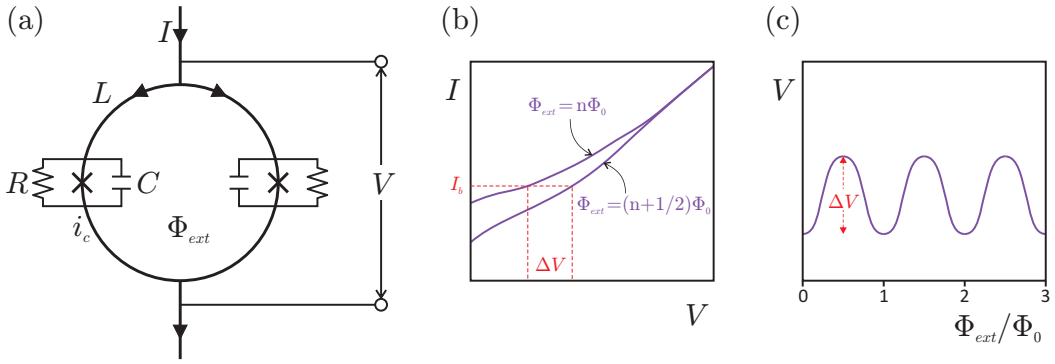

Figure 2.7: The dc SQUID: (a) Schematic; (b) The limiting I-V curves of a whole series of curves that depend on the applied flux; the operation point is set by the bias current I_b; (c) V-Φ characteristic in units of Φ_0 for constant bias current.

for bias current $I_b > 2i_c$.

In practice, each Josephson junction is in parallel with its self-capacitance C and a resistance R (see Figure 2.7(a)) in order to eliminate hysteresis in the I-V characteristic. Johnson noise in these shunt resistors (which is the source of intrinsic flux noise in the SQUID) imposes an upper limit on the SQUID inductance, namely

$$\frac{{\Phi_0}^2}{2L} \gg 2\pi k_B T.$$

Quantum interference is unobservable unless this criterion is satisfied. Due to this inductance constraint, the corresponding areas of planar SQUID devices are also small (typically $10^{-4} - 10^{-2}$ mm^2). Consequently, the majority of SQUID magnetometers involve a superconducting flux transformer to increase the effective area coupled into the SQUID. This will be described in Section 2.2.3.

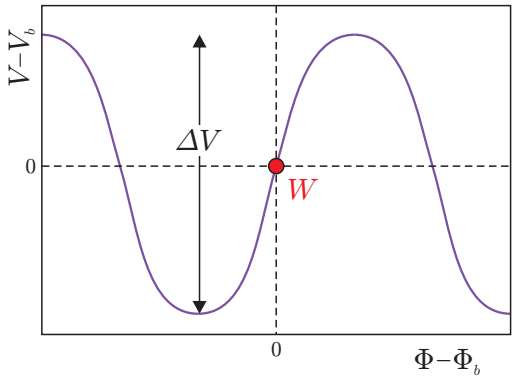

Figure 2.8: V-Φ characteristic of a dc SQUID biased with V_b and Φ_b. The voltage swing ΔV and working point W are shown.

In order to be able to detect changes in flux with a linear change in voltage, the SQUID is biased at the working point (as indicated by W in Figure 2.8), which is the steepest part of the V-Φ characteristic. This bias position is set by applying a voltage bias V_b and flux bias Φ_b to the SQUID. The gradient at the working point is the gain of the SQUID and is called the transfer coefficient, $V_\Phi = \frac{dV}{d\Phi}$. The aim is to adjust the bias position of the SQUID so this is maximised. The current bias I_b can also be adjusted to give the largest modulation depth, ΔV as this will also increase the transfer coefficient as well as the linear range.

Even at the optimal bias position, the dc SQUID is still only a linear flux to voltage transducer for a very limited flux range of $\sim \Phi_0/10$. This mode of operation is referred to as 'Open Loop' mode. To enable the SQUID to also detect much larger flux changes, its V-Φ characteristic must be linearised at the working point. This mode of operation is called 'Flux-Locked Loop' mode (FLL) and is discussed in the next section.

2.2.2 Flux-locked loop mode

To build a useful linear detector of magnetic flux, negative feedback techniques are employed to maintain the operating point of the SQUID constant by keeping a constant flux Φ_b in the SQUID. A simplified circuit diagram for FLL operation is shown in Figure 2.9. In the application of this system, the deviation of the SQUID voltage V from that at the working point V_b is amplified, integrated and fed back into the SQUID via a feedback resistor R_f and a feedback coil which is magnetically coupled to the SQUID via a mutual inductance M_f. The feedback flux is equal and opposite to the applied flux, maintaining the initial flux in the SQUID. The feedback resistor is in the kΩ range, making the impedance of the feedback coil negligible in the frequency range of interest.

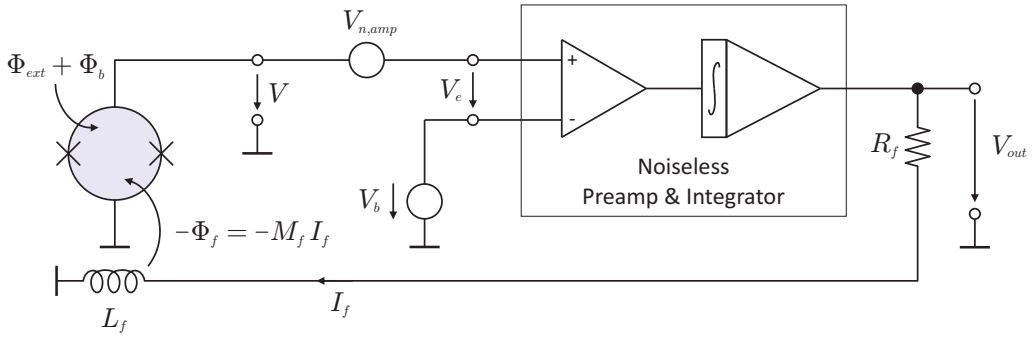

Figure 2.9: Idealised flux-locked loop circuit.

The gain in FLL mode is dependent on the feedback resistor as follows. An applied flux in the SQUID causes a voltage V_{out} at the output of the integrator. This drives a current V_{out}/R_f through the feedback coil. The feedback flux applied

to the SQUID, which is equal in magnitude to the applied flux in the SQUID Φ_{ext}, is given by:

$$\Phi_f = \frac{M_f V_{out}}{R_f} = \Phi_{ext}.$$

Rearranging for the output voltage of the integrator, we obtain

$$V_{out} = \frac{R_f}{M_f}\Phi_{ext}, \tag{2.26}$$

which is now linear with applied flux with the gain in FLL only depending on constant circuit parameters $G_{\mathrm{FLL}} = R_f/M_f$.

The 3dB bandwidth of the SQUID sensor, f_{3dB} is inversely proportional to R_f. For room temperature readout electronics, the bandwidth is limited by the total delay time between the SQUID and readout electronics. The distance is typically $\sim$1 m, limiting the $f_{3dB,max}$ bandwidth to about 20 MHz [4].

The total flux noise spectral density $S_{\Phi,FLL}$ of a dc SQUID operated in the above FLL circuit that takes into account flux noise from the preamplifier is given by

$$S_{\Phi,FLL} = S_{SQ} + \frac{V_{n,amp}^{\ 2}}{V_{\Phi}^{\ 2}}, \tag{2.27}$$

where S_{SQ} is the intrinsic SQUID flux noise spectral density and $V_{n,amp}^{\ 2}$ is the preamplifier voltage noise per unit bandwidth. The intrinsic SQUID noise arises from Johnson noise in the shunt resistors and can be lowered by operating the SQUID at lower temperatures. The noise contribution from the preamplifier is usually suppressed by increasing V_Φ, the transfer coefficient. This is necessary in order for the total noise to be dominated by the very low intrinsic SQUID noise, as typically the room temperature preamplifier noise contribution substantially exceeds that of the SQUID [4]. Section 2.2.4 describes the two-stage SQUID sensor used in this thesis, which uses a second stage SQUID amplifier to simultaneously reduce $V_{n,amp}$ and enhance V_Φ. Before this, we outline how a flux signal from the sample is coupled into the SQUID.

2.2.3 The input coupling scheme

As mentioned earlier, to improve the magnetic field resolution, a separate pickup coil having a much larger flux capture area than the bare SQUID is coupled to the SQUID via a multiturn spiral input coil. In this way, the effective area of the SQUID is enhanced to a value that may be 2 or 3 orders of magnitude higher than the bare SQUID, with a reduction in magnetic field noise. This coupling scheme, as first demonstrated by Friedman *et al.* [7] utilises a superconducting flux transformer and is intrinsically broadband, as we shall see.

The flux transformer consists of three key superconducting elements connected in series in a closed loop: the pickup (receiver) coil, the input coil and the Q-spoiler. As the flux in a superconducting loop must remain constant, a flux change Φ_p in the pickup coil induces a supercurrent i_s in the flux transformer analogous to Equation 2.24:

$$\Phi_p + (L_p + L_i)i_s = 0.$$

The flux coupled into the SQUID is thus:

$$\Phi_{SQ} = M_i|i_s| = \frac{\Phi_p M_i}{(L_i + L_p)}, \tag{2.28}$$

where L_i and L_p are the input coil and pickup coil inductances respectively and M_i is the mutual inductance between the SQUID and the input coil. This is independent of frequency, hence it is broadband. Maximum flux transfer occurs when the inductances are matched, $L_i = L_p$, so this is aimed for when designing the pickup coil. In practice, the pickup coil and SQUID are in separate locations connected by a shielded twisted pair, enabling the SQUID to be enclosed in a superconducting Nb shield whilst the pickup coil is exposed to dc and rf fields during the NMR experiment.

The Q-spoiler (or current limiter) forms the final part of the superconducting flux transformer and it is a row of hysteretic SQUIDs. These are superconducting below an adjustable critical current depending on its modulation bias. The Q-spoiler turns normal with a resistance of about 400 Ω when their critical current

is surpassed. This may occur during the transmitter pulse, through the small but inevitable cross-coupling between the transmitter and receiver coils. In this way the Q-spoiler serves to protect the SQUID from damaging high currents.

All three components of the flux transformer must be connected with twisted pairs routed through superconducting capillaries if they are in different locations with respect to each other. This reduces parasitic inductance/pickup of the leads going to the SQUID. The following section now examines two-stage SQUID detection, amplification and connection to room temperature electronics as a whole.

2.2.4 The two-stage dc SQUID sensor

The distinguishing feature of the two-stage SQUID sensor is the use of a second-stage SQUID as a low noise preamplifier that is inductively coupled to the first-stage sensor SQUID. It is a simple way of increasing the transfer coefficient of the SQUID and also has a low preamplifier voltage noise as it is operated at low temperatures. Figure 2.10 shows the configuration of a typical two-stage sensor.

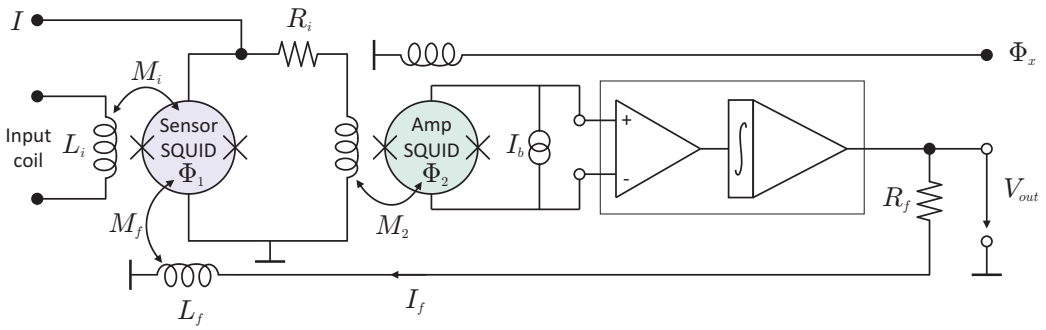

Figure 2.10: Configuration of a two-stage dc SQUID sensor.

The total noise is determined by the sensor SQUID as the transfer coefficient is enhanced as follows. The low-frequency small-signal flux gain at the working point G_Φ is the change in flux induced in the second SQUID ($\partial\Phi_2$) by a change in flux in the first SQUID ($\partial\Phi_1$), given by:

$$G_\Phi = \left(\frac{\partial\Phi_2}{\partial\Phi_1}\right)_W = \frac{M_2}{R_i} V_{\Phi 1}, \tag{2.29}$$

where V_{Φ_1} is the transfer coefficient of the unloaded sensor SQUID, R_i is the input resistance and M_2 is the input coil mutual inductance of the amplifier SQUID. As we use a current biased SQUID, the dynamic resistance of the sensor SQUID R_{dyn1} has been neglected as $R_i \gg R_{dyn1}$. The voltage generated across the amplifier SQUID is thus given by:

$$V_2 = V_{\Phi 2} G_\Phi \Phi_1, \tag{2.30}$$

where $V_{\Phi 2}$ is the transfer coefficient of the amplifier SQUID. Differentiating this with respect to the initial flux Φ_1 gives the transfer coefficient for the two-stage SQUID sensor:

$$V_{\Phi tot} = \frac{\partial V_2}{\partial \Phi_1} = G_\Phi V_{\Phi 2}, \tag{2.31}$$

where we can now see that the transfer coefficient of the amplifier SQUID has been enhanced by the flux gain.

For the sensors used in this thesis the second-stage amplifier SQUID is a SQUID array. By using an array of SQUIDs for the second stage, the the flux noise is further decreased by $1/N$ and the transfer coefficient increased by a factor N where N is the number of SQUIDs in the array [8]. Additional positive feedback (APF) is implemented on the sensor SQUID to skew the V-Φ characteristic such that the gradient is increased at the working point [5]. This increase in the transfer coefficient serves to further reduce the flux noise contribution from the preamplifier (Equation 2.27). When a suitable bias position has been found, these two-stage sensors are very convenient to use as their V-Φ characteristic is essentially single-SQUID-like. Details of the two-stage SQUID sensor can be found in [9].

The room temperature FLL electronics used (XXF-1) that connect directly to the SQUID sensor are supplied by Magnicon [10] and are controlled by a LabVIEW based program called SQUID Viewer. The program enables easy computer control of the SQUID bias position and feedback resistor R_f as well as the bandwidth through the adjustable gain-bandwidth product (GBP). There are many other controls available and details can be found in the relevant manual. The most relevant are the FLL/reset electronics. When the SQUID is put into the reset state, a TTL pulse to the electronics causes the SQUID to be put into the FLL

mode for the duration of the pulse. This function is used repeatedly during data capture.

To describe the performance of a complete SQUID system such as the two-stage SQUID sensor with associated room temperature electronics, the coupled energy sensitivity ε_c is the parameter often used for comparison. Essentially ε_c is the energy equivalent of the minimum detectable current in the input coil and is given by Equation 2.32. It is quoted in units of Planck's constant h, as it approaches the quantum limit of measurement.

$$\varepsilon_c = \frac{1}{2} L_i \frac{\langle {\Phi_N}^2 \rangle}{{M_i}^2} \tag{2.32}$$

Here, $\langle {\Phi_N}^2 \rangle = S_\Phi$ is the square of the total RMS flux noise.

2.2.5 Noise and shielding considerations

In a system with a sensitive detector such as a SQUID, it is important to try to decrease the environmental noise level as much as possible. The suppression of this noise forms a large part of any SQUID based experiment.

There are two main types of noise that need to be addressed: magnetic noise and rf noise. Magnetic noise comes from power lines at 50 Hz, the Earth's field and nearby moving objects such as cars, trains and elevators as well as mechanical vibrations in a magnetic field, referred to as magneto acoustics. These can be dealt with by using high permeability shields such as mu metal and by reducing vibrations as much as possible. The amplitude of the ringing due to magneto acoustic noise in the time domain is proportional to the square of the static magnetic field, ${B_0}^2$. It is also proportional to the current in the transmitter coil that generates the excitation field [2]. Fortunately, this coherent background can be subtracted away with good reliability using various methods, as will be shown in Sections 3.5.2 and 5.4.2.

Rf interference comes from radio and TV stations, nearby PCs and digital equipment. This noise can be eliminated by enclosing the cryogenic components, the leads connecting them to room temperature electronics and the electronics

themselves with a Faraday cage. Optical links between pieces of electronic equipment also decrease the transmission of electromagnetic interference to the experiment. Both shielding types are implemented in the experiments described in this thesis, as well as superconducting shields and enclosures used for low temperature components.

The thesis is now divided into two parts. Part I describes the use of these dc SQUID sensors to measure NMR signals from room temperature samples. Part II is an account of the experiment to measure the Knight shift of UPt_3 on a dilution refrigerator, where the high sensitivity of the SQUID was necessary to detect the small magnetisation.

Part I

NMR on Room Temperature Samples

Chapter 3

Ultra low field Room Temperature NMR

In biochemistry, NMR is routinely used to analyse and image organic materials non-destructively. Traditionally, the trend has been to go to higher and higher measurement fields in order to increase magnetisation of the sample and hence signal size. This is due to the conventional Faraday detection system where the signal size is proportional to ${B_0}^2$. When characterising a compound using NMR spectroscopy, fields of several tens of Tesla are used as this also increases the splitting between the spectral peaks (known as the chemical shift), giving better resolution for the determination of chemical structures. An alternative approach is taken here where we use our knowledge of the SQUID NMR technique to develop a compact broadband pulsed NMR spectrometer for the study of relatively small ($\sim$0.14 ml) liquid proton samples, using much *smaller* magnetic fields (in the microTesla (μT) to nanoTesla (nT) range) than are conventionally used.

This chapter first discusses the motivations behind performing NMR measurements at lower measurement fields and a description is given of the samples studied. There is a detailed description of the SQUID NMR spectrometer, together with its characterisation using samples of water and machine oil. Glycine is considered as a test chemical to demonstrate low field J-spectroscopy. Following this, efforts to increase the signal to noise ratio of the NMR line are documented.

3.1 Motivation for Low field Room temperature NMR

Low field room temperature NMR (RTNMR) has many advantages. In this section I outline the reasons for going to lower measurement fields in the area of magnetic resonance imaging (MRI) followed by magnetic resonance spectroscopy (MRS).

3.1.1 Magnetic resonance imaging

In medical imaging, there are cost and danger issues with high field MRI scanners, as well as the need for very homogeneous fields. Current human MRI systems range from 0.5 T up to an attempted ∼11.7 T [11], requiring homogeneities of less than ∼5 parts per million (ppm) over the imaging volume for submillimetre resolution images. Furthermore, linewidths of less than 9 Hz are required to produce an image of sufficiently high quality for a meaningful medical diagnosis [12]. These linewidths can only be achieved by the use of sophisticated and costly shimming techniques [13]. By going to lower measurement fields, this homogeneity condition can be relaxed as for a fixed relative homogeneity $\Delta B/B$, the broadening of the NMR line scales linearly with the strength of the measurement field as we saw in Section 2.1.4. So for a given field homogeneity, measuring at a lower field has the effect of sharpening the NMR line and increasing its size in the frequency domain. As the NMR line approaches the natural linewidth ($1/\pi T_2$) excellent resolution is achieved, with advantages for imaging and spectroscopy applications.

It has been shown [14] that the dependence of longitudinal relaxation rate (T_1^{-1}) on measurement field differs among the tissues in different parts of the body. Figure 3.1 shows the spread of relaxation rates for various human tissues from autopsy, including muscle, liver, lung and parts of the brain as a function of field and frequency [14]. The common imaging technique of T_1-weighted MRI uses a pulse sequence such that the signal size of each excited area depends on T_1. Thus, tissues with different T_1 will show up as different signal intensities in an image. A larger spread of T_1 relaxation rates therefore increases contrast in T_1-weighted MRI. As the figure shows, decreasing the measurement field from 1 T

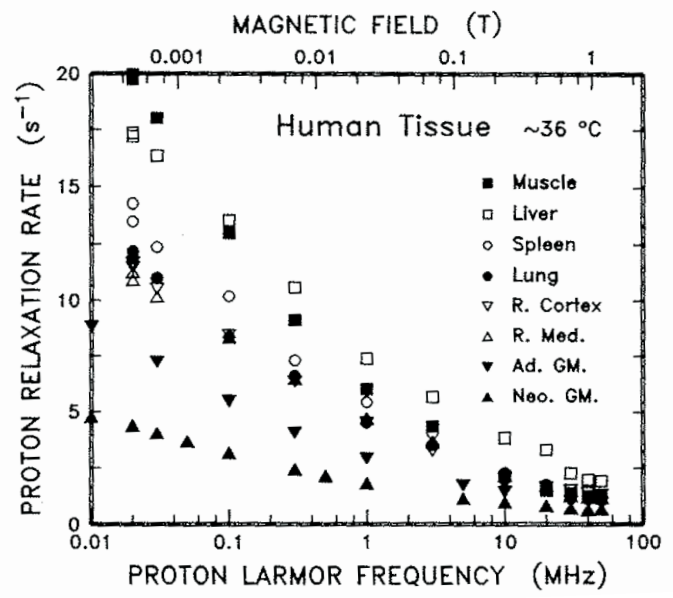

Figure 3.1: Spin-lattice relaxation rates ($1/T_1$) of human tissues from autopsy, near physiological temperature, including skeletal muscle (■), liver (□), spleen (○), lung (●), renal cortex (▽), renal medulla (△), adult grey matter (▼) and neonatal grey matter (▲) [14].

to 1 mT already increases the spread of rates by more than a factor of 8 for the various tissues shown. Hence, going to even lower fields would be advantageous for increasing contrast in T_1 weighted MRI.

Furthermore, the skin depth of metals is much larger at lower frequencies. The skin depth is the characteristic length scale over which an rf field penetrates a metallic substance and is proportional to $f^{-1/2}$. At a field of 50 μT, corresponding to the proton Larmor frequency of ∼2 kHz, the skin depth of aluminium is ∼1.8 mm, providing easy detection of the NMR signal through a 200 μm thick drinks can. This was illustrated by Mößler in a recent paper [15], where an image of a pepper inside an aluminium can showed no appreciable distortion due to the proximity of the metal. This suggests that at low enough fields, NMR measurements may be performed in the presence of metallic medical stents as well as in situations where storage, flow or reactions occur inside metallic pipes or reaction vessels. There is a second advantage concerning metals - the distortion in an image caused by a metallic implant can be decreased by going to low fields, as the local field inhomogeneity caused by the metal is proportional to the measurement field.

This suggests that imaging of patients with metallic implants is a possibility with SQUID-detected ultra low field MRI.

3.1.2 Magnetic resonance spectroscopy

NMR spectroscopy is also an invaluable tool in the natural sciences. It has been extensively used to study and determine the structure of chemical compounds as complex as proteins. At low magnetic fields, we lose chemical shift information as the splitting is proportional to the measurement field. However, useful information for structure determination can still be obtained from J-coupling or scalar coupling, which is preserved. This coupling arises from the interaction of different spin states through the chemical bonds of a molecule (an indirect interaction between nuclear spins, mediated by electrons) and results in the splitting of NMR signals into recognisable patterns based on the pairing of spin states. As a result, this J-coupling yields direct information about chemical bonding in a molecule. The strength of this coupling is field independent. This is very important as it means that the J-coupling constant can be measured with a high degree of accuracy, even in arbitrarily small magnetic fields.

The splitting is related to the molecular configuration in the following way. As an example, consider the molecule $CHCl_2CH_2Cl$ and its proton resonance spectrum (shown in Figure 3.2). In high magnetic fields, there are two sorts of hydrogen in this molecule labelled by greek subscripts α and β in Figure 3.2. The H_α proton resonates at a lower field than the H_β protons, due to their different chemical shifts. The two H_β protons have the same frequency since rotation around the carbon-carbon bond averages their environments and makes them chemically and magnetically equivalent. In the NMR spectrum, the H_β protons couple to the single H_α proton and so its spectrum is split into a 1:1 doublet. This arises because in the high temperature limit, for close to exactly half the molecules in the sample, the spin of the H_α nucleus will be oriented in the same direction as the field and in the other half the spin opposes the field. Thus, half the H_β nuclei have a slightly higher resonance frequency than the other half, which have a slightly lower resonance frequency. Both frequencies are equally displaced from the chemical shift position

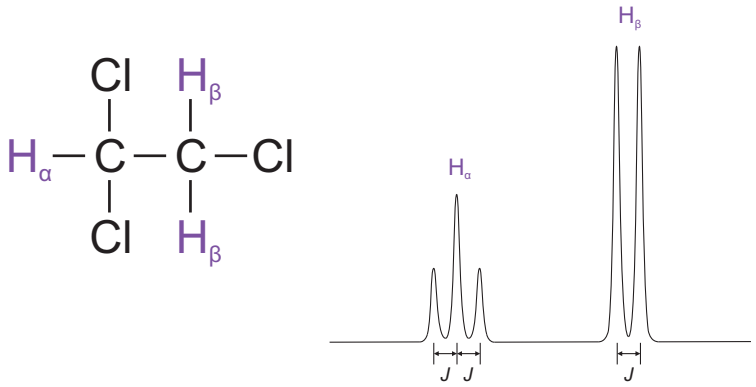

Figure 3.2: Chemical structure of $CHCl_2CH_2Cl$ and its proton NMR spectrum. The H_β protons are equivalent.

of the H_β nuclei, which is therefore at the centre of the doublet.

For the single H_α nucleus, the splitting is more complex as it sees the four possible spin combinations of the *two* H_β nuclei: $\uparrow\uparrow$, $\uparrow\downarrow$, $\downarrow\uparrow$ and $\downarrow\downarrow$. Thus its resonance is split into a triplet with a 1:2:1 intensity ratio, as there are two possible spin combinations that give zero additional field ($\uparrow\downarrow$ and $\downarrow\uparrow$). The J-coupling constant J, is given by the peak separation in Hz. In the example, as the spin-spin coupling is a mutual effect between the two groups of protons, the J coupling constant is the same for both multiplets. The integrated intensity of the peaks (area) is proportional to the number of excited nuclei; as there are two H_β nuclei and only one H_α nucleus, the area of the doublet is twice the area of the triplet.

Furthermore, there are two types of J-coupling: homonuclear and heteronuclear. If splitting is seen between two nuclear species of the same type, e.g. two ^1H as in the above example, then the J-coupling is called homonuclear. If the J-coupling is observed between different nuclear species with different gyromagnetic ratios (such as between ^1H and ^{13}C), then it is called heteronuclear. Typical values for heteronuclear J-coupling constants are $\sim 1 - 200$ Hz [16]. Homonuclear J-coupling is not observable at low fields when the chemical shift becomes negligible, as all nuclei with the same gyromagnetic ratio then become equivalent. For this reason, only heteronuclear splitting is observed. This simplifies the spectra slightly and although some bonding information is lost, we gain the enhancement of linewidth by going to lower fields. Appelt *et al.* recently showed that the ac-

curacy of the measured J-coupling constants in low fields was at least one order of magnitude better than the precision obtained with high field superconducting magnets [17]. Furthermore, as scalar couplings act as signatures of specific covalent bonds, this technique may be developed as a bond detector, as the J-coupling depends on bond strength as well as angle [18]. In theory, a chemical reaction can be followed by looking at the change in the J-spectrum of a substance.

At the time of writing, several authors ([17, 19–21]) have demonstrated the possibility of pure J-spectroscopy at low fields for ^{1}H,^{19} F and ^{31}P nuclei but none as of yet have been able to observe the ^{13}C J-spectrum due to its low gyromagnetic ratio and hence small signal size. As all organic substances contain carbon, this would be a very useful technique. One of the key motivations behind the experiments in this chapter was the possibility of observing such spectra using the low noise broadband SQUID spectrometer developed in this thesis. J-spectra from ^{1}H and ^{13}C could be observed simultaneously, with broadband excitation and detection using this technique.

The preliminary objective was to obtain SQUID NMR signals from simple liquid samples and to do this, a compact dipper probe configuration is used as it simplifies the shielding required. This spectrometer is described in detail in Section 3.4. For the longer term, a magnetically shielded room was purchased from Ammuneal, for which a low noise Dewar is being constructed to enable the measurement of larger samples as well as small body parts in vivo. This chapter documents preliminary experiments on and the development of the compact dipper probe setup. In the future, the spectral linewidth enhancement at low fields could also help in the determination of biomolecular structures and understanding the molecular basis of drug action. Together with the experience the Royal Holloway low temperature group has in the dc SQUID detection technique, it is seen that this idea of low field NMR at room temperature has wide scope for development.

3.2 NMR Samples

As this project was in its infancy, the preliminary experiments were kept simple (1D spectroscopy only) and proton NMR was performed on small samples of water. Machine oil and oil-water mixtures were also measured to illustrate the power of ultra low field NMR to simply and directly discriminate between components of a sample with different spin-spin relaxation times T_2. The amino acid glycine was looked into as a potential candidate for pure J-spectroscopy. The following sections describe these samples.

3.2.1 Water

The water used is de-ionised and distilled, to ensure high purity. Water was used as it has a very strong proton signal. This is due to its proton density ($N_v = 6.7 \times 10^{28}$ m^{-3}) and proton gyromagnetic ratio ($\gamma = 26.75 \times 10^7$ Hz T^{-1}) both being large. In organic chemistry and medicine, the proton signal is often measured as all organic molecules contain hydrogen and it produces a relatively strong signal. The human body for example contains approximately 60% water [22], so MRI of protons is very effective for imaging the body. With water at room temperature and in low magnetic fields, we are in the fast motion regime, where the correlation time τ_c is smaller than the Larmor period ${\omega_0}^{-1}$: $\omega_0 \tau_c \ll 1$ (discussed in Section 2.1.5). In this regime, $T_1 \simeq T_2$. The spin-lattice relaxation time of pure water is on the order of 2-3 seconds at room temperature [23], hence an equally long T_2 will give a very sharp signal in the frequency domain.

3.2.2 Machine Oil

The oil used was Shell Vitrea 33, a machine oil. This was chosen as it was a liquid sample that contained ^{1}H nuclei for performing NMR and it had a shorter T_2 to enable its relaxation to be differentiated from that of water. It has a calculated proton density of $\sim 2.58 \times 10^{28}$ m^{-3} and a density of approximately 872 kg/m^3 (see Section 3.5.8). From measurements at higher fields ($\sim$350 mT) on a simple conventional pulsed NMR spectrometer [24] at room temperature, T_1 was

measured to be approximately 47 ms. As the viscosity of oil is greater than that of water, the spins move slower and so motional averaging of the experienced field does not occur as efficiently as in water. This effect was discussed in Section 2.1.5. The result is, the oil has a shorter spin-spin relaxation time of 20-30 ms.

3.2.3 Glycine

Amino acids are the building blocks from which proteins are constructed. There are 20 common amino acids that combine to give the proteins needed in our bodies. All amino acids contain hydrogen and carbon - key nuclei for performing NMR. Glycine, being the simplest of the 20, was chosen as a sample to demonstrate low field J-spectroscopy with our spectrometer. Glycine has the chemical formula H_2NCH_2COOH. Its 3D structure is depicted in Figure 3.3 along with a simplified chemical structure. As 99 % of naturally occuring carbon is the non-NMR-active ^{12}C, it is necessary to chemically label at least one of the carbon atoms in the molecule with ^{13}C (which has $I = \frac{1}{2}$), in order to see J-coupling at low fields.

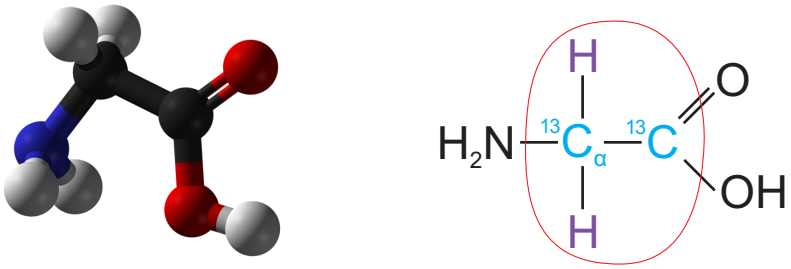

(a) 3D depiction (b) Chemical structure

Figure 3.3: The doubly carbonyl-labelled amino acid glycine. (a) Carbon atoms are black, hydrogen white, nitrogen blue and oxygen red. (b) Only the circled nuclei contribute to the J-spectrum of glycine.

Trabesinger *et al.* have measured the J-spectrum of a 1 M solution (1 mole of substance per litre of solution) of *singly* carbonyl-labelled glycine in a D_2O solvent as shown in Figure 3.4 using a SQUID magnetometer in a 3.7 μT measurement field [21]. They were able to just resolve the splitting of the NMR signal from the two equivalent protons (attached to the C) due to J-coupling to ^{13}C and measure a coupling constant of 5±1 Hz. The deuterium NMR peak is also visible as a singlet

at ∼15 % of the proton frequency but the ^{13}C triplet that should appear at 40 Hz is lost below the noise level. The prepolarising field used to magnetise the sample was ∼ 2 mT.

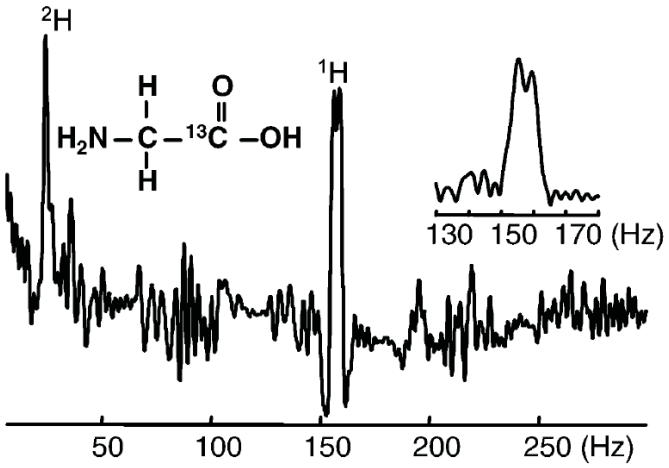

Figure 3.4: The J-spectrum of a 1 M solution of singly carbonyl-labelled glycine in a D_2O solvent as measured by Trabesinger *et al.* in a field of 3.7 μT after 5525 averages. The proton doublet is just resolved but the ^{13}C triplet is lost below the noise [21].

We have obtained a powdered glycine sample[1] which has been doubly labelled i.e. both the carbons have been replaced with ^{13}C, giving us the opportunity to observe a more complex carbon J-spectrum using our broadband setup, which has previously not been accomplished at low fields. The NMR active isotope ^{13}C has gyromagnetic ratio $\gamma = 6.69 \times 10^7$ Hz T^{-1}, four times smaller than that of protons. This means that the resonance frequency of a ^{13}C nucleus will be four times smaller than that of protons for a given field. However, as the magnetisation of the sample is proportional to γ^2, the signal size of the carbon signals in the frequency domain will be significantly smaller than that of the protons. A detailed signal size calculation for the J-spectrum of glycine along with the expected spectrum is given in Section 3.6.3.

The next section describes the prepolarising method used that enables signal detection at ultra low detection fields.

[1]From Dr. Thomas Eykyn, Clinical Magnetic Resonance group of the Institute of Cancer Research

3.3 Signal detection at ultra low fields

In ultra low static fields comparable to the Earth's field (μT), thermal polarisation at room temperature acquired by the sample is extremely small - on the order of 10^{-8}. Moreover, with the conventional rf tipping technique as described in Section 2.1.6, as the Larmor frequency decreases, the period of the resonant rf pulse gets longer, so that the pulse length required to tip the magnetisation into the measurement plane is likely to be much less than one period. In order to overcome these issues, the spins are prepolarised by a field much larger than the static field.

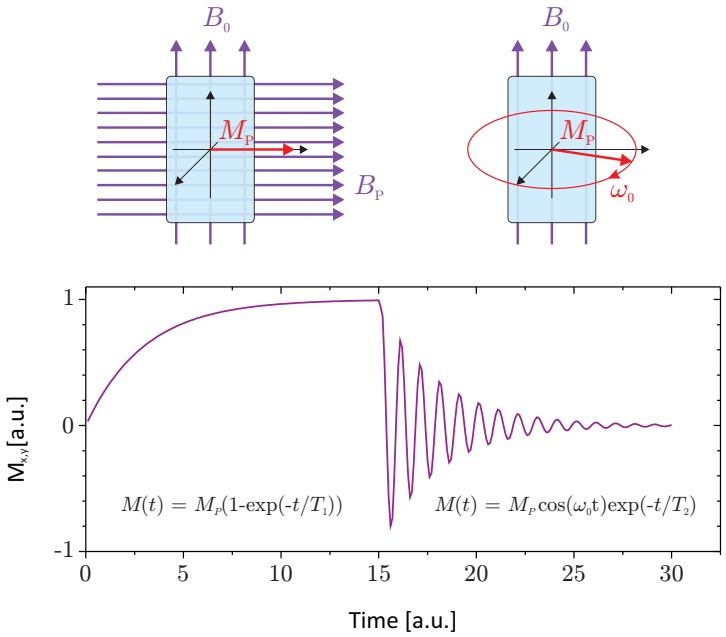

Figure 3.5: Schematic showing the orientation of the prepolarising pulse (top). Magnetisation in the measurement plane during and after a prepolarising pulse (bottom).

Prepolarising involves applying a second static field B_p of order mT at right-angles to the detection field B_0. In the present system (Figure 3.6), the z-axis $\equiv$ B_0. This B_p field is achieved by passing a dc current of about 1 A through the transmitter coil, producing a field of about 2 mT. The prepolarising field is left on long enough ($> 3\ T_1$) for an equilibrium magnetisation M_p to develop in the direction of the resultant field B, the vector product of B_p and B_0. As $B_p \gg B_0$, the

magnetisation is very close to being parallel to B_p, in the transverse plane (equivalent to the state after a conventional 90 ° rf pulse). When B_p is then turned off, the resultant field B shrinks in magnitude and rotates back to the z-direction. If the prepolarising field is turned off sufficiently slowly (adiabatically), the magnetisation "follows" B and ends up aligned with B_0. However, for maximum signal in the measurement plane we must turn off the prepolarising field sufficiently quickly (non-adiabatically) so the magnetisation is then left in the transverse plane. This increased magnetisation then begins to precess about and relax in the ultra low detection field B_0 where it is measured. This is shown schematically in Figure 3.5. The resulting FID is then essentially captured, filtered and Fourier transformed to give the characteristic NMR peak in the frequency domain.

The distinct advantage over conventional NMR spectrometers is that both the dc SQUID detection and prepolarising are broadband techniques. This makes measurements as a function of NMR frequency (and hence static measurement field) relatively simple. The experimental setup is described below.

3.4 The Room Temperature dc SQUID NMR spectrometer

In order for the spectrometer to function, the SQUID and other superconducting parts must remain below their respective superconducting transition tempertures (T_c) while the sample is kept at room temperature. As all the superconducting elements were Nb based ($T_c = 9.2$ K), liquid helium temperatures were adequate to be below T_c so no further refrigeration was necessary. The initial design thus consisted of a stainless steel dipper probe that was immersed in a Dewar of liquid helium on which the SQUID and superconducting NMR coils were mounted. Copper baffles within the stainless steel tube reduced radiation leaks to the cold end from room temperature. The three NMR coils (the magnet, transmitter and receiver) are arranged so that their three axes are perpendicular to each other. Inside the receiver coil, a small vacuum cell contained the sample heated to room temperature. A schematic of the dipper probe is shown in Figure 3.6. Figure 3.7

is a labelled photograph of the bottom section of the NMR dipper probe.

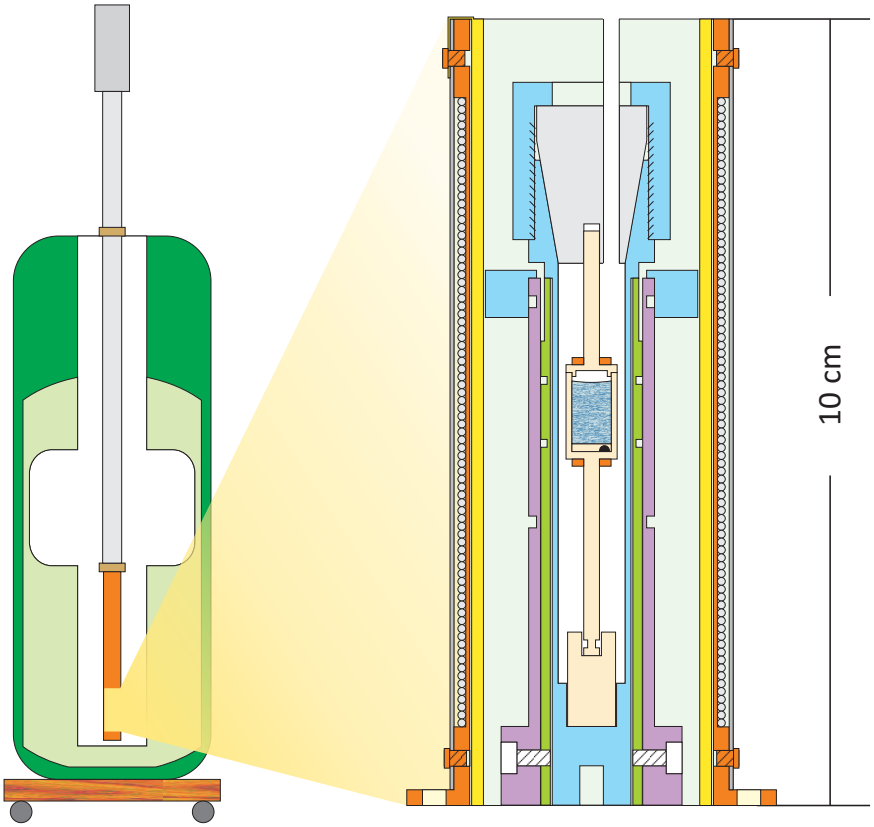

Figure 3.6: Diagram of RTNMR dipper probe in Dewar (left), with a section through the NMR coil area (right). The NMR coil formers are colour-coded: receiver green, transmitter purple and magnet orange. The Kel-F vacuum cell and support ring are blue. The inner shield is yellow.

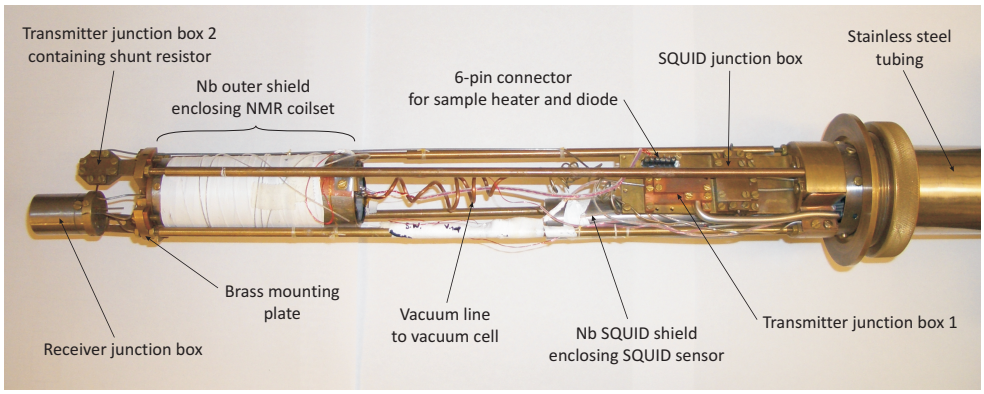

Figure 3.7: Photograph of bottom section of RTNMR probe. Various junction boxes are labelled that join the cold wires to those going to room temperature.

At most sites on the Earth's surface, the ambient magnetic field is in the range 30-100 μT, and, even in the absence of man-made electromagnetic interference, it fluctuates with a typical RMS amplitude of ∼1 nT [6]. As the measurement fields used in the experiments in this chapter were often much smaller than the Earth's field, the Dewar used was enclosed in a mu-metal can in order to shield out the

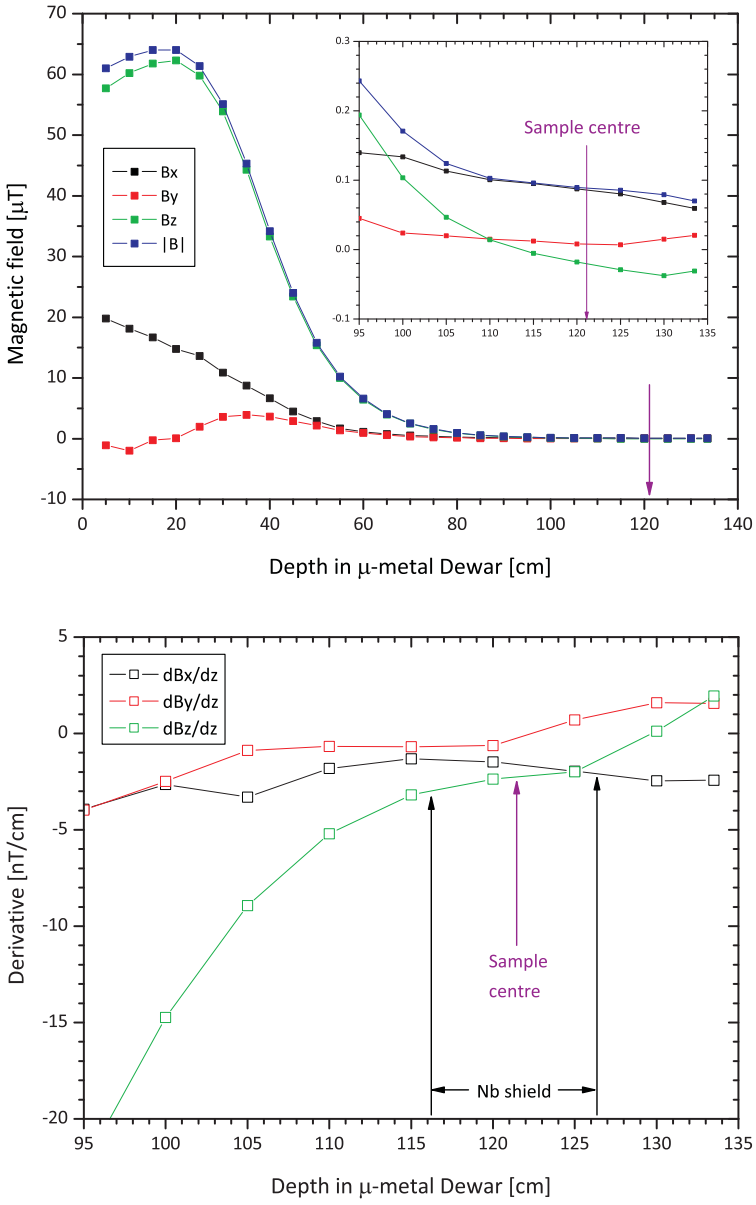

Figure 3.8: Magnetic field profile of the μ-metal Dewar. The magnetic field was measured in all three directions with z in the vertical direction, parallel to the static field magnet (top). The derivative of the field in the z-direction was also calculated (bottom). The sample position in the Dewar is shown.

Earth's field. Mu-metal is a nickel-iron alloy with a high magnetic permeability in low magnetic fields. This creates a low resistance path for the magnetic flux due to an external field so that flux does not penetrate the interior of the shielded device. Measurements of the magnetic field profile of the mu-metal-enclosed Dewar with a triple axis fluxgate magnetometer showed the most homogeneous area, which was chosen to be the sample position. Here, a field gradient of 2.5 nT cm^{-1} was measured in the vertical z-direction, with an absolute field magnitude of 20 nT (see Figure 3.8).

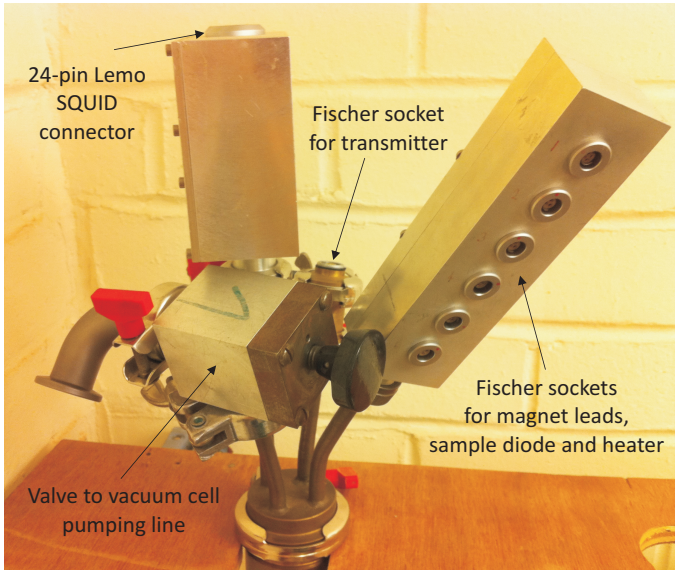

Figure 3.9: Photograph of the top of the RTNMR probe showing the room temperature connector boxes.

All electrical leads within the spectrometer setup were made into twisted pairs for carrying current in opposite directions. The wires were first protected from shorting by varnishing with GE varnish and threading through teflon capillaries. Each twisted pair was then shielded from rf interference by being routed through a stainless steel or niobium capillary. For the low temperature region, these capillaries began and ended in copper or niobium screened junction boxes as shown in Figure 3.7, or with one of the NMR coils. At the room temperature end (at the top of the probe) the capillaries terminated within aluminium connector boxes (Figure 3.9). All shielding was grounded by an electrical connection to the main

body of the probe, which was connected to ground through the Dewar neck. A description of the constituent parts that comprise the low temperature dipper probe section of the NMR spectrometer is given below.

3.4.1 The magnet

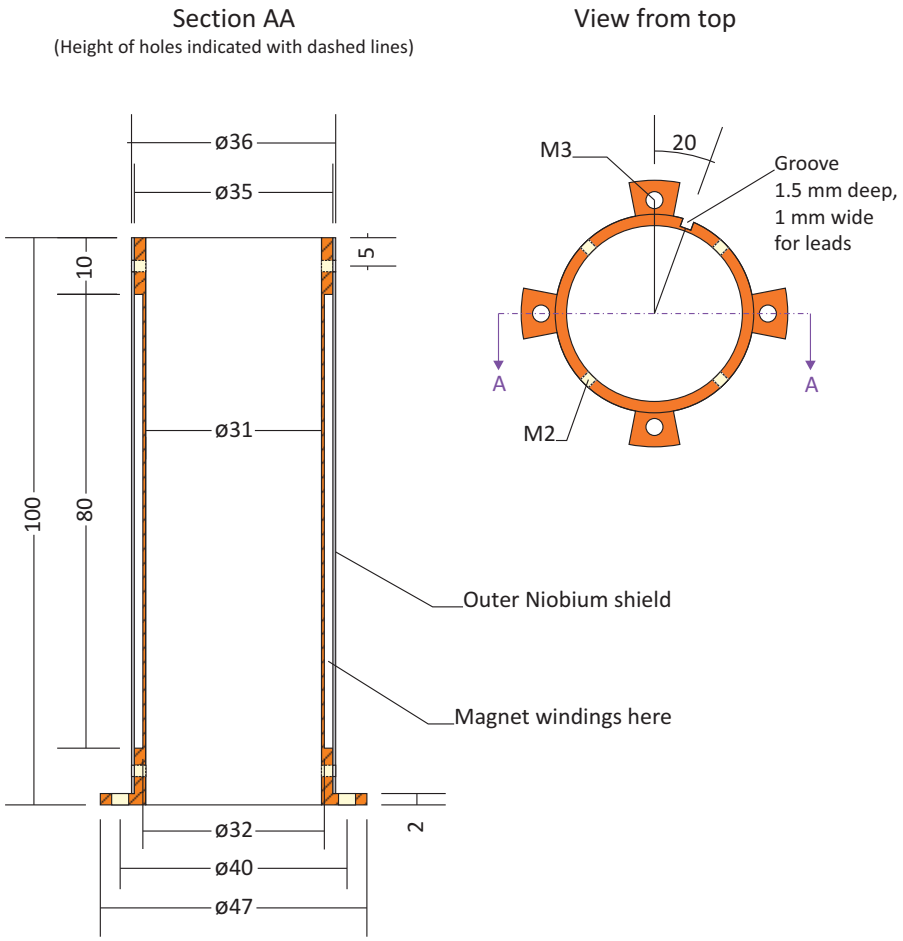

Figure 3.10: Diagram of copper magnet former.

The magnet that provides the static field is a superconducting solenoid wound from 106 µm ⌀ CuNi clad NbTi wire on a copper former 32 mm in diameter. The solenoid was 80 mm long (Figure 3.10). Wound by a former student Ketan Dandare, it was a two layer magnet with 727 turns in each layer, wound on top of an insulating sheet of 25 µm thick Kapton to prevent possible shorting of the windings to the copper former. GE varnish was used to secure the windings in

place. A superconducting cylindrical shield made of niobium (0.5 mm thickness) encases the magnet to shield against ambient magnetic field fluctuations. Fitted to the inner diameter of the magnet former is a second superconducting shield: the inner overlapping shield. The construction and function are explained in detail in Section 3.4.4. The measured field-current ratio with the inner shield in place is 2.73 mT A^{-1}. The homogeneity was measured to be ∼780 ppm (As shown in Section 3.5.5).

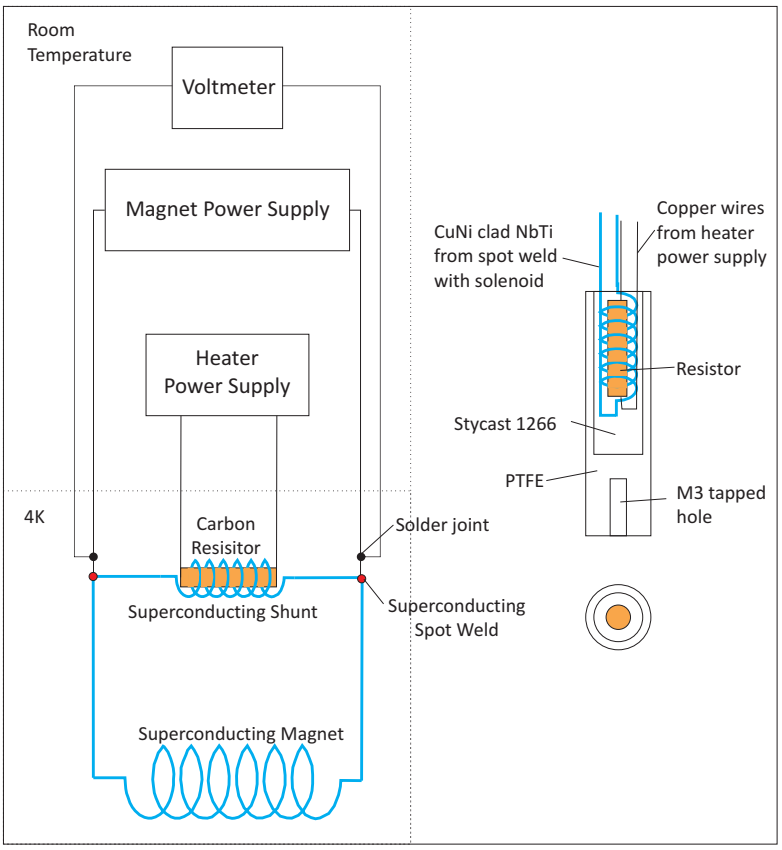

Figure 3.11: Left: Circuit diagram showing the wiring for the magnet's persistent heat switch system. Right: Diagram of the construction of the heat switch. Blue indicates a superconducting circuit.

The current is persisted in the magnet by means of a persistent heat switch in the coil circuit (Fig. 3.11). At 5 V bias, the heater makes a small section of the magnet normal, allowing current into the magnet from an external ramped power supply. A back emf observed across the coil using the voltage tap leads shows that the current is going into or out of the magnet. The heater is switched

off once the required current has been reached. Supercurrent flows, creating a constant magnetic field. Once the current had been put in, the magnet leads were disconnected from the probe at room temperature to avoid any unwanted pickup coupling to the probe during measurements.

3.4.2 The transmitter

This coil is predominantly used for applying the prepolarising field to the sample in the xy plane as well as for applying an rf pulse to tip the static magnetisation away from its equilibrium direction. It is necessary to minimise the cross-coupling of the three NMR coils as we do not want to overwhelm the receiver coil (and hence the SQUID) with strong fields from the magnet and transmitter. The orthogonal arrangement of the NMR coils is obtained by using a saddle geometry for the transmitter and receiver coils, both wound on cylindrical Kel-F formers and oriented so as to produce fields that are aligned 90° to each other. Kel-F (polychlorotrifluoroethylene or Fluorothene) was chosen due to its low proton content (estimated at $\approx$ 100 ppm), thus minimising any potential background ^{1}H signal [25]. It is also easily machinable compared to MACOR, a ceramic which has been traditionally used in the past [26, 27].

The optimum homogeneity for a saddle coil is obtained when the angular width of the coil is 120° and the length is twice the diameter [28]. The transmitter coil conforms to this geometry and has length 28 mm and diameter 14 mm, shown in Figure 3.12. There are 30 turns on each side, of bare NbTi wire (0.004" ⌀ bare NbTi, 0.005" ⌀ Formvar). A theoretical value for the field at the center of a saddle-shaped coil which is passing unit current in free space can be calculated using [29]:

$$B_{saddle} = \frac{N\sqrt{3}\mu_0}{\pi}\left(\frac{ag}{(a^2+g^2)^{\frac{3}{2}}} + \frac{g}{a(a^2+g^2)^{\frac{1}{2}}}\right) \tag{3.1}$$

where N is the number of turns on each side, a is the radius and $2g$ is the length of the coil. This gives $B_{saddle} = 3.187$ mT A^{-1} for dc currents. For an rf current, this corresponds to $B_1 = 1.593$ mT A^{-1} as we saw in Section 2.1.6.

In parallel with the transmitter coil there is a resistive shunt of 27 Ω for high

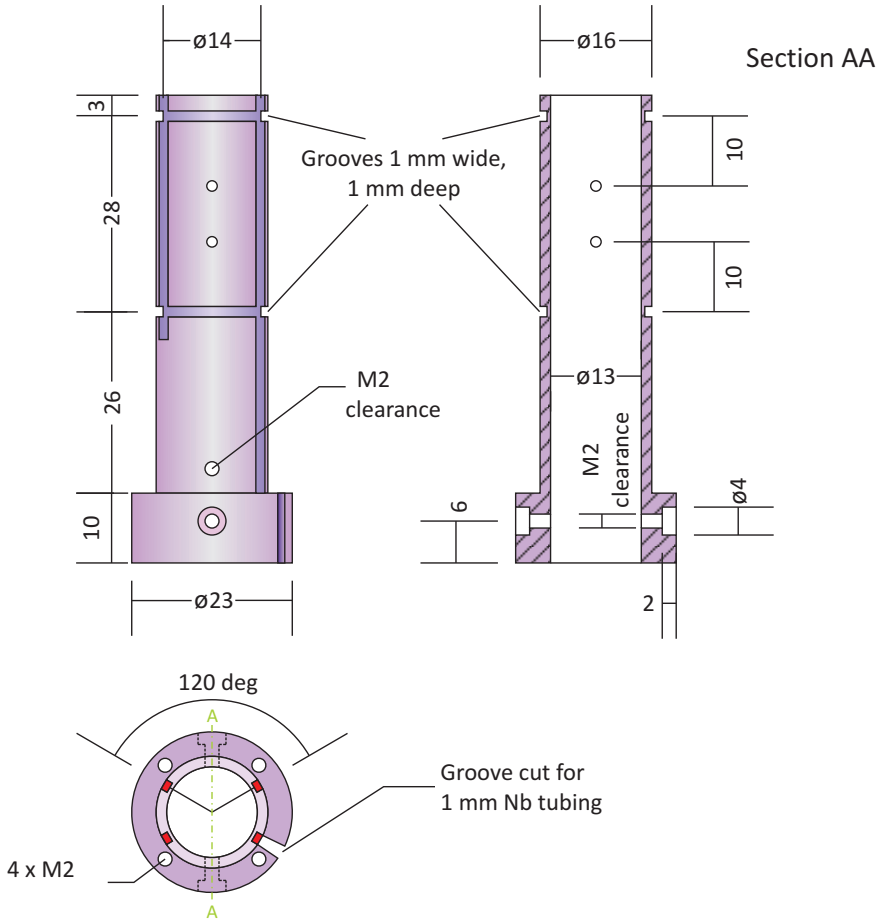

Figure 3.12: Diagram of Kel-F transmitter coil former.

frequency noise filtering. This causes any current noise well above the cut-off frequency $f_c = R_s/(2\pi L)$ to be shunted through R_s. Here, the calculated inductance is 145 μH giving $f_c = 30$ kHz, adequate for our frequencies of interest. The inductance was estimated by using the formula for a single rectangular loop [30] and using the value for the perimeter which the saddle coil would have if it was rectangular.

The shunt resistor and the inductance of the coil also determine the L/R time constant for the decay of pulses applied through the transmitter. After large amplitude prepolarising pulses are switched off, the induced voltage $-\frac{d\phi}{dt}$ across the coil and associated current can be very high. Through the small but inevitable cross-coupling between the transmitter and receiver coils, this can cause enough current in the input circuit to trap flux and irreversibly change the SQUID V-Φ

characteristic. The value of 27 Ω was found experimentally to be low enough to prevent this for the currents used (maximum of 630 mA, limited by the monitor resistors).

3.4.3 The receiver

The receiver coil closely surrounds the sample area and is the pickup coil for detecting the magnetisation. In the initial design by my predecessors, CuNi clad NbTi wire was used for the flux transformer and receiver coil as it was easier to solder to. The cladding was found to be responsible for the observed low frequency noise enhancement and was replaced with bare NbTi wire. Figure 3.13 shows the improvement.

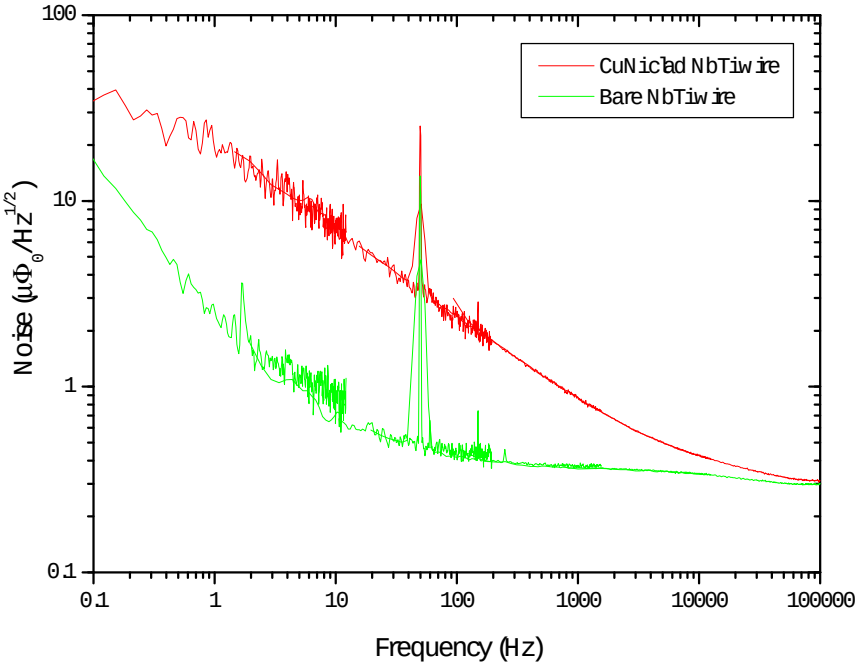

Figure 3.13: Comparison of noise spectra of CuNi clad NbTi wire (red) and bare NbTi wire (green) for the flux transformer.

This new receiver coil was wound on the same Kel-F former (Figure 3.14) and has length 7 mm and diameter 11 mm to enclose the sample cell. There are 5 turns on each side, of bare NbTi wire (0.004" ⌀ bare NbTi, 0.005" ⌀ Formvar). Like the transmitter coil, the wires were set in a Stycast mixture of 1266 and 2850FT

in a 1:1 ratio. The two wire ends were made into a twisted pair, fed through a teflon tube for protection and then a 1 mm ⌀ Nb tube for further shielding, ending in Nb screw terminals in a Nb junction box at the base of the probe (visible in Figure 3.7).

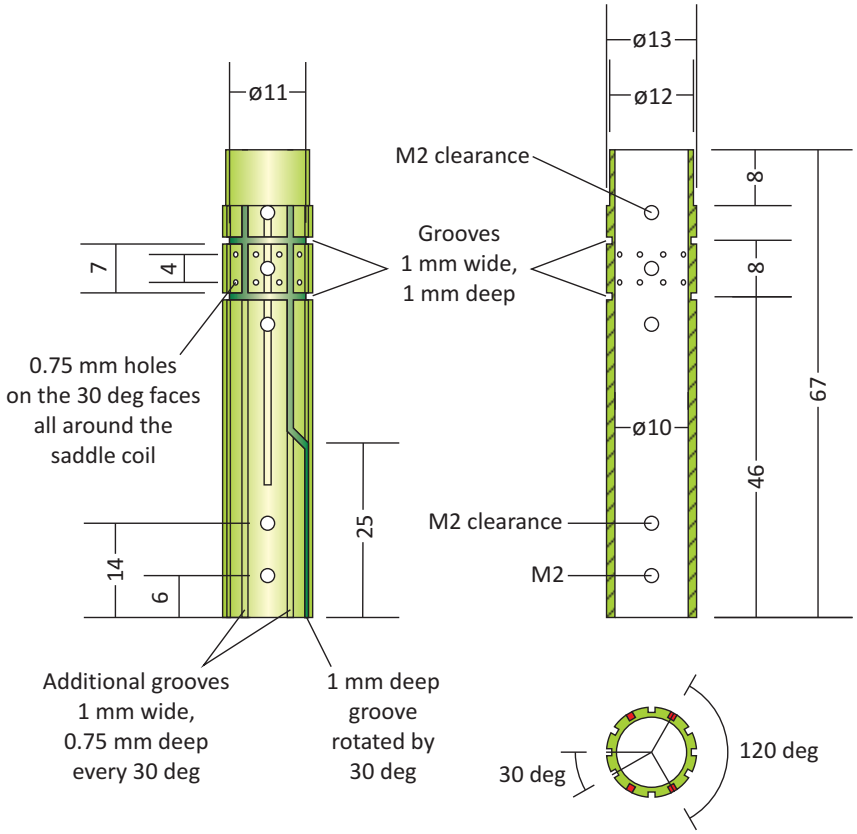

Figure 3.14: Diagram of Kel-F receiver coil former.

The measured inductance of the coil was 1.05 μH, matching closely with the SQUID input coil inductance of the two-stage sensor, $L_i = 1.1$ μH. As mentioned in Section 2.2.3, the inductances were matched for maximum flux transfer efficiency between the two coils. The calculated field current ratio using Equation 3.1 is $B_{1p} = 579$ μT A^{-1}.

The NMR coils were screwed onto the centre of a brass mounting plate. Four brass support posts were also screwed onto this plate to attach the experiment to the end of a 130 cm long, 1.75" outer diameter, stainless steel dipper probe. In order to reduce the movement of the receiver coil in the magnetic field, it was made

more rigid with a Kel-F ring that filled the space between the transmitter/receiver coilset and the inner shield. Dow Corning vacuum grease was used to secure it in place when cold.

3.4.4 The inner overlapping shield

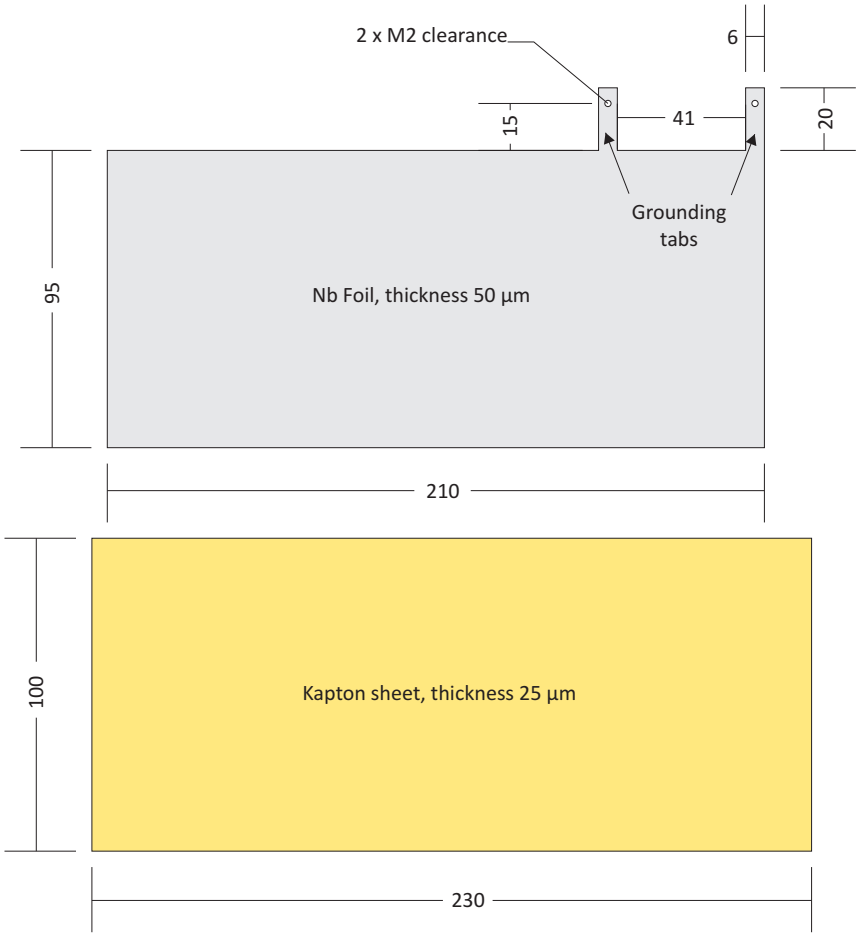

Figure 3.15: Net for making inner overlapping shield.

A grounded open-ended overlapping Nb shield in between the magnet former and the transmitter coil serves to shield the magnet former from strong transmitter pulses and to reduce the transient this causes in the time domain of our NMR signal. The low frequency transient arises from the decay of eddy currents in nearby metallic objects after the application of the transmitter pulse. This positive effect of the shield has been successfully demonstrated in past experiments [2, 27].

In reducing the transient, the inner shield also decreases the recovery time of the spectrometer after the excitation pulse as we will demonstrate in the UPt_3 experiment (Section 5.5). The inner shield also in principle improves the field homogeneity, making the NMR signal sharper although measurements showing the improvement were not performed. This concept was first demonstrated by Hechtfischer [31].

A sheet of niobium with a 25 μm insulating sheet of Kapton varnished onto it (GE varnish, CMR Direct) is rolled up onto a 0.5 mm thick cylindrical nylon former and held together with Stycast (1:1) to fit the inner diameter of the magnet former. This forms a roll of diamagnetic material when cooled, which has the boundary conditions of a diamagnetic cylinder, but still enables a field to enter the bore when superconducting due to the Kapton not allowing it to be a *closed* diamagnetic cylinder. Initially, a previously made two layer roll was used, made from a 50 μm thick foil of 99.9 % purity. Figure 3.15 gives the dimensions of the foil. In Section 3.7.8 the use of different foils for this inner shield is investigated.

3.4.5 The vacuum cell

The vacuum cell serves to thermally isolate the sample, heated to room temperature, from the helium bath. Figure 3.16 is a drawing of the vacuum cell. The vacuum cell fits inside the receiver coil and is held in place with an M3 nylon screw through its base, securing it onto the brass mounting plate.

The current vacuum cell was designed by Rainer Körber (Figure 3.16). The key feature is the screw-top Kel-F cap (M16 thread) combined with a Stycast 1266 cone lid on a Kel-F cell. On cooling, the thermal contraction of Kel-F is larger than that of Stycast 1266. This exerts an even greater force on the cone seal upon cooling. The downside to this was that pressure was exerted on the sample cell due to the vacuum cell contracting onto it, potentially enough to bend the cell and cause a thermal short to the helium bath. A space equivalent to the thickness of two sheets of masking tape was left in between the base of the sample cell and the vacuum cell to make room for this. The cone lid and entrance to the vacuum cell were greased with Dow Corning vacuum grease before closing the cell for each

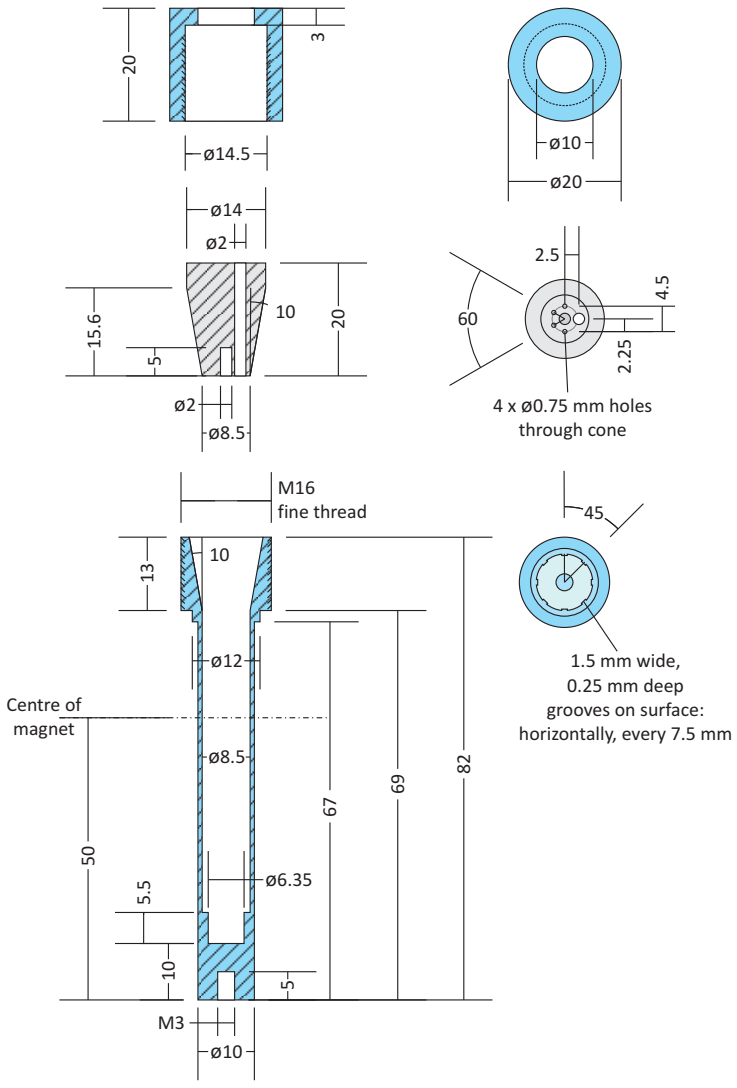

Figure 3.16: Drawing of vacuum cell. The screw cap and body are Kel-F, the cone lid is Stycast 1266.

cooldown and provided a very reliable vacuum seal for this setup.

Through the Stycast cone lid, a copper pumping line and four bare copper wire feedthroughs were set. The four feedthroughs connected the diode (sample thermometer which required a 4-point measurement) and heater wires from the vacuum cell lid to a 6-pin junction in the helium bath (labelled in Figure 3.7). From here, three twisted pairs of copper wire were routed through a teflon tube and a stainless steel capillary up to a 6-Fischer socket aluminium connector box at room temperature.

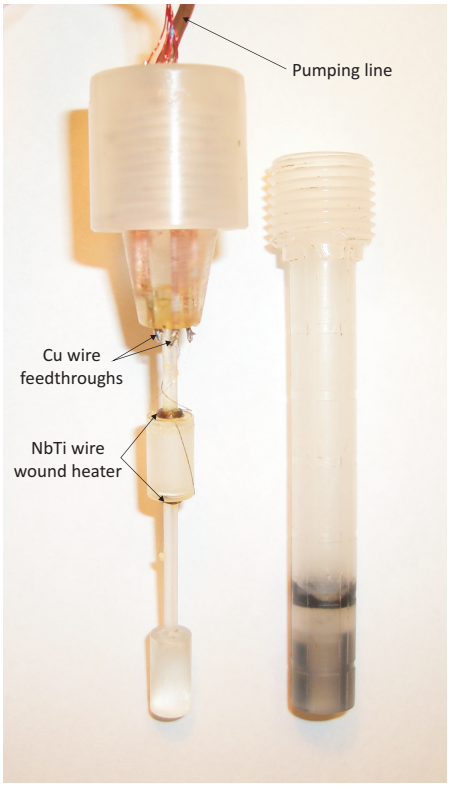

Figure 3.17: Photograph of sample cell and vacuum cell with heater and diode mounted.

3.4.6 The sample cell

The sample cell volume of ∼0.14 ml is smaller than previous low field SQUID NMR spectrometers for small liquid samples such as McDermott *et al.* (5 ml) [21, 32], demonstrating the sensitivity of our technique. The cell is made purely of Stycast 1266, a versatile epoxy. Despite the fact that Stycast 1266 epoxy contains an order of magnitude more hydrogen per unit mass than water, the short T_2 of the epoxy signal due to it being a solid meant it would not give a proton background [33]. Figure 3.17 is a photograph of the sample and vacuum cells. Figure 3.18 are the drawings for the sample cell itself.

The temperature of the sample was measured using a Lake Shore miniature silicon diode temperature sensor DT-421-HR (Figure 3.19). The platinum base was varnished onto the floor of the cell cup; its platinum leads passed through a hole in the base of the cup. The cell was filled to a depth of 1 mm with Stycast 1266, covering the diode to keep it isolated from the dielectric sample. The cell lid and

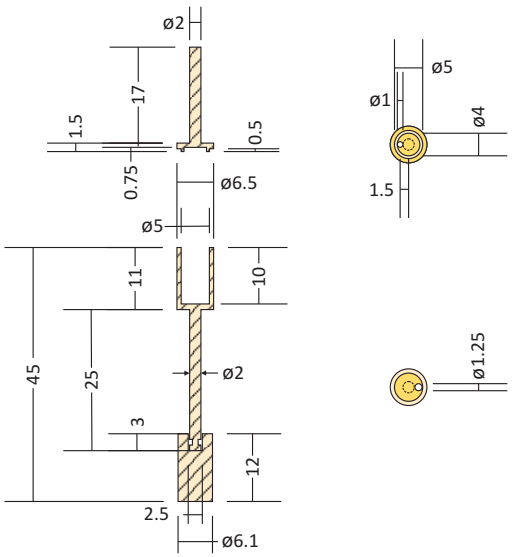

Figure 3.18: Drawings for sample cell made of Stycast 1266.

base were machined seperately from the cup and fixed together afterwards with Stycast 1266 epoxy. A four lead sensor voltage readout was used to read the diode. A twisted pair was soldered from the diode at the bottom of the sample cell to two of the copper feedthroughs in the cone lid of the vacuum cell. 100 μm ⌀ constantan silk bound wire was used here because of its low thermal conductivity at room temperature. The diode calibration used was the Standard Curve 10 calibration table that was supplied [34]. This was a voltage to temperature conversion that was expressed as a polynomial equation based on the Chebychev polynomials. A previously written LabVIEW program used the supplied Chebychev fit coefficients to plot and record the voltage as a temperature over time and was used for monitoring the sample. With the recommended measurement current through the diode of 10 μA (provided by a battery), the diode read ∼0.53 V at room temperature.

The initial water sample was injected through a 1 mm ⌀ hole in the lid with a syringe and the hole sealed with Stycast. Once dry, the sample cell was frozen and then pumped on in a bell jar for half an hour to ensure there was enough room for expansion when frozen and that it was leak-tight.

The sample is heated to room temperature by a resistive wire, wound non-inductively. The heater used was NbTi wire (50 μm bare ⌀) with resistance 867 Ω when not heated. A twisted pair made of a single length of this wire was wound

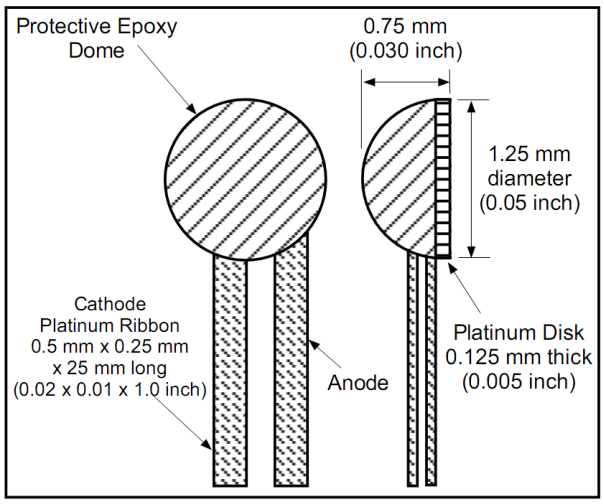

Figure 3.19: Diagram of silicon diode temperature sensor.

half on the bottom and half on the top of the sample cell and held in place using GE varnish. The bared ends were crimped with sterling silver tubing and soldered to the other two of the four pins at the bottom of the cone lid.

The sample cell was mounted into the vacuum cell using a dab of GE varnish onto the stalk and into the cone lid. Two sheets of masking tape were stuck onto the bottom of the sample cell before being pushed into position in the vacuum cell using the screw top lid. Once the varnish was dry the masking tape was removed (leaving enough room now for differential thermal contraction) and the vacuum cell reassembled.

Maintaining the sample at room temperature

With this geometry we achieve a relatively small distance of 1 mm between 4.2 K and the sample container. In order to keep the sample at room temperature, we consider the rate of radiative heat loss, $\dot{Q}$:

$$\dot{Q} = \varepsilon\sigma A(T_{hot}^4 - T_{cold}^4), \tag{3.2}$$

where ε is the emissivity and is approximated to be 1 in a worse case scenario, σ is the Stefan-Boltzmann constant and the area $A = 1.81 \times 10^4$ m^2 for the sample cell. From $T_{hot} = 305$ K to $T_{cold} = 4.2$ K, the radiative rate of heat loss is 89 mW. In

practice, in order to maintain the sample at this temperature the heater required a voltage of 16.01 V and a current of 17.14 mA, giving a power of 274 mW. This extra power needed can be explained by the radiative heat loss that is occuring from the parts of the heater that are not facing the sample cell, and also by small heat losses through the copper feedthroughs in the vacuum cell lid.

The vacuum cell wall is thin (0.5 mm in places) so there is a diffusive helium leak at room temperature but on cooling, cryopumping makes the helium condense onto the surface and the wall becomes leak-tight. Thus, the cooling procedure for a room temperature sample involved preheating the sample with 15.5 V for 5 mins until T_{sample} = 310 K whilst pumping on the vacuum cell with a leak detector. Then the probe was lowered into the helium bath until the cell was at a sufficiently low temperature for cryopumping to occur. This was seen as a drop in the leak rate and once this had occurred, the pump was disconnected from the probe. With this voltage on the heater, the sample temperature stabilised at 283 K with the probe fully immersed in helium. From this position, the sample temperature can be varied easily between 4.2 up to at least ∼310 K. The upper temperature limit of the sample cell was not investigated. In the event that the sample temperature dropped too fast, the cell was still in a safe position as there was enough volume left in the cell for expansion of the water when frozen.

3.4.7 The two-stage dc SQUID sensor C1c04-G25

State of the art SQUID sensors are continuously being developed at PTB in Berlin (Physikalisch Technische Bundesanstalt). The continuing collaboration that RHUL has with PTB has allowed for a periodic upgrade to the newest SQUID sensors. At the start of this work, the RTNMR probe was upgraded with the mounting of a two-stage SQUID sensor (C1c04-G25), replacing the SQUID array (C213-E25). The two-stage SQUID sensor has been described in Section 2.2.4 and is a low-T_c niobium sensor. This upgrade required an additional two connections to the SQUID from the room temperature electronics, giving seven in total. These are the ground connection (GND), the voltage and current bias lines for the amplifier SQUID (V_+ and V_-), the feedback flux modulation lines for FLL (Φ_+ and

Φ_-), the flux bias line for the amplifier SQUID (Φ_x) and the current bias line for the sensor SQUID (I). A twisted-seven was wound for these lines from 44 SWG (standard wire gauge) copper wire for the length of the probe, terminating in the copper SQUID junction box at 4.2 K. These lines were shielded from rf interference by being routed through teflon and a stainless steel capillary.

The new sensor consists of a single front-end sensor SQUID with double transformer coupling, read out by a second stage 16-SQUID array [9]. The SQUID sensor is fabricated on a 3 × 3 mm chip and is mounted onto a 12 × 15 mm yellow fibre board, held in a Stycast carrier with a teflon screw (Figure 3.20). Connections to the chip are made with Nb wire bonds to copper strips on the fibre board, which can be soldered to. The input coil, which is fabricated onto the chip is wire bonded to two PbInAu foils that end in niobium screw terminals for connecting the flux transformer. The new sensor also has an on-board chip heater, in order to expel any trapped magnetic flux in the SQUID sensor in situ by turning the superconducting components normal. This is controlled using the SQUID Viewer software.

This particular device has a coupled energy sensitivity ε_c of 50 h at 4.2 K. As we saw in Section 2.2.4 this quantity is the energy equivalent of the smallest detectable current in the SQUID sensor (Equation 2.32) and is a great improvement

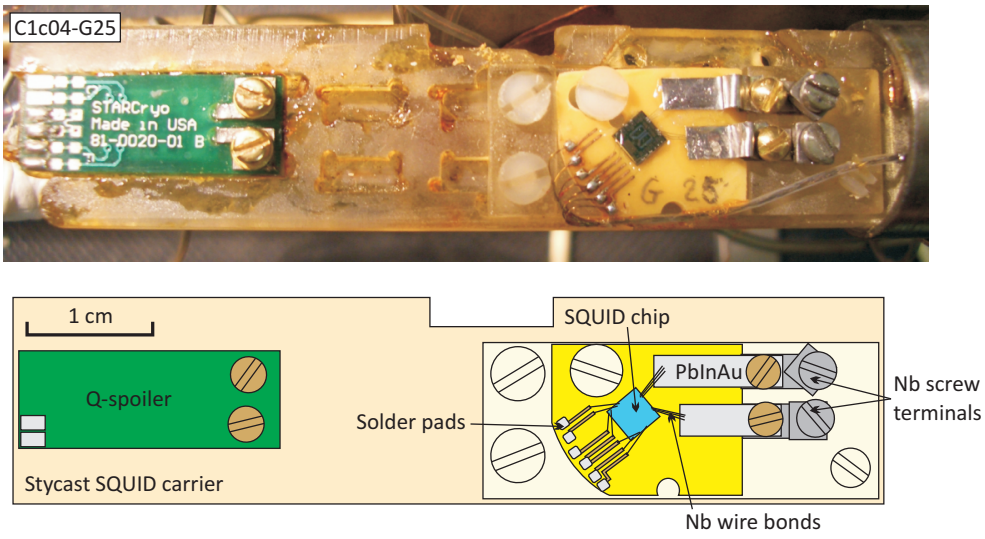

Figure 3.20: Photograph of two-stage SQUID C1c04-G25 and Q-spoiler with labelled schematic. The flux transformer is yet to be connected in this picture.

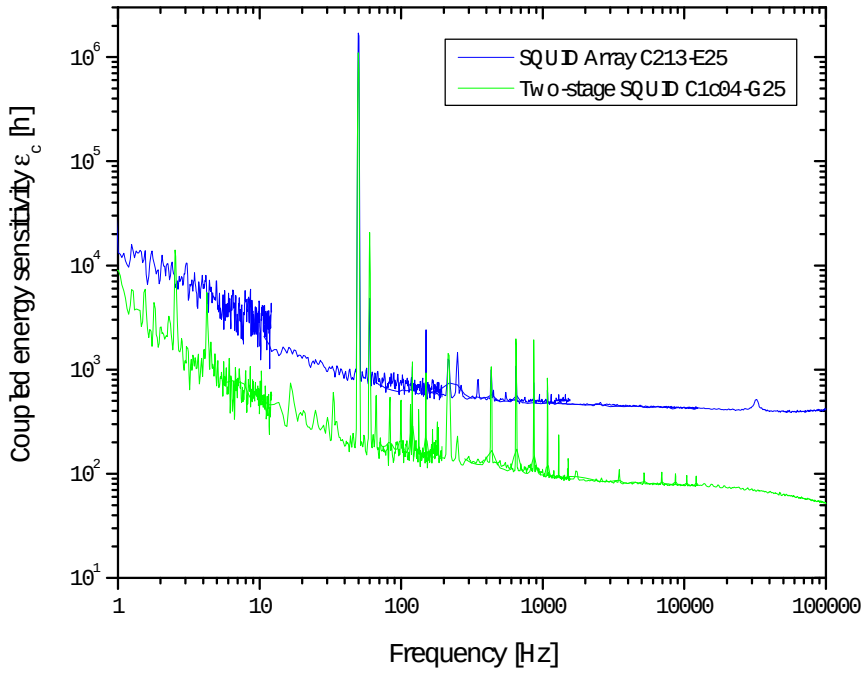

Figure 3.21: Comparison of coupled energy sensitivity of the SQUID array and the new two-stage sensor with the flux transformer connected and the cell at 4.2 K.

on the previous sensor, the SQUID Array C213-E25, which had an ε_c of 400 h at 4.2 K (Figure 3.21). The white noise floor is about 1 $\mu\Phi_0$ Hz$^{-1/2}$ down to 100 Hz with the flux transformer connected. The noise was measured with a low frequency spectrum analyser (Stanford SR760 [35]) with the SQUID in FLL mode, with the sample cell at 4.2 K. In detail, the input range used was -36 dBV (the maximum range without overloading the analyser) and the voltage noise was measured in V Hz$^{-1/2}$ for the frequency ranges given in Table 3.1. This was to improve the

Frequency range	**Number of averages**
0 - 100 kHz	10 000
0 - 12.5 kHz	10 000
0 - 1.56 kHz	10 000
0 - 195 Hz	3 000
0 - 12.2 Hz	3 000

Table 3.1: Frequency ranges and number of averages used to capture noise traces on the SR760 spectrum analyser.

frequency resolution of the captured data. The voltage noise is then normalised by the gain in FLL, G_{FLL} to give the flux noise (see Figure 3.24). For comparison, Table 3.2 lists the parameters of the SQUID array and the two-stage SQUID.

Parameter	**Symbol**	**Array** C213-E25	**Two-Stage** C1c04-G25
Input coil inductance	L_i	1.5 μH	1.1 μH
Mutual inductance SQUID-Input coil	M_i	1.1 nH	6.7 nH
White flux noise @ 100 kHz	Φ_N	0.27 $\mu\Phi_0/\sqrt{\mathrm{Hz}}$	0.84 $\mu\Phi_0/\sqrt{\mathrm{Hz}}$
Coupled energy sensitivity	ε_c	400 h	50 h
Number of wire connections		5	7

Table 3.2: SQUID parameters for the previous SQUID array compared to the new two-stage SQUID sensor. Both SQUIDs operated at 4.2 K. Sample cell at 4.2 K

3.4.8 The superconducting flux transformer

The Q-spoiler (Star Cryoelectronics) that forms a part of the superconducting flux transformer (see Section 2.2.3) is on a separate board and has an adjustable critical current of between 20 and 60 μA depending on the modulation bias. The SQUID chip and Q-spoiler are encased in a closed cylindrical superconducting Nb shield and located approximately 10 cm above the top of the magnet, to shield the SQUID sensor from external fields. The lid of the shield contained 1 mm ⌀ holes for the SQUID and Q-spoiler modulation lines and the flux transformer. The wire used for the flux transformer to connect the SQUID, Q-spoiler and input coil together was bare NbTi wire (0.004" ⌀ bare, 0.005" ⌀ Formvar). Superconducting connections were made with Nb screw terminals onto the bare wire. This wire was made into a twisted pair where possible and outside the SQUID shield, thread through teflon tubing and 1 mm ⌀ Nb tubing for shielding.

3.4.9 RTNMR spectrometer summary

Figure 3.22 is a schematic diagram of the RTNMR spectrometer including the room temperature electronics. The two-stage SQUID sensor is represented by a single SQUID with a feedback coil on the SQUID chip. The transmitter, receiver and magnet coils that have been described in this section have been labelled T_x, R_x and B_0 respectively. The superconducting flux transformer is also visible, with the input coil fabricated on the SQUID chip.

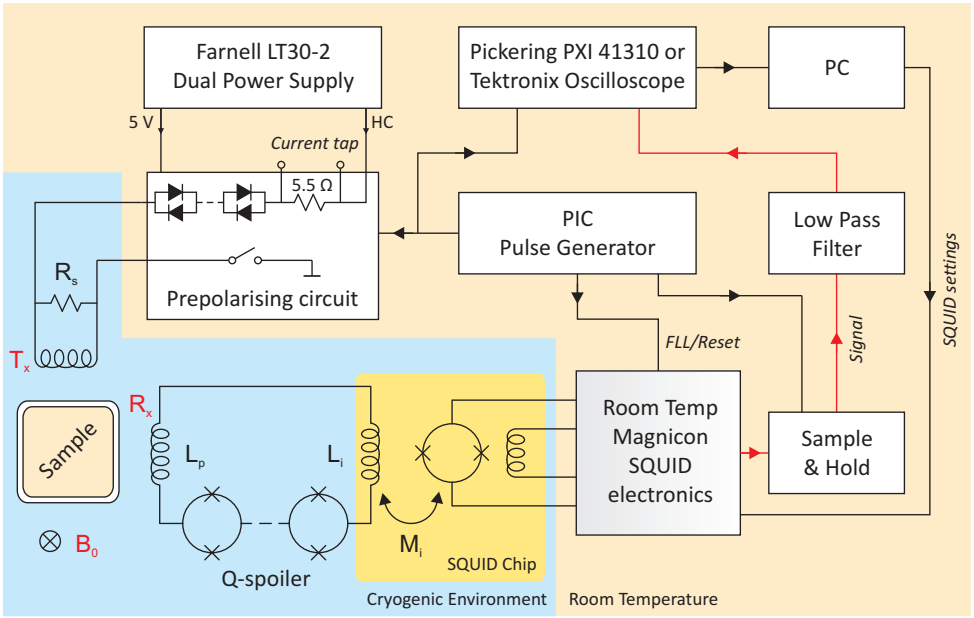

Figure 3.22: Schematic of RTNMR spectrometer.

3.4.10 SQUID setup and characterisation

The SQUID spectrometer was characterised with zero field in the NMR magnet. The bias position used was that supplied by PTB, which are the following: I = 37 μA; $\Phi_x = 6$ μA; $I_b = 7.3$ μA and $V_b = 125.78$ μV. These were set from the PC using the SQUID Viewer software [10]. The feedback resistor R_f used was 10 kΩ, and the gain-bandwidth product set to the lowest available, 0.23 GHz, as we are only interested in low frequency signals. The amp gain was set to 2000. This is just the gain when the SQUID is in open loop mode (amp mode).

V-Φ characteristic

The V-Φ characteristic is a good diagnostic of the SQUID sensor and was checked regularly between experiments. With the SQUID in amp mode, the V-Φ characteristic can be observed by using the internal generator of SQUID Viewer to flux bias the SQUID. A triangle wave modulation bias of amplitude 50 μA_{pp}, at the default frequency of 22 Hz was applied to the 1st stage via the feedback coil (Φ_b), to produce at least one flux quantum and see a V-Φ characteristic. This was viewed by looking at the SQUID output and the generator signal using the xy mode of an oscilloscope. Figure 3.23 shows the characteristic for the two-stage SQUID for an open input coil. The skewed shape is due to the APF implemented on the 1st stage as mentioned in Section 2.2.4.

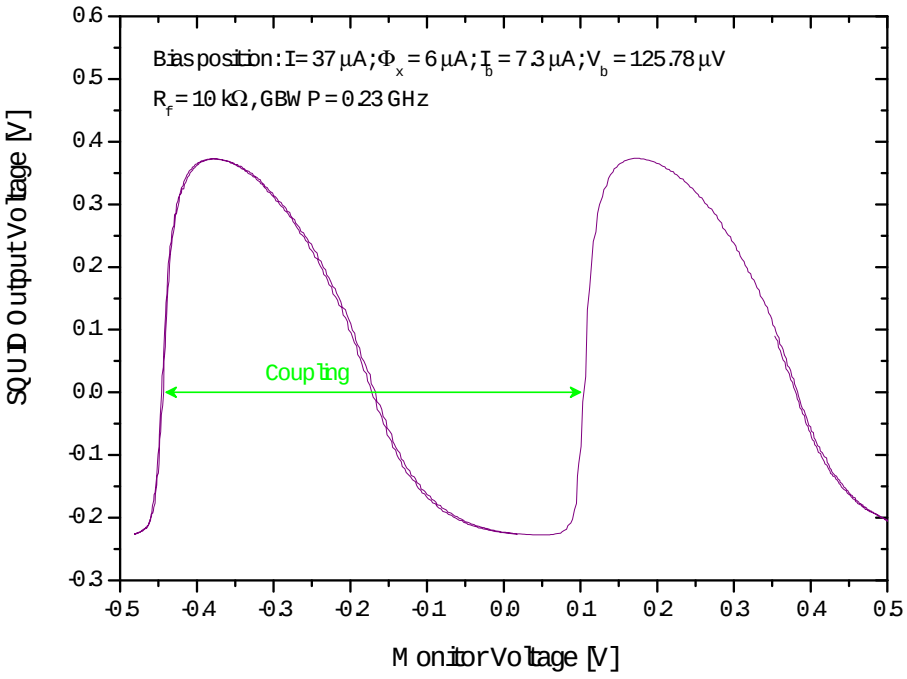

Figure 3.23: Squid V-Φ characteristic for the two-stage SQUID C1c04-G25, with an open input coil.

From this the modulation depth can be measured, giving $\Delta V = 600\ \mathrm{mV}_{pp}/2000$ gain $= 300\ \mu\mathrm{V}_{pp}$. The coupling (as indicated in Figure 3.23) is the period of the characteristic and gives the current needed in the feedback coil to produce one flux quantum in the sensor. This value is denoted by $1/M_f$, the reciprocal of the mutual

inductance of the feedback coil (refer to Figure 2.10 for clarity). In this case, the coupling is 550 mV/Φ_0. Multiplying this by 50 μA_{pp}/1 V (the peak to peak current of the generator) gives $1/M_f = 27.5$ μA/Φ_0. Finally, the characteristic is used to measure the gain in FLL. This is done by simply putting the SQUID into lock using the SQUID Viewer software, which causes linearisation of the characteristic, and measuring its gradient. This was measured as $G_{\mathrm{FLL}} = 280$ mV/Φ_0.

Transmitter-receiver cross coupling

The inverse of the mutual inductance between the transmitter and receiver coils, referred to as the T_x-R_x cross coupling, is also routinely measured. This is the current needed in the transmitter to couple one flux quantum into the SQUID sensor. This is a good diagnostic as if the flux transformer circuit was no longer superconducting or broken, we would measure reduced or no cross coupling. To measure the cross coupling, a cw signal (typically 64 Hz) was fed through the transmitter coil through a 10 kΩ resistor in series with the coil and the amplitude of the cw increased until a period of the V-Φ characteristic could be seen. The SQUID was kept in open loop mode and the SQUID output and cw input were viewed in xy mode on an oscilloscope. The coupling was measured as indicated in Figure 3.23 to be 140 mV/Φ_0 through 10 kΩ, which gives a T_x-R_x cross coupling of 14 μA/Φ_0. This is small compared with the previously measured value of $\sim$ 100 μA/Φ_0 for the SQUID array reflecting the factor of $\sim$6 better mutual inductance M_i between the input coil and the SQUID.

Spectrometer noise

The SQUID noise in FLL is also measured as a good diagnostic to confirm that the spectrometer is functioning normally. Figure 3.24 shows the noise spectrum as measured in Section 3.4.7 (Figure 3.21), reproduced in units of flux noise, $\langle \Phi_N \rangle$ in $\mu\Phi_0$ Hz$^{-1/2}$. Also shown is the SQUID noise with the spectrometer ready for data acquisition i.e. transmitter circuit connected and on and the sample at 300 K. The increase in white noise and pickup is attributed to electromagnetic interference from the room temperature instruments coupling into the SQUID via

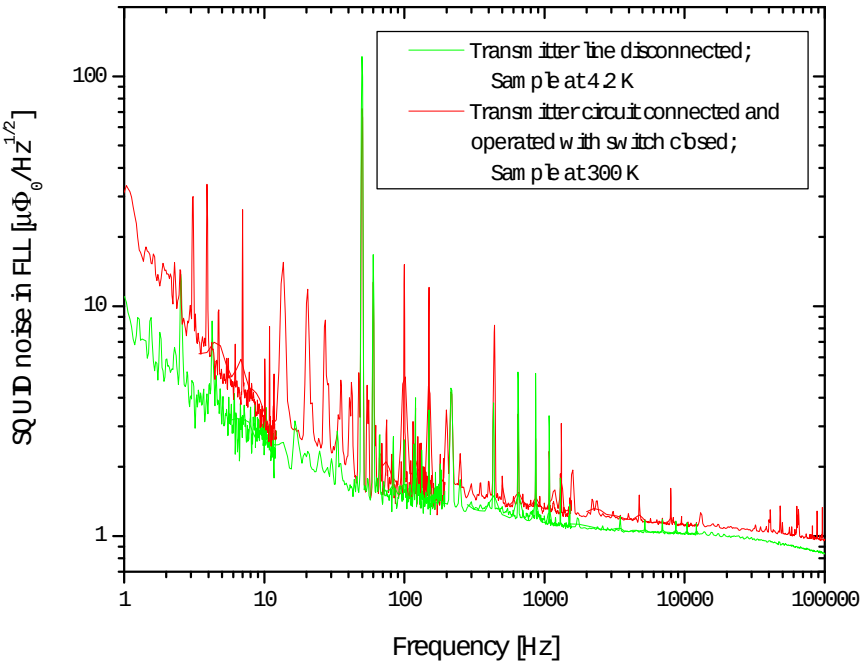

Figure 3.24: Flux noise of the two-stage sensor C1c04-G25 with the flux transformer connected and the cell at 4.2 K compared with slightly higher noise and increased pickup when the prepolarising circuit is connected to the transmitter and on, with the sample at 300 K.

the transmitter receiver cross coupling. The operation of the sample heater has a negligible effect on the noise spectrum. Knowing the noise level of the SQUID spectrometer is important as it enables one to calculate expected signal to noise ratios as will be shown in Section 3.6.3.

3.5 Spectrometer performance and results

In order to assess the spectrometer's performance, a sample of deionised, distilled water was used. The number of spins in the 0.14 ml sample was 9.3×10^{21}, calculated from the mass of water in the cell. After spectrometer characterisation, samples of oil and oil-water mixtures were investigated. The majority of results presented in this section have also been reported in a recent (2007 APL) publication [36].

3.5.1 Signal acquisition procedure

To observe the NMR signal in the low static field, the sample is first magnetised with a prepolarising pulse that is longer than $3 \times T_1$ in order for the magnetisation to grow sufficiently (see Section 3.3). A 10 s long prepolarising pulse was routinely used to magnetise the sample. To pass this dc pulse through the transmitter coil, the prepolarising circuit (see Figure 3.22) contains a switch which opens when a TTL pulse is received, for the duration of the pulse. The TTL pulse duration is controlled by a homebuilt PIC (programmable interface controller) pulse generator[2] (from its Master port). The amplitude of the prepolarising pulse is controlled by adjusting the voltage from a Farnell (LT30-2) power supply (labelled 'HC' for high current in Figure 3.22). The current through the transmitter coil is measured across a monitor resistance in series with the coil, which consists of four 20 Ω resistors in parallel, each with a maximum power rating of 500 mW. This limited the current for the prepolarising pulse with this setup to a maximum of 632 mA. Thus, a current of 630 mA was used for the prepolarising pulse, equivalent to a 2 mT dc prepolarising field at the sample. Finally, any unwanted leakage currents that could flow down to the transmitter whilst the pulse is off are filtered out by 8 pairs of crossed diodes.

The Reset cable from the SQUID electronics is connected to the PIC, and the SQUID put in FLL mode using the SQUID Viewer software. When the Reset cable is connected, the SQUID remains in open loop mode until a pulse is sent to the electronics through the Reset cable that puts the SQUID into FLL for its duration. Figure 3.25 shows a typical pulse sequence for capturing a low field signal for reference to the description that follows.

After an initial delay of 25-85 ms (depending on T_2^*) after the prepolarising pulse, the SQUID is put into FLL (Slave 1 port). This delay enables the largest part of the transient to decay away before capture, aiding subsequent background subtraction. This was acceptable as the water had a T_2^* much longer than this delay time. 1 ms after FLL mode is initiated, the sample and hold is triggered (Slave 2) to

[2]Built by Tom Crane, the PIC can be programmed to emit 4 V TTL pulse sequences through multiple output channels (8 masters and 3 slaves) where the pulse length and delay times between pulses can be specified. It is also used for triggering the various instruments.

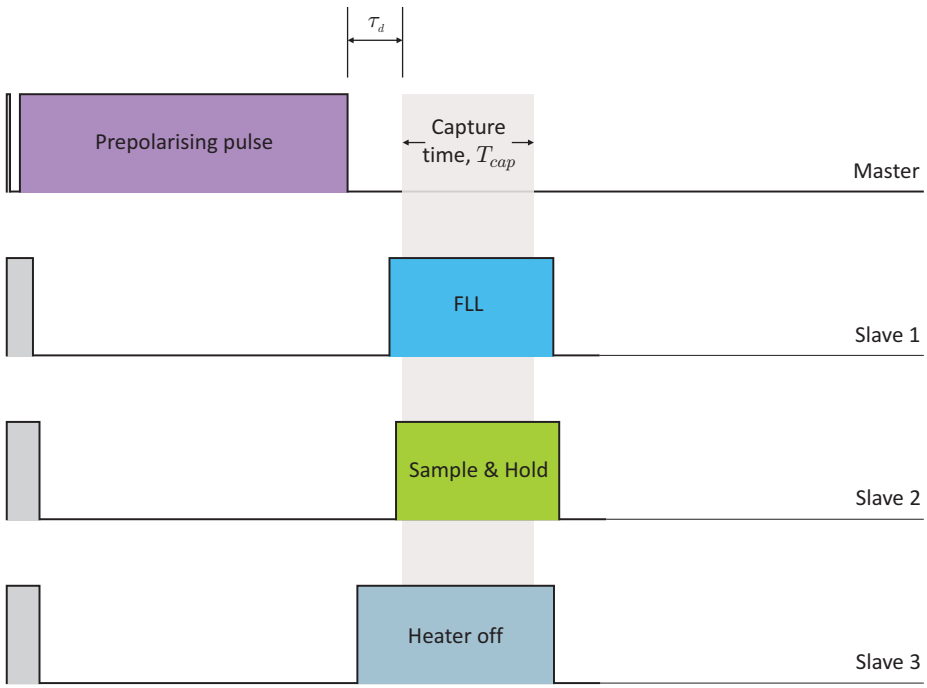

Figure 3.25: A typical pulse sequence for measuring the NMR signal from a room temperature sample (not to scale). The flow of data acquisition and instrument synchronisation is controlled by this pulse sequence from the PIC pulse programmer. The grey pulses are synchronising pulses only and are not emitted.

remove the arbitrary dc offset from the signal. The signal is then filtered using a low pass anti-aliasing filter with a cut-off frequency of $f_c = 1/2\pi CR = 13.4$ kHz, before finally being captured by an oscilloscope. This filter ensures that the captured time trace does not contain frequencies higher than the Nyquist frequency that may be aliased back into the signal for the lowest sampling rate used to capture the data (25 kHz).

The effect on the NMR signal of having the sample heater on continuously was compared with having the heater off (pulsed) during data acquisition. It was found that the signals were sharper when the heater was off during data capture, and that the inferred residual field gradient equalled the measured environmental gradient of 2.5 nT cm^{-1} as shown in Section 3.4 on p 59. This can be explained by considering that a current passing through the heater wire may create a field due to non-perfect field cancellation of the non-inductively wound windings. The heater was thus switched off during data acquisition. The sample heater was switched off

50 ms before the start of data capture (Slave 3) to ensure that the current through the heater had decayed to zero before data capture. In order to keep the sample within a stable temperature range of at most 9 degrees during signal averaging, it was found necessary to pulse the heater with an on/off ratio of 10 i.e. the heater must be on for 10 times longer than it is off. Thus, the capture time determined the repetition period of the pulse sequence.

For capturing the FID, the scope was triggered at the end of the prepolarising pulse (Master) then a subsequent delay, τ_d (shown in Figure 3.25), implemented until data capture. Data capture began 0.5 ms after sample and hold was triggered. Two different scopes were used to capture the signal depending on the capture time, T_{cap}: a Tektronics TDS410A digital oscilloscope and a Pickering 41310 12-bit PXI card with a LabVIEW scope vi. The Tektronics was used for $T_{cap} \gg 1.2$ s as the PXI card was limited to capturing a maximum of 120 000 points at its minimum sampling rate of 100 kHz. The signal was captured for at least $5 \times T_2^*$ so the FID was not truncated. Truncation manifests itself as sinc-like flanks in the frequency domain signal (see Figure 3.26), as well as in artificial linewidth broadening.

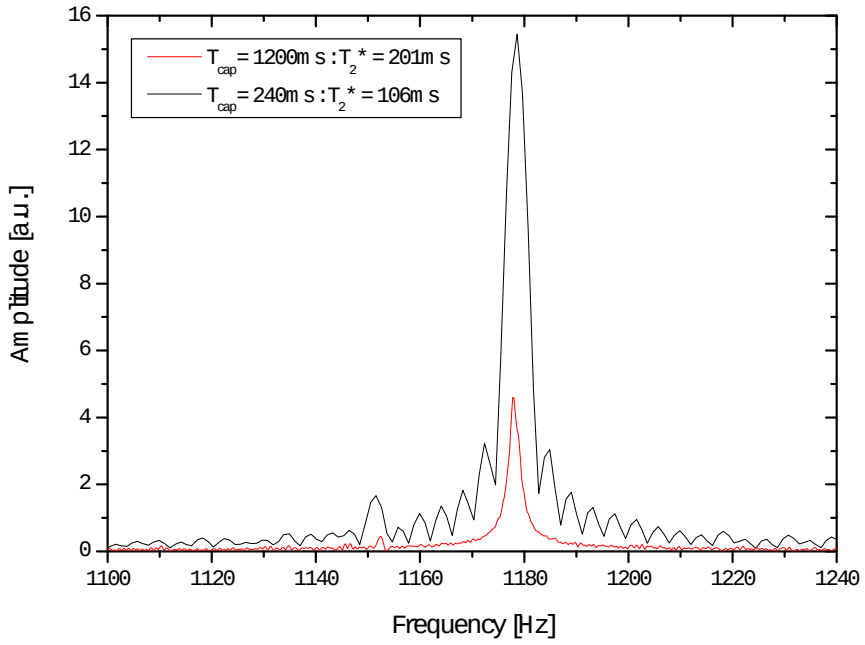

Figure 3.26: NMR line shapes for an adequate capture time of 5 T_2^* (red) and too short a capture time of 1.2 T_2^* (black).

The deadtime of the spectrometer, defined here as the delay time τ_d between the end of the prepolarising pulse and start of reliable data capture - was measured to be 300 μs after a 2 mT pulse (see Section 5.4.4 for method). This is significantly shorter than achieved in earlier work [21, 32] for which a deadtime on the order of tens of milliseconds was reported, due to the magnetic transients induced by the sudden switching of the prepolarising coil. In their setup, the relaxation of paramagnetic impurities in the Pyrex of the cryogenic insert was thought to be saturating the detector, necessitating the use of echoes in order to see the signal. The lack of paramagnetic impurities in the vicinity of the transmitter coil thus enables the measurement of the NMR signal directly from the FID, without the use of echoes.

3.5.2 Signal processing

As described in Section 2.1.7, in order to extract the NMR parameters such as the relaxation time T_2^* and the resonance frequency f_0, the captured FID must be Fourier transformed. However, even with the inner Nb shield in place, the shape of the transient that was superimposed onto the FID was problematic when trying to obtain a good lineshape after Fourier transforming the signal (as shown in Figure 3.27). Thus, before a Fourier transform was performed, an initial background subtraction routine was utilised (written in LabVIEW) that subtracted this transient. The transient is divided into a specified number of time intervals and a 3rd order polynomial is fitted and subtracted from each interval. As can be seen in Figure 3.27, this method was quite successful. It was important here to know the resonance frequency of the signal so it was not subtracted away during this process. This was ensured by making the interval length at least $10/f_0$.

Due to the large signal size of the water sample, it was usually not necessary to use further signal processing techniques in order to see a clear NMR peak in the frequency domain. However, for the lowest resonance frequencies below ~ 150 Hz when the $1/f$ noise started to increase, it was found that the signal clarity was improved by subtracting in the time domain, another NMR transient taken at a slightly different static field from the original FID. For reliable subtraction, the

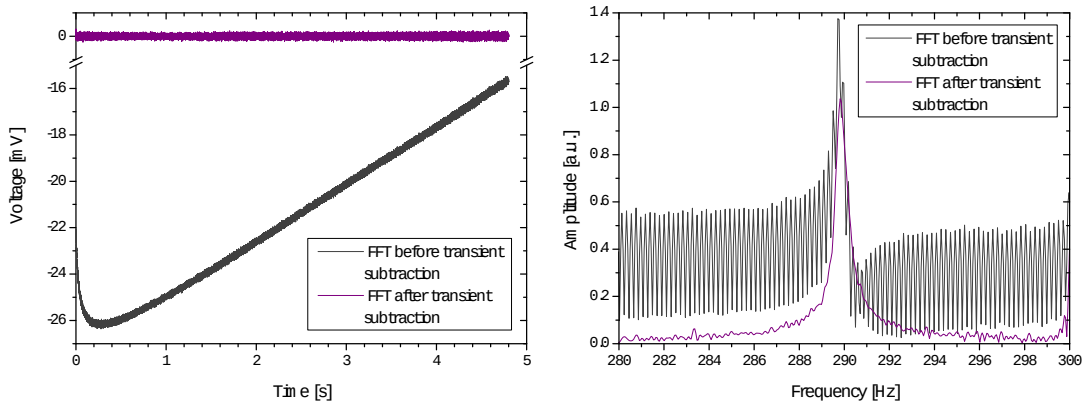

Figure 3.27: Left: Transient shapes before and after background subtraction using a 3rd order polynomial fit to 50 time intervals. Right: The Fourier transform of the transients.

background trace must have the same sampling conditions as the resonance trace i.e. temperature, prepolarising pulse amplitude, capture time and sampling rate. This effectively subtracted away the magneto acoustic background, as mentioned in Section 2.2.5. As the non-resonant nature of the prepolarising method excites all frequencies equally, this method results in the observation of two NMR peaks (a resonance for each static field).

The background subtraction and Fourier transformation of the transient were both performed in LabVIEW using a program written by Chris Lusher. The fast Fourier transform (FFT) algorithm requires the number of data points, N to be a power of two and so zero filling is used to pad the data out with zeros to the next highest power of two. Using this routine, the peak height in the frequency domain is given by Equation 2.23.

A Lorentzian fit was then performed to the square of the magnitude of the Fourier transform ($|F(f)|^2$) in Origin 7.0. The fit is performed to the following equation:

$$F(f) = \frac{2B}{\pi} \frac{\Delta\nu_{meas}}{4(f - f_0)^2 + \Delta\nu_{meas}^2}. \tag{3.3}$$

From this, the frequency f_0, linewidth $\Delta\nu_{meas}$ and B are obtained as fit parameters. The peak height of the magnitude of the FT is described by $H_0 = \sqrt{\pi B}$.

3.5.3 Water signals as a function of frequency

As the spectrometer is a broadband system, it was simple for NMR signals to be taken as a function of frequency or equivalently, field. Figure 3.28 shows proton NMR lines in water taken at 280 K ($\sim$ 7°C). The sharpening of the NMR line and consequent increase in signal size is shown for several positive currents in the static field magnet. The NMR signals show that when the measurement field is decreased from 10 μT to 1.5 μT, linewidths down to 0.25 Hz can be obtained. In Section 3.5.5, even narrower linewidths of 0.16 Hz are obtained due to a slight increase in sample temperature. In magnetic resonance spectroscopy, the spectrum can be very complex, with J-coupling constants (the splitting between NMR peaks) of only a few Hz (see Section 3.1). Therefore, having linewidths of only a fraction of a Hz shows promise for improving frequency resolution in low magnetic field spectroscopy, enabling a more accurate measurement of J-coupling constants.

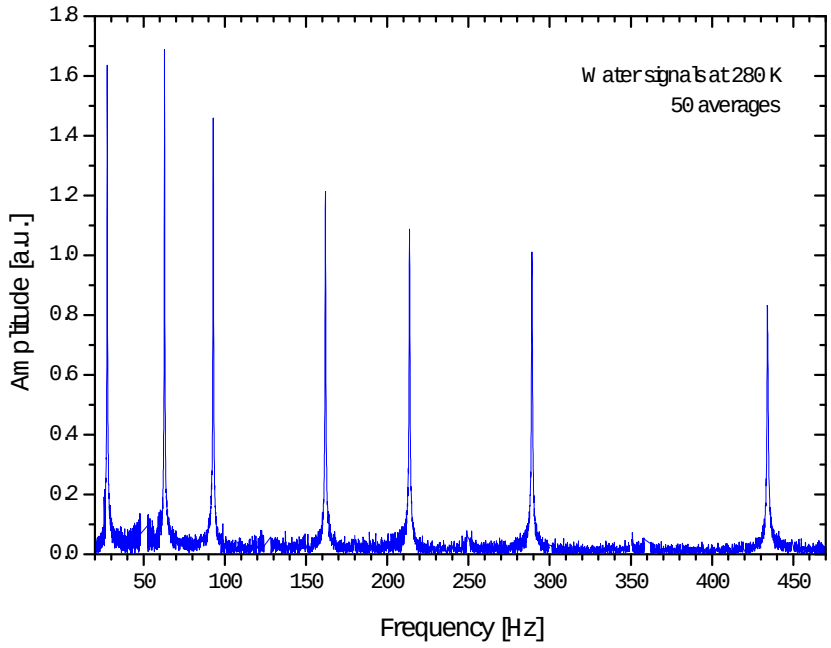

Figure 3.28: Signals from water at 280 K after a 2 mT prepolarising pulse for 10 seconds. 50 averages. The growth in signal size can be seen as B_0 is decreased from 10.2 μT to 648 nT. 50 and 60 Hz harmonics have been omitted for clarity.

As proof of principle, signals from water were obtained down to a resonance frequency of 4 Hz. The linewidth and static field of each signal is shown in Fig-

ure 3.29. These signals were taken with the same conditions as for those in Figure 3.28. The capture times here ranged from 4.8 s for the sharpest signals to 1.2 s for the broadest.

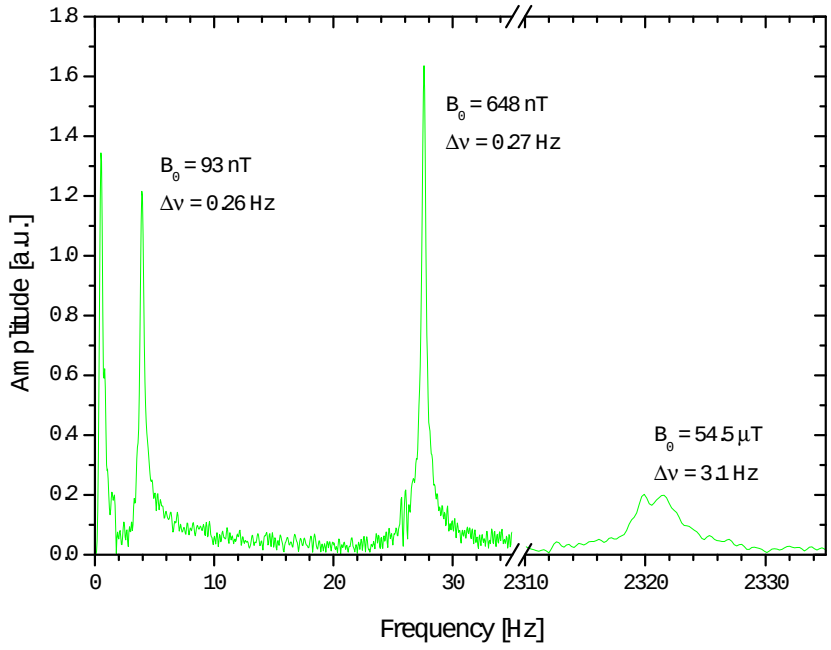

Figure 3.29: Signals from water at 280 K showing the linewidth becoming sharper as the measurement field is decreased.

3.5.4 Signal size calculations for water

Comparing the expected signal size in the frequency domain to the observed signal size enables one to see if the NMR spectrometer is understood. For a sample that has been excited using a prepolarising field B_p, this calculation is slightly different from that excited using an rf field. Calculations are presented here for the NMR signal from water shown in Figure 3.30.

Recall from Section 2.1.7 that the signal size in the frequency domain, H_0, for the FFT routine performed in LabVIEW is given by:

$$H_0 = \frac{AT_2^*}{2\Delta}, \tag{3.4}$$

where here the time between points captured, $\Delta = 10$ μs and A is the initial

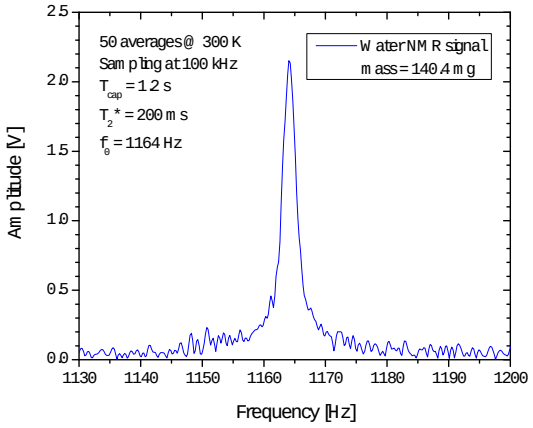

Figure 3.30: Signal from water at 300 K using a 2 mT prepolarising field, measured in a static field of $B_0 = 27.3$ μT.

amplitude of the FID in the time domain. To calculate A, we start with the initial magnetisation, M_0 and convert this into a voltage using SQUID parameters.

Following a prepolarising pulse of sufficient duration to build up the equilibrium magnetisation of the sample, the initial magnetisation is given by Equation 2.3 but with B_0 replaced by B_p:

$$M_0 = \frac{N_v \hbar^2 \gamma^2}{4 k_B T} B_p. \tag{3.5}$$

The number density of protons in water is $N_{V\ water} = 6.7 \times 10^{28}$ m^{-3}. The gyromagnetic ratio for protons is $\gamma_H = 26.75 \times 10^7$ Hz T^{-1}. $\hbar = 1.05 \times 10^{-34}$ J s and $k_B = 1.38 \times 10^{-23}$ J K^{-1}. Using $B_p = 2.0$ mT and $T = 300$ K, we obtain a magnetisation

$$M_0 = 6.38 \times 10^{-6} \text{ A m}^{-1}.$$

The flux picked up in the receiver coil, Φ_p, can be calculated using the principle of reciprocity [37]. The principle states that the current induced in a coil by a precessing magnetic dipole at a point P is related to the magnetic field that would be produced at P if there was a unit current flowing through the coil. It follows that

$$\Phi_p = B_{1p} M_0 V_s, \tag{3.6}$$

where the magnetic field per unit current of the pickup coil $B_{1p} = 579$ μT A^{-1}. The sample volume can be calculated knowing the mass (140.4×10^{-6} kg) and the

density of water at 300 K ($\rho_{300\ K} = 998.23$ kg m^{-3}), giving $V_s = 141 \times 10^{-9}$ m^3. This gives

$$\Phi_p = 5.22 \times 10^{-16} \text{ Wb} = 252 \text{ m}\Phi_0,$$

in units of the flux quantum, Φ_0. From this we can calculate the flux in the SQUID, Φ_{SQ}, coupled via the flux transformer and mutual inductance M_i between the input coil of the SQUID and the SQUID loop itself using Equation 2.28:

$$\Phi_{SQ} = \frac{\Phi_p M_i}{(L_i + L_p)}. \tag{3.7}$$

For the two-stage SQUID C1c04-G25, $M_i = 6.7$ nH, $L_i = 1.1$ μH and $L_p = 1.4$ μH, giving

$$\Phi_{SQ} = 676 \text{ } \mu\Phi_0.$$

Now we can calculate the initial amplitude of the FID in the time domain, A by multiplying by the gain in FLL ($G_{FLL} = 280$ mV Φ_0^{-1}):

$$A = \Phi_{SQ} G_{FLL} = 189 \text{ } \mu\text{V}. \tag{3.8}$$

Finally, the signal size (peak height) of the NMR line in the frequency domain can be calculated using Equation 3.4 and for the signal in Figure 3.30. This assumes we do not lose any signal size due to the deadtime of the spectrometer. This is valid because T_2^* is very long. The expected signal size is:

$$H_0 = 1.89 \text{ V},$$

which is acceptably close to the measured signal size of 2.15 V.

3.5.5 Reaching the intrinsic linewidth

By measuring the linewidths of the proton NMR signals from water as a function of frequency for both polarities of current in the magnet, it is possible to measure the homogeneity of the magnet, the residual field gradient at the sample due to the environment and the intrinsic relaxation time T_2.

The measured linewidth $\Delta\nu_{meas} = 1/(\pi T_2^*)$ is given approximately by

$$\Delta\nu_{meas} = \Delta\nu_{in} + |\alpha\nu + \beta|, \tag{3.9}$$

where $\Delta\nu_{in} = 1/(\pi T_2)$ is the intrinsic linewidth, α quantifies the broadening due to the magnet inhomogeneity and β is the environmental residual field gradient with zero current in the magnet. Figure 3.31 shows a plot of signals in the low field regime for two temperatures of the water sample. The linewidths for the higher temperature of 300 K are slightly narrower than those for the 280 K set due to motional narrowing as described in Section 2.1.5.

From a linear fit, the slope of both data sets at the higher frequencies gives $|\alpha| = |\Delta B/B_0| \sim$ 780 ppm over the sample volume. From the separation of the two slopes, $|\beta| \sim$ 50 mHz for Figure 3.31(a) and 31.5 mHz for Figure 3.31(b). The environmental residual field gradient was slightly different for every cooldown of the probe, reflecting the slightly different field gradients trapped in the superconducting shield each time. In the higher temperature run, this corresponded to a residual field gradient of $\sim$ 1 nT cm^{-1}, consistent with that measured at room temperature at the sample region in the absence of the dipper probe, using a fluxgate magnetometer (as shown on p. 61).

At zero current in the magnet, the 300 K data for both polarities of current converge to give a linewidth of $\sim$0.20 Hz. For one polarity of the current, the magnet contribution to the field gradient opposes the residual gradient, resulting in a narrower line at finite frequency, as shown in Figure 3.31 for the negative current data. A simple model of perfect compensation would result in $\Delta\nu_{in}$ being measured at a frequency of $\nu_{min} = |\beta/\alpha| \sim 40$ Hz, approximately consistent with these data. The residual field trapped in the shields is $\sim$50 nT, determined from the shift of the line on reversing the current in the NMR magnet (See Figure 3.32). Burghoff *et al.* [20] obtained similar linewidths from water (with $|\alpha| \sim$500 ppm) on a 20 ml sample taken in the extremely low residual field environment of the Berlin magnetically screened room, indicated in Figure 3.31(b). The combination of our compact shielding arrangement and the sensitivity of the two-stage SQUID

sensor allows us to perform high resolution spectroscopy on small samples, under far less stringent conditions and with potential portability.

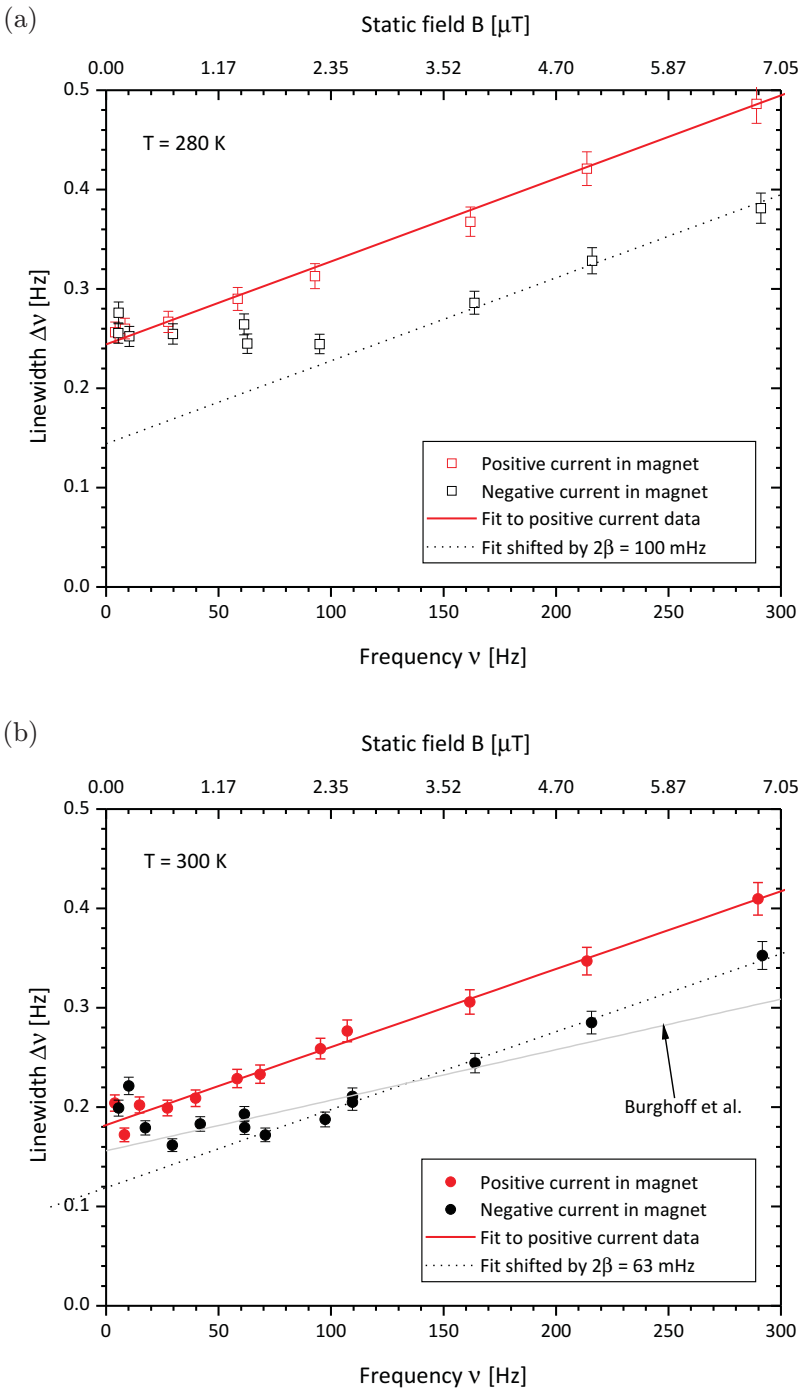

Figure 3.31: Linewidth of proton NMR signals from water plotted as a function of frequency for two different sample temperatures; (a) 280 K; (b) 300 K. 50 averages. The linewidths obtained in Berlin's magnetically shielded room is drawn in grey [20].

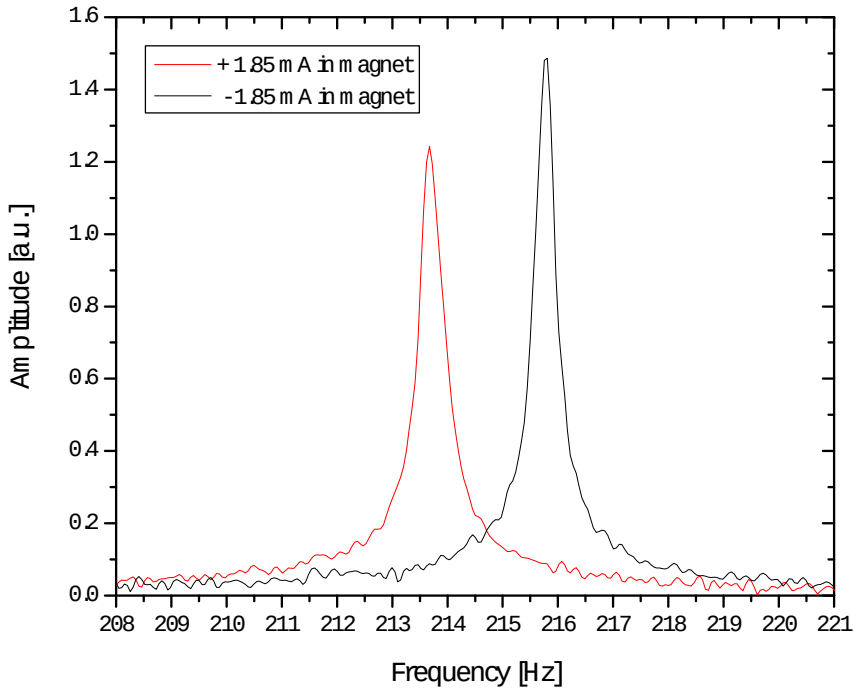

Figure 3.32: Signals at ∼215 Hz taken with the same current in the magnet but different polarities. The difference in the Larmor frequencies is 2.1 Hz, indicating a residual field of 50 nT trapped in the shields. $B_0 \sim 5.0$ μT.

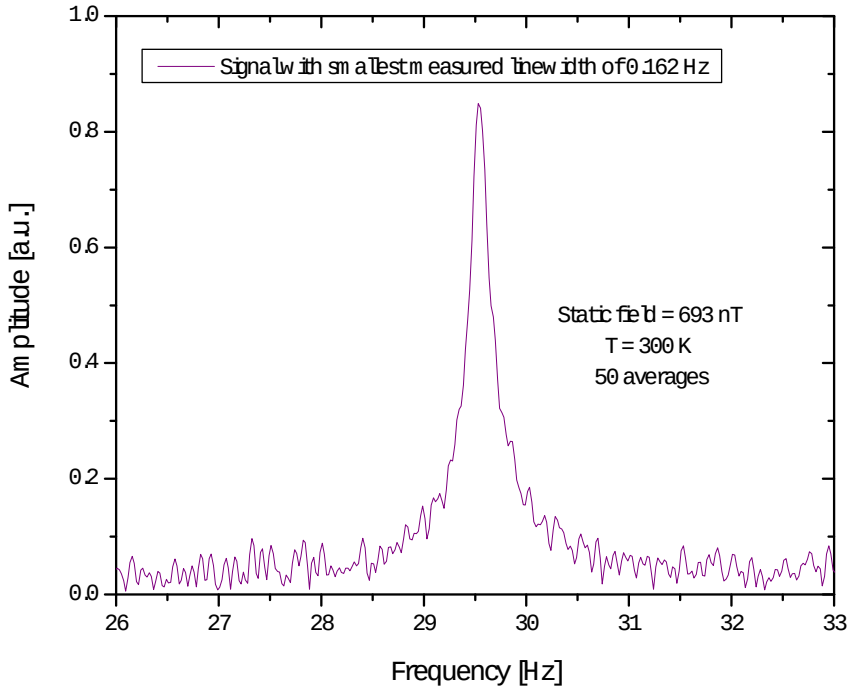

Figure 3.33: Water NMR signal with the narrowest linewidth.

The smallest linewidths observed were approximately 0.16 Hz, giving a T_2^* of 2.0 s (Figure 3.33). Although the data were routinely analysed with 50 averages for a better signal to noise ratio (SNR), with the low linewidths a SNR of ∼5 was possible in a single shot.

Signals from water were measured for fields up to ∼ the Earth's field for water. This is shown for the 300 K set in Figure 3.34.

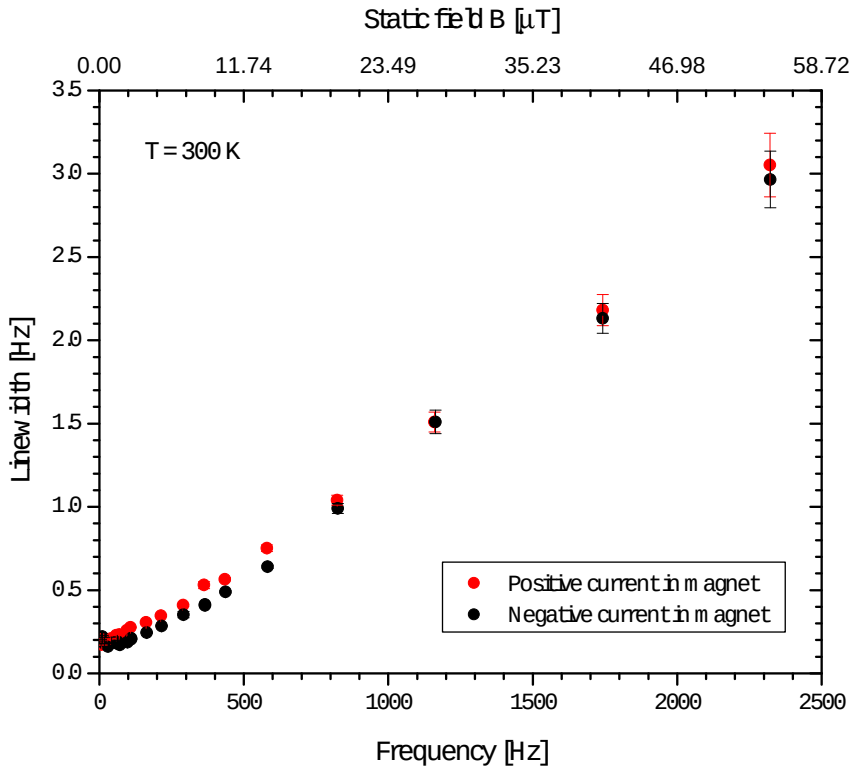

Figure 3.34: Signals from water at 300 K extended to higher fields.

3.5.6 Low field T_1 of water

Furthermore, the longitudinal relaxation time T_1 of water was measured at 296 K, in a measurement field of 1.69 μT. In such low measurement fields, a special spin manipulation pulse sequence had to be used in order to produce a measurable magnetisation that was allowed to undergo T_1 relaxation in the z-direction. This measurement was performed later on in the development of the RTNMR spectrometer, after several modifications had been made to increase the SNR (see

Section 3.7) but is documented here for clarity.

The principle behind the technique is as follows (refer to Figure 3.35 for guidance). The low measurement field B_0 is created by the magnet in the z-direction.

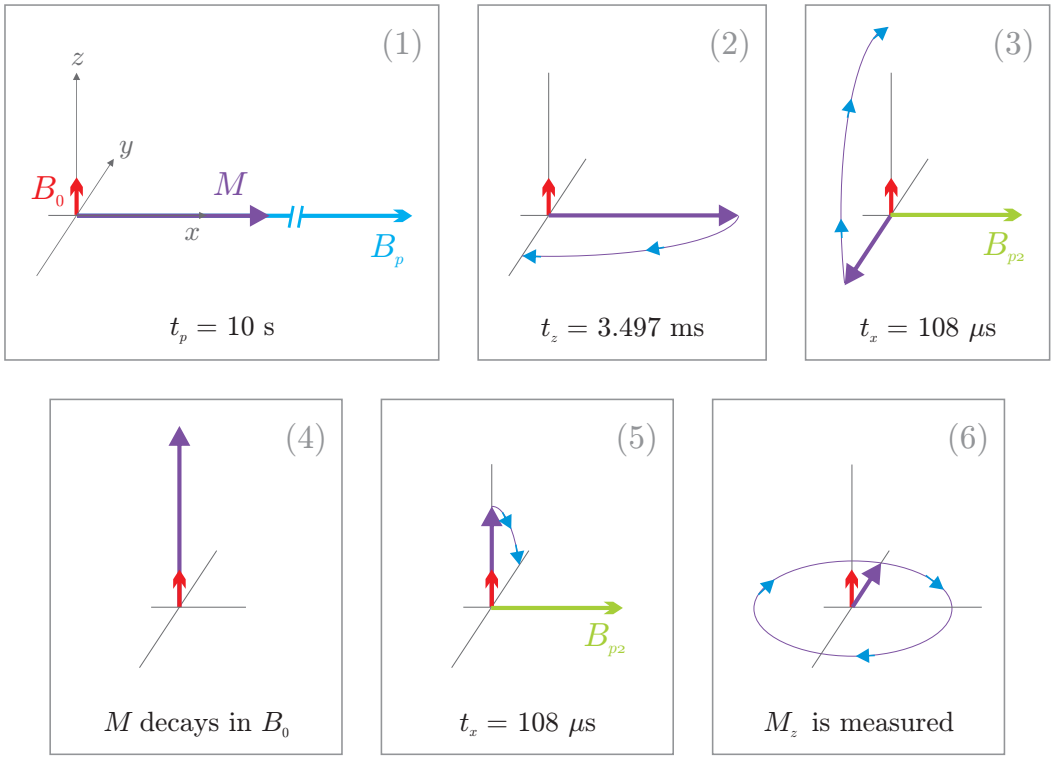

Figure 3.35: Pictorial representation of the pulse sequence used to measure T_1 at low fields. The various fields applied are shown; the magnetisation is shown in purple.

(1) A high field prepolarising pulse B_p is applied through the transmitter coil, to build up a magnetisation M in the x-direction. (2) This pulse is turned off and the magnetisation now only sees B_0. We wait a time t_z for M to rotate 90° around B_0 into the $-y$-direction. This corresponds to a quarter of the Larmor period for precession about B_0. (3) Then a smaller prepolarising pulse B_{p2} is applied through the transmitter, where $B_0 \ll B_{p2} \ll B_p$. Now, as $B_{p2} \gg B_0$, the magnetisation will precess about the x-axis. We again let M precess through 90° by leaving B_{p2} on for a time t_x, after which the magnetisation should be in the z-direction. (4) Here, M decays exponentially with time constant T_1 down to the equilibrium magnetisation of the low measurement field. (5) However, in order to measure the degree of relaxation after a particular time τ, we wait a time τ then again apply

the smaller prepolarising field B_{p2} for time t_x. This will cause the z-magnetisation to precess a further 90° into the measurement plane, where (6) its precession can be detected by the receiver coil. If the peak height of the magnitude of the NMR line in the frequency domain is plotted as a function of τ, a fit to an exponentially decaying function will yield the time constant T_1 as shown in Figure 3.36.

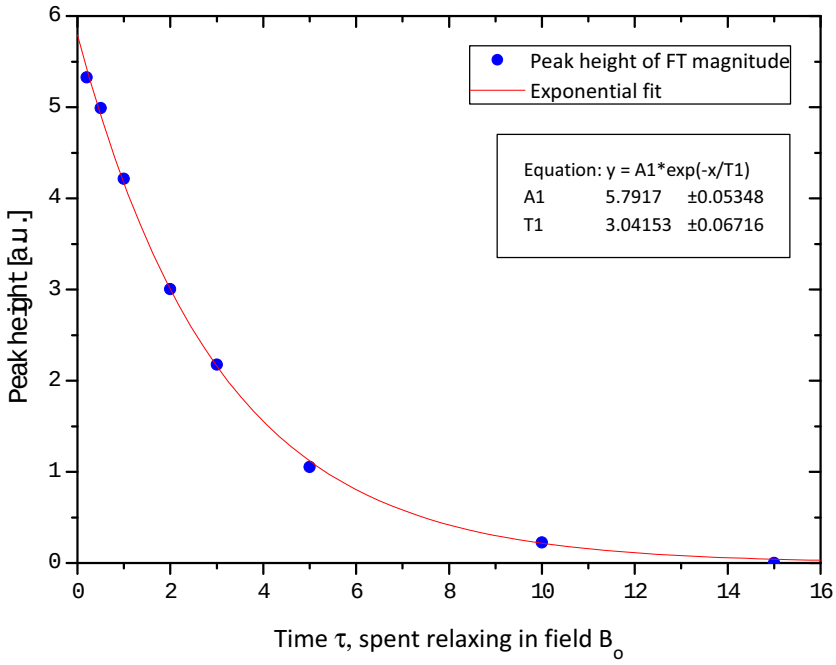

Figure 3.36: T_1 Relaxation of water at 296 K in a field of 1.69 μT from a higher than equilibrium initial magnetisation.

Practically, this experiment was achieved by using two signal generators to supply the required prepolarising pulses B_p (Stanford DS345) and B_{p2} (Agilent 33120A) to the Techron amplifier (described in Section 3.7.2). These were triggered by the PIC pulse generator. The initial prepolarising pulse, $B_p = 4.09$ mT, was applied for $t_p = 10$ s. The static field $B_0 = 1.69$ μT, giving $t_y = 3.497$ ms and $B_{p2} = 54$ μT, giving $t_z = 108$ μs. After a delay of 85.5 ms after the initial prepolarising pulse, data was captured for 4.8 s with a sampling frequency of 50 kHz. 10 averages were taken for each delay, τ. The sample heater was operated continuously as the background field gradient was sufficiently low to be able to see a sharp signal, resulting in a much shorter repetition time of ~ 17 s as opposed to $\sim$ 50s with the heater pulsed. Furthermore, no sample and hold was used in this

experiment.

Figure 3.36 shows the resulting T_1 relaxation, giving $T_1 = (3.04 \pm 0.07)$ s. The linewidths obtained from water at 300 K (Figure 3.31b) are therefore close to intrinsic with T_2 approaching T_1 as expected for the case when the motion of the spins is more rapid than the Larmor period, when $\omega_0 \tau_c \ll 1$ as described in Section 2.1.5.

3.5.7 Oil-water mixture

As the magnetic field approaches zero, we have seen that the measured relaxation times T_2^* approach T_2 due to the decrease in inhomogeneous broadening. This effect can be exploited together with the short deadtime of the spectrometer, to observe two proton T_2 components directly from the FID. Measurements from an oil-water mixture are presented in this section. The oil used was Shell Vitrea 33, a machine oil.

Characterising the new sample cell

A new sample cell was made for this experiment. This time the heater wire was changed to manganin wire (bare ⌀ 30 μm, resistance 1.09 kΩ) as we had run out of the original NbTi wire. Manganin was chosen as it has low thermal conductivity and high resistivity which help minimise the heat flow through the leads. By characterising this new cell using a water sample, it was found that although the residual field gradient was slightly larger (3.6 nT cm^{-1}) than for the previous cell (1 nT cm^{-1}) with the heater pulsed, in this case it did not have a great effect on the linewidth whether the heater was on permanently or pulsed during data capture. This made data acquisition about a factor of 10 faster, than with the previous heater. With the heater on during data capture, a residual field gradient of 5.6 nT cm^{-1} was measured.

3.5.8 Characterising the oil

To first characterise the Shell Vitrea 33 oil separately from the water, the above sample cell was emptied and filled with approximately the same volume of oil. The contents were weighed on a balance accurate to 0.1 mg giving the mass of the oil as 122.9 mg, inferring a density of 871.63 kg m^{-3}.

T_1 of the machine oil at 300 K was measured in the prepolarising field of 2 mT in order to be confident that the length of the prepolarising pulse is adequate for full sample magnetisation. This can be measured by plotting the NMR peak height of the FT as a function of the length of the prepolarising pulse, τ_p. The signals were initially excited using increasing lengths of the prepolarising pulse, starting from 2 ms up to 1 s, but allowed to decay and measured in the lower static field of 117 μT. The data was captured for 120 ms at 1 MHz sampling frequency, with a repetition time of 3 s. 500 averages were taken for each τ_p to obtain a good SNR. Figure 3.37 shows the measured NMR signals (left) and their peak height as a function of τ_p (right). Fitting the data to Equation 2.6c with $M(0) = 0$ and M_0 and T_1 as free parameters, T_1 was found to be (27.3 ± 2.7) ms.

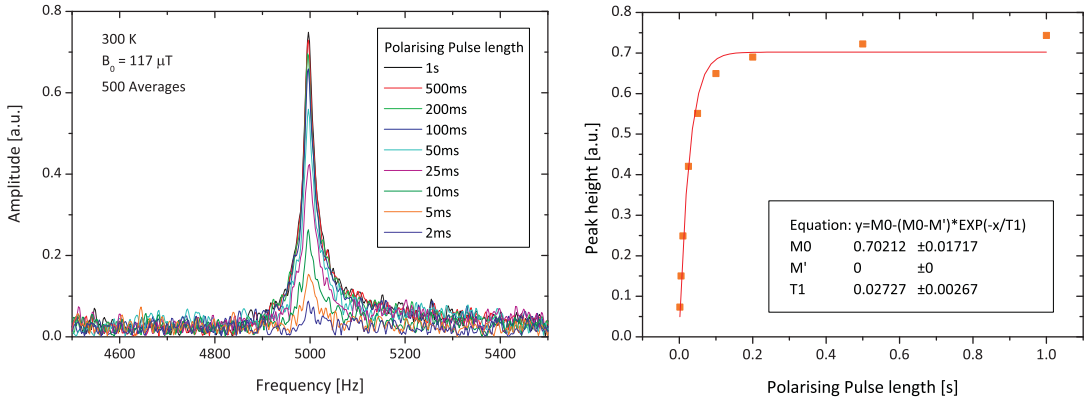

Figure 3.37: T_1 Relaxation of oil at 300 K in a field of 117 μT.

The length of the prepolarising pulse was also shortened to 1 s for maximum magnetisation in light of this result. This enabled many more averages to be taken in the same time, helping to get a clearer signal as the oil signal was inherently broader and smaller than the water signal. 500 averages were taken routinely, with a repetition time of 3 s (limited by the triggering speed of the PXI scope program).

NMR signals of the oil were also taken as a function of field in order to have an estimate of T_2^* at low fields. The narrowest linewidths obtained were just over 10 Hz, giving a T_2^* of ∼30 ms at room temperature (300 K).

By assuming that the volume of the oil sample is equal to the volume of the water sample used in Section 3.5.4, the spin density of the oil $N_{V\ oil}$ can be inferred, as the measured and expected signal sizes for water were very close. Analysing an NMR signal from oil taken in approximately the same static field as the water, this time one can begin with the measured signal size of the oil and calculate back to the initial magnetisation M_0. As all the parameters needed for this calculation are known (apart from the exact volume), this is a convenient way of calculating the spin density. The NMR signal from oil used in this estimation of $N_{V\ oil}$ is shown in Figure 3.38.

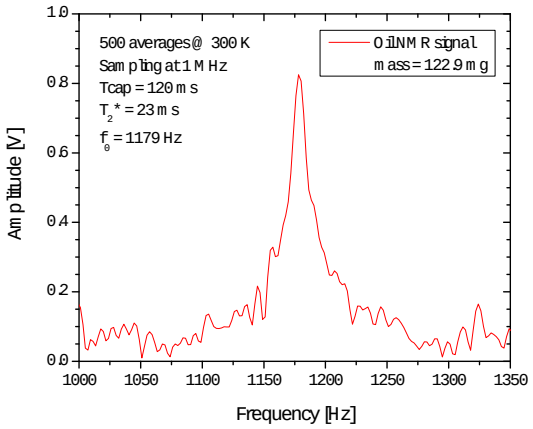

Figure 3.38: Signal from oil at 300 K using a 2 mT prepolarising field, measured in a static field of $B_0 = 27.7$ μT.

From Figure 3.38, the signal size $H_0 = 0.813$ V. The gain in FLL is 270 mV/Φ_0. Using the measured parameters given in the figure and the same SQUID parameters as in Section 3.5.4, the initial magnetisation is estimated to be $M_0 = 2.46 \times 10^{-6}$ A m^{-1}, using Equations 3.8, 3.7 then 3.6. Now using Equation 3.5, again with a prepolarising field of 2 mT, the calculated spin density for oil is $N_{V\ oil} = 2.58 \times 10^{28}$ m^{-3}. The number of proton spins in this sample is therefore 3.64×10^{21}.

To see how the temperature affects the NMR signal of oil, in particular at the

freezing temperature of water, a simple experiment was done to measure linewidth as a function of temperature (Figure 3.39). The dependence is attributed to the temperature dependent viscosity. By 278 K, the viscosity of the oil was so high that the signal could no longer be captured with the same pulse sequence. As shown for the water sample, this reduced T_2^* is attributed to motional narrowing. Figure 3.40 shows our measurements of the temperature dependence of the linewidth of the oil compared with its quoted viscosity, both normalized by their 300 K values. The intrinsic linewidth obeys the expected relationship $T_2^{-1} \propto \eta(T)T^{-1}$ where $\eta(T)$ is the temperature dependent viscosity [38].

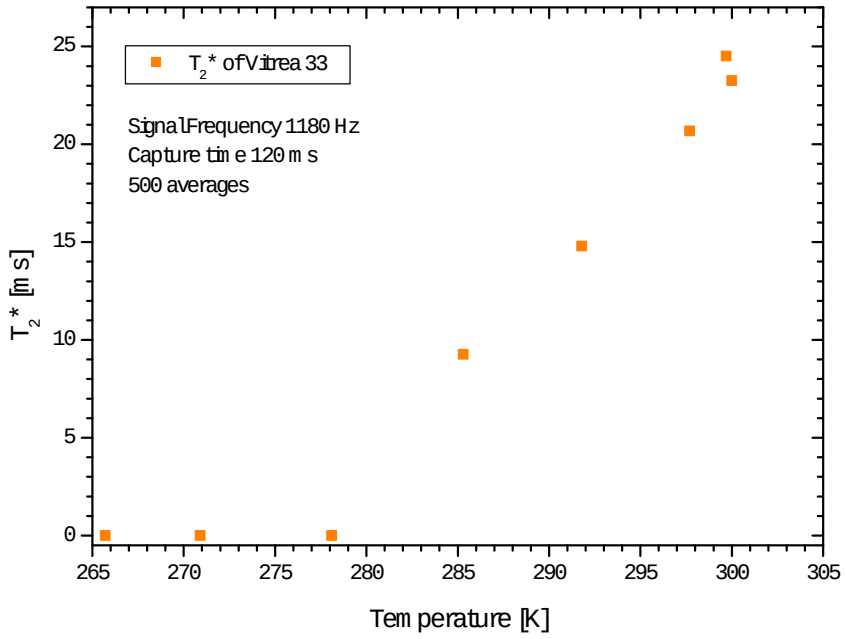

Figure 3.39: Temperature dependence of measured linewidth of Vitrea 33 oil.

The oil-water mixture

A 4:1 oil:water mixture by mass ratio was chosen to clearly show a two component signal. 100.3 mg of Shell Vitrea 33 oil and 25.0 mg of deionised water were injected into the sample cell and sealed. This has a calculated spin ratio of 1.77(oil):1(water) with a total of 4.82×10^{21} spins.

An NMR signal was taken at a measurement field of 55 μT at 300 K. A 2 mT prepolarising pulse was applied for 10 s to sufficiently magnetise both components

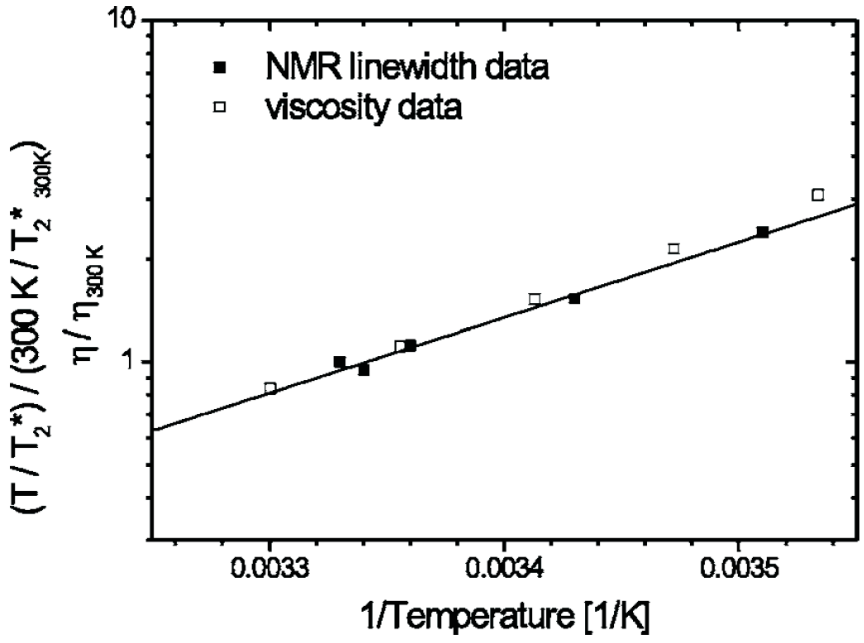

Figure 3.40: Temperature dependence of NMR linewidth and viscosity in Vitrea 33 oil normalised to 300 K values. The NMR sample contained 3.9×10^{21} protons, as determined from the signal size.

and the data captured 2.5 ms after this pulse for 600 ms. The Fourier transform of 500 averages can be seen by the red trace in Figure 3.41. A T_2^* of ∼20 ms is determined for the short component, in agreement with that measured on a pure oil sample at 300 K in this field.

In light of the previous viscosity experiment, data were also taken at 275 K, for which there is no oil contribution. This is shown by the data in blue in Figure 3.41. From comparison we can see that the oil contribution manifests itself in the wider flanks of the NMR line and a slight increase in signal size in the frequency domain.

In order to observe the two-component FID in Figure 3.42, a Gaussian filter of width 100 Hz centred at the Larmor frequency was used to extract the signal in the frequency domain, before inverse Fourier transforming back into the time domain. The nonexponential decay of the water component results from the field profile of the NMR magnet. A simulation of the two component signal was performed in Mathematica to aid the interpretation of the measured data and is shown in Figure 3.43.

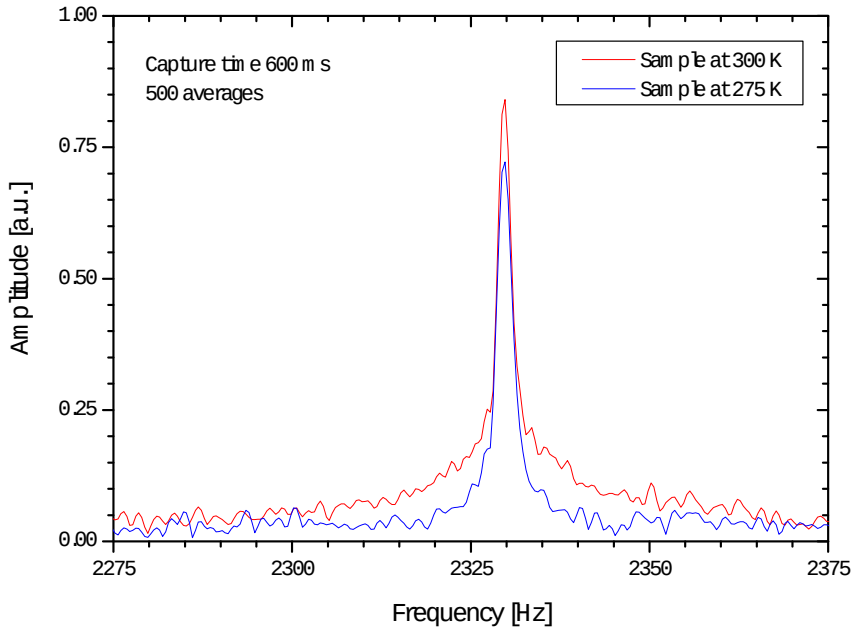

Figure 3.41: NMR lineshapes in the frequency domain of an oil-water mixture of 4:1 by mass at 300 K and 275 K. $B_0 = 54.7$ μT.

The two-component FID is clearly seen at 300 K in Figure 3.42. The fast decaying oil component and the slower water component is evident. The initial amplitude of the FID for this temperature is ~ 85 and is directly proportional to the number of spins in the oil-water sample. The initial amplitude of the FID for the water component can most clearly be seen in the trace taken at 275 K, when only the water protons contribute to the signal. Here, the initial amplitude is ~ 30. The ratio of these amplitudes is $30/85 = 0.35$. The estimated ratio of spins for this sample is almost identical:

$$\frac{\#\ \text{Spins(Water)}}{\#\ \text{Spins(Water)} + \#\ \text{Spins(Oil)}} = \frac{1.68 \times 10^{21}}{1.68 \times 10^{21} + 2.97 \times 10^{21}} = 0.36$$

This experiment showed that at low fields, the reduction in inhomogeneous broadening and short deadtime of the spectrometer allow two component relaxation to be seen directly in the FID, allowing the straightforward determination of the oil/water ratio. These results show promise as a technique for detecting relatively low levels of water contamination in oil samples.

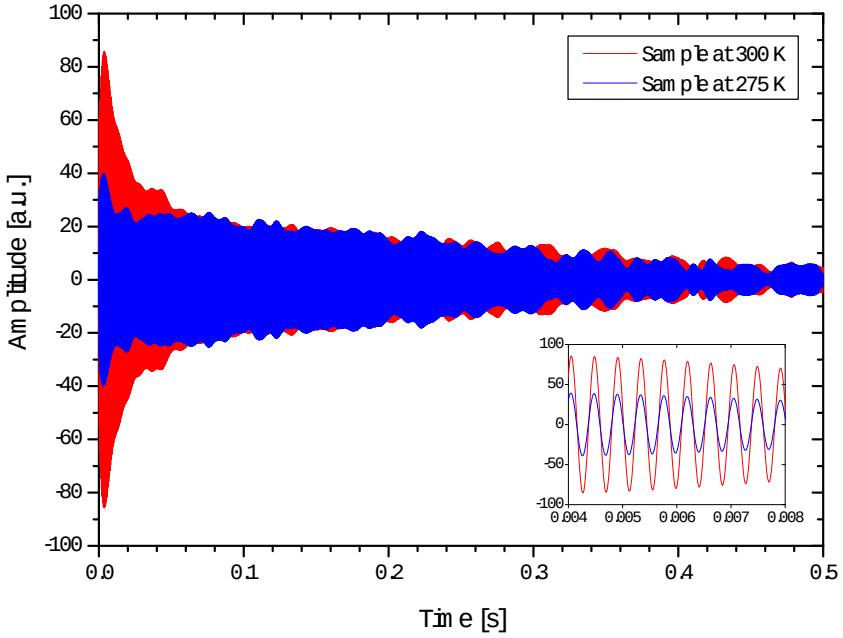

Figure 3.42: FID in the time domain of an oil-water mixture of 4:1 by mass at 300 K showing the two component decay and at 275 K showing only the water component. Inset: close-up of FID. $B_0 = 54.7$ μT.

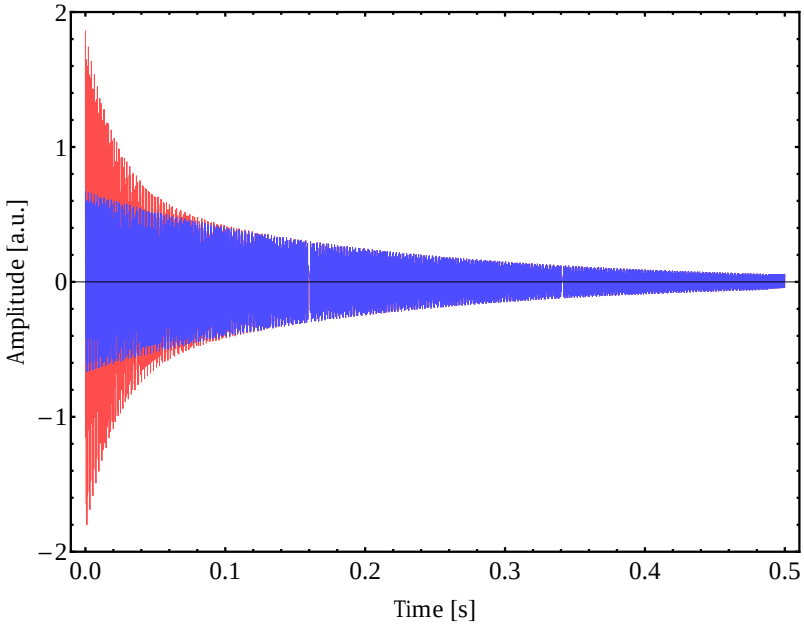

Figure 3.43: A simulation performed in Mathematica of the two component FID (red) and the water FID only (blue) for the signals measured in Figure 3.42.

3.6 Glycine signal size calculations

A sample of glycine as described in Section 3.2.3 has been acquired along with a ^{13}C NMR spectrum taken in a conventional high field NMR spectrometer (Figure 3.44), for testing in the RTNMR spectrometer. The main drive for the modifications to the setup presented in the following chapters was to try to observe a low field J-spectrum including the ^{13}C splittings that as of yet have not been observed at low fields [21]. From Figure 3.44, J-splittings of $^1J_{\mathrm{HC}_\alpha} = 143.8$ Hz and $^2J_{\mathrm{HCO}} = 5.3$ Hz are expected at low fields, as only heteronuclear splittings will be observed, as we saw in Section 3.1.2. The naming convention is to name the coupling constant

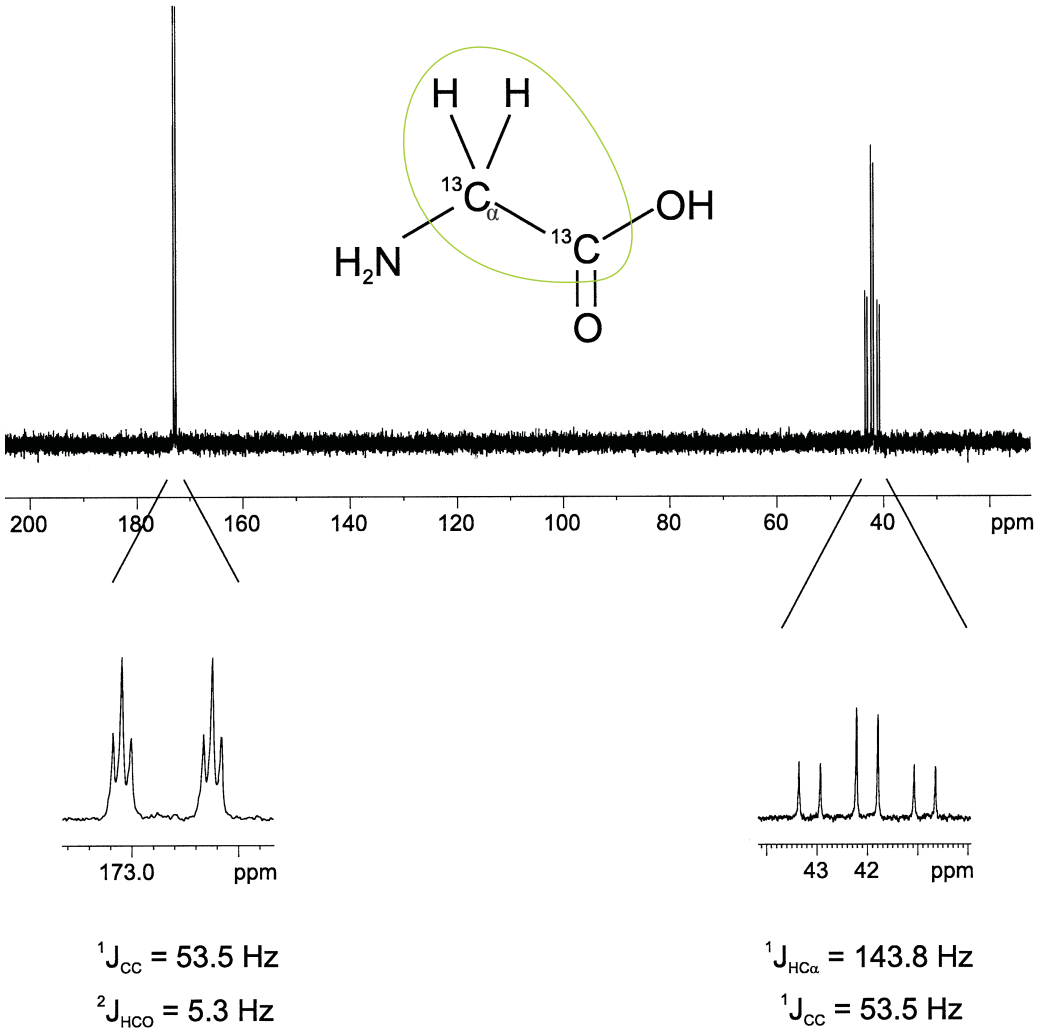

Figure 3.44: High field ^{13}C NMR spectrum taken with a conventional NMR spectrometer from Dr. Thomas Eykyn.

after the nuclei that are coupled, with the superscript denoting the number of bonds over which the coupling occurs. Thus, $^2J_{\mathrm{HCO}}$ is the coupling between the proton (circled) and the carboxyl carbon (attached to the oxygen), through two covalent bonds. J-couplings to hydroxyl and amino protons are rarely observed due to exchange decoupling as there is fast exchange of these protons with the ^{2}H in the solvent. The smaller $^2J_{\mathrm{HCO}}$ splitting, which is only just resolved in the high field spectrum, should be easily resolvable with the frequency resolution of our current system. However, in order to see whether or not the signals will be observable within a reasonable averaging time, the SNR of the expected J-spectrum of glycine was calculated.

3.6.1 D_2O as a solvent

To avoid spectra dominated by the solvent signal, most proton NMR spectra are recorded in a deuterated solvent. Glycine itself is a fine white powder. It must be dissolved in a solvent for NMR purposes as signals from immobile spins have very short relaxation times on the order of µs due to the lack of motional averaging. This leads to very broad linewidths, unsuitable for resolving J-spectra. Thus, deuterium oxide (D_2O) has been chosen as the solvent. The gyromagnetic ratios for the three nuclear spin species in glycine dissolved in D_2O are hydrogen: $\gamma_{^1\mathrm{H}} = 26.75 \times 10^7$ Hz T^{-1}, carbon-13: $\gamma_{^{13}\mathrm{C}} = 67.28 \times 10^6$ Hz T^{-1} and deuterium: $\gamma_{^2\mathrm{H}} = 41.07 \times 10^6$ Hz T^{-1}. This means that for any measurement field, the carbon and deuterium nuclei will resonate at a frequency ~ 4 times lower and ~ 6.5 times lower than the proton respectively.

Deuterium has spin $I = 1$, which gives rise to three Zeeman energy states ($m = -1, 0, 1$). The nuclear charge distribution is no longer spherical but ellipsoidal, as there is now a spin contribution from both the proton and neutron at the nucleus and the nucleus possesses an electric quadrupole moment, Q. NMR relaxation of quadrupolar nuclei occurs predominantly by interaction of the quadrupole electric moment of the nucleus with surrounding electric field gradients, which exert a torque on the nucleus. In a liquid, electric gradients will be small because of the Brownian tumbling of the molecules, which averages the electric field at any time

and in any position towards zero. Analogous to motional narrowing in the magnetic case, this motion causes slow spin-spin relaxation and narrow lines. Equation 3.10 is a simplified form of the quadrupole relaxation equation [18] which emphasises the importance of nuclear properties I and Q and of the maximum field gradient $-d_2V/dz^2$. The relaxation times T_1 and T_2 are equal:

$$\frac{1}{T_1} = \frac{1}{T_2} \propto \frac{(2I+3)Q^2}{I^2(2I-1)} \left(\frac{d_2V}{dz^2}\right)^2 \tau_c, \tag{3.10}$$

where τ_c is the correlation time discussed in Section 2.1.5 and is a measure of motion. Deuterium has a small quadrupole moment, so the interaction is small, and relaxation is slow [39]. Cope measures a T_1 of 0.41 s in pure D_2O at 25° C [40]. As $T_1 = T_2$, this gives an estimated intrinsic linewidth of 0.78 Hz. Thus, the glycine spectrum should not be masked by a broad deuterium signal from the solvent.

3.6.2 What *J*-couplings should we observe?

The expected broadband low field NMR stick spectrum of the doubly labelled glycine sample obtained is given in Figure 3.45.

The ^{1}H atoms circled in figure 3.44 are chemically and magnetically equivalent, giving rise to the spectrum of a single proton but with double the peak height. These protons will experience the field due to the two spin states of the α-carbon and will consequently be split into a doublet centred around the ^{1}H resonance frequency, with splitting $^1J_{\mathrm{HC}_\alpha}$ and intensity ratio 1:1. Similarly, coupling of the protons to the carbonyl carbon will create a second doublet, with splitting $^2J_{\mathrm{HCO}}$. The coupling of the protons to the closer carbon will be stronger than the second order coupling to a carbon two bonds away so $^1J_{\mathrm{HC}_\alpha} >^2 J_{\mathrm{HCO}}$. Thus, the ^{1}H-NMR spectrum consists of two sets of doublets, equal in height.

The α-carbon will see the field of the two equivalent protons it is bonded to and will split into a triplet with intensity ratio 1:2:1 and coupling $^1J_{\mathrm{HC}_\alpha}$. The carbonyl carbon will also see the field of these protons but two bonds away, so the NMR line will also be split into a triplet but with the smaller coupling constant $^2J_{\mathrm{HCO}}$. These peaks will be centred at the the ^{13}C resonance frequency. As the

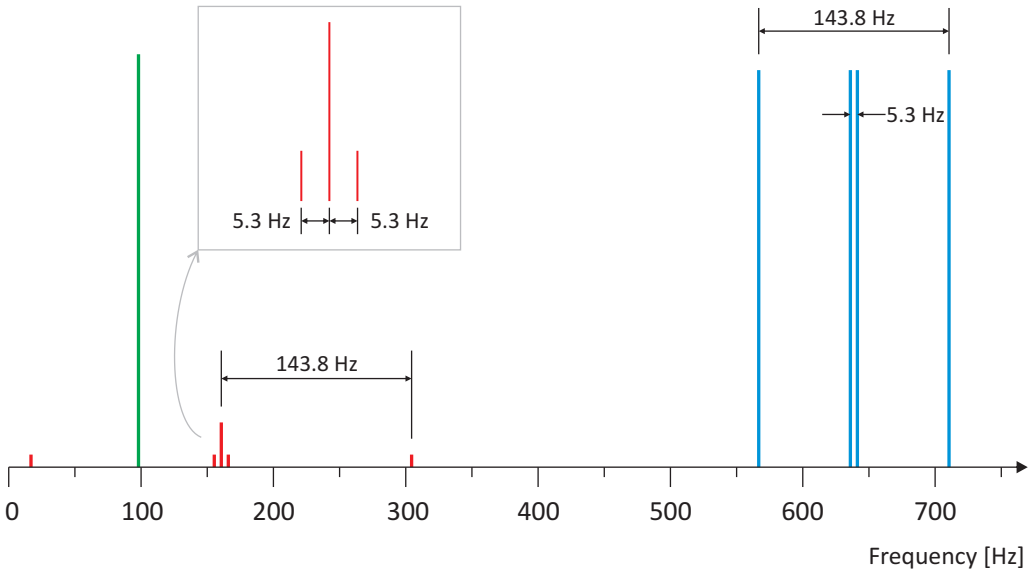

Figure 3.45: Expected broadband low field NMR spectra for doubly carbonyl labelled glycine in a D_2O solution at $B_0 = 15$ μT. The proton peaks are blue, carbon red and deuterium green. At low magnetic fields, there is no observable chemical shift, so the spectra for each nuclear species is centred on the resonance frequency for that nucleus given by $f_0 = \gamma B_0/2\pi$. The concentration of the glycine solution is 1 M.

central peak of each triplet will occur at the same frequency, its height will be four times larger than the four satellite peaks.

Finally, the single deuterium peak will be observed at its resonance frequency for a given static field.

John Clarke's group [21] have also measured a glycine J-spectrum in a deuterium solvent as shown by Figure 3.4 in Section 3.2.3. However, the glycine was only singly labelled with ^{13}C and the concentration was only 1 M. Moreover, they did not manage to detect the carbon signal as it was lost in the noise. For comparison, the theoretical spectrum for singly labelled glycine is also shown in Figure 3.46, normalised by the deuterium peak.

To observe the smallest J-coupling of 5.3 Hz, the linewidth of each NMR line must be smaller than 5.3 Hz, ideally a linewidth of at most ∼2.5 Hz is desirable to improve on the resolution obtained at high fields (Figure 3.44). However, we must reach a compromise between having narrow linewidths and having low noise, as although the linewidths become narrower as we go to lower fields, the noise

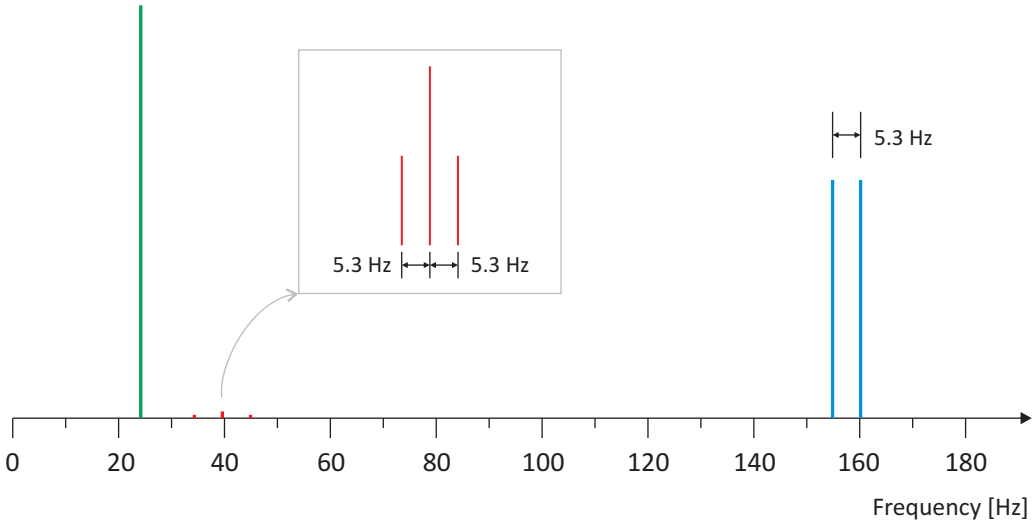

Figure 3.46: Expected broadband low field NMR spectra for singly carbonyl labelled glycine in a D_2O solution at $B_0 = 3.7$ μT, as measured by Trabesinger [21]. The concentration of the glycine solution is 1 M.

levels increase. As Figure 3.24 shows, the $1/f$ noise begins to have an effect below $\sim$ 100 Hz. It is well known that T_2 will get shorter and the linewidth will get broader as we increase the size of the molecule being studied [41]. As glycine is a small molecule, it is thus a valid assumption that its molecular motion when dissolved in water will be comparable to that of water, thereby giving similar T_2 and consequently linewidth in a given measurement field (see Figure 3.34). Thus, a 15 μT measurement field is a good compromise for the whole heteronuclear J-spectrum to have linewidths below 1 Hz and for all but the lowest ^{13}C peak to be above 150 Hz. Also, the deuterium peak will not overlap with any of the ^{13}C peaks at this field. Figure 3.45 shows the expected resonance frequencies for the glycine J-spectrum at this field.

3.6.3 Expected signal to noise

In order to now see if the J-spectrum of glycine (Figure 3.45) could be seen in a reasonable amount of averaging time, an estimate of the signal to noise ratio for the various NMR lines was made. First, the spin density for each nuclear species is calculated, followed by signal size calculations and finally signal to noise.

Spin density

The maximum solubility of glycine at room temperature is 25 g per 100 ml [42], equivalent to a 3.33 M solution.

Molecular mass of glycine = 75.045 g mol^{-1}

No. of moles in 25 g of glycine = 0.333 mol

Assume glycine takes up negligible volume when in solution.

No. of glycine molecules in 25 g = 0.333 mol $\times$ N_A = 2.005×10^{23},

where $N_A = 6.02 \times 10^{23}$ mol^{-1}, Avogadro's constant.

As the hydroxyl and amino protons do not contribute to the signal due to exchange decoupling, two carbons and two hydrogens contribute per glycine molecule to the J-spectrum. Spin densities of carbon and hydrogen are therefore equal.

$$\text{Spin density} \quad N_v = \frac{2 \times 2.005 \times 10^{23}}{100 \text{ ml}} = 4.01 \times 10^{27} \text{ m}^{-3}$$

Signal size in the frequency domain H_0

Analogous to the signal size calculation for water in Section 3.5.4, firstly the magnetisation of the sample for each nuclear species is calculated using Equation 3.5, reproduced here for convenience:

$$M_0 = \frac{N_v \hbar^2 \gamma^2}{4 k_B T} B_p,$$

where the gyromagnetic ratio γ is 26.75×10^7 Hz T^{-1} for ^{1}H and 67.28×10^6 Hz T^{-1} for ^{13}C. The prepolarising pulse B_p = 2 mT and T = 300 K. This gives

$$M_0(^1\text{H}) = 3.82 \times 10^{-7} \text{ A m}^{-1}$$
$$M_0(^{13}\text{C}) = 2.42 \times 10^{-7} \text{ A m}^{-1}.$$

Combining Equations 3.6, 3.7 and 3.8, the expression for the initial amplitude of the FID in the time domain, A, is:

$$A = \frac{G_{\text{FLL}} M_i}{(L_i + L_p)} B_{1p} V_s M_0. \tag{3.11}$$

Using the same parameters for the two-stage SQUID and pickup coil as in the calculation in Section 3.5.4 and assuming the same sample volume, V_s, we obtain:

$$A(^1\mathrm{H}) = 1.13 \times 10^{-5}\ \mathrm{V}$$
$$A(^{13}\mathrm{C}) = 7.16 \times 10^{-7}\ \mathrm{V}.$$

Assuming in the first approximation that the linewidths will be similar to those obtained for pure water, the signal size in the frequency domain H_0 can be calculated using:

$$H_0 = \frac{AT_2^*}{2\Delta}.$$

At a measurement frequency of $B_0 = 15\ \mu\mathrm{T}$ (corresponding to a proton frequency of ~ 640 Hz), we estimate a linewidth of $\Delta\nu = 0.75$ Hz using Figure 3.34. This corresponds to a $T_2^* = 1/(\pi\Delta\nu) = 424$ ms. An adequate $T_{\mathrm{cap}} = 2.4$ s and capturing 120 000 points gives $\Delta = 20\ \mu$s between points. The estimated signal size is thus:

$$H_0(^1\mathrm{H}) = 120.0\ \mathrm{mV}$$
$$H_0(^{13}\mathrm{C}) = 7.6\ \mathrm{mV}.$$

for no splitting of the NMR line. However, in a J-coupled spectrum, this magnetisation will be distributed among the peaks in proportion to their intensity ratios, giving the following signal sizes:

- 30.0 mV for each of the 4 proton peaks
- 3.8 mV for the centre carbon peak
- 0.95 mV for each of the 4 satellite carbon peaks
- (31.2 mV for the deuterium peak)

The deuterium signal size was also calculated using Equation 2.2 for spin $I = 1$, number density $N_V = 1.66 \times 10^{28}\ \mathrm{m}^{-3}$ [43] and assuming the same sample volume and linewidth as H_2O.

Signal to noise

As the estimated signal sizes are very small, it is meaningful to calculate the signal to noise ratio (SNR) to determine the number of averages required in order to see a clear NMR spectrum. The peak noise in the frequency domain arising from the measured SQUID noise can be calculated with the following formula [44]:

$$N_p = \frac{K_N^f}{\Delta}\sqrt{\frac{T_{\text{cap}}}{2}\langle S_V\rangle}, \tag{3.12}$$

where K_N^f is the ratio between the peak noise in the frequency domain to the RMS value of the noise and is ~ 2.5. T_{cap} is the capture time and S_V is the square of the total RMS voltage noise. At ~ 400 Hz, the SQUID flux noise is approximately $\langle \Phi_N \rangle = 1.75\ \mu\Phi_0\ \text{Hz}^{-1/2}$ from Figure 3.24 with the transmitter connected and the sample at 300 K. With a gain of $G_{\text{FLL}} = 280\ \text{mV}/\Phi_0$, this gives a noise level of $\langle S_V \rangle^{\frac{1}{2}} = 490\ \text{nV Hz}^{-1/2}$. Substituting $T_2^* = 424$ ms, $T_{\text{cap}} = 2.4$ s and $\Delta = 20\ \mu$s, we obtain:

$$N_p = 67.1\ \text{mV}.$$

In practice, the noise level is a factor of ~ 4 larger than this ideal value. It is therefore evident that none of the NMR lines in the spectrum of glycine will be visible in a single shot. Averaging of the transients in the time domain is required to bring down the noise by a factor of $1/\sqrt{N}$ for N averages. In order to accurately measure the J-coupling constants, it would be desirable to have a SNR of at least 5. Table 3.3 shows the calculated number of averages required in order to obtain this SNR for each of glycine's NMR peaks using the noise calculated using Equation 3.12. The corresponding time scale assumes a pulse sequence repetition time of 15.5 s for a 2.4 s T_{cap} with the heater on during data capture.

As is evident from the signal size calculations, to be in a position to observe a J-spectrum from nuclei other than protons within a reasonable time, it will be necessary to increase the SNR. In the actual experiment, the noise level calculated by Equation 3.12 is increased further by factors such as noise introduced into the system during data capture from equipment and poor background subtraction

NMR peak	Number of averages	Corresponding time
Proton peak	125	32 minutes
Carbon, central peak	7800	33.5 hours
Carbon, satellite peak	124 700	9 days

Table 3.3: An estimate of the number of averages required in order to see each NMR peak from glycine, with a SNR of 5. The approximate time this corresponds to is also shown.

routines. An effort is always made to reduce the noise, however, we must also try to increase the signal size. As the sample volume cannot be increased due to space constraints and the glycine solubility concentration is at a maximum, the focus was placed on increasing the strength of the prepolarising pulse. Increasing B_p by a factor x will increase the SNR by the same factor, reducing the number of required averages by $1/x^2$. The next section is an account of this effort.

3.7 Efforts to increase the signal to noise ratio

Without change to the experimental setup, the SNR of an NMR signal can also be increased by averaging but averaging N times only increases the SNR by a factor of $\sqrt{N}$. Moreover, time variations in the environmental field profile will begin to affect the linewidth of the signal so it becomes less beneficial to average for extended periods of time. The ultimate time limit would be how long a Dewar of liquid helium will last for (with this setup, ~ 3.5 days). For these reasons, various efforts were made to increase the signal size of the NMR peak amplitude in order to decrease averaging time and are documented in this section.

3.7.1 Review of prepolarising pulses

As mentioned previously, there are a few other workers who have successfully observed a low field J-spectrum of several compounds [17, 20, 21, 32] but none have been able to observe the ^{13}C spectrum. This would be advantageous as carbon is an essential and abundant element in organic chemistry and would open

up the possibility of low field J-spectroscopy to many more compounds. Here a brief comparison is made between the prepolarising pulses used in these previous experiments. Table 3.4 is a summary of the experimental conditions used by McDermott, Trabesinger, Burghoff and Appelt *et al.* to observe their respective J-spectra.

Author	**Nuclei**	B_p	**Volume**	**Averages**
McDermott *et al.*	^{1}H, ^{31}P	1 mT	3 ml	100
Trabesinger *et al.*	^{1}H, ^{31}P, ^{19}F	2 mT	5 ml	100-5525
Burghoff *et al.*	^{1}H, ^{19}F	0.25 mT	20 ml	50
Appelt *et al.*	^{1}H, ^{19}F	1 T	2 ml	1-9

Table 3.4: Summary of previous measurements of low field J-spectra [17, 20, 21, 32].

A large number of averages by Trabesinger *et al.* was needed to see the glycine spectrum (Figure 3.4). SQUID detection was implemented to observe the above spectra with the exception of Appelt *et al.*, who used a 1 T Halbach permanent magnet to prepolarise the sample in a remote location with respect to the receiver coil, before performing NMR in the Earth's field [17]. However, the factor that all these experiments have in common is that the sample volume is much larger than our setup, having typical volumes of a few ml compared with 0.14 ml in this setup. As the signal size in the frequency domain is proportional to $V_s B_p$ (Section 3.5.4), the prepolarising pulse can be small if the volume is increased. Thus, prepolarising pulses of 2 mT or less were adequate to observe a low field J-spectrum for the nuclei in Table 3.4. Being limited to a volume of 0.14 ml by the size of the sample region (Figure 3.6), the prepolarising pulse strength in this setup must be increased above the present maximum of 2 mT.

3.7.2 Increasing the prepolarising pulse with a Techron amplifier

As the current setup was limited to a maximum current in the polarisation coil of ∼630 mA, the first step taken was to introduce an AE Techron 7782 power

amplifier [45] and to modify the prepolarising pulse circuit to allow larger amplitude transmitter pulses, enabling larger prepolarising fields B_p. The Techron is an amplifier that has a long history of being used for whole body MRI systems. It is built to have a frequency bandwidth from dc to 50 kHz at rated power (4000 W peak output, 2858 W RMS into a 2 Ω load), which is ideal for our low frequency applications.

This upgrade required the installation of a 3-phase power supply and the experimental setup was moved into a new laboratory (W157). In order for the spectrometer to be able to carry high currents of up to 20 A, the following modifications to the existing dipper probe were carried out: The twisted pair of 160 µm ⌀ copper wire carrying this current down the length of the probe was replaced with 1 mm ⌀ copper wire. The transmitter junction box at 4 K and baffles were redesigned to accomodate this. The Fischer connector at the top of the probe was replaced with a 4-way Lemo connector (using 2 pins per lead) with a current rating of 10 A per pin. The crossed diodes at the output of the Techron were replaced

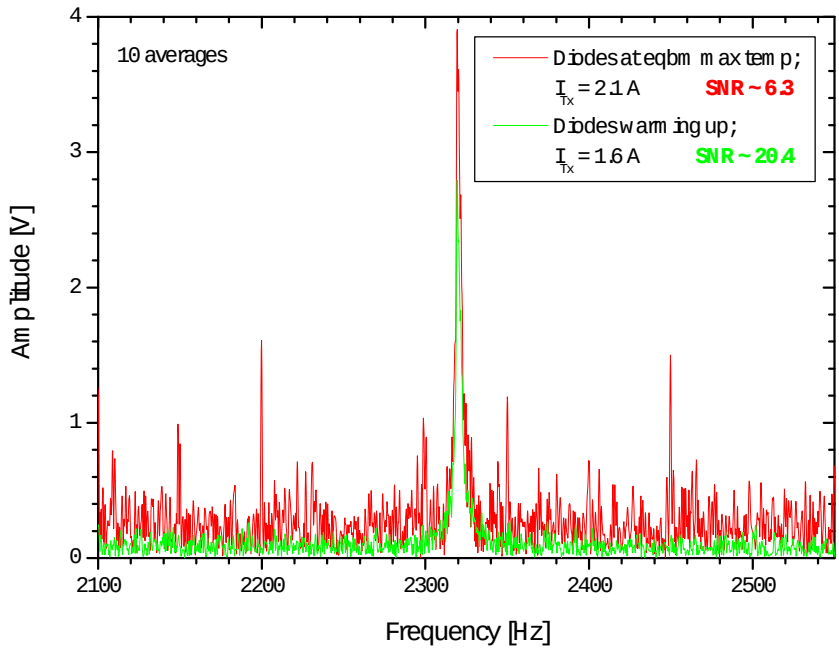

Figure 3.47: Difference in SNR for cool diodes (during the first 10 averages) and diodes operating at their maximum temperature (taken after pulsing for several minutes). The signal scales with I_{Tx} but the noise does not.

with Philips (BYV72EW-200) dual rectifier diodes, also with a current rating of 10 A per diode. Unlike the previous diodes, these were mountable, enabling them to be screwed down and heatsunk. 8 pairs were mounted in a large diecast box with a good thermal link to the box to enable the diodes to remain cool during large prepolarising pulses. This was in response to the observation that taking measurements when the diodes were cool results in a substantial decrease in the white noise as shown in Figure 3.47 (taken before the heat sinking was improved). The current through the transmitter was also found to be proportional to the diode temperature and so heat sinking them also ensured a more stable pulse height. Finally, the monitor resistors were replaced with three 1 Ω resistors in parallel (also mounted into the die cast box) giving a much lower total current monitor resistance of $\frac{1}{3}$ Ω. Additionally, a 5000 pF pi-filter on the output of the Techron filters out unwanted ac noise frequencies. Figure 3.48 is a schematic of the new prepolarising scheme.

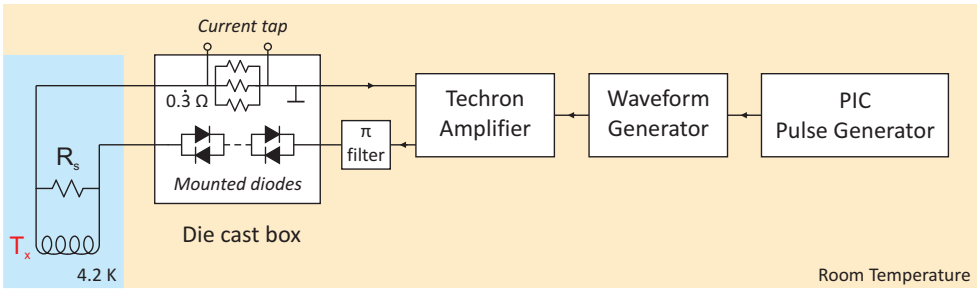

Figure 3.48: Diagram of new prepolarising circuit incorporating the Techron amplifier. See Figure 3.22 for comparison.

Software called the Arbitrary Waveform Composer [46] for the Stanford waveform generator (Model DS345) was used to define a square pulse for the Techron input. With this program, the Stanford could be programmed to give out any arbitrary pulse shape. With 10 000 points defining the pulse shape at 1 kHz frequency, it was used to output a 10 s long square pulse of programmable amplitude in order to vary the size of the prepolarising pulse. This was connected to the input of the Techron, which was operated in constant voltage mode. The voltage was amplified by 20 to give the prepolarising pulse.

Furthermore, a new 300 turn transmitter was designed and wound from 110 μm Cu clad NbTi, on a Kel-F former with a square split helmholtz geometry. This has a calculated field-current ratio of 25.6 mT A^{-1}. The critical current was measured to be 6.8 A. It was hoped that this new transmitter coil, together with the Techron, would be able to increase our SNR by at least an order of magnitude, by being able to generate a prepolarising pulse of up to $B_p = 170$ mT, compared to 2 mT previously. To test the Techron and the new setup, a new sample cell was machined and filled with deionised water. This cell had a 40 μm ⌀ NbTi heater (52 μm Formvar) of 1.1 kΩ resistance. Enamelled constantan wire of 80 μm ⌀ was used for the diode leads.

Unfortunately, the SNR improvement was not as straight forward as hoped. By using the new 300 turn transmitter coil together with the Techron, the signal quality became reduced with a test prepolarising field of just 15.4 mT, corresponding to an improvement of B_p by a factor of 7.7. Figure 3.49 shows NMR signals from water taken using this prepolarising field for both polarities of current in the magnet. The linewidth became very broad compared to the expected linewidth of ~ 1.5 Hz at this frequency (see Figure 3.34) and the environmental field gradient reversed compared to previously (Figure 3.32), indicating that a large field gradient had become trapped over the sample volume as a result of the large transmitter pulses. Using the measured linewidths from Figure 3.49, the difference in linewidth of 3 Hz indicates that the environmental residual field gradient $\beta \simeq 1.5$ Hz. This corresponds to 50 nT cm^{-1}, compared to 1 nT cm^{-1} as measured with the previous setup using a 2 mT prepolarising pulse (Section 3.5.5).

There was also increased pickup in the measured noise spectrum at low frequencies (below ~ 2 kHz) as well as an increase in the white noise floor by a factor of 2 below ~ 100 Hz as a result of this B_p. With a prepolarising field of 34.3 mT, the noise increased so much that the signal could not be seen at all above the noise after 10 averages. A possible explanation was that this line broadening was caused by flux becoming trapped in the inner overlapping Nb shield giving rise to a degradation in field homogeneity, as it was close in vicinity to the transmitter coil. It was thought that perhaps the Nb shield was trapping vortices in a mixed

state as it is a type II superconductor so an inner shield made of lead (type I) was made and tested. The lead foil used was 0.125 mm thick and of 99.99 % purity. A two layer shield was constructed and tested but there was no improvement on the Nb shield - in fact, the transient in the time domain was larger. It was decided to return to the 30 turn transmitter coil (now wound from Cu clad NbTi, B/I = 2 mT A^{-1}) for further testing, as its smaller size meant it was further away from the inner shield, possibly enabling larger prepolarising pulses to be applied before flux trapping became dominant.

3.7.3 Improvement in data capture

To capture the NMR signal, a new PXI card was also introduced and a LabVIEW scope program was written to take advantage of its benefits. This new NI PXI-5922 [47] has a variable 16-24 bit resolution depending on the sampling frequency (50 kHz to 15 MHz). For the low sampling rates routinely used in low field NMR, the highest resolution of 24 bits is used. The NI PXI card can acquire just over

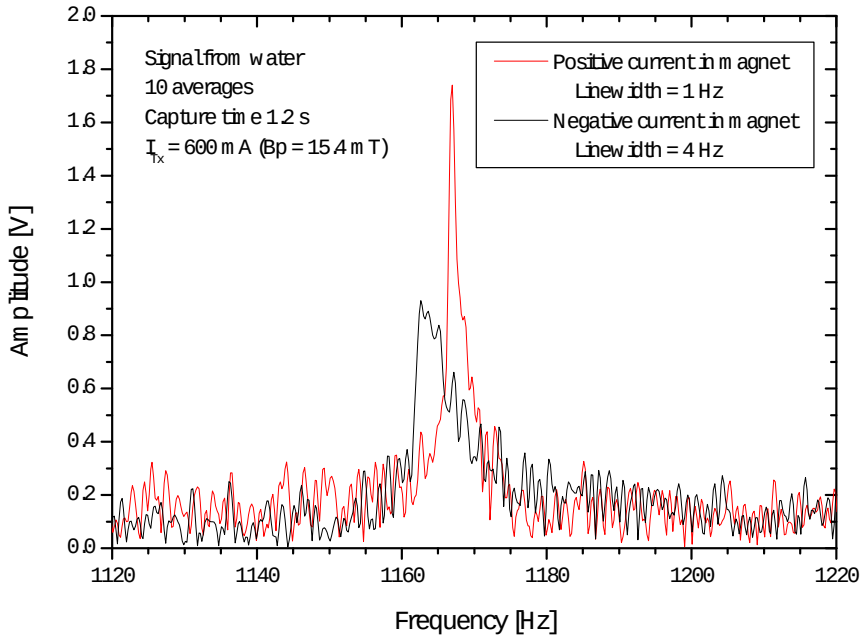

Figure 3.49: First NMR signals from water at 300 K taken with the 300 turn transmitter coil and Techron amplifier using a 15.4 mT prepolarising pulse. B_0 = 27.4 μT.

2 million data points per record, a vast improvement on the 120 000 pts for the Pickering card (as in Section 3.5.1), removing the need for the Tektronix oscilloscope for long capture times. The previous PXI card also used up memory storing the delayed data set on the scope (i.e. data taken from the time the scope is triggered to the time actual data is captured). The new program utilises a circular buffer memory, so delayed data does not take up valuable memory space.

3.7.4 Overall improvement in signal to noise

Despite not being able to increase B_p considerably, there was still a significant improvement with the modifications reported in this section. By using larger prepolarising pulses with the smaller transmitter coil, the SNR was increased by a factor of ~ 3.5, as can be seen in Figure 3.50. This was due to the increase in the

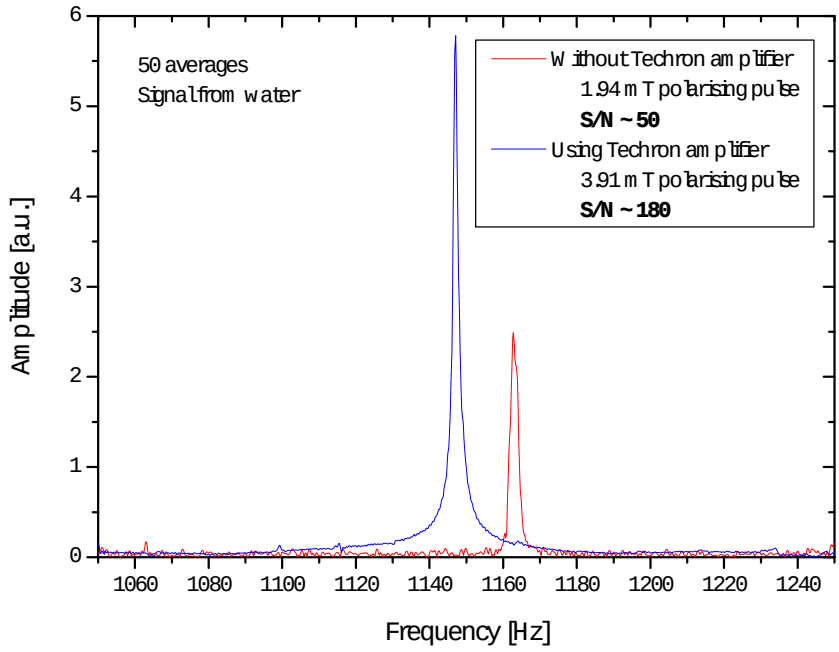

Figure 3.50: Improvement in signal to noise ratio after the Techron was introduced, larger prepolarising pulses applied and modifications to the setup made. $B_0 \sim 27.1$ μT.

prepolarisation field by a factor of just 2 but also a reduction in the white noise floor by a factor of ~ 3, mainly due to the heat sinking of the diodes. Routine frequency sweeps on water could now be performed with only 10 or even 5 averages,

with good signal to noise, compared to 50 previously.

3.7.5 Increasing homogeneity - winding a new magnet

It was found out through low field experiments with a newly wound, nominally identical magnet on a duplicate dipper probe, that the field homogeneity of the magnet was far better (at ∼150 ppm) than the existing magnet. This lead to the question of why my magnet homogeneity was so poor when fundamentally the magnets were made to be identical. On inspection of the windings, a small gap of ∼0.3 mm was found on the top layer. Simulations of this using the magnet program developed by Tom Crane revealed that this was accountable for the lower than predicted homogeneity of the magnet(see Figure 3.51).

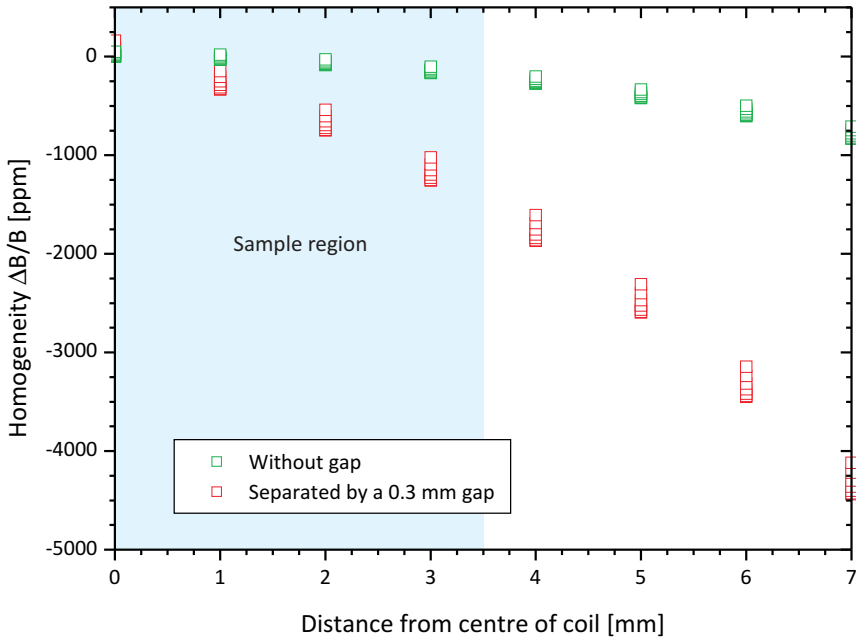

Figure 3.51: Homogeneity profile for a magnet modelled on two solenoids separated by a 0.3 mm gap and also with no gap.

A new magnet was thus wound on the existing copper former to the same specifications as in Section 3.4.1. The homogeneity was measured using NMR (with the technique described in Section 3.5.5) to be 130-150 ppm, almost five times better than with the old magnet (∼780 ppm). It was while this magnet was

being wound, that the following two experiments were performed on an essentially identical duplicate RTNMR dipper probe.

3.7.6 Limitations of the spectrometer

A systematic approach was taken to try to determine the maximum fields the inner shield could withstand without degrading the field homogeneity. In particular, we wanted to know if there was a threshold field over which linewidths started to broaden or if it was a gradual process. Figure 3.52 is the result of this run, performed on the duplicate RTNMR probe that had an essentially an identical setup. The static field was kept constant at 43.9 μT so the signal resonated at 1850 and 1885 Hz for ±15 mA in the magnet respectively. This field was chosen as a clear NMR line could be observed after only 5 averages, without requiring a second dataset for background subtraction. The sample heater was not pulsed

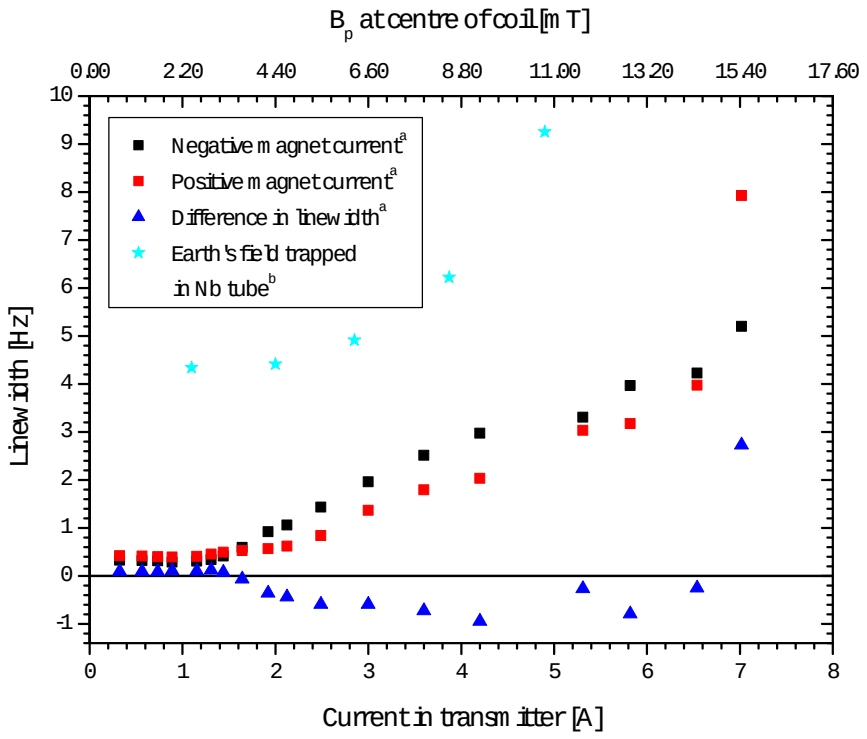

Figure 3.52: Measured linewidths for ±15 mA in the magnet (B_0 = 43.9 μT) for increasing transmitter pulse strengths. [a]Measured in an aluminium transport Dewar.

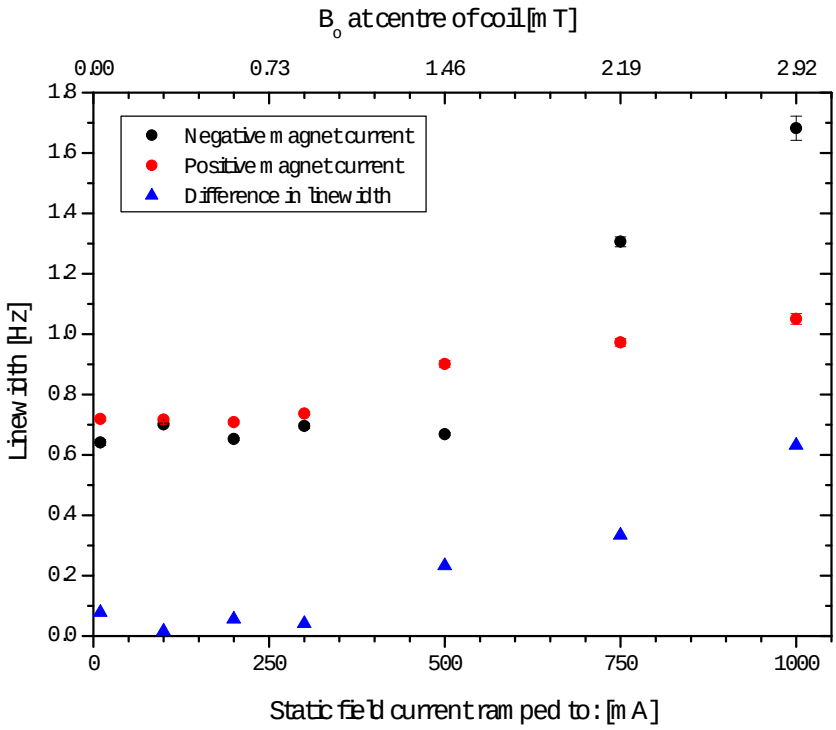

Figure 3.53: Measured linewidths measured at $B_0 = 29.6$ µT after the static field was ramped to higher fields. Current in the magnet was ramped to x mA in $x/10$ seconds. A 0.66 mT prepolarising pulse was used so it would not itself become the cause of flux trapping.

during data acquisition as the effect of the heater on the field gradient at the sample was small, compared to the field gradient broadening observed after large fields. Signals were taken for increasing transmitter pulses from 300 mA to 7 A corresponding to 0.66 mT - 15.4 mT at the sample.

Earlier measurements of NMR linewidth as a function of frequency after the static field had been ramped up to 2.9 mT (proton Larmor frequency of 123.5 kHz) and back to zero showed a permanent increase in linewidth. To quantify the limitations of the inner shield for fields parallel to the shield surface, the static magnetic field was ramped to increasing fields and the linewidth of signals measured after each ramp with a low ±10 mA in the magnet ($B_0 = 29.2$ µT) for data acquisition. Figure 3.53 shows that it seems the inner shield is more receptive to trapping axial magnetic fields than fields perpendicular to its surface, as at a static field of only 2.92 mT, the difference in the positive and negative linewidths, 2β is already

0.6 Hz, whereas for the transmitter coil (Figure 3.52), 2β is still constant at 0.1 Hz up to $B_p \sim 3.2$ mT. This experiment was also performed on the duplicate probe.

In order to observe the NMR spectrum of glycine with this dipping probe configuration, it will be necessary to overcome these problems and be able to increase the strength of the transmitter pulse.

3.7.7 Annealing attempt of the inner overlapping shield

The lower critical field of niobium (a type II superconductor) is approximately 100 mT [48]. What was the reason of flux trapping at much lower fields as low as a few mT? One proposal was that the critical field could be lowered by strain/stress in the material. Also, impurities in the sample may cause hysteresis and trapped flux. This is attributed to the fact that the normal cores which thread the superconductor in the mixed state can be pinned to imperfections in the material and cannot escape. Looking into several papers that investigated the magnetic properties of Nb [48–50], it was apparent that all the authors had treated their Nb samples by annealing and heating to various temperatures and in various atmospheres in order to optimise sample quality. This extensive treatment reduced gaseous impurities, carbon content and surface impurities so that the magnetisation curves were not hysteretic. Rose-Innes [51] also writes that the irreversibility of magnetisation curves of type II superconductors are caused by imperfections such as dislocations and chemical impurities. To try to overcome these issues, an attempt was made at annealing the inner overlapping Nb shield.

The process involved rolling up a sheet of the 50 μm thick Nb used previously (Section 3.4.4) cut to the required shape and holding it in place inside another Nb cylinder of diameter 27 mm (which is used to trap fields in Section 3.7.9). These were placed within an outer Nb shield of diameter 35 mm for protection. These were all placed in the centre of a vacuum furnace and annealed at 1200°C (the maximum temperature of the furnace) for 4 hours at a pressure of approximately 2×10^{-5} mbar, the lowest pressure attainable. After the anneal, the overlapping shield held its shape, an indication that some movement of the crystal structure had occurred.

Initial tests of this shield were carried out in a transport Dewar. Amongst them, the sample was exposed to a high prepolarising field of 13 mT (6.54 A current through the transmitter) and the linewidth of the original signal was measured. The justification of this single shot experiment was that we would like a factor of 20 improvement at least for the strength of the transmitter pulse and if the annealed shield could not take this large pulse, it was not good enough. It turned out that the signal after the large pulse was very broad - in fact, broader than with the untreated inner shield. Measurments performed in the mu metal shielded Dewar confirmed this degradation in performance and are shown in Figure 3.54. This was measured with the initial RTNMR probe with the new magnet. This result is most likely due to the vacuum conditions of the furnace - the pressure used of 2×10^{-5} mbar was unfortunately too high, with the result of adding even more impurities to the shield surface.

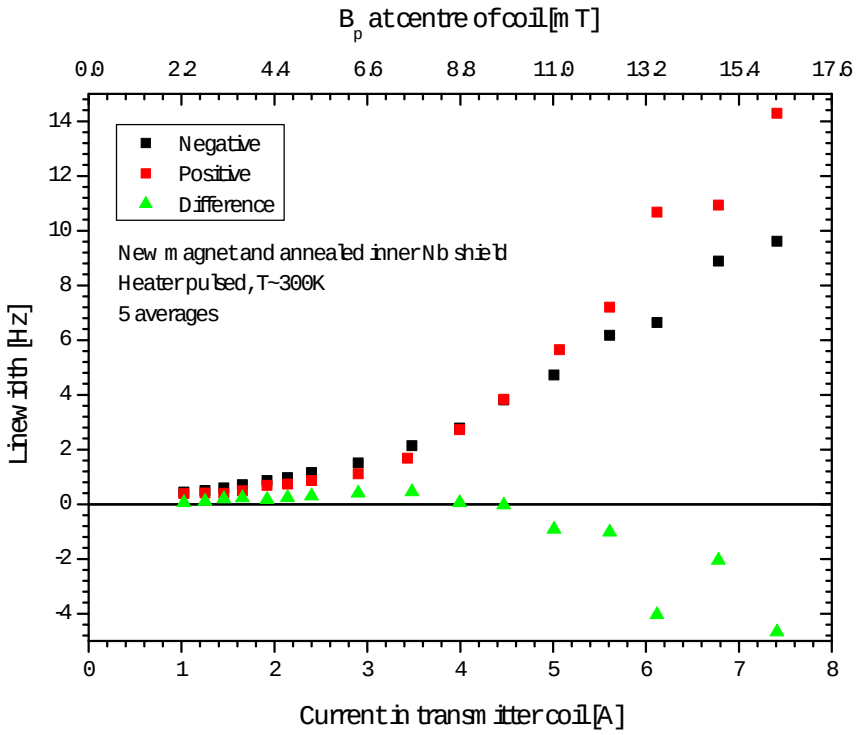

Figure 3.54: Measured linewidths for ±15 mA in the magnet for increasing transmitter pulse strengths.

3.7.8 Magnetisation measurements of niobium foils

With the intention of finding out why we were trapping flux in the Nb at applied magnetic fields far below the lower critical field of Nb, magnetisation measurements as a function of field at 4.2 K were carried out in the PPMS (Physical Property Measurement System). Magnetisation curves were obtained for various Nb foils; the untreated foil, the annealed foil, a second untreated foil (from a different batch) and a mini inner shield rolled up with Kapton using the untreated foil were measured. All sheets had a purity of 99.85% and a thickness of 50 μm.

The dimensions of each foil sample were ∼7 mm × 7 mm and were mounted so that the applied field would be parallel to the surface of the sheet. The sample was placed in the PPMS, which centralised it to within 1.2 mm of the centre of the magnet. All measurements were done at 4.2 K, after cooling in zero field. Dc magnetisation measurements involve physically moving the sample in and out of a coil set, and measuring the induced response. The following measurements were taken: The field was linearly increased from 0 to 300 mT at a rate of 19.5 mT/s, using a stepsize of 5 mT. Dc magnetisation was measured for each step. The field was then decreased to 0 mT in the same way; the same number of points were taken. The resulting plot is shown in Figure 3.55.

When the applied field is increased from zero, initially the Nb exhibits the Meissner state of perfect diamagnetism, shown by the negative slope that is equal to a susceptibility $\chi = -1$. When the lower critical current H_{c1} is reached, vortices begin to penetrate the metal, and the susceptibility begins to increase. When the magnetisation becomes zero, the upper critical current H_{c2} is reached, and the metal is no longer superconducting. Thus, the minimum in the M-H curve is an indication of the lower critical field. For an ideal specimen, with no impurities or crystalline faults, the magnetisation curve is completely reversible. Hysteresis of the curve indicates an imperfect sample, and a remaining positive magnetisation at zero field indicates that there is a residual flux density and we say the sample has trapped flux, and acts like a permanent magnet [51].

To measure the degree of trapped flux after lower applied fields, after the sweep the sample was warmed to 12 K, (above its transition temperature of 9.25 K) and

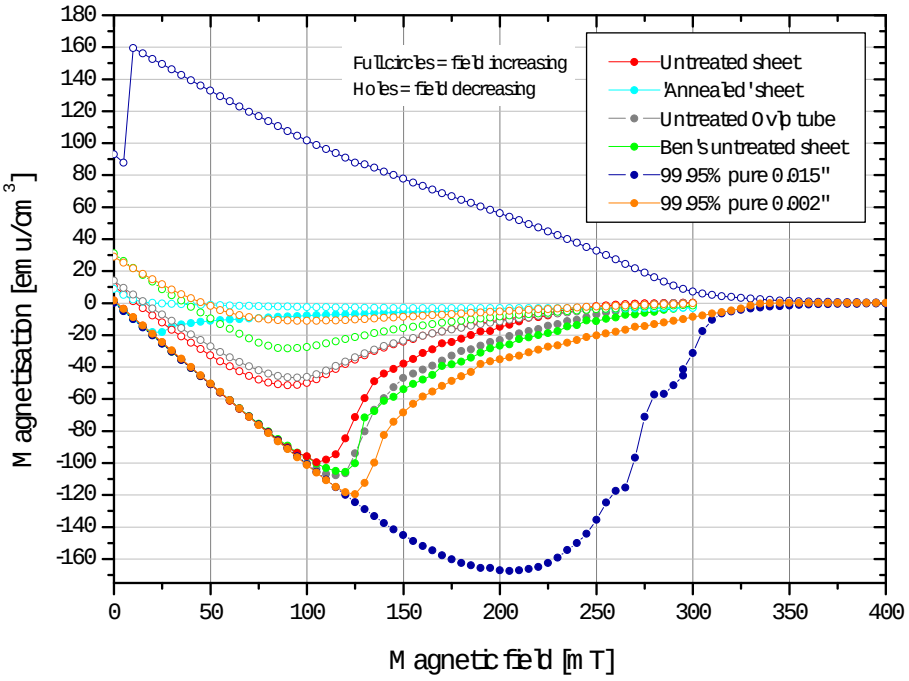

Figure 3.55: Dc magnetisation as a function of applied field measured for various Nb samples, scaled by their volumes. Note for the 0.005" and 0.002" thick Nb, the field was increased to 400 mT instead of 300 mT for the others.

cooled back down to 4.2 K in zero field. The field was then increased to x mT then to zero, for $x = 1$, 10, 50 and 100 at a constant temperature of 4.2 K. The dc magnetisation was measured for each sweep. The sample was heated to above its transition temperature and zero field cooled between each sweep. Figure 3.56 shows a plot of the difference in magnetisation measured between the field increasing and field decreasing sweeps and is a measure of trapped flux.

For our 'annealed' Nb, the lower critical field was measured to be only 25 mT (Figure 3.55). For the 0-50 mT and 0-100mT sweeps, this sample is therefore already in the vortex state when the magnetic field is reversed and reduced to zero, resulting in a higher trapped flux. Figures 3.55 and 3.56 show that deforming the sample by rolling it up does not deteriorate the shield's performance - it actually enhances it slightly! The very low H_{c1} of the annealed sample confirmed the NMR result that its performance is worse than for the untreated foil. All these foils have of course been annealed prior to delivery but the conditions of the anneal would not be disclosed by the supplier. The second batch showed more hysteresis and

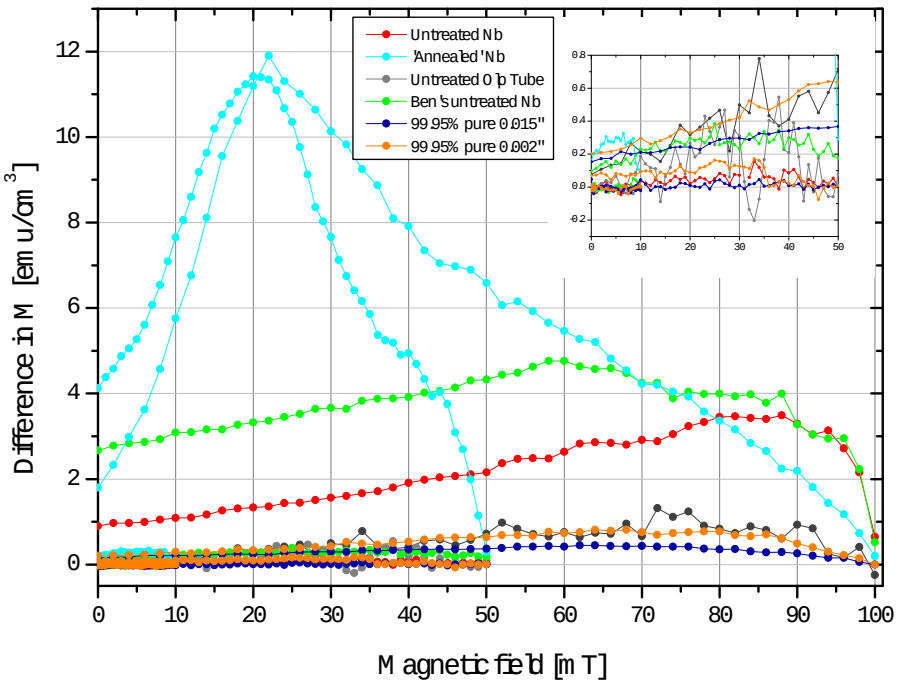

Figure 3.56: Trapped flux for different Nb samples. This was determined by the difference between the magnetisation going up in field to that going down.

trapped flux than our untreated foil, which could be caused by impurities in the Nb that may vary slightly from batch to batch. However, H_{c1} of the untreated foils were all 100 to 120 mT. These fields are much higher than any fields seen by the shield during an NMR experiment, even with the strongest pulses.

The results of the NMR and PPMS measurements on the attempted Nb annealing showed that purity was found to be a likely factor to explain flux trapping at low fields. It was decided to try to find the purest Nb sheets available. Very few companies supply 99.99% pure Nb and none of these offered this purity in sheet form. The purest Nb available was from Eagle Alloys in the US, who agreed to send a free sample of purity 99.95%, thickness 0.015" (380 μm). This was measured in the PPMS to see if purity did make a significant difference and the results (navy blue data in Figures 3.55 and 3.56) looked very promising. The lower critical field was surprisingly high at 200 mT and although there seemed to be a lot of trapped flux after returning from 400 mT, the low field ramps from 0-50 mT trapped the least flux out of all samples tested.

A sheet of thickness 50 μm and 99.95% purity was purchased and before a shield was constructed, screened in the PPMS. Unfortunately, the results (orange data) showed a magnetisation curve very similar to the second batch of Nb and the 0-50 mT sweeps trapped more flux that our untreated sheet. It was therefore decided not to go ahead with the construction of a shield in this purer material.

The final niobium foil to be tested in the PPMS was a lucky find of 70 μm thick, 99.9 % purity Nb. The lower critical field was measured to be $H_{c1} \sim 270$ mT, with magnetistion behaviour similar to the 0.015" sample. The longer length of this foil enabled a 5 layer inner shield to be constructed, following Hechtfischer [31] who made superconducting overlapping shields of lead that was 4 layers thick. Unfortunately, when tested on the spectrometer the performance was identical to the other shields, implying that the number of layers and perhaps the thickness of the Nb were not critical factors in determining the actual lower critical field.

3.7.9 NMR by trapping the Earth's field

Another suggestion to enable large transmitter pulses to be applied was to have a setup that didn't need an inner shield. The easiest way of realising this was to trap a magnetic field in a solid Nb cylinder situated where the inner shield would have been. This would serve as a magnet by trapping the field seen by the magnet as it underwent its superconducting transition. It would also serve the purpose of the inner shield, shielding the sample and transmitter from the magnet former. Using the annealed Nb cylinder from Section 3.7.7, initial tests were carried out by trapping the Earth's field in a transport Dewar.

It was found experimentally that the homogeneity was improved if the probe was cooled slowly. This is explained by Gallop [6] to be caused by thermoelectric gradients which result from temperature gradients, if such a shield is cooled rapidly in a non-uniform way. These currents can generate large fields which may become trapped and compressed by surrounding superconducting regions, giving rise to very non-uniform gradients. With this information in mind, the probe was cooled very slowly, over 5 hours. The minimum linewidth achieved in the Earth's magnetic field (48.2 μT) was (4.12±12) Hz - approximately double that obtained with the

usual setup. A similar test to that in Section 3.7.6 was carried out to see if this setup could take higher prepolarising pulses before the linewidth began to broaden. Unfortunately, as can be seen in Figure 3.52, the results for this setup were even worse than for the annealed inner shield.

3.7.10 Flux trapping in NbTi wire

The above investigations lead to the idea that perhaps other nearby superconducting elements may be trapping flux, such as the wire used for the receiver coil. Surprisingly, the NbTi receiver wire exhibited a lower critical field of $\sim$ 12 mT when screened in the PPMS. This may be due to stress in the wire causing inclusions in the crystal structure, which could work to lower H_{c1} [51]. As this wire was essential to the dipper probe design, further investigations in this direction were halted. In conclusion, it is very unlikely that this compact shielding configuration will enable the application of much larger prepolarising pulses than a few mT without significant broadening of the NMR line.

3.8 Concluding remarks and future directions

Although the dipper probe is a simple way to achieve fantastic environmental screening, it suffers from the inability to increase the prepolarising pulse due to flux trapping in nearby superconducting components. This trapped field gradient caused line broadening of the NMR signal, hindering the technique's ability to resolve a J-spectrum. However, there may still be some hope that other materials for the superconducting receiver wire would allow the prepolarising pulse to be increased further. Additionally, a magnetically shielded room has been purchased from Amuneal, which may be a solution that provides adequate shielding of environmental field gradients for low field measurements on larger room temperature samples outside of the cryostat. With this new design, the sample could be out of the cryogenic environment altogether, and be held against the base of the Dewar. The need for an inner overlapping shield would be eliminated, and is a promising step towards turning the benefits of low field NMR into a practical solution.

Part II

Knight Shift Measurements on Single Crystal UPt_3

Chapter 4

UPt_3 - a truly unconventional superconductor

In the year I was born, 1983, Stewart *et al.* submitted the original paper on the discovery of superconductivity in the heavy fermion compound UPt_3 with T_c ∼540 mK [1]. It is a nice coincidence that I am now studying this compound that has eluded theorists and experimentalists for decades with the unique unconventional nature of its superconducting state. Although many advances have been made in discovering and understanding its properties in the superconducting state, the symmetry of the superconducting order parameter, the precise shape of the gap function and the nature of its coupling to magnetism have proven difficult to pin down. By measuring the Knight shift of UPt_3 in low magnetic fields through NMR measurements on ^{195}Pt, I hope to contribute to the determination of the order parameter. In this chapter I first introduce NMR on type II superconductors, including the origin of the Knight shift and its temperature dependence for spin singlet and triplet superconductors. This is followed by a concise physical description of UPt_3 in the normal state and its phase diagram with multiple superconducting phases. To interpret the experimental data, the theoretical framework used involves the analysis of symmetry. The most popular candidate theories for the order parameter are described here, including their predictions of the Knight shift. A review of the main properties that have been measured in the superconducting state follows, with their implications on the possible candidate theories.

Finally, existing Knight shift measurements on UPt_3 are given, leading to the justification for the measurements performed in this thesis.

4.1 NMR on type II superconductors

In a superconductor in the Meissner state, a magnetic field only penetrates over a distance of order λ, the London penetration depth. This is a function of temperature as it is proportional to the density of Cooper pairs: $\lambda \sim n_s(T)^{-1/2}$. The difference between a type I and a type II superconductor is in the relative values of the penetration depth λ and the coherence length ξ. If the coherence length is the larger, the superconductor is called type I; if the coherence length is less than λ as is the case for UPt_3, then a vortex lattice may form in a magnetic field and it is called type II. In the experiments described in this thesis, the external field falls between the upper and lower critical fields of UPt_3, meaning that when in the superconducting state, the sample is in the mixed state. This has several consequences which must be taken into consideration when carrying out NMR experiments into the superconducting state. However, first we look at the origin of the Knight shift in metals, the main parameter which we aim to measure.

4.1.1 The Knight shift

In Section 2.1 it was shown that the resonance frequency of an NMR signal depends on the static magnetic field surrounding the nuclei in question. In a metal, the conduction electrons are delocalised and exist in eigenstates within an energy band, whose highest occupied state lies at the Fermi energy E_F. Unpaired electrons are found only if their energy is in the vicinity of E_F. In an externally applied magnetic field, unpaired s conduction electrons produce at the nuclear position an average static magnetic field. This field shifts the nuclear resonance frequency and is mediated by the hyperfine interaction. This displacement is called the 'Knight shift', named after Walter Knight who first observed the phenomenon in copper [53].

The Knight shift, K, is defined as the relative shift in NMR frequency for atoms

of a metal compared with the same atoms in a non-metallic environment and is given as a percentage:

$$K = \frac{\Delta f}{f_d} = \frac{f_m - f_d}{f_d}, \tag{4.1}$$

where in a given external field, f_m is the resonance frequency in the metal, f_d is the resonance frequency of the nucleus in a diamagnetic compound and Δf is the frequency shift. Experimentally, the Knight shift is calculated by measuring the resonance frequency of the UPt_3 NMR signal, $f_{\,\mathrm{UPt_3}}$ and knowing the applied field at the sample, B:

$$K = \frac{2\pi f_{\mathrm{UPt_3}}}{\gamma_{\mathrm{Pt\ bare}}\, B} - 1, \tag{4.2}$$

where $\gamma_{Pt\ bare}$ is the gyromagnetic ratio of the platinum in a diamagnetic solid.

In most metals, the Knight shift is positive, as the s conduction electrons align with the external field due to their Pauli temperature-independent susceptibility, χ_P. In this case, for a cubic lattice, the Knight shift is given by [54]:

$$K = \frac{\Delta f}{f} = \frac{\Delta H}{H} = \frac{8\pi}{3}\chi_P M \langle |\psi_F(0)|^2 \rangle_{Av}, \tag{4.3}$$

where χ_P is the spin contribution to the macroscopic susceptibility per unit mass, M is the mass of one atom and $\langle |\psi_F(0)|^2 \rangle_{Av}$ is the average probability density at the nucleus for all electronic states on the Fermi surface. If the electron distribution is not cubically symmetric about the nucleus, then electron density at points other than at the nucleus contributes to ΔH, and ΔH will depend to some extent on the orientation of the crystal with respect to H [55]. This is certainly the case for UPt_3, which is known to have an anisotropic Knight shift [56].

The situation is more complicated for transition metals with unfilled internal shells such as platinum, which has one electron missing from its $5d$ shell [57–59]. Since no contact hyperfine interaction is expected for d electrons, a contribution to K from the d-band susceptibility may arise only from exchange polarisation of inner s-shell electrons and the conduction s-electrons by the d electrons as shown by Heine [60]. The contribution to the spin susceptibility from this mechanism is negative and proportional to the number of unpaired d electrons as the d exchange

potential is attractive and pulls $\psi_{s,p}$ outwards, with a consequent reduction in $\psi_{s,p}(0)$ due to normalisation. Following Lee *et al.* [56], the total spin contribution from these interactions is represented by a hyperfine coupling constant A^s. There is also an orbital shift with coupling constant A^{orb}, which depends on orbital currents and scales with the temperature independent Van Vleck orbital paramagnetism:

$$K = K^s + K^{orb} = A^s\chi^s + A^{orb}\chi^{orb}. \tag{4.4}$$

The orbital shift is usually small and positive and is unaffected by the onset of superconductivity. Thus, a measurement of the Knight shift as a function of temperature enables us to directly probe the spin susceptibility, χ^s. By plotting the measured Knight shift against the susceptibility χ^s with temperature as an implicit parameter, the gradient of the linear relation gives A^s and the intercept at $\chi = 0$ gives K^{orb}. These parameters have been measured for UPt_3 by Kohori [61] on UPt_3 powder and by Lee [56] and Tou [62] on single crystal whiskers and wafers respectively. These experiments are discussed in Section 4.6. We now focus on how the Knight shift is expected to behave into the superconducting state for even parity spin singlet superconductors and odd parity spin triplet superconductors.

4.1.2 Knight shift for spin singlet superconductors

Below T_c in spin singlet superconductors, the conduction electrons start to form Cooper pairs with antiparallel spins. The spin wave function is given by [63]

$$\phi^{\text{spin}}_{\sigma_1,\sigma_2} = \frac{1}{\sqrt{2}}(|\uparrow\downarrow\rangle - |\downarrow\uparrow\rangle) \tag{4.5}$$

and the Cooper pairs have a total spin $\mathbf{S} = 0$ and for conventional BCS s-wave superconductors, the total angular momentum $\mathbf{L} = 0$ but in general $\mathbf{L}$ is always even. This class of superconductors also include d-wave superconductors such as $YBa_2Cu_3O_7$ with $\mathbf{L} = 2$ [64]. As the temperature is lowered into the superconducting state, there are less and less unpaired electrons that contribute to the Knight shift. The spin susceptibility therefore decreases to zero exponentially for $T \to 0$

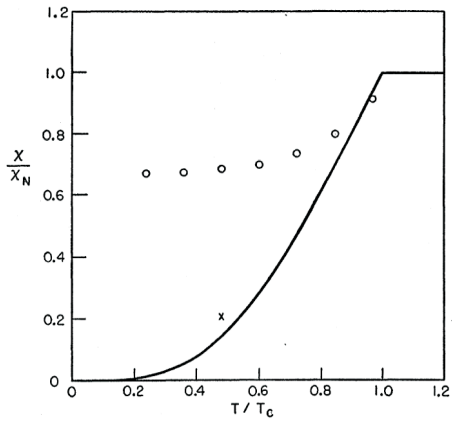

Figure 4.1: The temperature dependence of the susceptibility of a spin singlet superconductor (the Yosida function) shown by the solid line [65]. The susceptibility is normalised by the normal state susceptibility. The circles show measurements taken on a colloid of Hg, by Reif [66].

and the Knight shift is expected to decrease towards the residual orbital part. The Knight shift in metals was observed to approach zero as $T \to 0$ for the simple metal, aluminium [67]. This dependence is given by the Yosida function [65] and is shown in Figure 4.1 by the solid line. For mercury (an s-wave superconductor), the shift was reduced considerably but remained finite at $T = 0$ (circles). As these measurements were performed on small mercury particles (mostly less than 500 Å in diameter), the mean free path for electrons is reduced; this could also occur in the presence of impurities. The result is a mixing of up and down spin states because of spin-orbit interactions. In effect, the presence of strong spin-orbit scattering can mask the decrease in Knight shift to a large extent.

4.1.3 Knight shift for spin triplet superconductors

For a spin triplet superconductor, such as a p ($\mathbf{L} = 1$) or f-wave ($\mathbf{L} = 3$) superconductor, the conduction electrons form Cooper pairs with parallel spins and $\mathbf{S} = 1$. The spin wave function is:

$$\phi^{\text{spin}}_{\sigma_1,\sigma_2} = \begin{cases} |\uparrow\uparrow\rangle \\ \frac{1}{\sqrt{2}}(|\uparrow\downarrow\rangle + |\downarrow\uparrow\rangle) \\ |\downarrow\downarrow\rangle \end{cases} \tag{4.6}$$

corresponding to the three spin projections $S_z = +1, 0, -1$ respectively. The total angular momentum **L** is odd. The pairing state is represented by a 3-dimensional vector $\mathbf{d}(\mathbf{k})$, whose spin-dependent magnitude and direction vary over the Fermi surface in **k** space [68]. The significance of the **d**-vector is explained in more detail in Section 4.4.1. Here we specify that the orientation of the vector is always perpendicular to **S** such that $\mathbf{d}\cdot\mathbf{S}= 0$. The strength of the spin-orbit coupling has significant consequences on the behaviour of the Knight shift for triplet superconductors, as strong spin-orbit coupling tends to pin the **d**-vector to a crystal axis, causing anisotropy in the Knight shift.

In the simple case of equal spin pairing (anisotropic triplet model) [69], the spin state of the Cooper pair is a linear superposition of the $S_z = +1$ and $S_z = -1$ states only i.e. $|\uparrow\uparrow\rangle + |\downarrow\downarrow\rangle$. For weak spin-orbit coupling, the Knight shift K^s remains unchanged from its value in the normal state, as the Cooper pairs are allowed to align with the external magnetic field **B**. However, if due to strong spin-orbit coupling the **d**-vector becomes locked to a crystal axis, x, then K^s will be unchanged for $\mathbf{B} \perp x$ but reduce to the orbital part for $\mathbf{B} \parallel x$.

For the general triplet pairing case (isotropic triplet model), i.e. $|\uparrow\uparrow\rangle + \frac{1}{\sqrt{2}}(|\uparrow\downarrow\rangle + |\downarrow\uparrow\rangle) + |\downarrow\downarrow\rangle$, only the Cooper pairs with zero spin projection will contribute to a decrease in the spin susceptibility below T_c for weak spin-orbit coupling. Thus, K^s reduces to 2/3 of the normal state value as $T \to 0$. In the case of strong spin-orbit coupling, K^s will reduce to 2/3 of the normal state value for **B** perpendicular to x and reduce to the orbital part for **B** parallel to x.

4.1.4 The Diamagnetic shift

When measuring the Knight shift, particularly in low magnetic fields, there is an additional shift in the NMR resonance frequency of type II superconductors on formation of the Abrikosov lattice. In the mixed state a lattice of normal state filaments (vortices) parallel to the field penetrate the superconductor, with the density of vortices increasing with applied field. As the external field can only exist in these filaments, the average field within the sample is smaller than the applied field and so the diamagnetic shift is a negative, field dependent contribution to K.

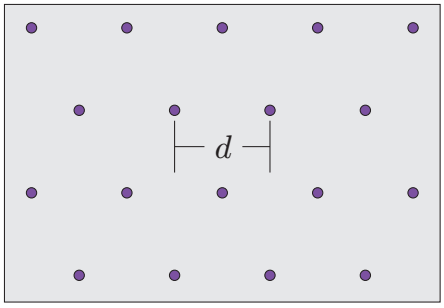

Figure 4.2: Two-dimensional hexagonal lattice of vortex cores. The radii ξ and separation d of the vortices have been drawn to scale for UPt_3 in a field of ∼70 mT.

Since the interaction between vortices is repulsive, the vortices assume the arrangement that will keep them furthest apart - this is the two-dimensional hexagonal lattice structure as measured by Huxley *et al.* [70] for UPt_3 and is depicted in Figure 4.2. As each vortex contains a flux quantum Φ_0, the average field inside the superconductor $\langle B_{in} \rangle$ is given by:

$$\langle B_{in} \rangle = \frac{\Phi_0}{\frac{\sqrt{3}}{2} d^2}, \tag{4.7}$$

where $\frac{\sqrt{3}}{2} d^2$ is the area per vortex. The distance between vortices, d, can be estimated by assuming that for applied fields B_{app} much greater than the lower critical field B_{c1}, $\langle B_{in} \rangle \approx B_{app}$ in Equation 4.7. As B_{c1} is below ∼8 mT [71] for applied fields along the c-axis down to ∼ 300 mK, this condition is satisfied for the experiments in this thesis.

For applied fields in the mixed state where $\xi \ll d \ll \lambda$, the vortices form a rather dense lattice and the interactions extend to distant neighbours. In this regime, the dependence of the internal field on the applied field has been calculated by de Gennes to be [72]:

$$\langle B_{in} \rangle = B_{app} - B_{c1} \frac{\ln(\beta e^{-1/2} d/\xi)}{\ln(\lambda/\xi)}, \tag{4.8}$$

where B_{c1}, ξ and λ are temperature dependent quantities and β is a numerical lattice constant which is $\beta = 0.381$ for a hexagonal lattice. From this, we can

calculate the diamagnetic contribution to the Knight shift as follows:

$$K^{dia} = \frac{\Delta B}{B_{app}} = \frac{\langle B_{in} \rangle - B_{app}}{B_{app}} \tag{4.9}$$

Measurements of the London penetration depth λ and coherence length ξ have been performed by several groups: most recently Kleiman *et al.* [73] measured $\lambda_{\parallel}(0) = 4220$ Å, $\lambda_{\perp}(0) = 7150$ Å and $\xi_{\parallel}(0) = 157$ Å, $\xi_{\perp}(0) = 93$ Å and Yaouanc *et al.* [74] measured $\lambda_{\parallel}(0) = 4260$ Å and $\lambda_{\perp}(0) = 6040$ Å. A subscript $\parallel$ ($\perp$) indicates that the measurement was performed along the UPt_3 c-axis (in the basal plane). For reference, the crystal structure of UPt_3 is shown in Figure 4.5.

The diamagnetic contribution to the Knight shift as a function of temperature can be estimated in the following way. The temperature dependence of the lower critical field B_{c1} can be taken from Figure 4.10 [71] by performing a linear fit to the data above and below T_c^-, normalising the temperature by using the reduced temperature T/T_c^+. The Ginzburg-Landau parameter λ/ξ is temperature independent. The temperature dependence of the coherence length is given by Equation 4.10 [72].

$$\xi(T) = 0.74\xi_0 \left(1 - \frac{T}{T_c}\right)^{-\frac{1}{2}} \tag{4.10}$$

By substituting these temperature dependences into Equation 4.8 and using Equation 4.9, Figure 4.3 shows the diamagnetic shift as a function of reduced temperature obtained for an applied field of 71.5 mT parallel to the c-axis. This is the static NMR field used for the experiments in this thesis. In this direction, we use the average value of $\lambda_{\perp}(0) = 6600$ Å and $\xi_{\perp}(0) = 93$ Å. From Equation 4.7, this corresponds to a vortex separation of $d = 1830$ Å. Figure 4.4 shows the form of the diamagnetic correction as a function of applied magnetic field parallel to the c-axis for a nominal temperature of 0.9 T/T_c^+. By measuring the Knight shift as a function of temperature in different static NMR fields, it will be possible to separate out this field-dependent diamagnetic contribution to the Knight shift.

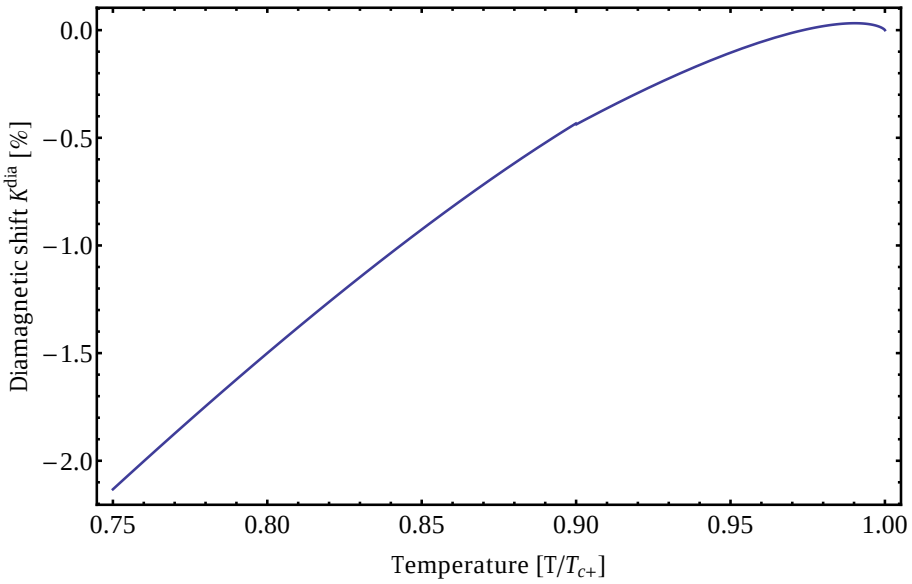

Figure 4.3: Estimated diamagnetic shift $K^{dia}(T) = \Delta B/B$ for UPt_3 as a function of temperature with a magnetic field of 71.5 mT applied along the c-axis.

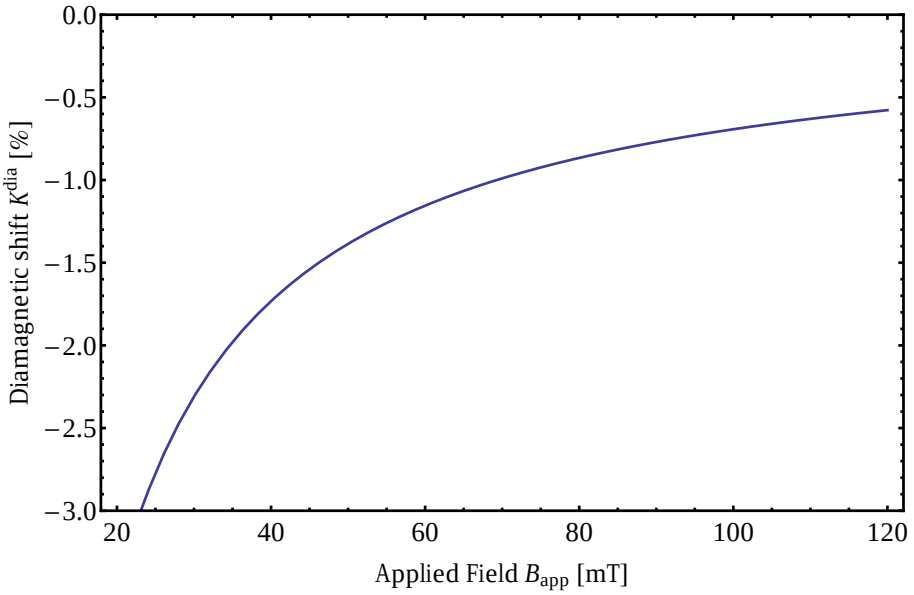

Figure 4.4: Estimated diamagnetic shift $K^{dia} = \Delta B/B$ for UPt_3 as a function of magnetic field applied along the c-axis at 0.9 T/T_c^+.

4.1.5 Influence of the vortex lattice on T_2^*

From the frequency of the NMR line, we have seen that Knight shift measurements tell us about the electron spin susceptibility of the system as we go into the superconducting state, which can be used to determine the spin state of the Cooper pair. In addition, from the NMR lineshape information can be obtained concerning the spatial variation of magnetic field within the superconducting sample. In this section, we discuss the influence of the vortex lattice on the measured spin-spin relaxation time T_2^*.

When the sample is in the superconducting mixed state at fields just above B_{c1}, the vortices are very spread out as $d \gg \lambda$. At these low fields, as the distribution of the magnetic field inside the sample is least homogeneous, so a broadening of the resonance line is expected. At the other extreme, for fields just below B_{c2}, the vortices are very close together and $d \ll \lambda$. The magnetic fields of the vortices overlap each other significantly and the field profile becomes very homogeneous. Consequently, linewidth broadening becomes negligible. In the regime $\xi \ll d \ll \lambda$, there is little dependence of the linewidth due to the vortex lattice on the applied field. This contribution to the broadening can be estimated by [72, 75];

$$\delta B \approx \frac{\Phi_0}{\lambda^2 \sqrt{16\pi^3}}, \tag{4.11}$$

where $\Phi_0 = 2.07 \times 10^{-15}$ Wb is the flux quantum and λ the London penetration depth. The contribution of the vortex lattice to the measured T_2^* is then:

$$T_{2\,\mathrm{VL}}^* = \frac{2}{\gamma \delta B}, \tag{4.12}$$

with γ, the gyromagnetic ratio of ^{195}Pt in UPt_3. These equations will be used to analyse the data in Section 6.3.2 where the linewidth is measured as a function of temperature into the superconducting mixed state. T_1 relaxation is discussed alongside previous NMR data in Section 4.5.3. The following section looks at a few of the relevant experiments on what has been deduced about the compound so far.

4.2 UPt_3 in the Normal state

UPt_3 is the archetype of a heavy fermion system. The normal state at sufficiently low temperatures has the qualitative properties of a Fermi liquid (as shown below) but with strong mass renormalisation. The experimental criterion for a heavy fermion system is an anomalously large value for the coefficient γ, of the linear electronic term in the specific heat $C = \gamma T$ [76]. For ordinary metals such as copper and nickel, γ is of the order of l-10 mJ $mol^{-1}K^{-2}$. For UPt_3, γ was measured to be orders of magnitude larger at 422 mJ $mol^{-1}K^{-2}$ [77]. Such a large γ-value is usually explained by the existence of heavy electrons or quasiparticles at the Fermi surface. In the case of UPt_3, it is an f-electron system with a partially filled $5f$ uranium shell and it is the strong coupling between these uranium f-local moments and conduction electrons that make them heavy. The effective mass of these quasiparticles is the equivalent of 180 times the free electron mass (assuming a spherical Fermi surface), hence the name heavy fermions.

4.2.1 The crystal structure

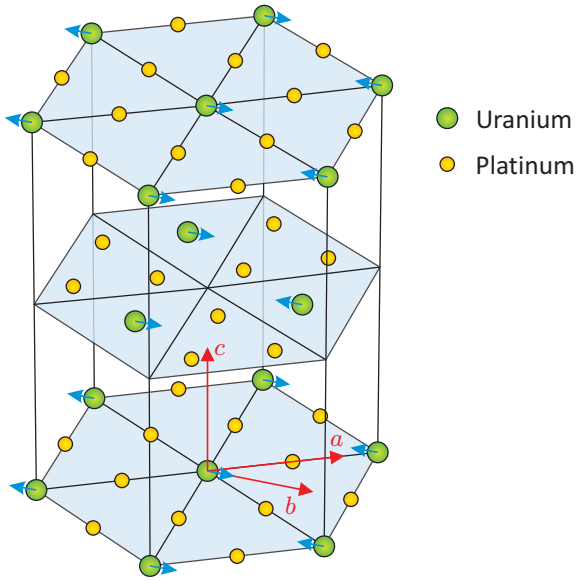

Figure 4.5: Crystal structure of UPt_3 assuming a hexagonal structure. Blue arrows indicate the ordered magnetic moments within the basal planes in the antiferromagnetic state below $T_N \sim 5$ K.

The crystal structure of UPt_3 is depicted in Figure 4.5 with the three crystallographic axes a, b and c labelled. The uranium atoms form a close packed hexagonal structure. The symmetry of this compound belongs to the point group D_{6h}, relevant for the theoretical approaches described in Section 4.4, although a slight trigonal distortion has been reported by Walko *et al.* [78]. This distortion causes the U and Pt atoms to not lie in the same plane in the z-direction, lowering the symmetry of the crystal.

4.2.2 Fermi surface

The Fermi surface has been measured with the de Haas-van Alphen effect and successfully compared with band structure calculations most recently by McMullan *et al.* [79]. It has a complex topology and consists of six sheets. The experimental evidence strongly favours the model in which all three of the uranium $5f$-electrons are delocalised in UPt_3.

4.2.3 Low temperature resistivity

The itinerant quasiparticles in UPt_3 can carry charge and heat. The electrical resistivity ρ is characterised by a well defined T^2 law, valid for both crystal directions (parallel and perpendicular to the c-axis) from T_c up to a temperature of about 1.5 K and is given by

$$\rho(T) = \rho_0 + AT^2, \tag{4.13}$$

where the inelastic scattering coefficient A has been measured to be $A = 0.55 \pm 0.05$ $\mu\Omega$cm K^{-2} for currents $J \parallel c$ and $A = 1.55 \pm 0.1$ $\mu\Omega$cm K^{-2} for $J \parallel a, b$ in several studies [80]. ρ_0 on the other hand, which depends only on the concentration of impurities, varies by a factor of 10 or so with $\rho_0 = 0.2 - 2$ $\mu\Omega$ for $J \parallel c$ and $\rho_0 = 0.6 - 6$ $\mu\Omega$ for $J \parallel a, b$. As this shows, conduction is anisotropic with resistivity being lowest along the c-axis and highest perpendicular to it. The resistivity is used to calculate the skin depth of UPt_3 in estimates of the NMR signal size in Section 6.4.1.

4.2.4 Susceptibility

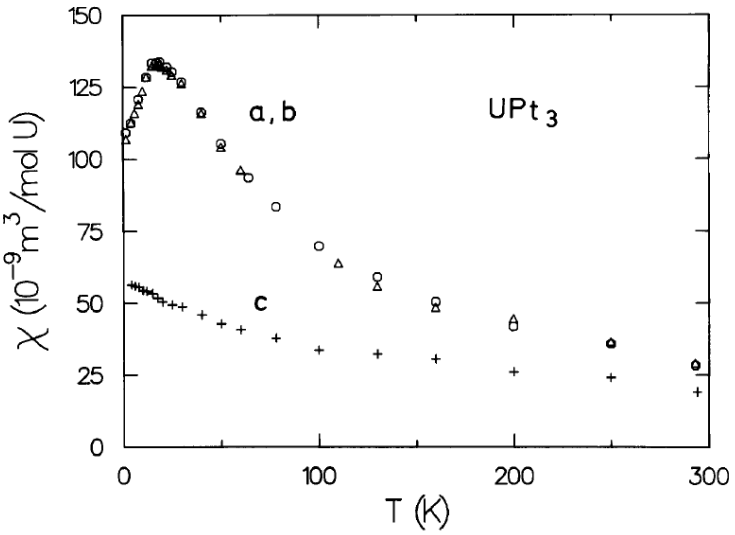

Figure 4.6: Susceptibility as a function of temperature for a UPt_3 single crystal along the three crystal axes as measured by Franse [81].

The measured temperature dependence of the ac susceptibility of single crystal UPt_3 is shown in Figure 4.6 [81]. The region above 20 K can be fitted to a Curie law $(1/T)$ temperature dependence. The susceptibility is highly anisotropic and can be explained by the different contributions from the Van Vleck and Pauli parts of the susceptibility. Along the c-axis, the Pauli contribution dominates, whereas the susceptibility in the basal plane is dominated by the Van Vleck contribution and is considerably larger [82]. Measurements of susceptibility can also be used to determine the orientation of the crystal and ensure that the crystal structure is hexagonal and that there are no stacking defects, which could cause an isotropic susceptibility. The orientation of the UPt_3 crystal measured in this thesis was indeed confirmed using susceptibility measurements in Section 6.1.2.

4.2.5 Antiferromagnetism

The most important magnetic property of UPt_3 is the small-moment antiferromagnetic phase, which develops below the Néel temperature of $\sim$5 K. This was first seen through neutron diffraction studies, most notably by Aeppli *et al.* [83] with

an unusually small ordered moment of $0.02\mu_B$/U atom and found to coexist with superconductivity [84]. The moments are directed along the b-axis and are shown in Figure 4.5. Due to the fact that this ordering has only been seen in neutron and x-ray scattering experiments [85] and not in the NMR [62], specific heat [86], magnetisation [87] or zero field muon spin resonance (μSR) experiments [88], it has been suggested that the ordering may not be static but nearly static. This idea has been supported by recent magnetoresistance measurements, which show that antiferromagnetism in UPt_3 is strongly fluctuating [89]. This antiferromagnetism is important as it may be crucial in explaining the superconducting phase diagram, as detailed in the following section.

4.3 The H-T phase diagram

UPt_3 is a rare instance in nature of a superconductor with multiple superconducting phases. Due to this property, it has been characterised as the metallic analogue of ^{3}He. There are two phases A and B that exist in zero magnetic field. As UPt_3 is a type-II superconductor, for each of the A and B phases there exists a low field Meissner phase and a high field vortex phase. By applying a larger magnetic field, the C phase appears thus giving five superconducting phases in total (see Figure 4.7). The phase diagram is also anisotropic. The anisotropy of the upper critical field H_{c2} is discussed in Section 4.5.4. However, measurements for the lower critical field H_{c1} showed an approximately isotropic H_{c1}, as will be shown in Section 4.5.5. The observation of multiple superconducting phases is direct evidence for a multi-component superconducting order parameter i.e. that there exist internal degrees of freedom in the superconducting state. We review how this phase diagram was formed.

4.3.1 The A-B splitting

Improvements in sample quality allowed Fisher *et al.* to resolve a double peak in heat capacity measurements for the first time [91], showing the splitting of the superconducting transition at zero field. The two transition temperatures are

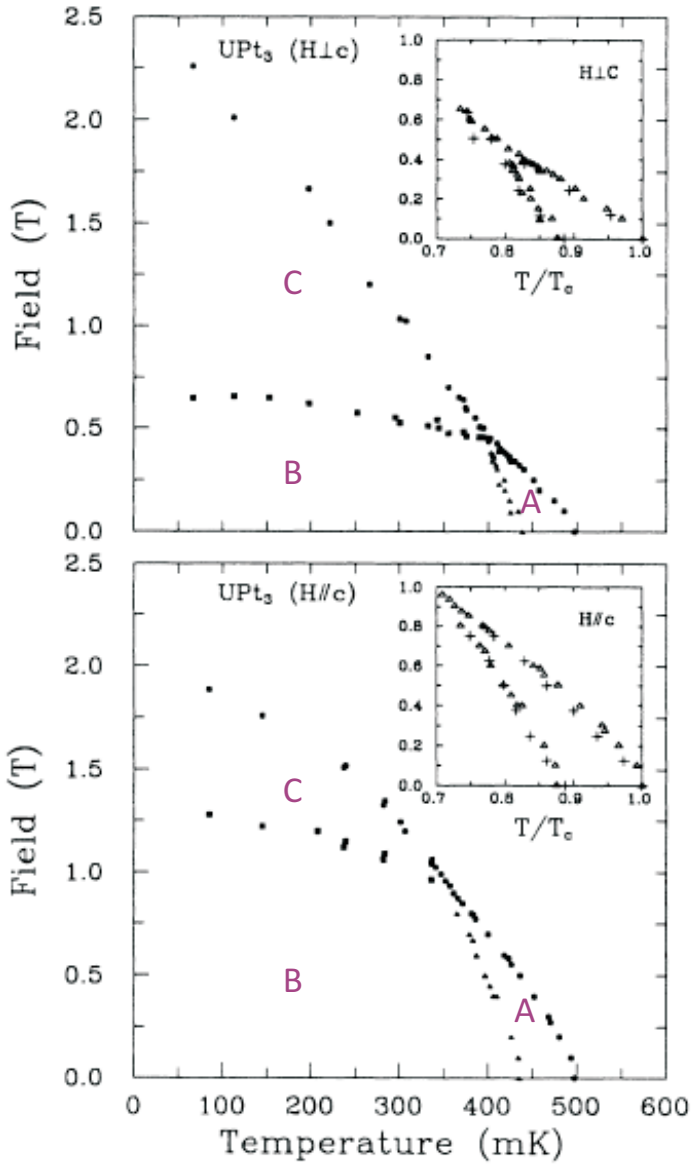

Figure 4.7: Phase diagrams obtained from ultrasound velocity measurements for two different orientations of the applied field [90].

commonly referred to as the upper and lower transition temperatures, T_c^+ and T_c^- respectively and mark the phase boundaries between the normal, A and B phases. The transition temperatures are strongly dependent on sample quality but the splitting between the two is quite reliably 50-60 mK in zero field across several samples [80]. The closeness of T_c^+ and T_c^- in temperature suggests that they have a common origin and points to the existence of an internal degree of freedom in the superconducting order parameter.

4.3.2 Pressure measurements

Evidence for a possible coupling between the multiple superconducting phases and antiferromagnetism came from studies on UPt_3 under hydrostatic pressure. Hayden *et al.* performed neutron-scattering experiments on single crystals pressurised using ^{4}He for pressures up to $\sim$6 kbar [92]. A comparison with the data of Trappmann *et al.* [93] who measured the pressure dependence of the specific heat shows that both the small moment antiferromagnetism (measured at 1.8 K) and the A-B splitting are suppressed at very similar pressures (4-5 kbar), suggesting that the antiferromagnetic order may be responsible for the double superconducting transition.

4.3.3 Tetracritical point

Naturally, the measurement of the transition temperatures was continued as a function of magnetic field. The first complete phase diagram in the field-temperature plane for UPt_3 derived from a single measurement technique is credited to Adenwalla *et al.* who made longitudinal ultrasonic velocity measurements [90]. The phase diagram was measured for different orientations of the applied field and is shown in Figure 4.7 and clearly show three superconducting phases labelled A, B and C corresponding to different order parameter symmetries. There is a tetracritical point at ambient pressures for both orientations of the field where these superconducting phases appear to meet with the normal phase. This moves to lower fields as the field is rotated away from the c-axis into the basal plane. The magnetic fields used in the work described in this thesis are very low (of order mT) so the C phase is not probed. Bruls *et al.* also measured a similar phase diagram by studying elastic constants, ultrasonic attenuation and ac susceptibility [94].

4.4 Unconventional superconductivity

Evidence of unconventional superconductivity can be seen in many physical properties. It is defined as a superconducting state for which the order parameter has

a smaller rotational symmetry group than that of the normal metallic crystal [95]. This means that the symmetry of the superconducting gap function is lower than the symmetry of the Fermi surface. Conventional superconductivity on the other hand, as described by BCS theory has an s-wave order parameter, which has an isotropic gap function that is constant in k-space. This has the same symmetry as the Fermi surface, which is spherical.

Conventional s-wave electron-phonon coupling in principle cannot occur in heavy fermions, as such heavy conduction electrons cannot escape fast enough from a location where it has caused a lattice distortion, in order to reduce the Coulomb repulsion of its partner [96]. For UPt_3, the fact that the H-T phase diagram has multiple superconducting phases is proof itself of unconventional symmetry, as the s-wave state is unique. The central issue has been to identify an order parameter that is consistent with this phase diagram. What follows is a short description of the theoretical models that are the most likely candidates for the interpretation of experimental data on UPt_3 including their predictions on the gap function and Knight shifts, which can be tested experimentally.

4.4.1 Theoretical frameworks

The theoretical framework that has most commonly been used considers the possible forms of the Cooper pair wavefunction with respect to the point group of the crystal, ${D_{6h}}^1$. The point group of a crystal is a set of symmetry operations such as rotations and reflections around a fixed point that leave the crystal unchanged. As the point group is finite, the number of representations (and corresponding Cooper pair wave functions) that must also transform in the same way is also finite. There are six representations of the pure rotation group D_6 which are subdivided into one and two dimensional representations, meaning the order parameter has one and two components respectively. A_1, A_2, B_1 and B_2 are 1D representations while E_1 and E_2 are 2D. When the inversion symmetry of UPt_3 is taken into account, we can further assign an even (g for *gerade*) or odd (u for *ungerade*) parity for

[1] for *dihedral*, indicating that the group has a 6-fold rotation axis plus a twofold axis and mirror plane, perpendicular to that axis.

each of these representations, giving 12 in total. The notation is then E_{1g}, E_{1u} etc, each with their own form of the superconducting gap function, which is the orbital part of the Cooper pair wave function. For conventional s-wave superconductivity only, the representation would be A_{1g}.

The superconducting gap function Δ is a single parameter in BCS theory. For unconventional superconductors, this is generalised to a $\mathbf{k}$ dependent function, encompassing all possible Cooper pairing states:

$$\Delta(\mathbf{k}) = \begin{pmatrix} \Delta_{\uparrow\uparrow}(\mathbf{k}) & \Delta_{\uparrow\downarrow}(\mathbf{k}) \\ \Delta_{\downarrow\uparrow}(\mathbf{k}) & \Delta_{\downarrow\downarrow}(\mathbf{k}) \end{pmatrix}, \tag{4.14}$$

where $\mathbf{k}$ is the wavevector. Following the review by Joynt and Taillefer [80], this gap function can be expressed in terms of a spin-independent scalar component $\psi(\mathbf{k})$ and a spin-dependent vector component $\mathbf{d}(\mathbf{k})$:

$$\Delta(\mathbf{k}) = i[\psi(\mathbf{k}) + \mathbf{d}(\mathbf{k}) \cdot \boldsymbol{\sigma}]\sigma_y, \tag{4.15}$$

where $\boldsymbol{\sigma} = \{\sigma_x, \sigma_y, \sigma_z\}$ is the vector of the Pauli spin matrices. A state in which $\mathbf{d}(\mathbf{k}) = 0$ is said to be a "singlet" state ($\mathbf{S} = 0$) where the gap function has the form [63]:

$$\Delta(\mathbf{k}) = \begin{pmatrix} 0 & \psi(\mathbf{k}) \\ -\psi(\mathbf{k}) & 0 \end{pmatrix}. \tag{4.16}$$

A state in which $\psi(\mathbf{k}) = 0$ is said to be a "triplet" state ($\mathbf{S} = 1$), such that the gap function is:

$$\Delta(\mathbf{k}) = \begin{pmatrix} -d_x(\mathbf{k}) + id_y(\mathbf{k}) & d_z(\mathbf{k}) \\ d_z(\mathbf{k}) & d_x(\mathbf{k}) + id_y(\mathbf{k}) \end{pmatrix}. \tag{4.17}$$

As pairs of fermions must have antisymmetric wavefunctions under particle exchange due to the Pauli exclusion principle, $\Delta_{\alpha\beta}(\mathbf{k}) = -\Delta_{\beta\alpha}(-\mathbf{k})$. Thus, $\psi(\mathbf{k}) = \psi(-\mathbf{k})$ and $\mathbf{d}(\mathbf{k}) = -\mathbf{d}(-\mathbf{k})$. Under the parity operation $\mathbf{k} \to -\mathbf{k}$, $\psi(\mathbf{k})$ is even and $\mathbf{d}(\mathbf{k})$ is odd, hence the often quoted names "even parity" for spin singlet pairing and "odd parity" for spin triplet pairing.

4.4.2 Candidate theories

For theoreticians to explain the superconducting phase diagram, in particular the small double transition into the A and B phases, a symmetry breaking field (SBF) is required to break the degeneracy of the order parameter. This SBF is required in all theoretical approaches described here. Of the above representations, the strongest candidates are the two dimensional E representations E_{1g} by Park and Joynt [82] and E_{2u} by Sauls [97]. These are called 'orbital scenarios', as the degeneracy of the pairing function is assumed to arise from the orbital part of the pairing function. An alternative 'spin scenario' proposal for a candidate order paramter is the Spin triplet theory by Machida [98], for which the degeneracy of the pairing function arises from the spin part of the pairing function. A detailed description of these theories is not attempted in this section. Below is a brief account of the key points of these three most promising theories that are relevant for interpreting the experiments that follow, along with their predictions for the Knight shift experiment.

E_{1g} and E_{2u} representations

The E representation models are two dimensional, which simply means the order parameter and hence the gap function are described by two terms, a real and an imaginary term. The real component of the order parameter turns on at T_c^+ (A phase) and the imaginary component turns on at T_c^- (B phase), creating a complex order parameter state. For both these models, strong spin-orbit coupling is assumed [99], so that $\mathbf{d} \parallel c$ and the Cooper pair spin vector is locked in the basal plane [95]. The E_{1g} model is the realisation of spin-singlet, d-wave pairing. E_{2u} describes spin-triplet, f-wave pairing [97]. The SBF that breaks the basal plane symmetry of the hexagonal crystal, lifting the degeneracy of the two-component order parameter, may have its origins in the antiferromagnetic order measured below 5 K (as we saw in the pressure measurements of Section 4.3.2) or the measured trigonal distortion in the crystal structure. At the time of writing, this is still unresolved.

Various experiments are in principle able to discriminate between these E rep-

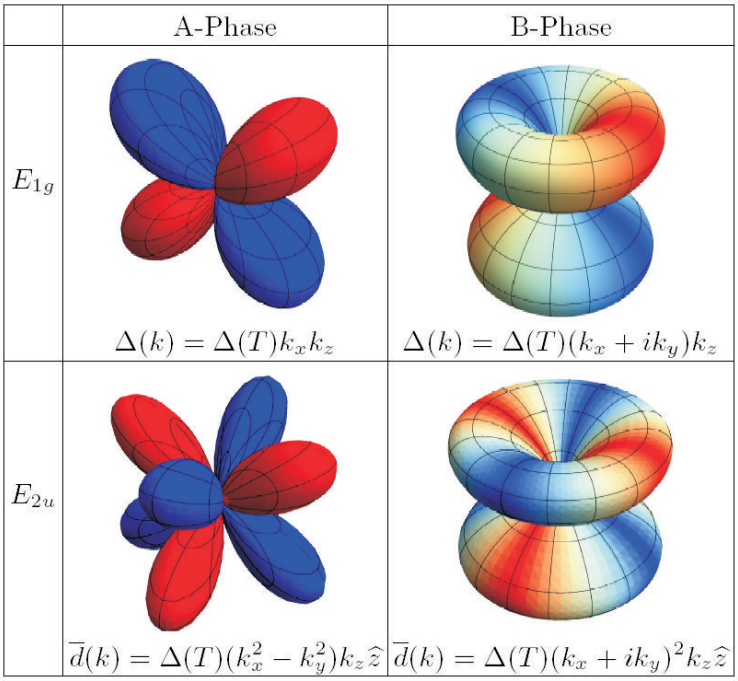

Figure 4.8: Graphical depictions of the E_{1g} and E_{2u} models of the order parameter for UPt_3 for the two superconducting phases A and B [100].

resentations by measuring the nodal structure of the gap function. These include thermal conductivity, ultrasonic attenuation and Josephson junction measurements detailed in Section 4.5. Focus has been placed on measuring the low temperature B phase, as experimentally it is easier to probe since it is accessible over a larger temperature range than the A phase. As in the review by Joynt and Taillefer [80], the gap structures for the B phase are called "Hybrid I" and "Hybrid II" for the E_{1g} and E_{2u} representations respectively. A graphical depiction is shown in Figure 4.8 (from [100]). The Hybrid II gap structure (which originally had only point nodes) was proposed on phenomenological grounds [95]. This has been theoretically justified in a recent Rapid Communication by Micklitz and Norman [101] who showed that in crystals with a twofold screw axis such as UPt_3[2], line nodes for odd-parity Cooper pair wave functions may occur. Both models for the order parameter of UPt_3 therefore lead to an excitation gap with a nodal line in the basal plane and point nodes along the $\pm c$ directions for the low temperature

[2]A rotation by 180° about the c-axis followed by a translation of half a lattice vector leaves the crystal unchanged.

B phase. The difference in the excitation spectrum for these two states is that the gap opens linearly for small angles away from the c direction for the E_{1g} order parameter, but quadratically for the E_{2u} order parameter [102], a subtle difference that is often difficult to discriminate experimentally.

A more decisive approach is to measure the Pauli spin susceptibility, through the Knight shift, into the superconducting state along all three crystal axis orientations for a single crystal of UPt_3. This makes it possible to more clearly discriminate between the two representations described above, as explained in Sections 4.1.2 and 4.1.3. For the E_{1g} model, superconductivity affects the Pauli susceptibility in a drastic fashion, as this is a singlet state. The Pauli term is reduced to zero at 0 K. In the clean limit (negligible spin-orbit scattering), the Knight shift should decrease for all field orientations as $T \rightarrow 0$, approaching the orbital shift K^{orb}. For the E_{2u} model, strong spin-orbit coupling locks the spin vector to the basal plane such that $\mathbf{d} \parallel c$. Below T_c, the Knight shift is expected to be suppressed for fields $B \parallel c$ but with no suppression for $B \perp c$.

Spin triplet theory

In this theory, the symmetry of the Cooper pairs belongs to the odd-parity, spin triplet pairing state, where the **d**-vector has three components. In terms of experimental signatures, the most significant difference in this alternative theory is that the effective spin-orbit coupling felt by a Cooper pair is assumed to be weak, or not strong enough to lock the spin degree of freedom to the crystal direction. In this model, antiferromagnetic fluctuations in the hexagonal plane are responsible for breaking the triple degeneracy of the spin and creating multiple superconducting phases. The nodal structure of the gap function was not a crucial part of the spin triplet scenario but based on recent results [70, 103] favouring the E_{2u} type gap structure as we will see in the next section, a re-examined scenario was put forward that includes this type of gap symmetry [104, 105].

The original Spin triplet theory predicted that the Knight shift should remain constant for all orientations of the field as the spins are free to rotate with the field due to weak spin-orbit coupling. However, in light of the Knight shift experiment

by Tou *et al.* [106], a revised explanation is given that tries to explain their results [107]. In doing so, in effect their predictions for the Knight shift have become the results of Tou's experiment. Section 4.6.4 will cover this experiment in detail.

4.5 UPt_3 in the Superconducting state

For conventional superconductors, the gap function is isotropic and the density of quasiparticle states has a gap of Δ_0. This leads to an exponential temperature dependence of various low temperature thermal properties. For unconventional superconductors, there will be nodes and/or lines in the gap function, and the generic form of the density of states at low energies will depend soley on their topology, leading to different power law dependencies [108]. These power laws are only expected to apply for $T \ll T_c$ i.e. the B phase, and are a way of probing the orbital part of the wavefunction. The spin part may be accessed by looking at the magnetic response such as the Knight shift, which is the focus of the following section. Here we review the superconducting state of UPt_3 through its thermodynamic and transport properties and their theoretical implications on the gap function.

4.5.1 Thermal conductivity

Thermal conductivity is a directional probe as heat currents can be applied along a chosen axis, enabling the measurement of nodes in the gap for certain **k** directions. If a node lies in the measured direction, this will be seen as an enhanced thermal excitation of quasiparticles as they do not need any energy to be excited. The thermal conductivity κ was measured along both crystal directions (b and c axes) below 0.3 T_c and the ratio κ_c/κ_b was found to extrapolate to a large finite value between 0.4 and 0.58 at zero temperature by Lussier *et al.* [109]. By comparison with both the Hybrid I and II gaps, they conclude that their results are in excellent agreement with the E_{2u} gap.

4.5.2 Transverse ultrasonic attenuation

Transverse ultrasonic attenuation is also a highly directional tool as it involves two independent vectors: the propagation direction $\mathbf{q}$ and the polarisation ϵ. When sound waves are sent through a metal at low temperatures, they are attenuated primarily by electrons, thus becoming a tool for investigating the geometric properties of the superconducting gap. The attenuation is largest when the polarisation is along an antinode of the order parameter, and it is smallest when the polarisation is along a nodal direction. Historically, Shivaram *et al.* [110] were the first to provide evidence of a highly anisotropic gap as they found that the attenuation $\alpha_{ab}(\epsilon \parallel a, \mathbf{q} \parallel b)$ is linear in temperature, while $\alpha_{ac} \sim T^3$.

A later study by Ellman *et al.* [111] measured transverse sound attenuation of the A and B phases in zero field as a function of temperature and found that there was a slight increase in slope when passing through the A phase. This is explained by assuming that there are more quasiparticles in phase A than would be present if phase B extended up to the same temperature, implying that there are more nodal lines in the gap structure of phase A. An analysis by Graf *et al.* [97] comes to the conclusion that the ultrasonic attenuation data are in excellent agreement with theoretical calculations for the E_{2u} model of the A and B phases but unsatisfactory for all other models, independent of the orientation of the $\mathbf{d}$-vector, thus not excluding the spin triplet theory.

4.5.3 NMR relaxation rate

The nuclear magnetic relaxation rate $1/T_1$ of ^{195}Pt in UPt_3 was measured as a function of temperature by Kohori *et al.* [112]. As the sample was in powder form (of 70-200 μm in size) this is a directionally averaged quantity but nevertheless gives clues to the structure of the gap function. In metals, spin-lattice relaxation is mediated by the hyperfine interaction between nuclei and the conduction electrons, hence T_1 is dependent on the number of conduction electrons taking part in the relaxation process. Due to the Pauli principle, only the conduction electrons with enough thermal energy k_BT around the Fermi energy can contribute to the

relaxation process. This was the case for UPt_3 where it was found that the relaxation rate $\sim T$ in the normal state below 4.2 K, which is known as the Korringa law, indicating Fermi liquid behaviour. Below T_c, the rate drops faster as $\sim T^3$, signifying a gap with a line node. This is consistent with E_{1g}, E_{2u} with $\mathbf{d}\| c$ and polar gaps (with no line node at the equator). The absence of a Hebel-Slichter peak is also a clear sign that s-wave BCS superconductivity is not observed. Figure 4.9 shows the relaxation rate T_1^{-1} as a function of temperature as measured by Kohori *et al.* [112]. The relaxation rates for the range of temperatures explored within this thesis are marked.

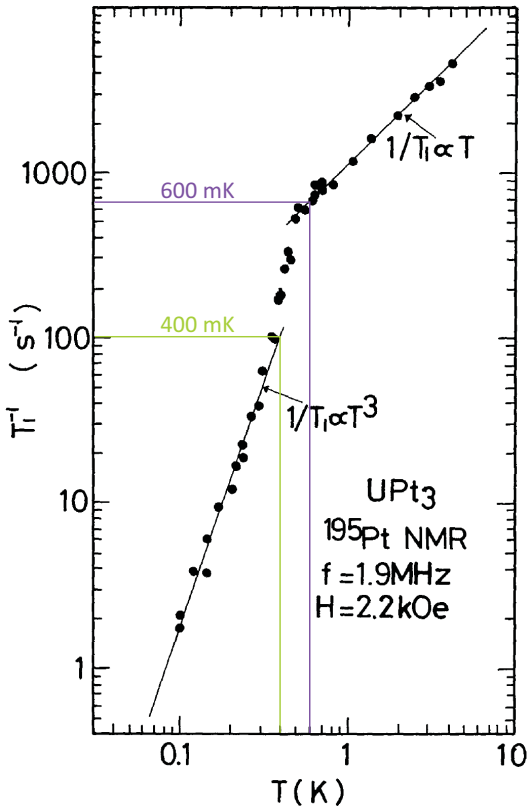

Figure 4.9: The temperature dependence of T_1^{-1} for ^{195}Pt in UPt_3 powder. After Kohori *et al.* [112]. The expected T_1s for 600 mK and 400 mK are $\sim$ 1.4 ms and 10 ms respectively.

4.5.4 Anisotropy of upper critical field H_{c2}

The H-T phase diagram of UPt_3 (Figure 4.7) clearly shows that the upper critical field H_{c2} is anisotropic, i.e. it depends on the direction of the applied field.

Although not a transport property, it nevertheless gives information about the pairing function. The upper critical field $H_{c2}^{\perp}$ for the basal plane exceeds that for the c-axis at low temperatures. For spin singlet states, H_{c2} is bounded by the paramagnetic effect for all directions of field. But for spin triplet states, there is no paramagnetic suppression of superconductivity if the external field is perpendicular to the direction $\mathbf{\Delta}$ along which the Cooper pairs have zero total spin, i.e. $\mathbf{\Delta} \cdot \mathbf{S} = \mathbf{0}$, whereas the magnetic field of other orientations will be a pair-breaking source [95]. The odd-parity E_{2u} representation with *strong* spin-orbit locking of $\mathbf{d} \parallel c$ quantitatively accounts for the anisotropy of the paramagnetic limit of H_{c2} observed at low temperatures. This cannot be explained by the spin triplet theory as they assume weak spin-orbit coupling, which would not cause anisotropy. However, Machida *et al.* explain that the anomalous $H_{c2}^{\perp}$ curve instead indicates a new phase above the C phase [98] but this has not yet been found despite careful sound attenuation experiments.

4.5.5 Lower critical field H_{c1}

The lower critical field as a function of temperature has been measured by a few groups [71, 113, 114]. Magnetisation measurements by Vincent *et al.* are reproduced in Figure 4.10. Although their data seem to show little anisotropy

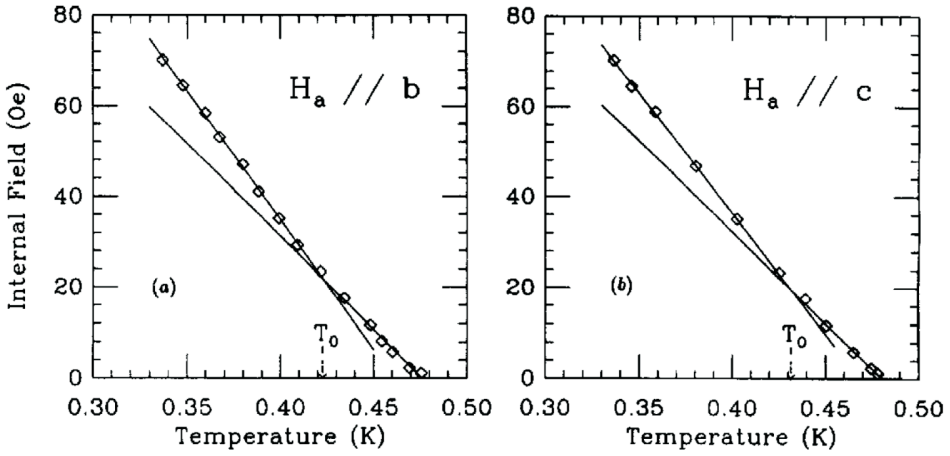

Figure 4.10: Lower critical field H_{c1} as a function of temperature for applied fields along the b and c-axes [71].

along the two crystal directions, the A-B phase transition can be clearly seen by a change in slope of H_{c1}(T).

4.5.6 Other recent experiments

A few recent experiments are also worth mentioning, which also probe the gap function but do not have power law dependences on temperature. Firstly, small-angle neutron scattering experiments have been performed by Huxley *et al.* to measure the flux-line lattice formed through the A-B phase transition [70]. The magnetic field was applied along the c-axis at different temperatures, and the sample cooled to a lower temperature for measurement. At the lowest temperatures (the B phase), a hexagonal flux-line lattice is formed in the basal plane. In the temperature range corresponding to phase A, two new hexagonal lattice orientations form at $\pm 15^\circ$ from the a direction. This is taken as evidence for the E_{2u} type gap as this orienting effect of 15 $^\circ$ is predicted, unlike the E_{1g} model.

Secondly, the phase of the superconducting order parameter of UPt_3 has been probed by Josephson interferometry by Strand *et al.* [100]. As it can be seen from Figure 4.8, another way to differentiate between the two E representation order parameters is by the periodicity of phase winding. A rotation of 90° about the c-axis causes a phase shift of $\pi/2$ in the E_{1g} model but π in the E_{2u} model. By wrapping a Josephson junction around the corner of the UPt_3 crystal, the resulting diffraction pattern will become dependent on the phase difference between the two edges. The resulting diffraction pattern was compared to simulations for the two models and the measured π phase shift for the 90° rotation is in agreement with the E_{2u} order parameter.

In a more recent experiment [115], the same group measured the critical current of a Josephson junction between two superconductors (one of them being UPt_3 the other Pb) as a function of k-space. The angular dependence of the gap magnitude was measured, providing further verification of the E_{2u} symmetry picture. Moreover, they confirmed the location of a line node that is present in the gap of the high-temperature component of the order parameter but not the low temperature component, again supporting the E_{2u} symmetry picture.

4.6 Previous Knight shift measurements

Most of the experiments mentioned above give evidence for the orbital part of the order parameter by measuring the gap function. However, as it can be seen from Figure 4.8, due to the similarity between the gap functions it is difficult to precisely distinguish between the E_{1g} and E_{2u} representations on the basis of power law dependencies of measured quantities alone. However, the extensive data gathered thus far, convincingly points to the E_{2u} model. A more straightforward way of discriminating between the different order parameters is to perform Knight shift measurements into the superconducting state, which measures the spin part of the order parameter as NMR probes the spin susceptibility of the electrons. The predictions for the Knight shift have very different signatures as we saw in Section 4.4.2.

Unfortunately, the results of such a Knight shift measurement [62, 106] were not fully compatible with the E_{2u} theory; this will be addressed in Section 4.6.4. This has been a much less explored area of UPt_3 as NMR on metals requires a very sensitive setup, due to the small signal sizes obtained from single crystals. This is because the signal only comes from within approximately half the skin depth of the metal due to the skin effect. Here, a review of the Knight shift measurements on UPt_3 to date is given, leading to the motivation for the Knight shift measurements performed in this thesis.

4.6.1 The Lee experiment on whiskers

Lee *et al.* (1993) measured the Knight shift of aligned single crystal whiskers of UPt_3 in the normal state, for temperatures from 50 K down to 4 K [56]. The Knight shift of 1000's of UPt_3 whiskers at a resonance frequency of 11 MHz (B_0 ∼1.246 T) was measured by the spin echo method, with ^{63}Cu as the field reference marker. The angular dependence of the Knight shift was measured at a temperature of 4.94 K with linewidths of 50 kHz (typically for fields perpendicular to the c-axis). Their measured Knight shifts in the normal state were $K_\perp = -9.0$ % and $K_\parallel = -1.8$ %.

As discussed in Section 4.1.1, from Equation 4.4 the hyperfine coupling constant for the spin susceptibility, A^s and the residual orbital part of the Knight shift, K^{orb} for each crystal axis direction can be obtained from a linear fit to a plot of $K_\parallel$ ($K_\perp$) vs. $\chi_\parallel$ ($\chi_\perp$), with temperature as the implicit parameter. Lee measured $A^s_\parallel = -69$ kOe/μ_B and $A^s_\perp = -92$ kOe/μ_B from the gradient and $K^{orb}_\parallel = 3.5$ % and $K^{orb}_\perp = 5.5$ % from the intercept at $\chi = 0$.

The spin-spin relaxation rate was also measured down to 4 K and was found to be independent of temperature across the temperature range investigated for both orientations, with $T_{2,\perp} \sim 38$ μs and $T_{2,\parallel} \sim 83$ μs.

4.6.2 The Kohori experiment on polycrystalline powder

The first to measure the Knight shift of UPt_3 into the superconducting state was Kohori *et al.* (1987) who measured polycrystalline UPt_3 crushed into a powder of ~ 70 μm in diameter in order for full rf penetration into the sample [61]. As the sample was not a single crystal, a composite NMR spectrum was obtained with contributions from all axis orientations. Nevertheless, they were able to extract two peaks corresponding to fields parallel and perpendicular to the c-axis. The signals were obtained using a spin echo method and the Knight shift was found to remain constant into the superconducting state (60 mK) at a resonance frequency

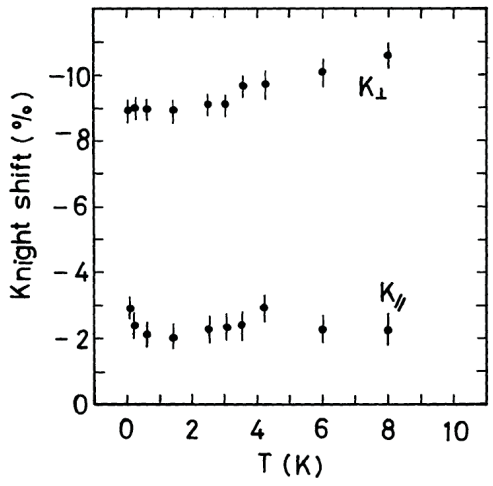

Figure 4.11: T dependence of the ^{195}Pt Knight shift in polycrystalline UPt_3 powder [61]. The Knight shift has not been corrected (see footnote on p. 159).

of 4.4 MHz (B_0 ∼0.51 T). However, it cannot be completely ruled out that this invariance in Knight shift is not associated with spin-orbit scattering as was the case for the measurements on small particles of Hg (Figure 4.1). Nevertheless, their measured Knight shifts in the normal state were $K_\perp = -8.4$ % and $K_\parallel = -1.4$ % [3] and the temperature dependence is shown in Figure 4.11.

4.6.3 The Körber experiment on single crystals

Most recently (2005), Körber measured the Knight shift of a single crystal UPt_3 wafer of ∼ elliptical shape ($5.2 \times 4.1 \times 0.46$ mm) from 600 mK down to 300 mK [2]. Measurements were performed on the same dilution fridge used in this thesis prior to the modifications described in Chapter 5. The two measurement fields used were 31.85 mT and 85.28 mT corresponding to ^{195}Pt resonance frequencies from UPt_3 of 280 kHz and 750 kHz respectively.

Unfortunately, the crystal orientation was not as quoted and in fact, measurements were made with the c-axis at 30° to the static field. A tipping pulse of 50 μs length with a current of 1.25 A_{pp} was applied every second, giving a tipping angle of 45.5°. Data acquisition commenced 95 μs after the middle of the pulse and was captured for 600 μs. 20,000 averages were taken for each resonance trace. The T_2^* relaxation times in the normal state were ∼100 μs in the 85.28 mT field. The background subtracted FID was Fourier transformed and the resonance frequency compared with that of a known ^{195}Pt marker to extract the Knight shift. Figure 4.12 shows the measured Knight shift for the two fields, as a function of temperature. No diamagnetic correction is included, justified by the lack of evidence for formation of an Abrikosov lattice as no significant line broadening was observed.

The NMR line could only be measured down to a temperature of 300 mK for the sample used due to a reduction in signal size with decreasing temperature below T_c. This was explained in the context of the filamentary model [117] which describes impure, inhomogeneous specimens that consist of superconducting inclusions in

[3] As a newer value of the gyromagnetic ratio for Pt was found ($\gamma/2\pi = 9.094$ MHz T^{-1} instead of 9.153 MHz T^{-1}), the Knight shifts quoted here have been revised accordingly following [116].

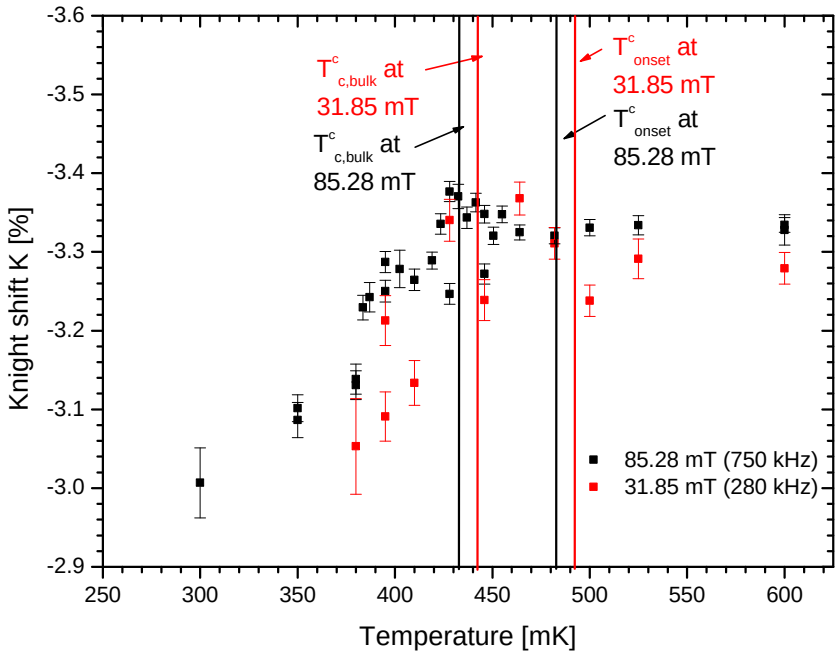

Figure 4.12: T dependence of the ^{195}Pt Knight shift for H at 30° to c. Red: 31.85 mT, black: 85.28 mT. From Körber [2].

the form of filaments and/or flakes that are randomly distributed in a background matrix. These filaments generally have a spread of transition temperatures due to the non-uniform stress within the sample. As the temperature is lowered, more and more filamentary areas become superconducting, so that the average conductivity of the sample increases in the region of the transition temperature. This results in a better shielding of the applied ac field during the NMR excitation pulse, so less spins are excited. This description of the sample was further supported by the low T_c (first onset of superconductivity) of 498 mK and the broadness of the transition of $\sim$ 30 mK as well as a decrease in the signal size with decreasing temperature below T_c, when extrapolated to the middle of the tipping pulse.

4.6.4 The Tou experiment on single crystals

To date, this is the only experiment that has been performed on single crystal UPt_3 into the superconducting state along all three crystallographic directions [106] (1998). It was a very comprehensive set of experiments that unfortunately do

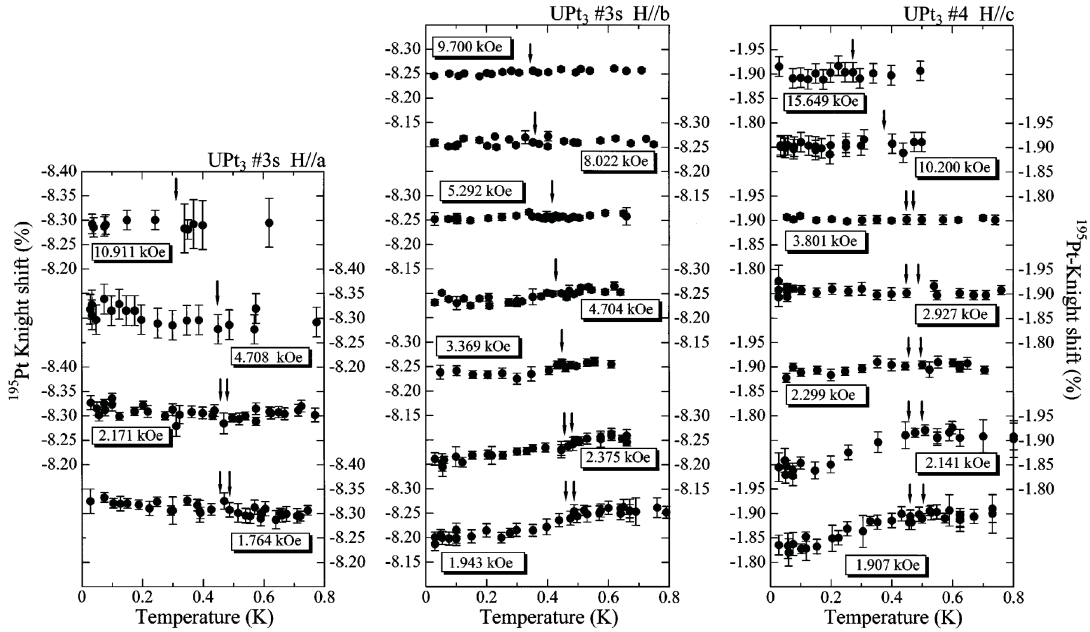

Figure 4.13: T dependence of the ^{195}Pt Knight shift at various magnetic fields for $H \parallel a, b, c$ from left to right. Arrows (↓) show T_c^+ and T_c^-. From Tou *et al.* [106].

not agree with all of the experimental evidence presented in Section 4.5. In their paper, measurements of the Knight shift are reported in static fields of 1.565 T down to 176 mT and down to 28 mK in temperature. The single crystals used have dimensions $2 \times 2 \times 5$ mm (#3) and $1 \times 1 \times 4$ mm (#4). The crystals have a residual resistivity ratio of $RRR \sim 510$ and a transport mean free path of $l_{tr} \geqslant$ 2000 Å and so the author rules out spin-orbit scattering due to impurities explicitly.

The temperature independent orbital contribution to the Knight shifts were estimated to be $K_{\parallel}^{orb} = 0.7\%$ and $K_{\perp}^{orb} = 1.95\%$ by fitting a Curie Weiss law to their Knight shift data above 30 K [62]. Their main Knight shift results are shown in Figure 4.13. The Knight shift was found to remain constant into the superconducting state for static fields above 500 mT regardless of field orientation. In static fields below 500 mT, $|K_a|$ *increases* slightly below T_c, which is attributed to a very small diamagnetic shift ($K^{dia} \sim -0.08$ %) such that K_a remains unchanged through T_c when this is taken into consideration. $|K_b|$ decreases slightly in fields below 500 mT and $|K_c|$ decreases slightly below 230 mT.

As mentioned in an earlier section, the above results can be explained by the

revised Spin triplet theory [107]. Tou infers from his measurements that the spin-orbit coupling is weak, so that at high fields (C phase), the Zeeman energy is greater than the spin-orbit coupling so that the **d**-vector is allowed to rotate such that $\mathbf{d} \perp H$. The spin vector aligns with the field, keeping K constant through T_c. Below ∼500 mT (B phase), the **d**-vector becomes pinned to the b-axis, so the Knight shift is reduced for fields parallel to b. For fields below ∼230 mT, the Cooper pair spin vector becomes spontaneously pinned to the a-axis, giving the observed result. Since the Cooper pair spins are rotated by relatively small fields, the authors argue that any scenario based on strong spin-orbit coupling fails to interpret the experiment. From these results, Tou concludes that UPt_3 is the realisation of a spin-triplet odd-parity superconductor with equal spin pairing and weak spin-orbit coupling, in support of the Spin triplet theory. However, it is not discussed why the Knight shift does not approach the orbital contribution K^{orb} at low temperatures, even though it is predicted by the author to be much smaller than that measured by Lee *et al.* [56].

Furthermore, this theory still assumes a controversial weak spin-orbit coupling which is inconsistent with the explanation of H_{c2} anisotropy. As we saw in Section 4.5.4, in order to explain the H_{c2} measurements along the c-axis, a Pauli limiting effect is required due to strong spin-orbit coupling locking the **d**-vector to the c-axis. In response to this, Machida argues that the anisotropic behaviour of H_{c2} is not evidence of the absence of the Pauli limiting of the upper critical field, but, together with the rotation of the **d**-vector at low fields, that it indicates a new phase above the C phase. However, this new superconducting phase has yet to be observed in experiments.

Moreover, in an earlier experiment on the same single crystals of UPt_3 [62], Tou *et al.* measured the Knight shift down to 28 mK for higher static fields from 440 mT to 1.56 T, applied along the c and a-axes. It was also found that the Knight shift was constant for $H \parallel c$ but again a slight increase in $|K_a|$ was measured for $H \parallel a$ deep into the superconducting state, attributed to the diamagnetic shift. However, the size of this diamagnetic shift is inconsistent with the later experiment [106], as it was measured to be greater for these larger static fields, when diamagnetic

effects should be smaller for lower fields (see Figure 4.4).

4.7 Motivation for low field measurements

In general, the pairing symmetry consists of the orbital part and the spin part in the pairing wave function. The former determines the gap topology. The latter characterises the spin structure of the Cooper pair, which is related to the spin susceptibility of the system and can be probed by the NMR Knight shift experiments. From the various experiments described in Section 4.5, it seems clear that the orbital part of the order parameter has been determined to be that of the E_{2u} representation, with strong spin-orbit coupling. However, the NMR Knight shift experiments of Tou *et al.* appear to be in conflict with this hypothesis. A good model must be consistent with all experimental data. Clearly in the case of the order parameter of UPt_3, this is not the case.

Further, it is not clear why the change in the Knight shift as the temperature is lowered through T_c is so small, since spin-orbit scattering has been ruled out and why K does not converge towards the residual orbital shift. A consistent treatment of the diamagnetic shift must also be made, especially if the measured changes in K are very small. The dependence of the diamagnetic shift on applied field can be determined by performing Knight shift measurements of UPt_3 into the superconducting state as a function of applied field.

Two UPt_3 single crystals have been obtained from Andrew Huxley that will enable a measurement of the Knight shift along all three crystal directions. By repeating the experiment of Tou *et al.*, I hope to try to resolve the above issues. NMR on metals is inherently difficult due to the skin effect prohibiting the excitation of spins deep into the metal. By exploiting the sensitivity of the two-stage SQUID sensor on a dilution refrigerator designed for such an experiment [2], NMR measurements at lower fields are possible, ensuring more spins are excited. By going to lower fields than Tou *et al.* (190 mT), we will also be measuring unexplored regions where the external field has an even smaller effect on the Cooper pairs and it would be very interesting to see how $K(T)$ develops.

Chapter 5

The cryostat and the UPt_3 dc SQUID NMR spectrometer

This chapter contains a description of the experimental setup used to perform low field NMR measurements on single crystal UPt_3 at milliKelvin temperatures. The cryostat and the dc SQUID NMR spectrometer used in this thesis was developed by Megan Digby and Rainer Körber and detailed accounts of its characterisation and developments made before the start of this work can be found in their theses [2, 26]. When the first NMR signals from UPt_3 were observed, it was apparent that modifications to the setup needed to be made in order for the Knight shift experiment to succeed. Namely, a new field marker using ^{3}He was implemented and together with an inner overlapping Nb shield, facilitated the measurements presented in Chapter 6. These modifications are also described in this chapter.

5.1 The cryostat and SQUID installation

To perform measurements as a function of temperature on the UPt_3 sample through its transition temperature of ~ 550 mK, a ^{3}He - ^{4}He dilution refrigerator was used. The minifridge, (so called because of its small size) has a base temperature below 20 mK. Together with a PID controller (see Section 5.1.4), stable sample temperatures could be maintained between 1 K and base temperature for several months.

5.1.1 The ^{3}He $-^4$ He dilution refrigerator

The dilution fridge is a very popular cooling technique in the millikelvin range as the cooling process is continuous and the cooling power is considerable at low temperatures. Detailed reviews of dilution fridges can be found in many texts - most notably Pobell [118] and for a more practical approach, Richardson and Smith [119]. Here, only a brief overview is given.

Figure 5.1 is a schematic diagram of the minifridge below the 4 K plate at the top of the IVC (Inner Vacuum Can). The main components of a dilution fridge are the 1 K pot, the still, the heat exchangers and the mixing chamber, which are all thermally isolated from the 4 K bath. A ^{3}He - ^{4}He mixture (commonly called *mash*) is circulated within the fridge and a room temperature gas handling system by the use of backing and roots pumps. The diagram shows the fridge during normal operation. When cooled below a critical temperature of 0.87 K, the helium mixture undergoes phase separation into a concentrated phase rich in ^{3}He floating on top of a dilute phase of 6.5 % ^{3}He in an inert ^{4}He superfluid background. With the correct mixture (concentration and volume), this phase separation line lies in the mixing chamber. The cooling occurs due to the difference in enthalpy of the two phases; when atoms of ^{3}He are pulled down across the interface from the concentrated to the dilute phase, it takes energy (analogous to evaporative cooling). The theoretical cooling power is given by:

$$\dot{Q} = 84\dot{n}T^2, \tag{5.1}$$

where $\dot{n}$ is the ^{3}He flow rate in moles s^{-1} and T is the temperature of the mixing chamber. For the minifridge, a typical circulation rate is $\dot{n} = 50$ μmol s^{-1}. With the mixing chamber at 20(600) mK, the theoretical cooling power is $\dot{Q} =$ 1.7 μW(1.5 mW). The dilute phase in the mixing chamber is connected to the still, where the liquid/gas interface of the mixture should be. At the optimal still temperature of 700 mK, the vapour pressure of ^{3}He is two orders of magnitude larger than that of ^{4}He. By pumping on the still with a pump at room temperature, ^{3}He is preferentially removed from the liquid surface, lowering the concentration

of ^{3}He in the still. This creates a chemical potential gradient between the still and mixing chamber and it is this that is responsible for pulling the ^{3}He across the phase boundary in the mixing chamber. In order for this cooling to occur continuously, all the ^{3}He that is pumped away from the still is recondensed into the fridge through the condenser, which is cooled to around 1.4 K by the pot. The main impedance just below the pot creates a high enough pressure to ensure that all the ^{3}He is liquid before reaching the cooler stages of the fridge. Below this impedance, the condenser line is thermally anchored to the still and there is a secondary flow impedance to maintain the pressure to keep the ^{3}He liquid. Continuous heat exchangers thermally connect this line to the cold, dilute ^{3}He mixture leaving the mixing chamber, cooling the ^{3}He further before it reaches and replenishes the ^{3}He-rich phase in the mixing chamber.

The flow of the mixture is controlled via a room temperature gas handling system (GHS) operated via a sequence of Swagelock valves. Here, the mixture is cleaned through a nitrogen trap followed by a helium trap, which freeze out any impurities before the mixture enters the cryostat via the condenser. The flow rate is monitored with a flow meter and the pressure at various stages of the fridge by several pressure gauges. The GHS also incorporates several safety pressure valves, which open when the differential pressure is above 800 mbar, releasing the mixture into the dumps.

5.1.2 Overview of the cryostat

The minifridge is based upon a customised Oxford Instruments Model 15 Dilution Unit [120], which is lowered into a superinsulated Cryogenic Dewar [121] with a winch and screwed down with several Allen bolts and a greased O-ring seal. At the top of the fridge, a 9 mm thick brass plate forms the base for all electrical connections and circulation ports into and out of the fridge.

For fridge operation, the pot and still pumping ports as well as the condenser return line enter the cryostat through the brass plate. These ports are connected to the GHS with flexible pumping lines that electrically insulate the cryostat from the GHS. The helium trap is positioned just before the condenser return line,

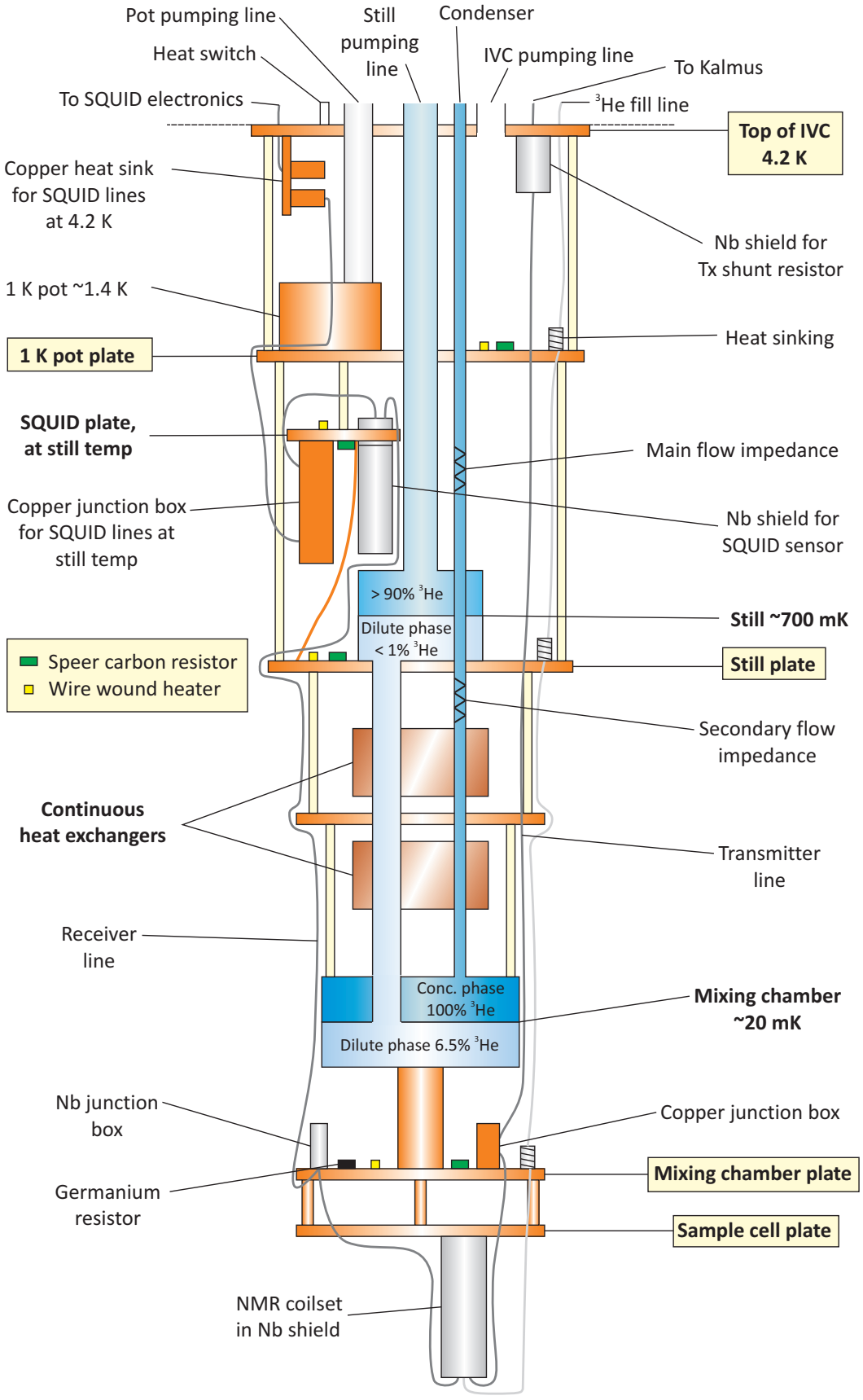

Figure 5.1: Schematic diagram of cryostat below the top of the IVC.

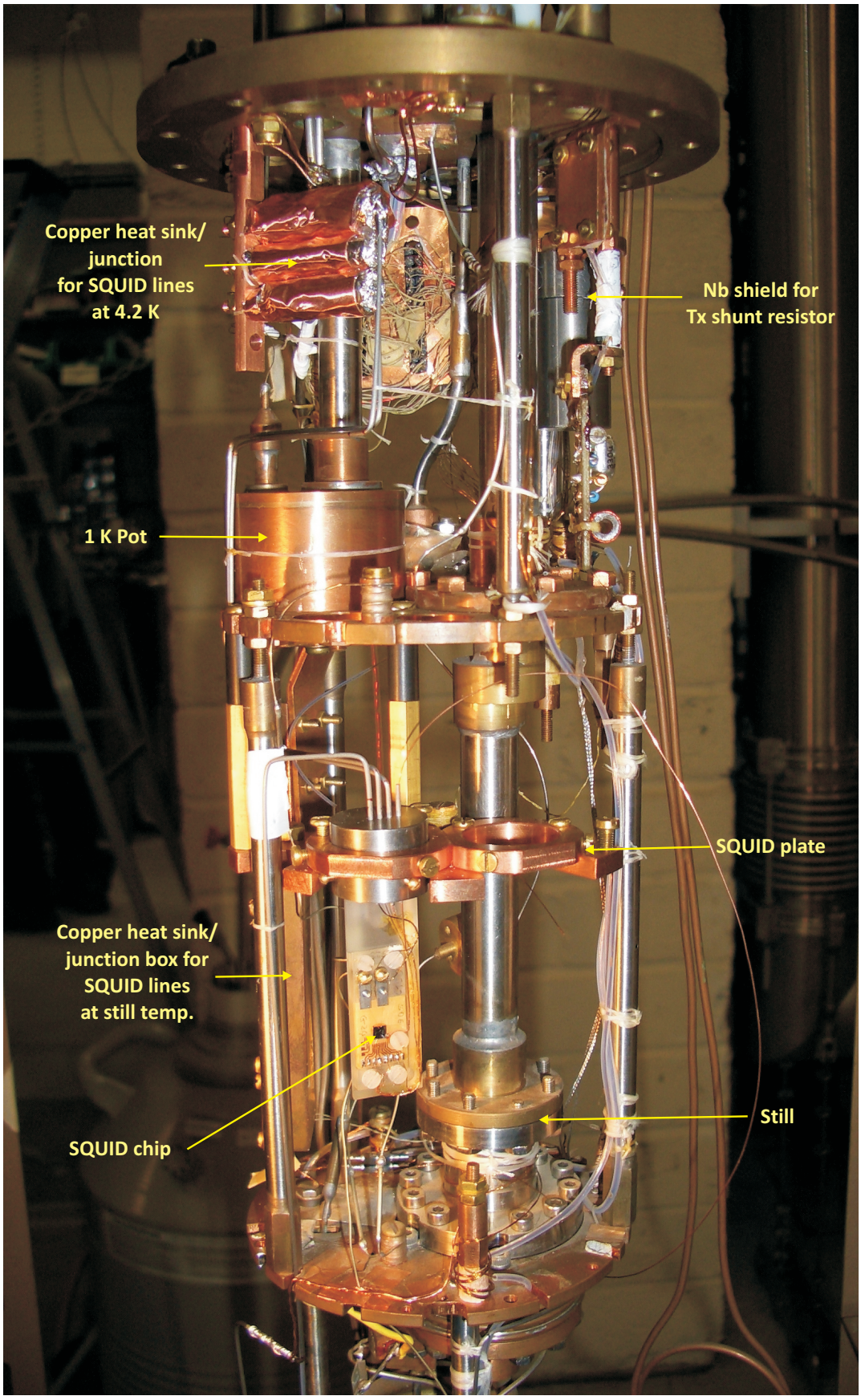

Figure 5.2: Photograph of the minifridge below the IVC top plate down to the still plate.

ensuring that impurities due to possible leaks in the GHS are frozen out before entering the fridge. There is also a pumping port with a speedy valve for pumping out the IVC. A HiP valve [122] to a fill line that extends down to the sample plate for a disused ^{3}He melting curve thermometer was also present, which was utilised in a modification to install a ^{3}He marker (described in Section 5.6).

The electrical connections on the brass plate used in this experiment include an aluminium box with a 24-pin Lemo connector for mounting the Magnicon SQUID electronics [10]. For the NMR, there is a 3-pin Fischer connector to the transmitter coil circuit and a 10-pin Veralco type connector for the magnet's current, persistent heat switch and voltage tap leads. For monitoring and adjusting the fridge temperature, a 24-pin Fischer connector leads to the resistance thermometers and heaters for the pot, still, SQUID plate and mixing chamber. Finally, two BNC sockets at the centre of a 6-port aluminium connector box lead to a resistor mounted onto the outside of the IVC for heating.

The IVC is made of brass and is vacuum sealed using an indium wire seal. Figure 5.2 is a photograph of the minifridge below the IVC 4.2 K plate down to the still. As the IVC is always submerged in the helium bath, it remains at 4.2 K. The persistent heat switch for the magnet is located on top of the IVC, in the helium bath. Within the IVC, heat sunk at 4.2 K, a Nb box encloses a 330 Ω shunt resistor for the transmitter coil.

A polished copper radiation shield is attached onto the still plate and encloses everything below. This shield protects the colder parts of the fridge from thermal radiation from the 4.2 K surface of the IVC by making it light-tight. Awkward holes in the still plate were covered with copper tape. Within this shield are the continuous heat exchangers and the coolest part of the fridge - the mixing chamber. The copper mixing chamber plate is mounted onto the bottom of the mixing chamber with a copper post, on which are the copper and niobium junction boxes for the transmitter and receiver lines respectively. Finally, the copper sample plate is mounted and thermally connected to the bottom of the mixing chamber plate with four copper posts. The NMR coil set containing the UPt_3 sample are attached to the bottom of the sample plate. These will be described in Section 5.2.

5.1.3 Installation of the two-stage SQUID

As there was no SQUID sensor mounted on the minifridge at the start of this work, all of the wiring for the SQUID from the brass top plate of the cryostat to the two-stage SQUID had to be assembled. This section details the connections that were made from the top of the cryostat to the SQUID. Although lines for two SQUIDs were mounted down to 4.2 K, only one SQUID sensor was used in this work.

The two-stage dc SQUID sensor C506-G24

The two-stage SQUID sensor mounted for this experiment is the C506-G24 model. Table 5.1 is a summary of the main parameters. This generation of sensor has several new features compared to the C4 generation SQUID used in the room temperature spectrometer (Section 3.4.7). Firstly, the chip is now directly coolable, meaning the SQUID chip is thermally connected to a ∼3.5 mm diameter gold washer, patterned onto the SQUID carrier. This enabled the SQUID to be heat sunk to the still as opposed to the 4 K plate for the previous experiment [2], which should lead to a reduction in the intrinsic SQUID noise as we saw in Section 2.2.2. To heatsink the SQUID, the end of a length of 315 μm diameter bare copper wire was fashioned into a hook shape and flattened, before being screwed down onto the heat sinking washer with an M2 teflon screw. The other end was screwed tightly

Parameter	Symbol	Two-Stage C506-G24
Input coil inductance	L_i	1.8 μH
Mutual inductance SQUID-Input coil	M_i	9 nH
Mutual inductance of feedback coil and 1st stage	$1/M_f$	41.6 μA/Φ_0
Mutual inductance of 1st stage and 2nd stage	$1/M_{fx}$	44.9 μA/Φ_0
White flux noise @ 100 kHz	Φ_N	0.37 μ$\Phi_0/\sqrt{\text{Hz}}$
Coupled energy sensitivity	ε_c	10 h
Number of wire connections		9

Table 5.1: SQUID parameters for the two-stage SQUID sensor C506-G24, operated at still temperature (∼700 mK). The noise given is measured with UPt_3 in the superconducting state (fridge at base temperature).

onto the copper SQUID plate (see Figure 5.1), which was heat sunk to the still.

Figure 5.3 is a photograph showing the SQUID sensor mounted onto the cryostat with the heatsink, bias wires and flux transformer connected. The C5 SQUID also has an integrated on-chip Q-spoiler with a critical current of between 6 and 20 μA depending on the modulation current and a normal resistance of 860 Ω. These two additional leads makes this SQUID a 9-wire sensor. Also visible in Figure 5.3 are the Nb blocks to replace the PbInAu foils for the superconducting connection to the input coil. These are now more robust and the circular washers never touch each other, making it easier to connect up the screw terminals for the flux transformer.

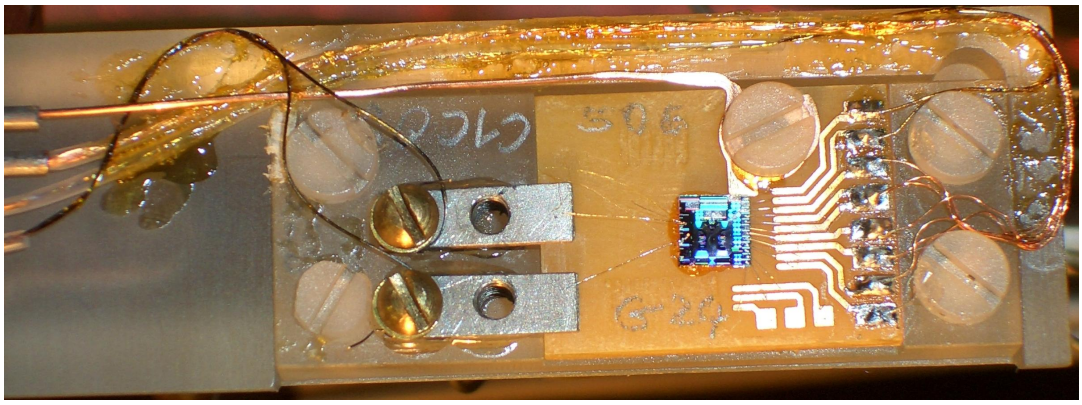

Figure 5.3: Photograph of the two stage SQUID sensor C506-G24 with the bias wires and flux transformer connected. The copper heatsink wire is also visible under the central teflon screw.

Mounting the SQUID onto the minifridge

To reduce the heat leak from room temperature into the fridge, any lines must be heat sunk at several places down to the destination temperature. For the SQUID lines, there were two main copper junctions that served as heat sinks. Shown in Figures 5.1 and 5.2, these were at 4.2 K just below the top of the IVC (copper posts) and on the SQUID plate (copper box at $\sim$ 700 mK). As a second SQUID may be mounted onto the dilution fridge in a future experiment, the SQUID plate was designed by Ben Yager to hold two Nb SQUID shields. The SQUID plate was heat sunk to the still plate below using a bare copper wire bundle made from a

length of twisted 0.71 mm ⌀ wire.

Thus, a twisted-seven and Q-spoiler modulation lines were installed for *two* SQUIDs from the room temperature SQUID connector box to the 4.2 K heat sink. The twisted-sevens separately and the Q-spoiler modulation lines together were each fed through a teflon tube for protection and a stainless steel tube (1.6 mm outer ⌀) for shielding, through a stainless steel port down to the 4.2 K heat sink. This bundle of three tubes were heat sunk with brass bristles at two places before 4.2 K to further decrease heat transmission from room temperature. Previously, the transmitter and SQUID lines ran through the same stainless steel tube, which was not ideal as stray fields from the transmitter pulses could inductively couple into the SQUID receiver lines. At the 4.2 K heat sink, the SQUID lines were soldered onto 280 μm thick PCB board solder pads and wrapped around the copper several times.

From the 4.2 K heat sink onwards, only lines for one SQUID were continued. These SQUID lines were encased in teflon and shielded through 1 mm ⌀ Nb tubing, which was bent to the required shape using a jig made by John Taylor. Table 5.2 gives details of the wires used for each stage.

Section	**SQUID 7-wire bias**	**Q-spoiler modulation**
300 K to 4.2 K	44 SWG Copper	80 μm ⌀ Constantan
4.2 K to SQUID plate	106 μm ⌀ CuNi clad NbTi	106 μm ⌀ CuNi clad NbTi
SQUID plate to SQUID	44 SWG Copper	106 μm ⌀ CuNi clad NbTi

Table 5.2: Wiring for the two-stage SQUID from room temperature to the SQUID.

Superconducting wire was used in the section between 4.2 K and the SQUID plate as it is a poor thermal conductor at these temperatures.

5.1.4 Thermometry and temperature control

All five thermometers used for monitoring the fridge are temperature dependent resistors. As shown in Figure 5.1, Speer carbon resistors are mounted on the pot plate, SQUID plate, still plate and mixing chamber plate. The mixing chamber

Speer has been calibrated by Simon Kingsley against a ^{3}He melting curve thermometer on a different cryostat and is valid in the range 25 mK to 500 mK. For higher accuracy at the mixing chamber at the temperatures of interest, a commercial germanium resistor (Lakeshore, model GR-200A-250CD) is also used. This is used within the calibration range of 365 mK to 6 K using the provided calibration equations and is the primary thermometer used for temperature control of the sample.

These resistances are measured using a resistance bridge (Picowatt, model AVS-47A [123]). Before this work, the fridge thermometers were only read individually and manually. A LabVIEW program was written to control the resistance bridge remotely. This program is able to monitor, set, plot and log the various temperatures on the fridge. When the sample temperature was not being stabilised, it is possible to plot the temperature of each stage of the fridge as fast as every minute for diagnostic/monitoring purposes. This program was originally written to aid with the filling of the ^{3}He cell as described in Section 5.6.3.

Wire wound resistive heaters are also present on the pot plate, SQUID plate, still plate and mixing chamber plate, for heating various stages of the fridge to optimal temperatures. The heater on the mixing chamber plate was used together with a PID (Proportional Integral Derivative) controller to stabilise the sample temperature to within $\sim \pm 0.05$ mK. The PID is a homebuilt controller built by Alan Betts. In essence, it calculates the difference between the target resistance of a thermometer and the actual resistance over time and outputs an according current to the heater to correct for this difference.

5.2 The UPt_3 dc SQUID NMR Spectrometer

The dc SQUID NMR spectrometer used in this experiment is very much like that described for the room temperature experiment (Section 3.4) except the conventional rf tipping technique is used instead of the prepolarising technique. The spectrometer in this low temperature experiment also uses a superconducting flux transformer as an input circuit and is a broadband technique. This results in

fast recovery times at low frequencies, which is impossible with tuned detection circuits. This advantage is essential for NMR on metals as relaxation times are typically very short, in the order of µs.

Figure 5.4 is a schematic of the SQUID spectrometer used in this experiment. Here, the rf tipping pulse is provided by a waveform generator (Agilent 33120A signal generator [124]) and amplified by a commercial amplifier (Kalmus 275LC-CE [125]). After the amplifier, a 5000 pF pi-filter and crossed diodes filter out any high frequency interference and leakage noise from being sent to the transmitter when the pulse is off. As for the room temperature spectrometer, a PIC pulse generator controls the pulse sequence. The NMR voltage signal from the SQUID is first sent through a high pass filter with cut-off frequency of 14 kHz to remove the large low frequency transients, enabling data to be captured with the lowest input range of a 12-bit PXI card (Pickering PXI 41-310 [126]).

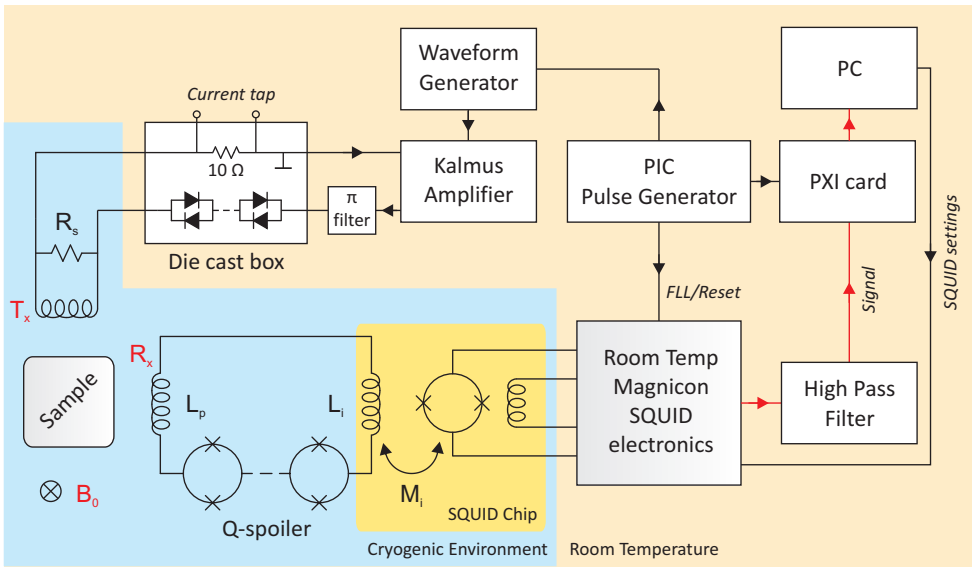

Figure 5.4: Schematic diagram of the UPt_3 SQUID spectrometer.

The NMR coilset and cell described in this section were developed by Rainer Körber and are documented in his thesis [2]. A lot of work was done on reducing the coherent background signal, termed magneto acoustics, arising mainly from the receiver coil vibrating in a magnetic field. This coherent background was reproducible and its magnitude found to be proportional to the square of the

static field B_0 and to the current in the transmitter coil which generates the rf field. However, the amplitude of this background was problematic as it was many times the UPt_3 signal size in the frequency domain. His design involves an NMR cell in which the transmitter and receiver coils are mechanically decoupled, reducing the coherent background resonances due to the transmitter pulse by a factor of about 10. This enabled the coherent background to be subtracted away with greater accuracy, reducing the noise level. This background subtraction method is slightly different to that used in the room temperature experiment and will be shown in Section 5.4.2.

5.2.1 The magnet

The magnet that provides the static field is a superconducting solenoid wound from 106 μm ⌀ CuNi clad NbTi wire on a copper former 23 mm in diameter. The solenoid is 80 mm long and has 14 layers with approximately 740 turns in each layer. There is a short to the magnet former which necessitates the use of a floating magnet power supply. A cylindrical shield made of niobium (0.5 mm thickness) encases the magnet to shield against ambient magnetic field fluctuations and improve field homogeneity. The measured field-current ratio is 85.17 mT/A. The measured homogeneity is ∼460 ppm. The maximum attainable field is about 250 mT [2]. The magnet is operated with a persistent heat switch system as described earlier in Section 3.4.1.

5.2.2 The transmitter

The transmitter coil is wound on a Kel-F former in a saddle coil geometry. The total length of the former is 70 mm with an outer diameter of 16 mm. The coil itself has height 27 mm and diameter 14 mm with 15 turns on each side, wound from 50 μm outer ⌀ CuNi clad NbTi wire. The coil dimensions follow the ratios given in Section 3.4.2 for optimum field homogeneity. The current through the transmitter circuit during a tipping pulse, I_{in}, is determined by measuring the voltage across a 10 Ω monitor resistor at room temperature in series with the

transmitter circuit (refer to Figure 5.4). The lead solder tubing that shielded the transmitter leads against electrical and magnetic noise was replaced with a more robust 1 mm ⌀ Nb tubing. This reached from within the Nb shield at 4.2 K (enclosing the shunt resistor) to the copper junction box on the mixing chamber plate, labelled in Figure 5.1.

The frequency response of the transmitter circuit

Unlike the room temperature experiment where dc currents were sent through the transmitter coil, the UPt_3 experiment applies rf currents for excitation to minimise sample heating. The current through the transmitter coil I_{trans} has the following dependence on frequency when the coil is shunted by a resistor R_s:

$$\frac{I_{\text{trans}}}{I_{\text{in}}} = \frac{1}{\left(1 + \frac{\omega^2 L^2}{{R_s}^2}\right)^{\frac{1}{2}}}. \tag{5.2}$$

The calculated inductance is $L = 36.5$ μH [30] and the shunt resistor is 330 Ω. This shunts noise above a cut-off frequency of $f_c = R_s/(2\pi L) = 1.44$ MHz through the shunt resistor, imposing a maximum frequency limit for rf excitation. This shunt resistance was chosen to sufficiently filter out high frequency noise such that the SQUID does not lose lock.

5.2.3 The receiver

The receiver coil is also wound on a Kel-F former with saddle coil geometry. The outer diameter of the former is 9 mm, resulting in a 1.5 mm gap between the transmitter and receiver coils, providing the mechanical decoupling. The coil has height 7 mm and diameter 7 mm with 7 turns on each side, wound from 50 μm ⌀ bare NbTi wire. The calculated inductance is 2.07 μH, closely matching the input inductance of the two-stage SQUID of 1.8 μH, for maximum flux transfer efficiency (see Section 2.2.3). The receiver coil is mounted onto a copper isolation mass with Stycast 2165 MM, which was further supported by four copper posts to increase rigidity. Figure 5.5 is a schematic of the supported vibration isolation design [2].

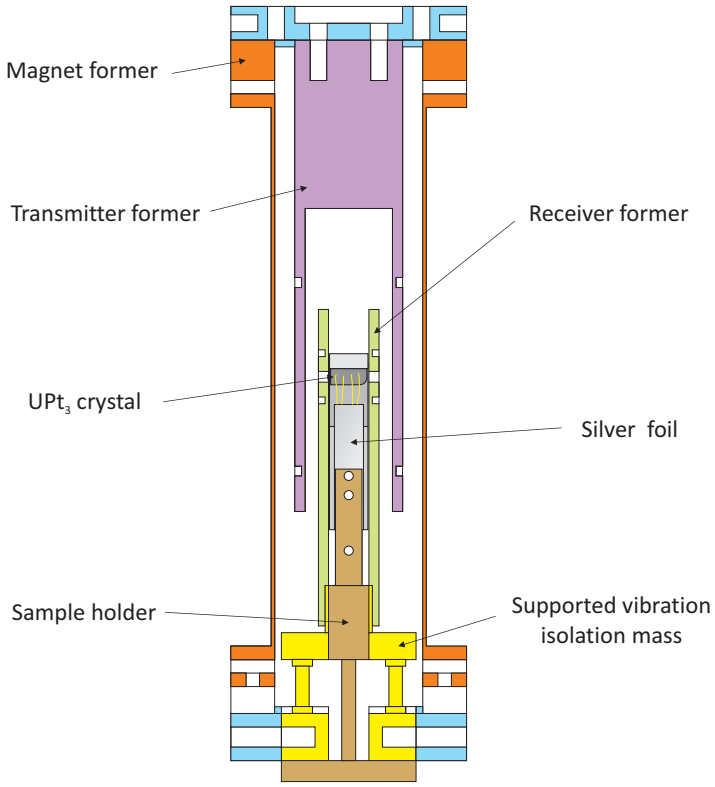

Figure 5.5: Schematic diagram of the NMR coilset for the minifridge and sample holder for UPt_3.

The sample holder is screwed in place inside the receiver coil by two M2 screws. The receiver coil and sample holder assembly is then bolted to the bottom of the NMR magnet. The lead solder tubing for the receiver leads running from the SQUID shield to the Nb junction box on the mixing chamber plate was replaced with 1 mm ⌀ Nb tubing. The twisted pair was also remade from bare NbTi wire (0.004" bare ⌀, 0.005" Formvar ⌀).

5.2.4 Mounting the sample

The UPt_3 crystal chosen to be measured first was Sample 1. Initially this was chosen as it has the largest surface area, which was thought to help provide a larger signal size as the rf pulse only penetrates the surface over a characteristic length given by the skin depth. However, in Section 6.4.1, we compare the expected signal size of UPt_3 in the normal state with the actual signal size and obtain a

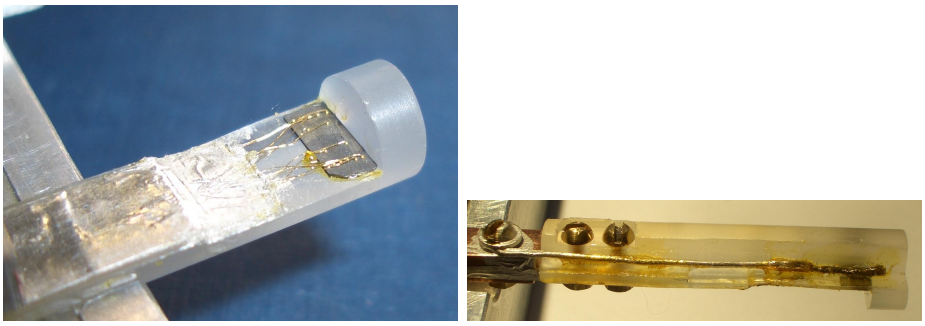

(a) UPt_3 Sample 1 (b) Platinum marker

Figure 5.6: Sample holder shown mounted with (a) UPt_3 sample and (b) platinum marker.

good estimate if we only consider an effective volume which does not take into account the surfaces perpendicular to the receiver coil. This means that it is not the total surface of the crystal that gives an indication of signal size; however, this was a recent analysis which we will return to in Section 6.4.3.

The other practical reason why Sample 1 was chosen was that the gold heat sinking wires bonded to this sample were considerably longer than for Sample 2 ($\sim$ 7 mm *c.f.* 3 mm), so the heat sink can be away from the sample, out of the receiver coil. It was decided to measure the c-axis first (i.e. with the c-axis parallel to the static NMR field). The reasoning will be given in Section 6.2. The sample holder used was machined from a cylindrical length of Kel-F and screwed onto a copper stand. The sample was mounted with the correct orientation by aligning the straight edge of the crystal against a step machined into the holder and varnished with GE varnish (see Figure 5.6(a)). With this orientation, the static magnetic field B_0 is parallel to the plane of the wafer, minimising demagnetisation effects.

Heat sinking

The heat sinking of the sample was made through the 14 gold wires of 50 μm ⌀, bonded to the sample. These wires were sandwiched between two sheets of 99.99% pure 25 μm silver foil (RRR = 490) with silver epoxy. The epoxy was left to cure at room temperature for 24 hours in a custom made clamp that applied a small pressure on the gold wires to ensure a good contact. The result can be seen

in Figure 5.7 which was taken through a microscope. The gold wires were long enough so a $\sim$ 2.5 mm gap could be left between the crystal and the silver foil so the silver would not be in the receiver coil. The silver foils were sandwiched between two copper slabs and screwed in place, so there was good thermal contact with the copper base of the sample holder. In this way, the UPt_3 crystals were heat sunk to the sample plate and the mixing chamber of the dilution fridge.

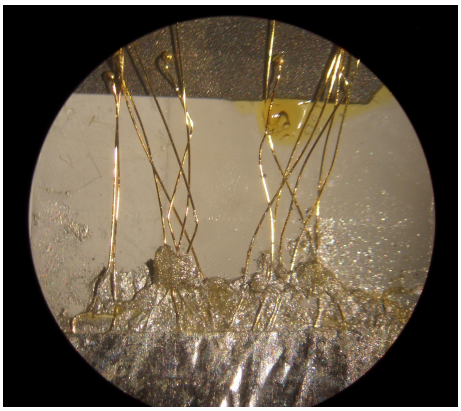

Figure 5.7: Photograph taken through a microscope, showing the heat sinking of the UPt_3 sample. The impression made by the gold wires in the silver foil is visible, indicating a good contact.

The adequacy of the heat sinking through the gold wires can be judged by calculating the electrical resistance R_{el} between the sample and the silver foil heat sink, as this is where the thermal link is weakest. In the previous experiment using this setup [2], the UPt_3 wafer samples were heat sunk to the silver foil using silver epoxy with a calculated resistance of $R_{el} = 38\ \mu\Omega$, which proved adequate for the pulses applied. For the gold wires the resistivity is assumed to be $\rho_{el} = 1.63 \times 10^{-10}\ \Omega$m at 4.2 K as measured by Körber. The length of the wires from the sample to the Ag foil are at most 5 mm each, giving a resistivity of $R_{el} = \rho_{el}(l/A) = 30\ \mu\Omega$ for all 14 wires. As this is comparable to the resistance for the previous experiment, we can conclude that the UPt_3 crystal is heat sunk satisfactorily.

Platinum marker

In order to determine the Knight shift (Equation 4.2), it is necessary to know precisely the value of the local magnetic field B. A platinum marker was used as it has a known Knight shift and gyromagnetic ratio, enabling the magnetic field to be determined from the resonance frequency of its NMR signal. A bundle of platinum wire previously designed and constructed [2] was mounted onto the rear side of the Kel-F sample holder (see Figure 5.6(b).) This bundle is made of 100 ^{195}Pt wires, 25 µm ⌀ and 5 mm long, welded to a 0.5 mm ⌀ annealed silver wire to achieve good thermal contact. The silver wire was screwed tightly onto the copper sample base and the contact coated with silver paint, heat sinking the platinum bundle to the mixing chamber. The bundle was further secured with GE varnish onto the Kel-F holder to minimise vibrations.

Once mounted, the positions of the UPt_3 crystal and the platinum marker are such that they are as centrally positioned as possible within the receiver coil without physically touching each other, enabling the most precise field measurement. The number of excited spins in the platinum sample is 6×10^{19} [2], originally designed to give the same signal height as the UPt_3 signal in a previous experiment.

5.3 SQUID setup and characterisation

Before the two-stage SQUID was mounted onto the minifridge, it was tested on a simple dipper probe at 4.2 K without the NMR coils connected. Measurements of the V-Φ characteristic and noise in FLL were taken as described in Section 3.4.10 to ensure that the SQUID was operational. After mounting onto the minifridge, similar tests were repeated. In this section, the method for optimising the bias position of a two-stage SQUID and the subsequent noise spectrum is shown.

5.3.1 Optimising the bias position for a two-stage SQUID

The two-stage SQUID C506-G24 was not supplied with the optimal bias settings. Moreover, the optimal bias position was quite sensitive to changing experimental

conditions and so the SQUID had to be retuned on occasion. It may be that the SQUID bias position is sensitive to temperature and so operating the SQUID at 4.2 K or at pot temperature ($\sim$ 1.4 K) may provide a more stable operating temperature and bias position compared to the still. Although we gain an improvement in noise due to the lower operating temperature as Johnson noise is proportional to $\sqrt{T}$, the still temperature was found to be slightly dependent on the sample temperature and so was not constant for the duration of a run.

Nevertheless, the bias position was optimised as follows (refer to Figure 2.10 and Section 2.2.4 for guidance). First, the amplifier SQUID is tuned. With zero field in the magnet, the SQUID Viewer program is used to set all the bias positions (I, Φ_x, I_b, V_b and Φ_b) to zero. The generator palette is used to produce a 22 Hz triangular waveform with a peak to peak current of 50 μA through the Φ_x coil, coupling flux into to the amp SQUID in order to view its response. The SQUID output and generator are viewed on an XY plot on an oscilloscope. The I_b is increased until a V-Φ characteristic is visible and then V_b is increased until the characteristic crosses the horizontal axis. The amplifier SQUID is optimised for highest gain so I_b and V_b are fine-tuned until the slope of the characteristic is made as steep as possible.

Now the sensor SQUID is tuned. To do this the amplifier SQUID is put into FLL mode, so that the first stage SQUID characteristics can be seen. The bias current I is increased until parasitic resonances disappear, signified by the observation of a smooth V-Φ characteristic. Then Φ_x is tuned to give a smooth V-Φ with a large swing. As the noise is dominated by the sensor SQUID, it was optimised to give lowest noise. To do this, various bias positions (I and corresponding values of Φ_x) were found for further increasing bias currents I, through the sensor SQUID. The SQUID noise in FLL was measured at 90 kHz (arbitrary) using a spectrum analyser (Stanford SR760 [35]) at each bias position. The (I, Φ_x) pair that gave the lowest noise was chosen as the optimal bias position, along with the I_b and V_b determined for the amplifier SQUID.

5.3.2 SQUID properties

The V-Φ characteristic at the optimised bias position is much like that shown in Figure 3.23 and so is not shown here. A feedback resistor of 7 kΩ and GBP of 0.47 GHz was used throughout the experiments in the rest of this thesis. Although the bias position was adjusted periodically, the SQUID gain in FLL remained constant at $G_{\mathrm{FLL}} = 300$ mV/Φ_0. The 3dB bandwidth was measured using a commercial high frequency spectrum analyser (HP 3588A [124]) with a 2 mV_{rms} excitation to be 5.5 MHz. The transmitter-receiver cross coupling was measured to be 22 μA/Φ_0 using the method described in Section 3.4.10.

5.4 Data acquisition and analysis methods

Initial attempts to measure an NMR signal from UPt_3 in the normal state proved very difficult. Following the same signal acquisition procedure as Körber in his experiment to measure a single crystal UPt_3 wafer [2], the UPt_3 signal was searched for at a resonance frequency of 750 kHz assuming a Knight shift of -1.9 % in the normal state for this field orientation [106]. From rearranging Equation 4.2 this corresponds to a static field of $B_0 = 84$ mT in the magnet. However, initially only the NMR signal from the Pt marker could be seen above the noise. This section describes the techniques necessary in order to observe the first UPt_3 signals in the normal state, at a temperature of 600 mK.

5.4.1 Signal excitation and detection

The technique of rf tipping is used to excite the spins in this experiment, as described in Section 2.1.6. The plan of action begins with estimating the expected Knight shift of UPt_3. Then an excitation frequency is chosen (based on a region of low magneto acoustics as measured previously [2]). Using Equation 4.2, the static field required in order for UPt_3 to resonate at this frequency is calculated and the corresponding current is persisted in the NMR magnet.

The pulse sequence is much simpler than that of the room temperature ex-

periment and only the master port of the PIC is required to generate a repeated sequence of two pulses. The reader is asked to refer to the spectrometer schematic on p. 174 to aid with the following description. An initial 10 μs long pulse from the PIC is used to trigger a waveform generator to send a 50 μs long cw pulse with the UPt_3 resonance frequency through the transmitter coil in order to tip the magnetisation away from equilibrium. For a fixed length pulse, the tipping angle of the magnetisation is determined by the amplitude of the transmitter pulse (as given by Equation 2.16) and is controlled by the Kalmus amplifier. The peak to peak current through the transmitter circuit is determined by measuring the voltage across a 10 Ω monitor resistor in series with the circuit using a digital oscilloscope. This initial PIC pulse also arms an oscilloscope program on a 12 bit PXI card (which was later upgraded to a 14 bit PXI card in Section 6.2.4).

After the end of the tipping pulse, a second pulse from the PIC triggers the SQUID into FLL. The scope program is programmed to start taking data 5 μs after the SQUID is put into FLL for the duration of the capture time, T_{cap}. The repetition time of the pulse sequence is set to 1 s. This was found to be long enough for the equilibrium magnetisation to return after each excitation as both T_1 and T_2 of UPt_3 were in the order of μs (as we saw in Sections 4.5.3 and 4.6) and also slow enough so that the sample temperature remains constant. Platinum also has a short T_1 of 1 ms [118] and the T_2^* was measured to be ~ 300 μs.

The number of averages is set on the PXI scope program, which carries out the signal averaging and saves the time trace.

5.4.2 Background subtraction method

If the resonance trace is taken as described in the previous section is Fourier transformed, the signal in the frequency domain is dominated by a large amplitude magneto acoustic response due to the tipping pulse around the resonance frequency. The magnitude of this coherent background is proportional to the square of the static field B_0 and to the current in the transmitter coil which generates the rf field. The predominant cause was found to be due to the receiver coil vibrating in a magnetic field [2]. As the UPt_3 NMR line is completely masked by this response

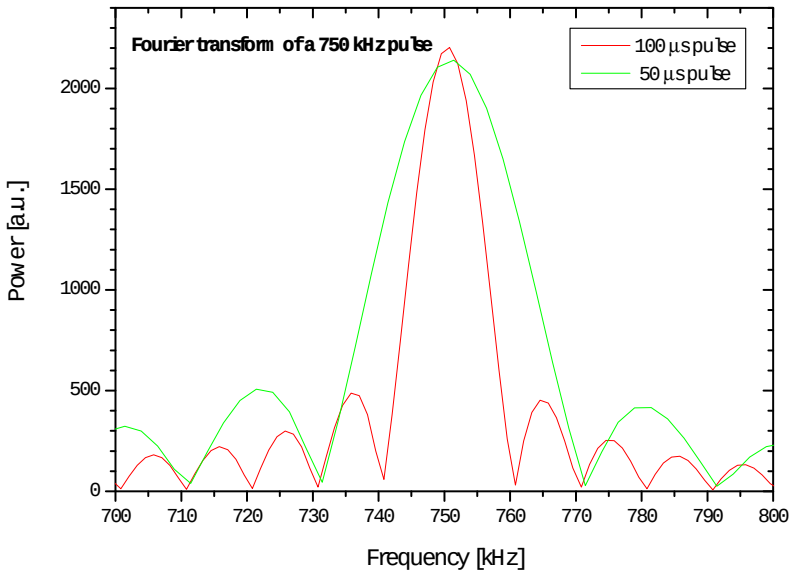

Figure 5.8: Fourier transform of two 750 kHz sine pulses of different lengths as measured from the Agilent 33120A signal generator [124]. At the minima, the pulse has no spectral density, so spins will not be excited at these frequencies.

in the frequency domain, it is necessary to perform background subtraction in order to see the signal.

In pulsed NMR, the Fourier transform of a transmitter pulse of frequency f_0 and length τ is a sinc function centred on f_0 with equally spaced minima above and below f_0 with spacing $\Delta f = \tau^{-1}$. This power spectrum indicates the frequencies that will be excited by the pulse, and is shown in Figure 5.8 for a 750 kHz pulse. This is used to aid the background subtraction of magneto acoustics in the following way. Firstly a resonance trace is taken using the method described in the previous section. For the background trace, the excitation pulse is kept constant but the field is moved so the resonance frequency now coincides with a minimum of the transmitter pulse power spectrum. The resulting spectrum will then have nearly identical magneto acoustic resonances but no NMR signal. Thus, this signal can be subtracted away from the resonance signal in the time domain after being multiplied by a scaling factor of $(B_{res}/B_{bg})^2$ to leave just the NMR line. In this way, the magneto acoustic resonances can be subtracted away to about 2 %. The efficiency of this background subtraction method will be shown in the following chapter (Figures 6.4 and 6.8).

It was found that the background subtraction procedure was more reliable if two backgrounds were taken above and below the resonance frequency, at the first minima of the power spectrum. However, with the platinum marker always resonating ~ 12 kHz lower than UPt_3 at 84 mT, backgrounds were taken at $f_0 - \Delta f$ and $f_0 + 2\Delta f$ to leave a cleaner noise floor around the resonance frequency.

5.4.3 Enhancing the signal by apodisation

Much like the time transient measured in the oil-water mixture in the room temperature experiment, the FID in this experiment contains two signals, UPt_3 and the Pt marker. The signal with the faster transverse decay time (in this case UPt_3) can be enhanced by multiplying the FID with a decaying exponential function with time constant T_{fil} as given in Equation 5.3. This is known as apodisation or applying a T_2^* filter.

$$y = \exp\left(\frac{-t}{T_{fil}}\right) \tag{5.3}$$

The resulting spectrum becomes smoother, but the amplitude of the NMR line decreases to A_f and the linewidth broadens to T_{2f}^* as given by the equations below.

$$\frac{1}{T_{2f}^*} = \frac{1}{T_2^*} + \frac{1}{T_{fil}} \tag{5.4}$$

$$A_f = A\frac{T_{fil}}{T_{fil} + T_2^*} \tag{5.5}$$

A T_2^* filter with $T_{fil} = 300$ μs was routinely used to analyse the UPt_3 signals in this thesis.

5.4.4 Measuring the deadtime of the spectrometer

As the tranverse decay time of UPt_3 is very fast, on the order of tens of μs, it is important to try to capture data from as close to the end of the transmitter pulse as possible to lose as little signal as possible. The deadtime of the spectrometer was measured for different tipping pulse amplitudes with the following method. A tipping pulse of length 100 μs was sent through the transmitter coil, modulated with a constant small amplitude cw signal. The SQUID was put into FLL 5 μs after

the end of the pulse and the small amplitude cw signal was detected through the T_x-R_x cross coupling. The deadtime is a measure of how quickly the SQUID can recover from the tipping pulse and capture the time transient accurately. Figure 5.9 shows the resulting transients for different currents in the transmitter circuit. The time after which the small amplitude cw signal can be reliably captured gives the deadtime of the spectrometer for that particular amplitude of tipping pulse.

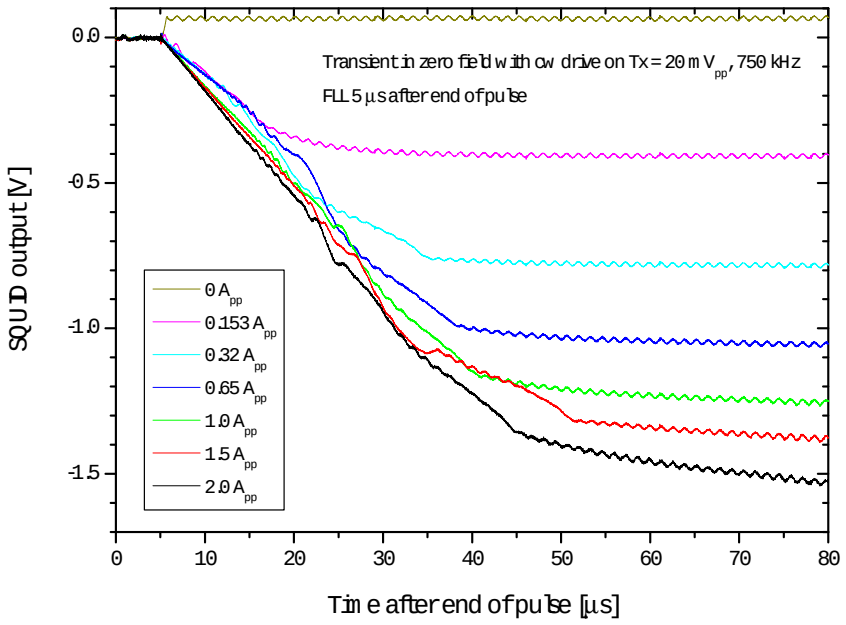

Figure 5.9: Transient following a 100 µs transmitter pulse at 750 kHz with a superimposed small amplitude cw signal. The SQUID is put into FLL 5 µs after the end of the pulse.

5.4.5 UPt_3 signal with platinum marker

Following the methods to enhance the signal quality, a UPt_3 NMR signal was finally observed in a field of 84 mT. A tipping pulse with $f_0 = 750$ kHz, 1.25 A_{pp} of length 50 µs was used for excitation, following Körber [2]. The time trace was captured 50 µs after the end of the pulse for 600 µs at a sampling rate of 50 MHz, with the 12 bit Pickering PXI card. 10 000 averages were taken for the resonance trace and each of the high and low field backgrounds (at the first low field minimum and second high field minimum), with a repetition rate of 1 s. Figure 5.10 shows

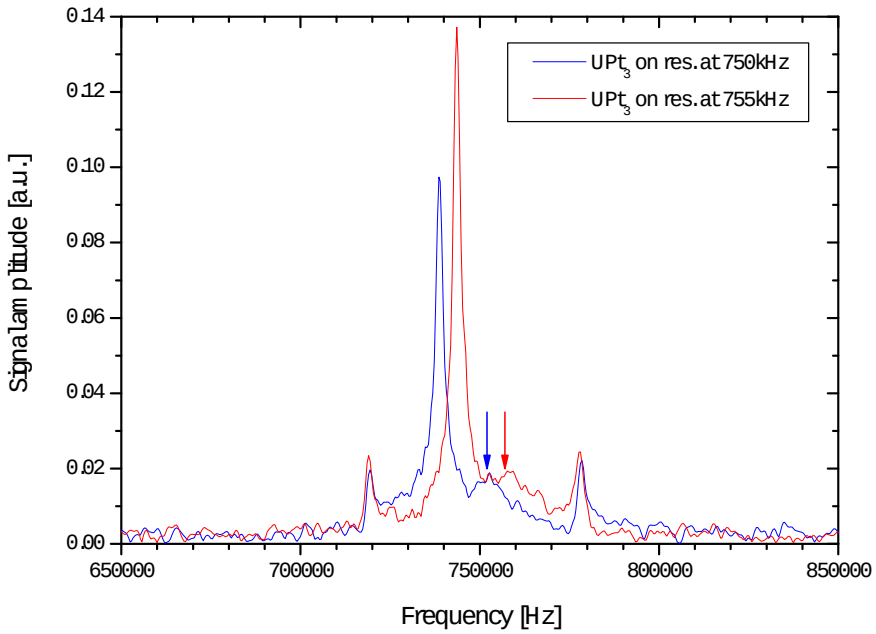

Figure 5.10: Clearest UPt_3 NMR signals that could be observed using the platinum marker. The arrows point to the UPt_3 signal that is hidden in the shoulder of the large platinum signal. A T_2^* filter with $T_{fil} = 300$ µs was used.

the clearest UPt_3 signal that could be obtained (blue trace).

The Knight shift of platinum metal is -3.44 % and the gyromagnetic ratio of platinum in a diamagnetic solid is $\gamma_{Pt\ bare} = 5.714 \times 10^7$ Hz T^{-1} [118]. Rearranging Equation 4.2, this means that at 84 mT, the UPt_3 with a Knight shift of -1.9 % should resonate at 750 kHz and the Pt marker should resonate at 738.2 kHz. This agrees quite well with the NMR spectrum obtained. However, to confirm that this small peak was indeed the UPt_3 signal, the static field was increased so the resonance occurred 5 kHz higher and the resonance data retaken with the same pulse sequence. The UPt_3 hump was seen to also move 5 kHz higher, strengthening the case that we were finally observing the UPt_3 NMR line. The same backgrounds were used, hence the small remnant peaks either side of the UPt_3 signal from the Pt marker signal are visible at the same frequency for both traces. As apparent from Figure 5.10, an accurate determination of the resonance frequency of UPt_3 could not be made due to the dominating Pt marker signal. It was clear that a measurement of the Knight shift could not be performed with the current experimental setup, which ended the first run.

For the second run of the dilution fridge, two major changes were implemented. Firstly, a new inner overlapping Nb shield was constructed to try to reduce the deadtime of the spectrometer. Secondly, the Pt marker was replaced by a ^{3}He marker. Subsequently, the new setup was characterised using the ^{3}He marker using an improved NMR signal fitting routine. This paved the way for the measurement of the Knight shift of UPt_3 which will be discussed in Chapter 6.

5.5 Inner overlapping shield

Following the experiments in Section 3.7.8 where different Nb foils were investigated as materials for inner shields, an inner shield for the minifridge was constructed using the 70 μm thick, 99.9 % purity Nb. The construction is similar to the shield described in Section 3.4.4 but with smaller dimensions. The nylon former was 19.5 mm o.d. and 18.5 mm i.d. and 82.5 mm long, with a 5 layer inner shield wrapped on top, making the shield o.d. 21.5 mm to fit snugly in the magnet former with a 1.25 mm gap to the transmitter coil. There was no need for Stycast to hold the shield together as instead, the Kapton sheet was cut 4 cm longer than the Nb and stuck down to the shield with GE varnish and the shield wrapped with PTFE tape. As the Nb shield could only be 70 mm in length, a nylon spacer was made to fill the gap between the nylon and the magnet former at the top of the shield, with two M2 screw holes to hold the shield in place. The shield was grounded through one tab to the magnet former using a screw contact.

The deadtime experiment from Section 5.4.4 was repeated with this inner shield (after the installation of the ^{3}He marker) and was found to be significantly shorter than that measured without an inner shield. Figure 5.11 is a summary of the measured deadtimes for both configurations. The experiment was repeated with a high pass filter on the output of the SQUID, as this filter was used in the actual experiment to measure UPt_3 and was found to not affect the deadtime. A 28 μs shortening of the deadtime was found for 1.5 A_{pp} transmitter pulses, which is the amplitude used in the Knight shift measurements of Chapter 6.

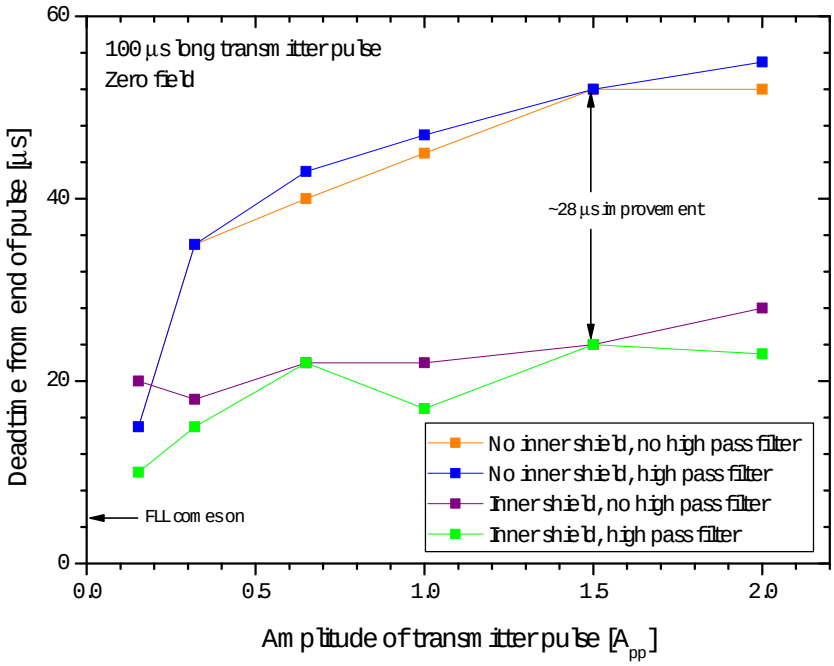

Figure 5.11: Comparing deadtime of setup with and without an inner overlapping shield.

5.6 Helium-3 as a marker

In my opinion, the most significant modification made to the setup for measuring the Knight shift of UPt_3 was the implementation of a ^{3}He marker for local field determination at the sample. As a ^{3}He melting curve thermometer had been used on the minifridge in a previous experiment, the fill line (which was well heat sunk down to the mixing chamber) and ^{3}He gas handling system were already in place [127]. Only the cell had to be constructed. The gyromagnetic ratio of ^{3}He is 2.038×10^8 Hz T^{-1}, so that it resonates at a frequency ~ 3.6 times higher than the UPt_3 resonance. Additionally, it is not a metal so it will not be a source of Johnson noise in the flux noise spectrum and will not heat up during tipping pulses due to eddy current heating. This section discusses the number of spins available from a potential volume that would fit inside the existing sample space, the construction, testing and mounting of the cell onto the minifridge, and the procedure determined to fill the cell.

5.6.1 Number of spins required for ^{3}He marker

The sample space available on the reverse of the Kel-F sample holder can be seen in Figure 5.6(b). Considering for simplicity a cylindrical cell volume, the maximum diameter to fit safely within the receiver coil former is 1.5 mm. The length of the volume can be made to fill the receiver coil which is $\sim$ 6 mm tall. If the cell is made of Stycast 1266, the inner diameter of the cell can be machined to be as large as 1.1 mm. This gives an effective volume inside the receiver coil of 5.70 mm^3. The molar volume of liquid ^{3}He is $V_m = 36.84$ cm^3 mol^{-1} [118] giving 9.02×10^{19} spins.

In order to obtain a comparable signal size to the platinum marker, we can calculate the required number of ^{3}He spins assuming for the worst case scenario that the T_2^* for helium is the same as that for platinum and is limited to 300 µs due to the environmental field homogeneity. Using the equations in Section 3.5.4, we can see that in order to obtain the same signal size in the frequency domain, the number of ^{3}He spins required is simply:

$$N_{\text{He spins}} = \frac{N_{\text{Pt spins}}\gamma_{\text{Pt}}^2}{\gamma_{\text{He}}^2} \tag{5.6}$$

which gives $N_{\text{He spins}} = 4.40 \times 10^{18}$ spins. Thus, with the above design for a ^{3}He cell, we will have a factor 20 more spins than in the platinum marker. Indeed, the ^{3}He signal at 750 kHz could be seen with a single shot, with a SNR of about 60 and a 95 Hz linewidth, corresponding to a T_2^* of 3.3 ms. The linewidth is thus a factor of 10 sharper than the platinum marker signal, leading to an improvement in frequency and therefore field resolution by the same factor. This makes ^{3}He an excellent marker.

5.6.2 Design and testing of the ^{3}He marker

Figure 5.12 shows the construction of the Stycast 1266 ^{3}He cell. The silver fill line (0.76 mm o.d.) was fixed into the cell with Stycast 1266 after keying the surface of the fill line with a needle file for a better seal. A length of wire was fed through the fill line while the Stycast dried, and moved every now and again so that it

would not become blocked.

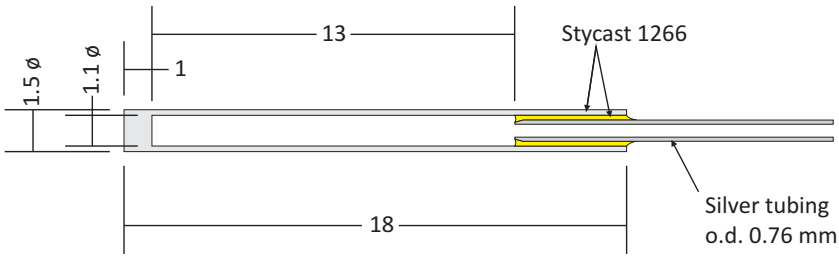

Figure 5.12: Diagram of ^{3}He cell used as a field marker.

Once assembled, the fill line of the cell was connected to the ^{3}He gas handling system (GHS), shown in Figure 5.13. The cell was pumped out using the KF-16 flange on the GHS with a leak detector until the LR (leak rate) reached the base LR of 1×10^{-10} mbar l s^{-1}. The Gems pressure gauge on the GHS has an offset of -0.668 mV at zero pressure, when biased with a 10 V power supply. The pressure calibration to convert from voltage into bar is:

$$P(\text{bar}) = \frac{V_{Gems}(\text{mV}) + 0.668 \text{ mV}}{0.896 \text{ mV/bar}} \tag{5.7}$$

as calibrated using the pressure gauges on the GHS.

The cell was leak tested at room temperature by enclosing it in a ^{4}He atmosphere after which the LR rose to 1×10^{-5} mbar l s^{-1} in under a minute. This is attributed to the diffusive LR through the walls of the cell. The cell was then mounted inside a vacuum can on a dipping probe and filled with $\sim$ 300 mbar of ^{3}He. The LR was monitored by a leak detector on the vacuum can. A diffusive LR of 1.2×10^{-7} mbar l s^{-1} was observed at room temperature, which dropped to 1.4×10^{-9} mbar l s^{-1} when the probe was lowered into liquid helium. Cryopumping is occuring on the walls of the cell, making it leak tight when cold, similar to the room temperature vacuum cell. The cell was tested for ^{3}He pressures up to 1 bar and found to be leak tight.

In order to mount the cell onto the minifridge, the copper sample holder was modified to accomodate the fill line. A 1 mm deep, 1 mm wide groove was machined out of the stalk and one of the slots at the base of the sample holder was made

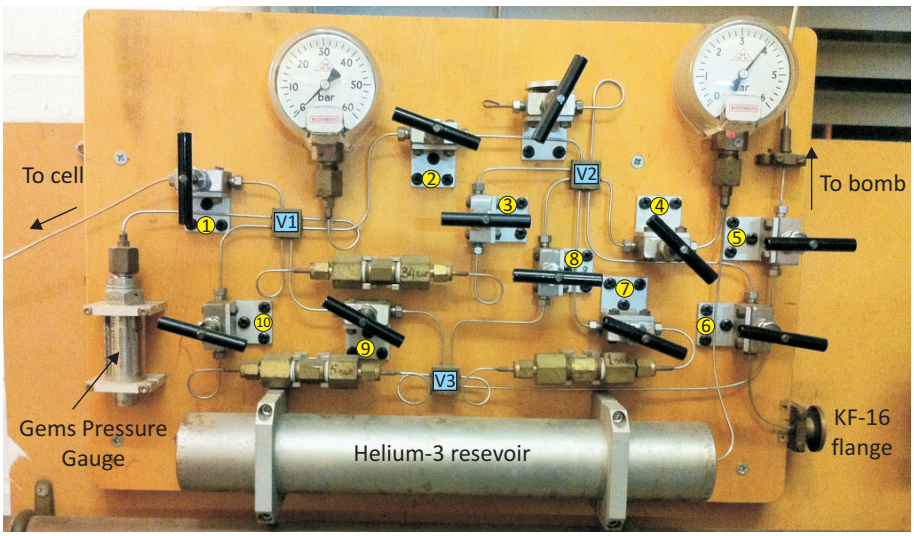

Figure 5.13: Photograph of ^{3}He gas handling system.

8 mm long. The cell was mounted onto the sample holder and secured with GE varnish, inserted into the receiver cell and left to dry. The receiver coil assembly was then inserted into the NMR coil assembly and screwed in. The fill line was extended to connect with the end of the existing fill line to room temperature by soldering up lengths of sterling silver tubing. Once mounted, the cell was leak tested at room temperature with a leak detector pumping on the HiP valve to the cell at the top of the cryostat (referred to as HiP 0). When the base of the magnet was sprayed with helium gas, the diffusive leak rate through the cell wall was measured to increase to 3×10^{-8} mbar l s^{-1} over 30 seconds before dropping, confirming that the cell was not blocked. The lower diffusive leak rate is because half of the cell has been varnished.

5.6.3 Procedure to fill the ^{3}He cell

The procedure to fill the cell has now been well established for this fridge. The HiP valves on the ^{3}He GHS will be referenced by their number, as shown in Figure 5.13. Before filling the ^{3}He cell, it is pumped out at room temperature using a pumping trolley via HiP 0, 1, 2 and 6. The Gems pressure gauge is read with a Keithley multimeter and measures the pressure of the volume connected to V1 in volts,

which is converted into bar using Equation 5.7. A LabVIEW program was written for the AVS resistance bridge (Section 5.1.4) to monitor and plot the temperature at the mixing chamber (MC) every second (Channel 1, Speer carbon resistor) as an indication of warm ^{3}He reaching the MC.

The fridge is cooled to base temperature with all HiP valves closed except for 0 and 1 so the pressure in the cell can be monitored. When the temperature of the MC has stabilised at base temperature, ^{3}He is essentially let into the cell until the temperature stops increasing on the MC thermometer. This is an indication that the ^{3}He level is above the MC and so the cell is filled. This amount of ^{3}He has been measured to be the equivalent of 14.36 bar of ^{3}He in one 'shot' volume, which includes V1, from HiP 0 at the cryostat to 2, with 9 and 10 closed. In practice, the following procedure is repeated (about four times) until the cell is filled:

1. Close HiP 0 and 1 to cell.
2. Open HiP 4 and 2 to fill V1 and V2 with ^{3}He from the resevoir.
3. Close HiP 2 to resevoir. Open 1.
4. Measure Gems pressure of this 'shot' volume.
5. Open 0 slowly to cell until the pressure in the cell reads zero. The temperature should increase at the MC and then start to cool again.

At low mK temperatures, the vapour pressure of ^{3}He is close to zero [118], so that the ^{3}He will always be drawn into the cell. This is why it was decided to fill the cell at the lowest temperature possible. When the MC temperature no longer increases with the addition of more ^{3}He, HiP 0 is closed to the cell, HiP 4 is closed to the resevoir and the GHS pumped out with the bomb via 5. All valves are closed with the exception of HiP 1 and 0, which are left open to the cell for safety.

5.7 Characterisation of setup with inner shield

The presence of the inner overlapping shield can substantially modify the field-current ratio of the transmitter pulse [2]. When a pulse is applied, mirror currents build up on the inner shield that oppose the transmitter pulse, reducing the effec-

tive magnetic field at the sample. Thus, the field current ratio was remeasured for this new setup using the helium marker.

Significant field trapping in the inner shield and hysteresis in the field-current ratio of the magnet were also found in the previous experiment by Körber, when the static field was increased above 36.5 mT. This is reminiscent of the flux trapping observed in the room temperature experiment, but at much higher fields (by a factor of ~ 10), detected using samples with a much broader linewidth (also by a factor of ~ 10). As the helium marker is used as the local field calibration, it was not necessary to have such a precise knowledge of the field-current ratio, as the power spectrum of the transmitter pulse will excite a range of frequencies around resonance, determined by the length of the pulse (see Figure 5.8). Nevertheless, measurements of the B/I for the magnet were also performed to test this new setup. Details of these measurements are given in this section but first we describe the new Fourier transform and fitting routine developed in order to more accurately fit to the NMR data.

5.7.1 Python fitting program

The Fourier transformation and background subtraction of the time trace was performed using the a program written in Python by Lev Levitin and Michael Neumann and replaced the LabVIEW written program used in the room temperature experiment. Firstly, background subtraction of the time traces is performed, scaled to the static field using the following equation:

$$s = r - 0.5\left(\frac{I_r}{I_{lf}}\right)^2 b_1 - 0.5\left(\frac{I_r}{I_{hf}}\right)^2 b_2 \tag{5.8}$$

where r, b_1 and b_2 are the resonance, low and high field backgrounds respectively and I_r, I_{lf} and I_{hf} are the currents used in the magnet for the three traces. If there is a large transient at the start of the resulting time trace s, this can be truncated off. Any mismatch between the start and end of the signal is taken into account by subtracting off a best fit straight line between the start and end of the trace, as this could cause ripples in the Fourier transform. The trace is then zero-padded

up to 2^{17} points and a specified T_2^* filter is applied. An FFT is performed on the resulting time trace for a specified frequency interval. The effect of passing the signal through a high pass filter with a known 3dB bandwidth is modelled and is also subtracted away from the spectrum.

The program also performs a Lorentzian fit to the NMR line between specified frequencies. In the room temperature experiment, the analysis was performed in Origin 7.0, where a Lorentzian was fitted to the square of the magnitude of the Fourier transform (Section 3.5.2). As we saw in Section 2.1.7, the Fourier transform of an FID is a complex function, which can be expressed as a real and imaginary quantity (or equivalently, magnitude and phase). This Origin analysis, therefore does not take into account the phase of the signal. In the Python fitting algorithm, a least squares fit is made to both the real and imaginary parts of the Fourier transform, therefore taking the phase into consideration. In this way, it gives a more complete fit. Figure 5.14 is an example of the real and imaginary fit to the Fourier transform of an NMR signal from UPt_3.

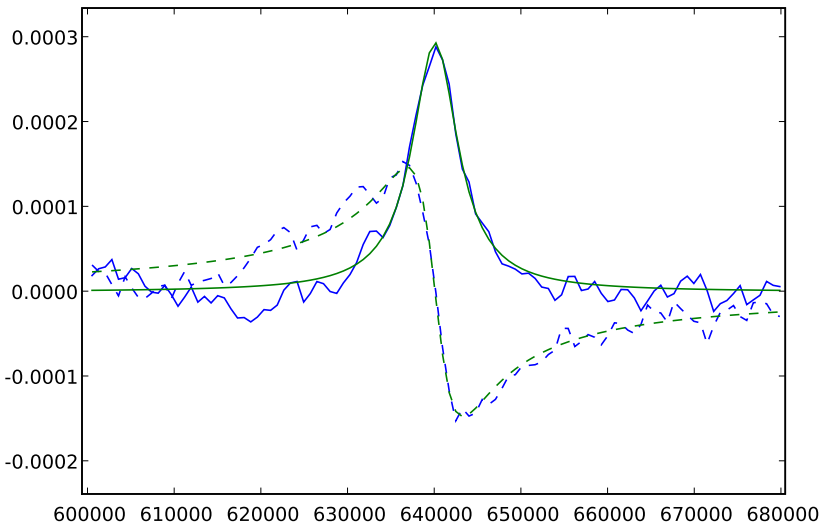

Figure 5.14: An example of Python's least squares fit to the real and imaginary parts of the Fourier transform of an FID. The x axis is the frequency in Hz. The signal is the UPt_3 NMR signal from Figure 6.10.

The fit is made to Equation 2.20 and as an output, the fitting parameters f_0, T_2^* and A are given, where A is the initial amplitude of the FID in the time domain.

In the Python FFT routine, the height of the NMR line is given by Equation 2.22 multiplied by an arbitrary constant of 10^6 Δ. Thus, unlike the LabVIEW FFT routine, the amplitude in the frequency domain does not depend upon the sampling frequency. To convert between signal sizes in the frequency domain (from H_0(Py) in Python to H_0(Lab) in LabVIEW), the following equation can be used:

$$H_0(\text{Lab}) = \frac{H_0(\text{Py})}{10^6 \Delta}, \tag{5.9}$$

where Δ is the inverse of the sampling frequency.

5.7.2 Transmitter B/I

Using Equation 3.1, the theoretical field-current ratio of the transmitter coil is $B_{saddle} = 1.59$ mT A^{-1}. As discussed in Section 2.1.6, this rf pulse corresponds to $2B_1$, so the tipping pulse is $B_1 = B/I_{th} = 797$ μT A^{-1}. This can be verified experimentally by measuring the current through the transmitter coil required to produce a 90° pulse using a sample with a known gyromagnetic ratio γ. Using the ^{3}He marker, the peak height of the NMR line was measured for increasing current in the transmitter circuit. A 750 kHz transmitter pulse was used, of length 100 μs. This is the resonance frequency of ^{3}He in the static field $B_0 = 23.1$ mT. The FID was captured for 15 ms as T_2^* is $\sim$ 3 ms in this field. Due to the excellent SNR, only a single shot measurement was required.

Figure 5.15 shows a sinusoidal fit to the peak height, where a current of 362 mA$_{pp}$ = 181 mA amplitude is required for maximum signal height, or a 90° pulse. However, this current corresponds to the total current I_{in} in the transmitter circuit, which is composed of a 330 Ω shunt resistor parallel to the coil. The current through the transmitter coil I_{trans} can be calculated using Equation 5.2 using a frequency of 750 kHz which gives $I_{\text{trans}} = 160.5$ mA.

The B_1 field required for a 90° pulse is derived from Equation 2.16 and is:

$$B_1(90°) = \frac{\pi}{2\gamma\tau} \tag{5.10}$$

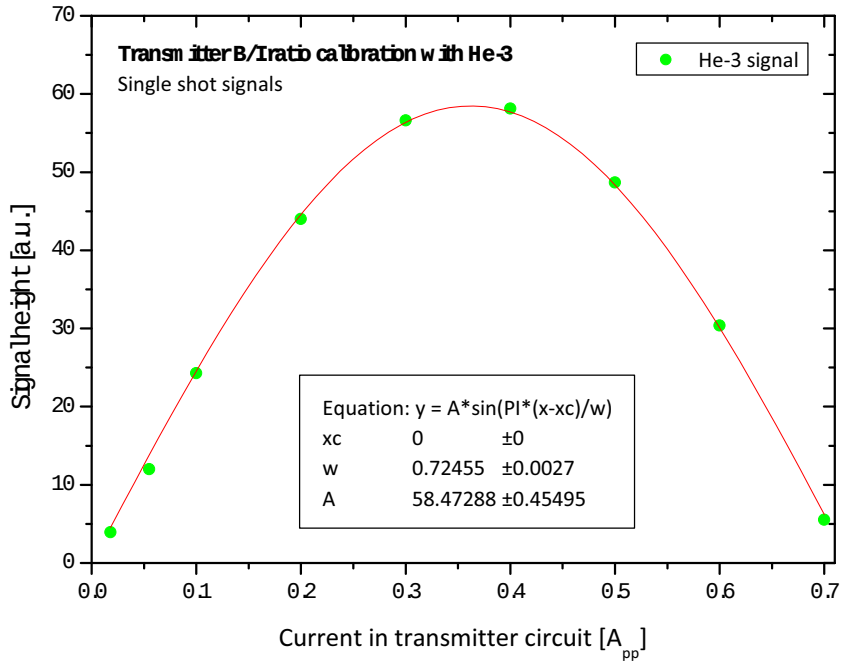

Figure 5.15: Determination of transmitter B/I. The peak amplitude of NMR lines from ^{3}He are measured as a function of current in the transmitter circuit using a 750 kHz 100 µs long transmitter pulse.

where $\tau = 100$ µs is the length of the tipping pulse and $\gamma = 2.038 \times 10^8$ Hz T^{-1} for ^{3}He, giving $B_1 = 77.1$ µT. The measured B/I for this transmitter coil with the inner Nb shield in place is therefore 480 µT A^{-1}. This is 60 % of the theoretical B/I which reflects the field cancelling effect of the inner overlapping shield.

5.7.3 Magnet B/I

The field-current ratio B/I of the magnet was also determined using NMR signals from ^{3}He. The resonance frequency f_0 of the NMR line was measured for both positive and negative currents in the magnet, and the corresponding resonance field inferred from the relation $B_0 = 2\pi f_0/\gamma_{^3\mathrm{He}}$. In general, the field B has the following dependence on the current I:

$$B = aI + b \tag{5.11}$$

where a is the field-current ratio and b a small intercept signifying the trapped environmental field. Figure 5.16 shows this dependence for which a linear fit gives $a = 83.39$ mT A^{-1} and $b = 44.2$ µT, which is comparable to the Earth's magnetic field. When the above B/I was measured, the largest field that had been applied was 46.3 mT. However, even after higher fields of up to 73.6 mT were applied, the trapped field was never more than 120 µT. This is very small compared to a previously made inner shield on this fridge [2], which was found to trap 1.95 mT after the static field was ramped to only 63.9 mT. The previous shield was made from 2.5 layers of 50 µm thick, 99.9 % purity Nb, much like the initial shields made for the room temperature experiment. Thus, on this fridge the improved performance of the new inner shield can be appreciated.

With the new ^{3}He marker in place and the spectrometer characterised, the task of optimising the signal quality and SNR of the UPt_3 NMR signal began. This investigation is summarised in Section 6.2 in the following chapter, where many NMR measurements of UPt_3 in the normal state were performed. The inherently minute signal size of the UPt_3 NMR line in comparison to the noise level was a difficult obstacle to overcome.

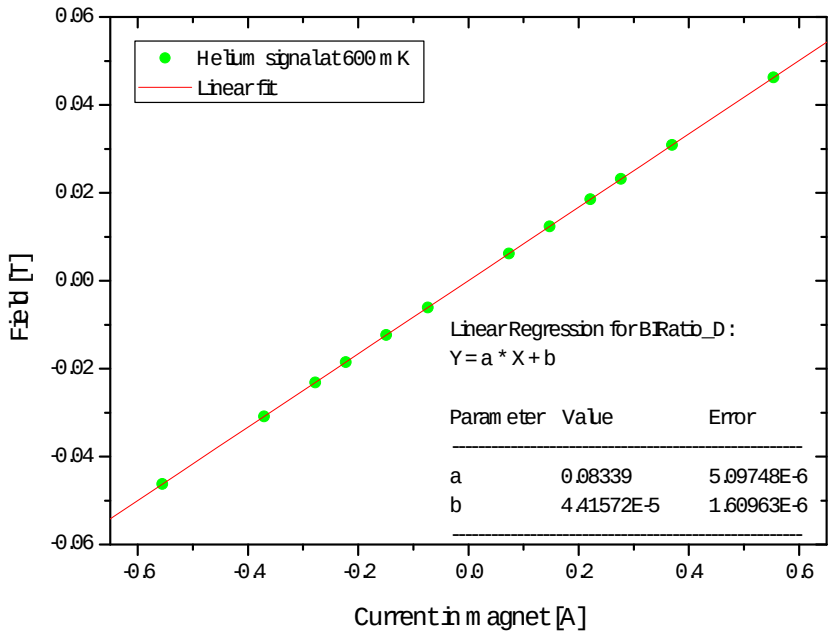

Figure 5.16: Determination of magnet B/I ratio by measurement of ^{3}He signals.

Chapter 6

NMR on single crystal UPt_3

In this chapter, I present NMR measurements taken on single crystal UPt_3 using the modified dc SQUID NMR spectrometer as described in Chapter 5, with the inner overlapping shield and helium marker. Two rectangular single crystal wafers were obtained[1], cut so that each physical edge of the wafer is aligned with one of the three principle axes of the hexagonal crystal. The low temperature measurements presented in this chapter refer to Sample 1 (see Figure 6.1), mounted with the c-axis parallel to the static field produced by the NMR magnet. The sample characterisation is also presented in this chapter although chronologically, these measurements were performed before all modifications to the cryostat were made. This is followed by the NMR experiment to measure the Knight shift as a function of temperature and a study of the signal to noise ratio.

6.1 The UPt_3 single crystals

In order to be able to make a direct comparison of experimental results with theory, we must carry out NMR measurements of UPt_3 with the static field parallel to each of the three crystallographic axes in turn. The predictions for the Knight shift along the three axes are given in Section 4.4.2. Single crystal wafer samples with known orientations were used as they allow the Knight shift measurement to be taken as a function of crystal direction. The two crystals obtained and their

[1]Supplied by Prof. Andrew Huxley from the University of Edinburgh

quoted orientations with respect to the hexagonal crystal structure are shown in Figure 6.1. The crystals were grown by the Czochralski process under ultra high vacuum (UHV) and annealed for 7 days at 950°C. The residual resistivity ρ_0 is typically around 0.2 μΩ cm for current $J \parallel c$ [128].

6.1.1 Size and mass of crystals

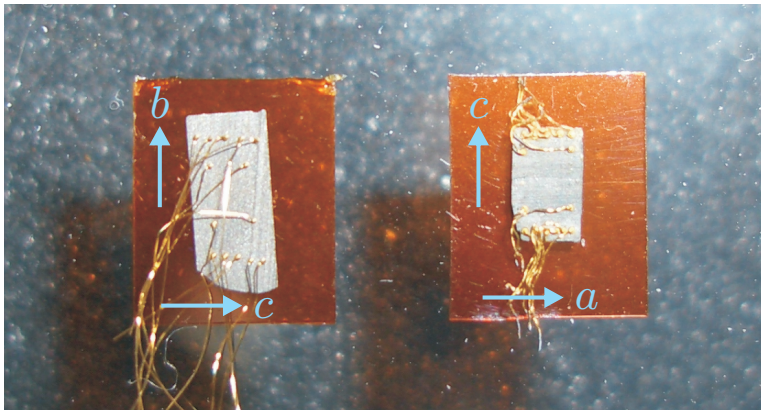

Figure 6.1: Photograph of the two UPt_3 samples mounted on Kapton foil. Sample 1 is on the left, Sample 2 on the right. The crystal axes are shown.

Each sample came with 14 gold wires of 50 μm ⌀ bonded to the surface for heat sinking. The physical dimensions were measured with a vernier caliper to be approximately $(2.3 \pm 0.05) \times (5.2 \pm 0.05) \times (0.2 \pm 0.02)$ mm^3 for Sample 1 and $(2.0 \pm 0.05) \times (3.25 \pm 0.05) \times (0.5 \pm 0.02)$ mm^3 for Sample 2. The thicknesses of the wafers were inferred from the density of UPt_3 of 19.40×10^3 kg m^{-3} [129] and their quoted masses of 43 mg and 60.5 mg for Samples 1 and 2 respectively.

6.1.2 Confirmation of crystal orientation

The first measurements performed on the single crystals were dc magnetisation measurements as a function of temperature in the normal state from which the susceptibility χ was calculated. These were taken using a standard physical property measurement system (Quantum Design PPMS). The measurement of $\chi(T)$ enables the determination of the crystal axis orientation as the susceptibility of UPt_3 is strongly anisotropic and is known (see Figure 4.6). Susceptibility mea-

surements also ensure that the crystal structure is hexagonal and that there are no stacking defects, which could cause an isotropic susceptibility [130].

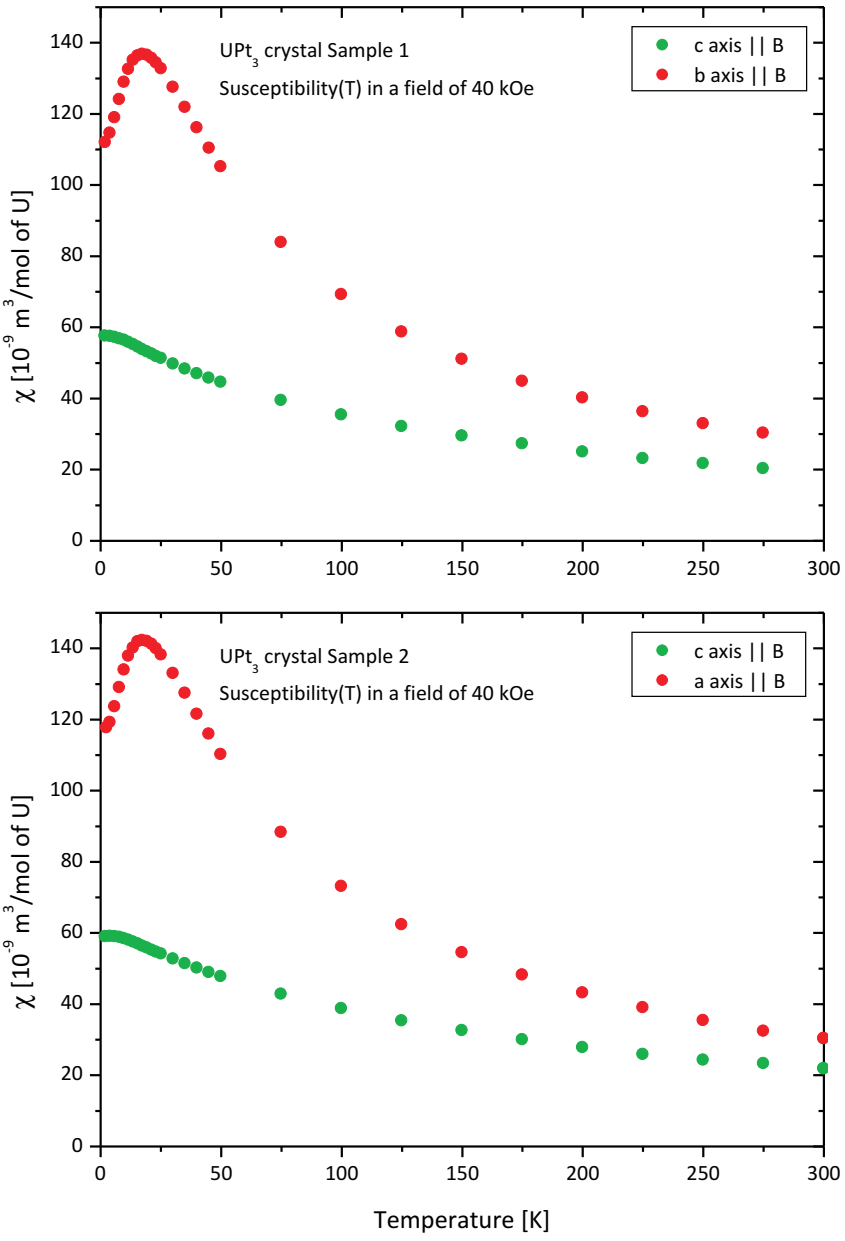

Figure 6.2: Susceptibility as a function of temperature for UPt_3 crystal Sample 1 (top) and Sample 2 (bottom).

The samples were mounted by using a small dab of GE varnish onto 127 μm thick Kapton foil as shown in Figure 6.1. The background signal for the foil had previously been measured and was shown to be negligible [2]. The Kapton was mounted into a PPMS sample straw with the crystal axis of interest parallel to

the magnetic field. Dc magnetisation measurements were performed in a magnetic field H_0 of 4 T from 275 K to 2 K (the base temperature of the PPMS). In such a measurement, the sample is magnetised by a constant magnetic field and the magnetic moment of the sample is measured inductively. The susceptibility is calculated from $\chi = M/H$ by dividing the measured magnetisation by the applied field and multiplying by a conversion factor $4\pi \times 10^{-6}/n$ where n is the number of moles of uranium in the sample. It must be noted that this method cannot differentiate between the different orientations in the hexagonal plane (i.e. a and b axes give the same $\chi(T)$ dependence). Nevertheless, it was sufficient to confirm that the c-axis was in the quoted direction. Both UPt_3 samples were measured in the PPMS. Figure 6.2 shows the measured $\chi(T)$ for both UPt_3 crystals, which show excellent agreement with literature [81] (see Figure 4.6 on page 143). Hence, the crystal axes have been confirmed to be those given and no stacking defects seem to be present.

6.1.3 Measurement of T_c by mutual inductance

As can be seen in the phase diagram of Section 4.3, the low (mT) measurement fields used in the experiments in this thesis mean that we will be exploring the superconducting A and B phases of UPt_3. Although the upper transition T_c^+ is visible in many types of experiments, the lower transition T_c^- has mainly only been seen in specific heat, thermal expansion and ultrasound measurements [80]. Likewise, with the mutual inductance method used in this work it will be shown that we were only able to observe the upper transition. However, a comparison of the transition temperatures measured in various experiments shows that although T_c^+ can vary by up to 80 mK or so, the difference in the two transition temperatures is reliably ~ 55 mK [80]. Therefore we can infer T_c^- from a measurement of T_c^+ with reasonable confidence.

In this study, T_c^+ was measured using a method that exploits the inevitable inductive cross coupling between the transmitter and receiver saddle coils that surround the UPt_3 crystal, when mounted on the dilution fridge. The change in susceptibility of the crystal as it goes through the superconducting transition

is reflected in a change in the mutual inductance between the two coils. The mounting of Sample 1 onto the cryostat is described in Section 5.2.4. To reiterate, its orientation is such that the c-axis is parallel to the static field produced by the superconducting solenoidal NMR magnet. The axis of the receiver coil is perpendicular to the crystal surface and the axis of the transmitter coil is parallel to the b-axis. This setup also allows the superconducting transition temperature T_c to be measured in different static fields applied by the NMR magnet. With this method, T_c can be measured with the sample in exactly the same conditions as in the subsequent NMR experiments and using the same germanium sample thermometer, making it a desirable technique compared to, say, a standard ac susceptibility measurement on a different fridge. In the following section we discuss the principles behind this measurement technique.

The theory behind the technique

The mutual inductance measurement involved using an EG&G DSP lock-in amplifier (model 7265 [131]). The internal oscillator of the lock-in was used to send an ac signal of $f = 317$ Hz into the transmitter coil through a 10 kΩ resistor in series with the coil. At these low frequencies, the shunt resistor across the transmitter can be ignored and all the current is assumed to flow through the transmitter coil. A signal is detected orthogonally by the receiver coil via the cross coupling of the two coils, a mutual inductance M_{TR}, so that the flux in the receiver coil is given by Eqn. 6.1.

$$\phi_p = I_T M_{TR}(\chi), \tag{6.1}$$

where I_T is the current in the transmitter coil and M_{TR} depends on the sample susceptibility χ. The flux in the receiver coil is coupled to the SQUID via the superconducting flux transformer with the SQUID continuously operated in flux locked loop mode (FLL). The flux transferred to the SQUID has the dependence

$$\phi_{SQ} = \frac{\phi_p M_i}{(L_i + L_p)}, \tag{6.2}$$

where M_i is the mutual inductance between the SQUID and the input coil, L_i is the input coil inductance and L_p is the receiver coil inductance. Finally, the measured output voltage V_{out} is determined by the SQUID gain in FLL and is given in Eqn. 6.3.

$$V_{out} = G_{FLL}\phi_{SQ} \tag{6.3}$$

At higher frequencies, the magnetisation of the sample may lag behind the applied ac drive field, an effect that is detected by the lock-in amplifier. The susceptibility at finite measurement frequency is a complex variable:

$$\chi(\omega) = \chi'(\omega) + i\chi''(\omega) \tag{6.4}$$

with χ' as the in-phase, or real, component and χ'' as the out-of-phase, or imaginary, component. χ' is related to the magnetic energy stored in the volume occupied by the sample and in general reflects the shielding ability. χ'' is related to the energy absorbed by the sample from the ac field. In the case of conducting samples, the mechanism is through eddy current heating. When a magnetic sample is placed inside the two coils, the mutual inductance is multiplied by a factor $1 + F\chi$ where F is the fill factor, which expresses to what extent the volume enclosed by the coil is filled by the sample. The above considerations lead to the following expression for the output voltage measured by the lock-in amplifier:

$$V_{out} = \frac{G_{FLL}M_iI_T}{(L_i + L_p)}M_{TR}(1 + F(\chi' + i\chi'')) \tag{6.5}$$

The lock-in amplifier measures the real and imaginary parts of the output voltage with respect to the internal reference oscillator. An external voltage source could also be simultaneously measured. This was used to monitor the temperature of the mixing chamber via the channel 0 (Ge resistor) output of the AVS bridge. The mixing chamber was allowed to cool from 600 mK to base temperature by switching off the heater on the mixing chamber. A LabVIEW program was used to record the $\mathrm{Re}(V_{out})$, $\mathrm{Im}(V_{out})$ and Ge resistance every second for 5000 points, such that the temperature decreased from 600 mK to 427 mK, adequately below

the lower transition temperature. Data was only taken on cooling for convenience.

This measurement was performed in zero field and also in a field of 84.60 mT. This field was originally chosen as it corresponded to the static field for which we were looking for a UPt_3 NMR signal to resonate at a Larmor frequency of 755 kHz. The results are discussed in the following section.

Analysis and discussion of results

Figure 6.3 shows the mutual inductance measurement as a function of temperature. The real and imaginary parts of V_{out} (Equation 6.5) are plotted.

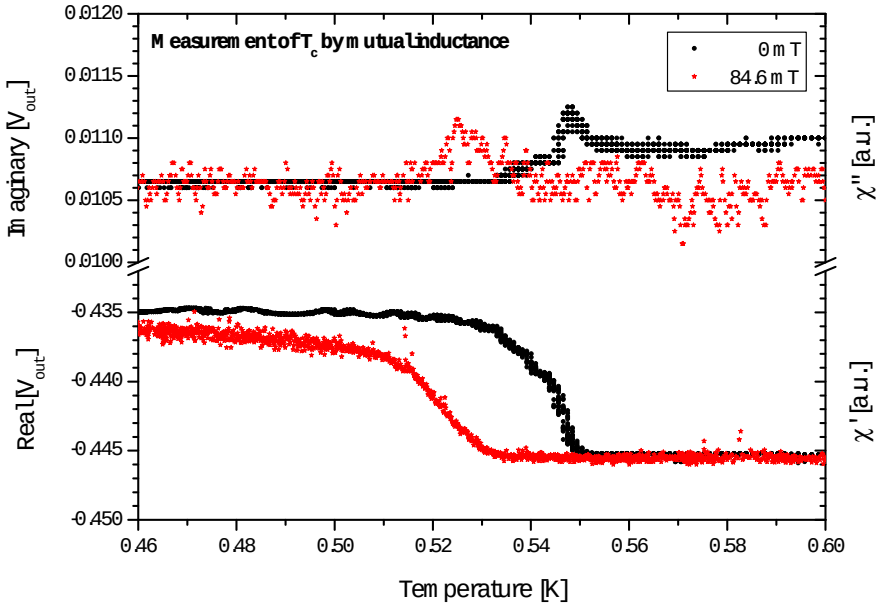

Figure 6.3: The superconducting transition temperature for UPt_3 crystal Sample 1, measured using a mutual inductance measurement on the cryostat with a lock-in amplifier.

The ac current that was sent into the transmitter coil from the lock-in amplifier was measured to be 33.3 μA_{rms} across a 10 kΩ resistor in series with the coil. The inductive cross-coupling between the transmitter and receiver coils due to their non-perfect alignment is measured by the SQUID as in Section 3.4.10 to be 22 $\mu A/\Phi_0$ with UPt_3 in the normal state. This is the current needed in the transmitter to couple one flux quantum into the SQUID sensor. Thus, the current sent into the transmitter corresponds to a flux of 1.50 $\Phi_{0\ rms}$ coupled into the

SQUID. Using Equation 6.3 with the SQUID gain in FLL of 300 mV/Φ_0, the calculated voltage is $|V_{out}| = 450\ mV_{rms}$ assuming that in the normal state χ is negligible. This agrees with the zero field measured voltage in the normal state at 600 mK, which is calculated using:

$$|V_{out}| = \sqrt{X^2 + Y^2} \tag{6.6}$$

The values were determined to be $X = -445.2\ mV_{rms}$ for the real part of the measured voltage and $Y = 11.0\ mV_{rms}$ for the imaginary part (from Figure 6.3). The measured $|V_{out}| = 445.3\ mV_{rms}$.

Figure 6.3 shows that as the temperature is decreased, a peak in the imaginary part of the susceptibility and a change of slope of the real part of the susceptibility can be seen. I attribute this to T_c^+ as it is the first transition that is reached when cooling from the normal state. It is also within the range of previous measurements of T_c^+ on different single crystals [80]. There are no features in the mutual inductance measurement that indicate the lower transition T_c^-. In zero field, from the temperature at which the peak in $\mathrm{Im}(V_{out})$ occurs, a T_c^+ of (548±3) mK is measured. Defining the transition as the temperature at which $Re(V_{out})$ has increased by half of the total change, a T_c^+ of (544±4) mK is measured. Similarly for the transition in a field of 84.60 mT, $T_c^+ = (525\pm5)$ mK and (520±6) mK are measured from the imaginary and real parts of V_{out} respectively. With these definitions, in zero field the average $T_c^+ = (546\pm4)$ mK and in 84.60 mT the average $T_c^+ = (522.5\pm6)$ mK. From these, the inferred lower transition temperature in zero field is therefore $T_c^- = \simeq 491$ mK and in 84.60 mT $T_c^- = \simeq 468$ mK.

As mentioned in Section 4.3, the transition temperatures at zero field measured by several groups differ by quite a large margin (ranging from 490 to 580 mK for T_c^+) due to differences in preparation techniques and resulting quality of each sample. The relatively high value of our measured T_c^+ of 546 mK compared to the average accepted value of 530 mT [80] attests to the quality of the sample. As for the measured T_c^+ in a field of 84.6 mT, Adenwalla *et al.* measure a T_c^+ that is only ~ 8 mK below T_c^+ in zero field, inferred from their phase diagram [90]

(Figure 4.7). Bruls *et al.* on the other hand measure a T_c^+ that is ~ 16 mK below T_c^+ in zero field [94]. The most recent measurement (1994) by Löhneysen [132] determine a difference of 11 mK. The T_c^+ I measure is (23.5 ± 6) mK lower than that in zero field. This difference may be due to differences in sample quality and measurement technique, moreover, as I am confident in the shielding of external fields in this low field measurement, I conclude this is a reliable value.

6.2 UPt_3 in the normal state

In this section, NMR measurements of UPt_3 in the normal state are presented. These measurements were carried out above T_c at a temperature of 600 mK. The static NMR field orientation parallel to the c-axis ($B \parallel c$) was chosen to be measured first as the linewidth should be approximately twice as sharp compared to when $B \perp c$, giving a signal that is twice as high in the frequency domain. This was inferred from measurements of the spin-spin relaxation time by Lee *et al.* [56] as given in Section 4.6.1, who measured $T_2^* \sim 83$ μs. Previously on this dilution fridge, Knight shift measurements were made by Körber [2] on UPt_3 with the field at an angle of 30° to the c-axis. It would also be interesting to make a comparison with these results. Initially, NMR signals in the normal state were measured to optimise the signal acquisition procedure for the most accurate and reliable Knight shift measurements presented in Section 6.3.

6.2.1 Fine tuning of signal acquisition parameters

Initial NMR measurements were taken at a resonance frequency of 515 kHz for UPt_3 in the normal state. This frequency was chosen as it was a quiet frequency away from a particularly prominent pickup spike at 405 kHz, also visible in the SQUID noise spectrum as measured by an HP spectrum analyser.

A 50 μs long excitation pulse with 1.5 A_{pp} was chosen as the ideal tipping pulse for several reasons. Firstly, although the maximum signal size is obtained for a 123° tipping angle for metallic samples [133], this requires a large amplitude tipping pulse, which results in increased magneto acoustic resonances. As the

signal size does not go up linearly with tipping angle, the SNR was optimal when a 1.5 A_{pp} tipping pulse was used, corresponding to a tipping angle of 54°. The tipping angle can be calculated using Equation 5.2 to calculate the current flowing through the transmitter coil and Equation 2.16. The decay of an NMR signal is considered to begin from the middle of the rf excitation pulse [26], thus, a short pulse length is desirable. However, in order to produce a significant tipping angle, the amplitude must be large to compensate for the short pulse length. The pulse length and amplitude chosen was therefore a compromise.

For this experiment, the above tipping pulse was generated by an Agilent 33120A function generator and amplified by the Kalmus amplifier. The SQUID was put into FLL 25 µs after the end of the pulse and data acquisition commenced 5 µs after FLL for 850 µs. In the analysis (described in Section 5.7.1) it was necessary to truncate a further 15 µs from the start of the dataset to aid with background subtraction. This corresponds to the data being captured 70 µs after

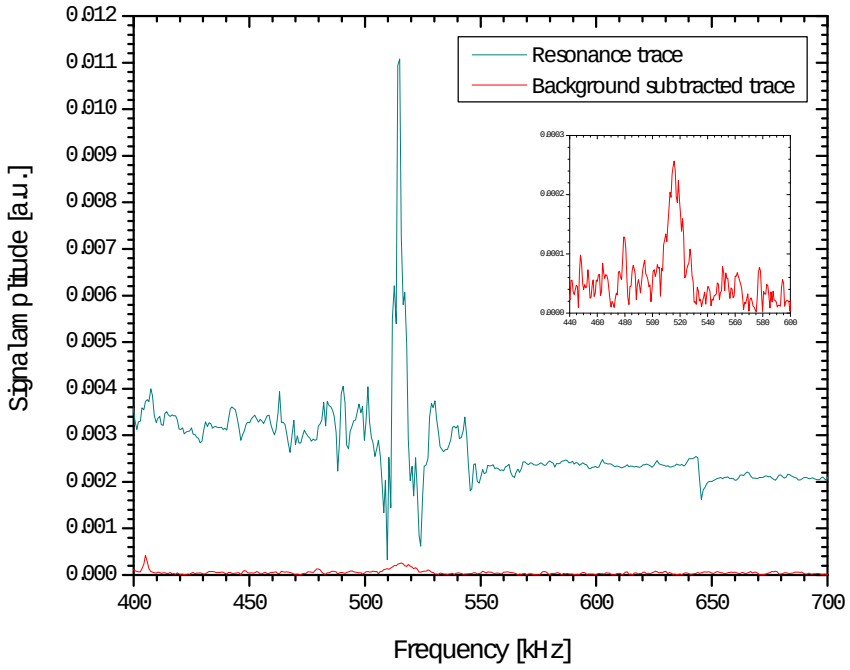

Figure 6.4: Background subtracted UPt_3 signal at 515 kHz with the Fourier transform of the resonance trace, showing the magneto acoustic resonances. The inset is a close-up of the UPt_3 signal. 10 000 averages each for resonance and background.

the middle of the pulse. 10 000 averages were taken with UPt_3 on resonance at $f_0 = 515$ kHz with a repetition time of 1 s. Backgrounds were taken each with 5 000 averages with UPt_3 on resonance at $f_0 \pm 20$ kHz, corresponding to the first minima of the tipping pulse power spectrum as described in Section 5.4.2. Figure 6.4 shows the background subtracted spectrum of a UPt_3 signal in the normal state at ∼515 kHz, together with the Fourier transform of the resonance trace only, showing the large magnitude of the magneto acoustic resonances that had to be subtracted away.

6.2.2 The ^{3}He marker in practice

Recall from Section 4.1.1 that in order to measure the Knight shift, an accurate determination of the resonance frequency for the UPt_3 signal for a known magnetic field is required. To fully benefit from using ^{3}He as a local field calibration (described in Section 5.6), it is necessary to be able to excite an NMR response from both the marker and the UPt_3 without changing the field. With the large magnetisation available from the ^{3}He marker, it was possible to do just this. Figure 6.5

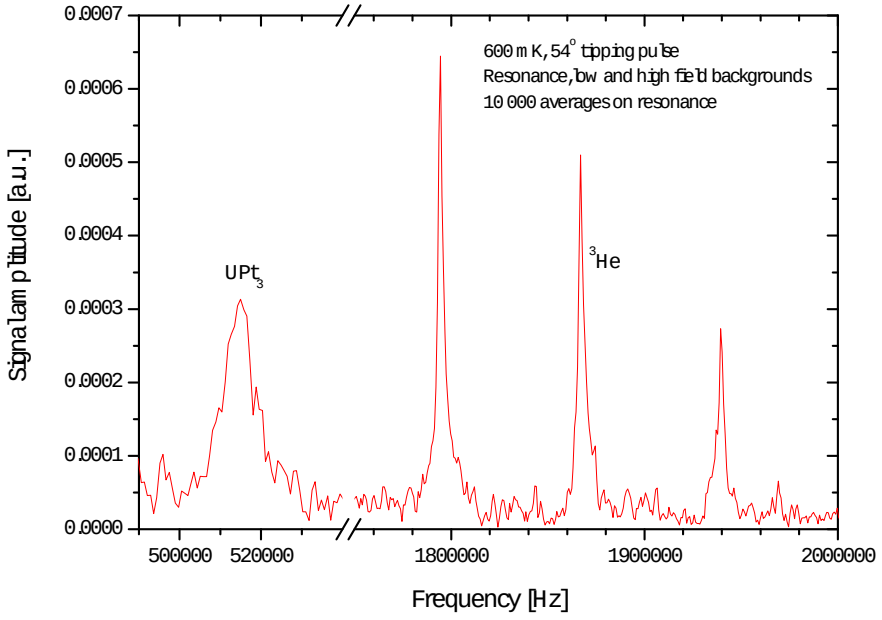

Figure 6.5: UPt_3 NMR signal at 515 kHz alongside the ^{3}He marker NMR signals. The three ^{3}He peaks are from the UPt_3 resonance, high and low field backgrounds.

shows that the three ^{3}He marker signals from the resonance and two background traces can also be seen in the NMR spectrum, excited only by the UPt_3 515 kHz tipping pulse. This was an unexpected extra as for the central ^{3}He resonance peak at ∼1.867 MHz, only 0.45 % of the power from the 515 kHz tipping pulse is exciting the ^{3}He spins. The observed ^{3}He magnetisation is partially saturated as the T_1 relaxation time for ^{3}He is on the order of tens of seconds at 600 mK [134], much longer than the repetition time of the pulse sequence. Nevertheless, the ^{3}He peak is strong enough to enable the determination of the local field at the sample through measurement of its resonance frequency and Equation 2.1: $\omega_0 = \gamma B_0$. Knowing the exact field, the gyromagnetic ratio of UPt_3 can be calculated by measuring the resonance frequency of its NMR signal and the Knight shift follows from Equation 4.2 in Section 4.1.1.

6.2.3 Stability of the Knight shift

The Fourier transforms in Figure 6.6 are five consecutive measurements of the NMR line. The background traces were taken at the same time as the first resonance trace, then an additional four resonance traces were taken consecutively over a period of 32 hours and analysed using the same backgrounds. Over the course of two weeks, the signal in the normal state was repeatedly measured. The signal processing and fitting were performed using the Python script described in Section 5.7.1 for both the UPt_3 line and ^{3}He resonance line. The measured resonance frequencies were then used to determine the Knight shift using Equation 4.2. As apparent from the figure, the signal to noise ratio was poor. The linewidth of the signal was much broader than expected, with $T_2^* \sim 67$ µs in comparison with Körber, who measured $T_2^* \sim 100$ µs at 750 kHz. This is discussed further in Section 6.4 where comparative signal to noise calculations are performed. This poor SNR could be caused by many factors but the end result was that the measured Knight shift had a lot of scatter with an average value of -1.60 % with a standard deviation of 0.10 %. This value of the Knight shift is in agreement with that measured by other groups (see Section 4.6) although a little lower than that measured by Tou *et al.* [106] of -1.9 % for this crystal orientation at a static field of 191 mT.

When detecting a possibly very small change in the Knight shift of the order of the standard deviation, this sort of scatter was not satisfactory.

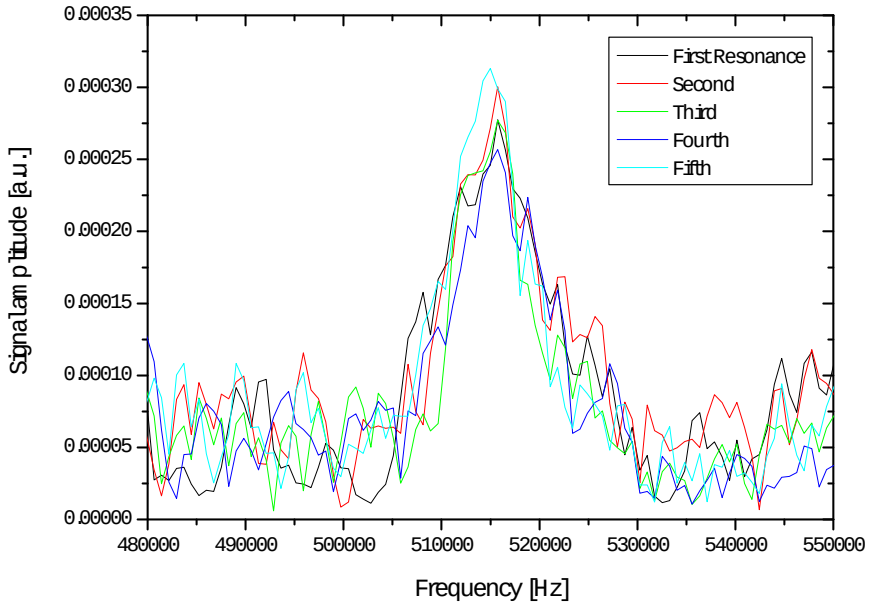

Figure 6.6: Several consecutive UPt_3 NMR signals at a resonance frequency of 515 kHz. All signals have the same two backgrounds; the resonance trace was captured repeatedly over the course of 36 hours. 10 000 averages were taken.

6.2.4 Magneto acoustic measurements

As we saw in Figure 6.4, the background resonances are many times the size of the NMR line. The quality of the NMR signal is dependent on how well the backgrounds can be subtracted from the signal. It therefore makes sense to try to minimise the initial amplitude of the background noise and lower the amplitude of the magneto acoustics by choosing a quiet working frequency. Previous work on lowering the magneto acoustics for this spectrometer was summarised on p. 174. This frequency dependence was mapped out in a constant magnetic field of 59.8 mT and is shown in Figure 6.7. When scaled to the equivalent field and transmitter current, the ringing amplitudes are very similar to that measured by Körber up to 360 kHz (the maximum frequency measured) [2]. To obtain these traces, a 50 µs tipping pulse of 1.5 A_{pp} amplitude was applied to the sample. The resulting response was picked up by the SQUID from 50 µs after the pulse and averaged

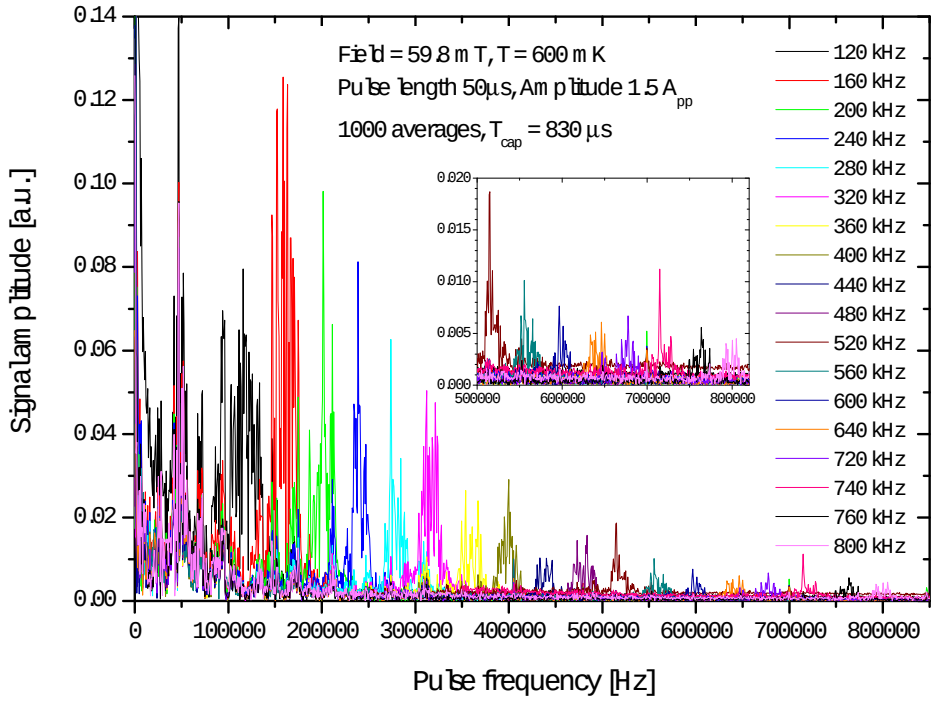

Figure 6.7: Measurements of magneto acoustics in response to different tipping pulse frequencies.

1000 times to reduce the white noise level. The frequency was varied from 120 to 800 kHz. It can be seen that there are a few quiet regions in the frequency domain; the magneto acoustics at 640 kHz seemed particularly low and so was chosen as a working frequency. Figure 6.8 shows the reduced magneto acoustic background at 640 kHz and the improvement in background subtraction compared to Figure 6.4 at 515 kHz.

To verify that this frequency was an improvement on 515 kHz, several measurements were taken in the normal state at 640 kHz with the same conditions as for the data in Figure 6.6. The number of averages was also increased to 20 000 for each resonance trace to further increase the SNR. Figure 6.9 shows three traces taken consecutively. These measurements were repeated over the course of two weeks and a Knight shift of -1.63 % with a standard deviation of 0.07 % was measured. The results of this investigation lead to the choice of 640 kHz as a working frequency for the Knight shift vs. temperature measurements into the superconducting state.

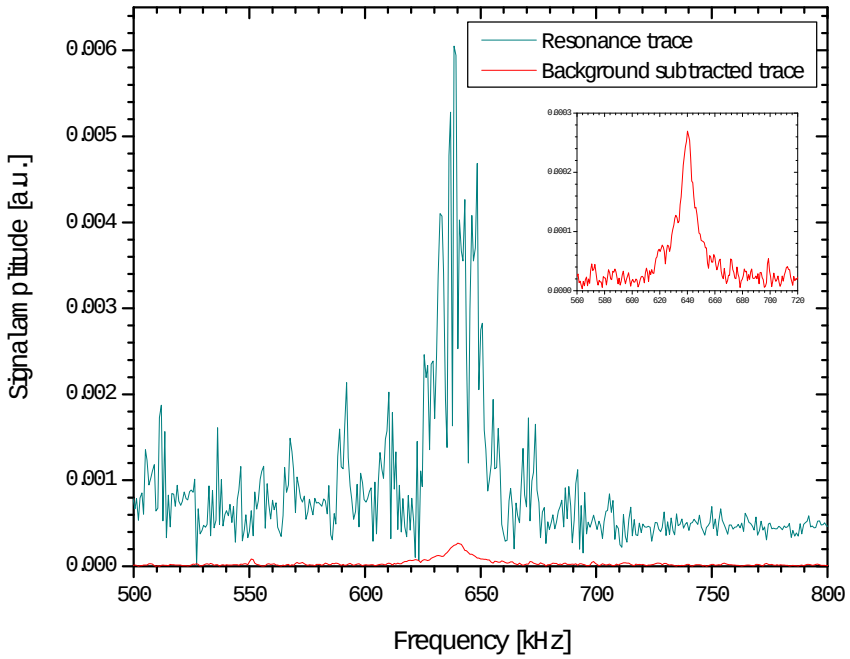

Figure 6.8: Background subtracted UPt_3 signal at 640 kHz with the Fourier transform of the resonance trace, showing the magneto acoustic resonances. The inset is a close-up of the UPt_3 signal. 20 000 averages on resonance.

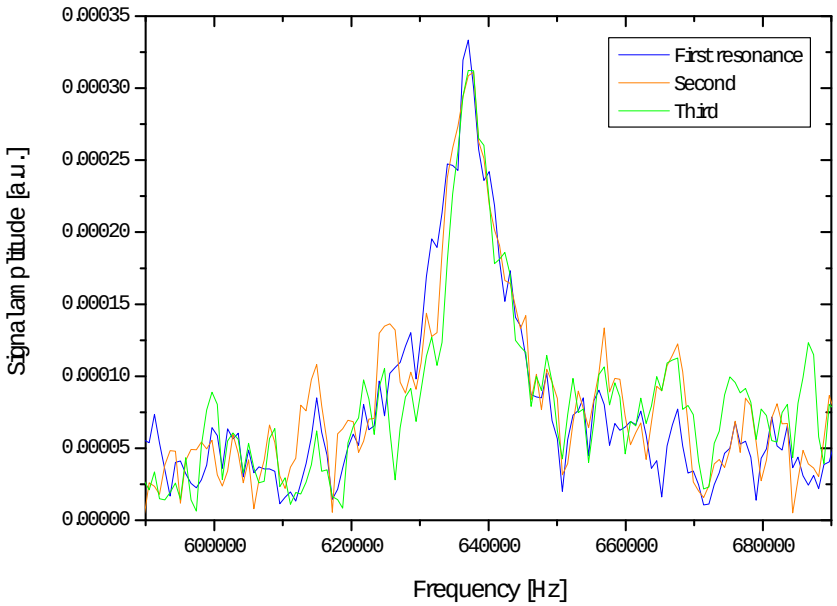

Figure 6.9: Three consecutive UPt_3 NMR signals at a resonance frequency of 640 kHz. All signals have the same two backgrounds; the resonance trace was captured repeatedly over the course of 26 hours. 20 000 averages were taken.

The accuracy of the Knight shift measurement was improved further before the results of the following section were obtained. In particular, it was noticed that the 24 pin Lemo connector on the aluminium SQUID box at the top of the cryostat (for connecting the Magnicon SQUID electronics box) was coming loose. As this Al box formed a vacuum with the IVC, it could not be opened and the connector tightened without stopping circulation of the fridge. If the SQUID electronics were not securely plugged into the Lemo connector, an increase in the white noise floor of a factor of 10 would be seen in the Fourier transform, due to the break in the rf shielding. In fact, for both the room temperature and minifridge experiments, the SQUID noise level could be reduced by wrapping the plastic SQUID electronics box in aluminium foil. Cable ties were also used to secure the electronics box in the connector but during the following warm up of the fridge, the Lemo connector was tightened.

The homebuilt pulse programmer (PIC) and Agilent function generator described in Section 5.2 were replaced with a single PXI module (NI PXI-5412 [47]) with a LabVIEW program written by Lev Levitin that carried out both tasks. This was a significant modification as the PIC was found to be a source of an anomalous 31 kHz noise that would interfere with the time trace during data capture. The Pickering 12 bit PXI card was also upgraded to a 14 bit card (NI PXI-5122 [47]). However, as the minimum input range of the card was 200 mV_{pp} compared to 50 mV_{pp} for the Pickering card, there was no improvement in the vertical resolution.

With these improvements, the Knight shift of UPt_3 in the normal state at 640 kHz was remeasured with a value of -1.64 % and standard deviation 0.05 %. An example of an NMR signal with the improved signal to noise is shown in Figure 6.10. The expected signal to noise ratio was calculated for the above signal to be 11.6 and agrees well with experiment. Full calculations are given in Section 6.4.

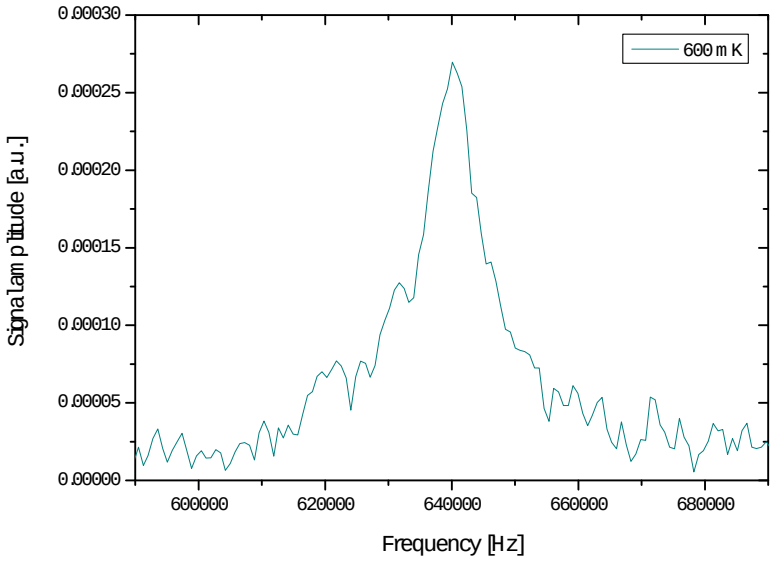

Figure 6.10: UPt_3 in the normal state taken after various improvements in the setup were made. 20 000 averages were taken. Data captured 70 µs after middle of pulse.

6.3 UPt_3 into the superconducting state

NMR signals from UPt_3 were measured as a function of temperature into the superconducting state at a frequency of 640 kHz only ($B_0 \sim 71.5$ mT). Measurements were also attempted at a lower frequency of 200 kHz but due to the higher magneto acoustics (Figure 6.7) and subsequent poor background subtraction, it was not possible to obtain reliable Knight shift measurements at this frequency. This would be desirable in order to separate out the field dependence of the diamagnetic shift from the Knight shift as discussed in Section 4.1.4.

6.3.1 Measurement procedure

Here the optimised measurement procedure for acquiring the UPt_3 signals taken in this section is given. The static field was applied at 600 mK, with UPt_3 in the normal state. Unnecessary equipment such as the magnet power supply and amplifier was disconnected from the cryostat so as not to introduce any noise into the sample region that could manifest itself as trapped flux in the inner Nb shield upon cooling, thereby degrading the field homogeneity. The sample was then

allowed to cool to the desired temperature, monitored by a germanium resistor on the mixing chamber, which was stabilised with a PID controller (described in Section 5.1.4). The NMR tipping pulse was then applied, generated by a LabVIEW program written for the NI PXI-5412. The pulse was 50 μs long and 1.5 A_{pp} with a frequency of 640 kHz, giving a tipping angle of 53° and was applied every second. The SQUID was put into FLL 25 μs after the end of the tipping pulse and data was captured 5 μs after FLL by a second PXI card (NI PXI-5122) configured to be an oscilloscope.

The FID was captured at a sampling frequency of 100 MHz for 850 μs, longer than $5T_2^*$ to avoid truncating the decaying signal and distorting the lineshape. The expected T_2^* was $\sim$ 125 μs according to the linewidths obtained by Körber [2]. Data was captured for the high (low) field background with 10 000 averages. The field was then changed to the resonance field while maintaining the temperature constant and 20 000 averages were taken on resonance. Finally, the field was changed for the low (high) field background trace and 10 000 averages taken.

It was found that there was no dependence of the Knight shift on how the field was applied for the small field changes needed to take the backgrounds, i.e. whether the sample was warmed up to the normal state for each small change of the measurement field or whether the measurement field was changed while in the superconducting mixed state, for each of the background and resonance traces. Naturally, to save time, the field-cooled method was only used for the initial application of the background field.

The captured transient shape was also found to be temperature dependent (Figure 6.11), so a set of backgrounds had to be taken for each temperature. Resonance and background traces were always captured within a transfer window as a helium transfer in between traces was found to destroy the background subtraction procedure. A possible reason for this could be that the vibrations of the fridge are dependent on the helium level in the Dewar. Thus, the magneto acoustics may have different characteristic frequencies after a transfer that cannot now be subtracted away. For best reliability, the resonance and background traces were taken as close together in time as possible.

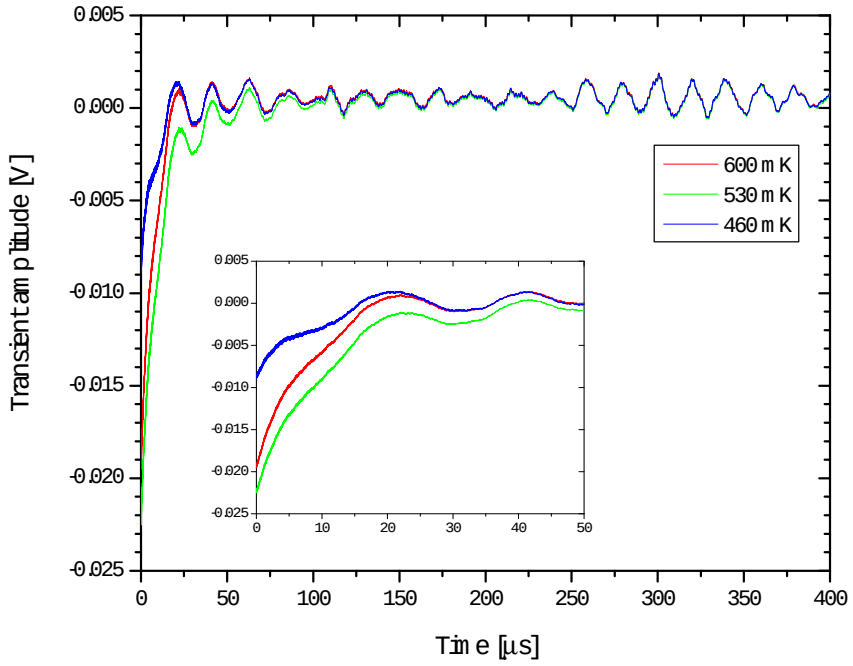

Figure 6.11: Captured raw resonance time traces for different sample temperatures. 20 000 averages, before signal processing.

The signal processing and analysis of the traces are carried out using the Python script as described in Section 5.7.1. Here, background subtraction procedures are implemented and after a further truncation of 15 µs from the start of the trace, a T_2^* filter is applied (see Section 5.4.3 for an explanation) with a filtering time constant of $T_{fil} = 300$ µs. The magnitude of the resulting Fourier transform is shown in the upper half of Figure 6.12 for a selection of temperatures ranging from 600 to 400 mK in a field of 71.5 mT. The frequency axis has been shifted to coincide with the 600 mK dataset, to take into account the slight changes in measurement fields ($\sim$ 200 µT), equivalent to 1.8 kHz between the traces. This serves to show the increase in resonance frequency with decreasing temperature more clearly. The corresponding shifted ^{3}He marker signals are shown in the lower half of Figure 6.12, showing that the UPt_3 traces have been aligned correctly. The following sections analyse these NMR signals in detail.

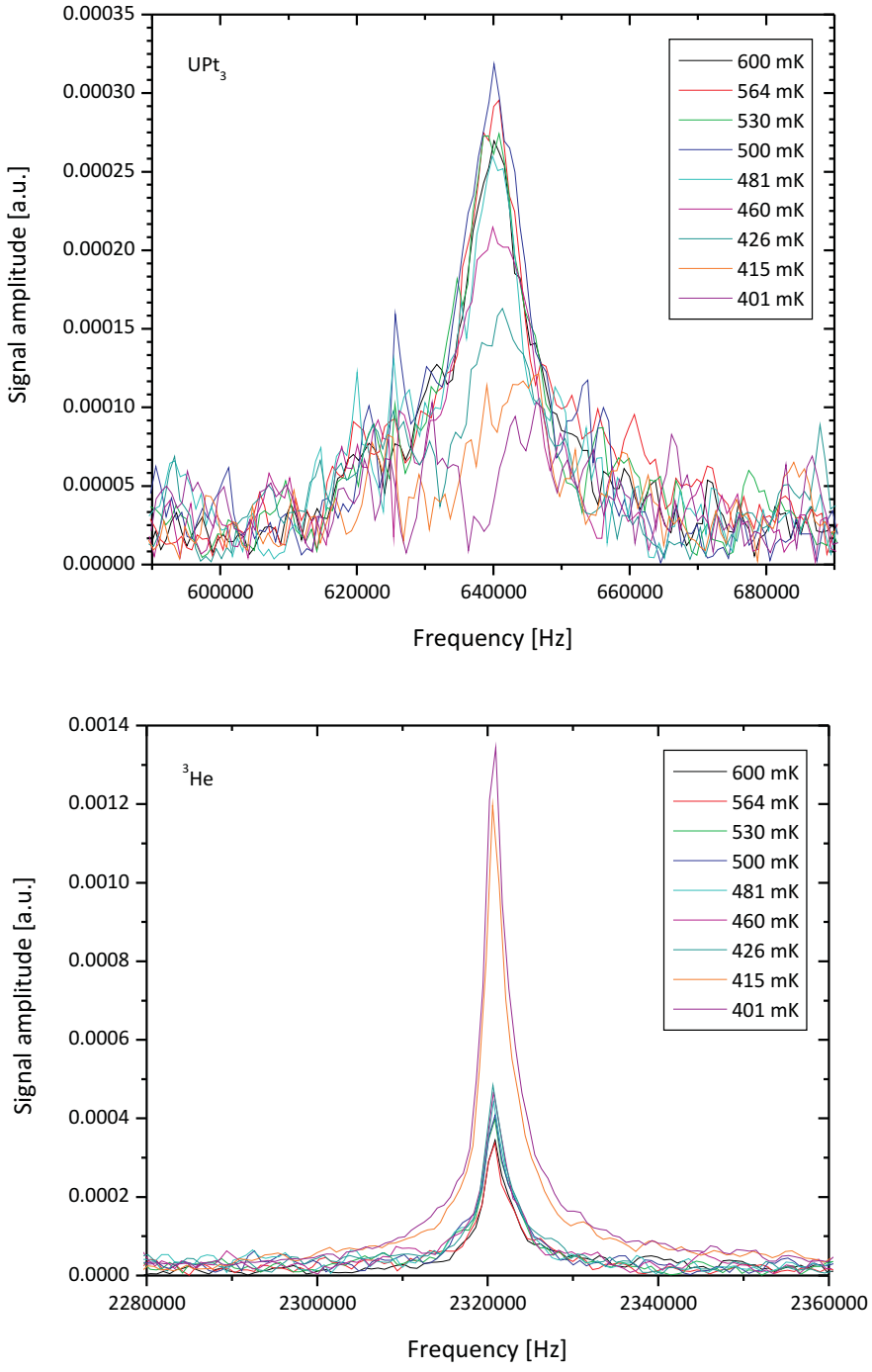

Figure 6.12: Upper figure: NMR signals from UPt_3 with $B \parallel c$ into the superconducting state. 640 kHz pulse, 50 µs long, 20 000 averages in a field of 71.5 mT. Lower figure: ^{3}He marker signals from the same traces, showing the equivalence of the measurement field.

6.3.2 Temperature dependence of T_2^*

The measured spin-spin relaxation time T_2^* is affected by the local field distribution of the nuclear spins. In a type II superconductor such as UPt_3, the formation of the Abrikosov vortex lattice in the superconducting state above the lower critical field B_{c1} creates a magnetic field distribution within the sample. This causes the homogeneity of the local field to worsen and as a consequence, the NMR relaxation is faster and the linewidth is broadened. This effect was discussed in Section 4.1.5. Although the static fields are much lower than used in previous work, they are still much larger than B_{c1}, which is below ~ 8 mT (see Section 4.5.5), thus we expect the formation of a vortex lattice in the superconducting state.

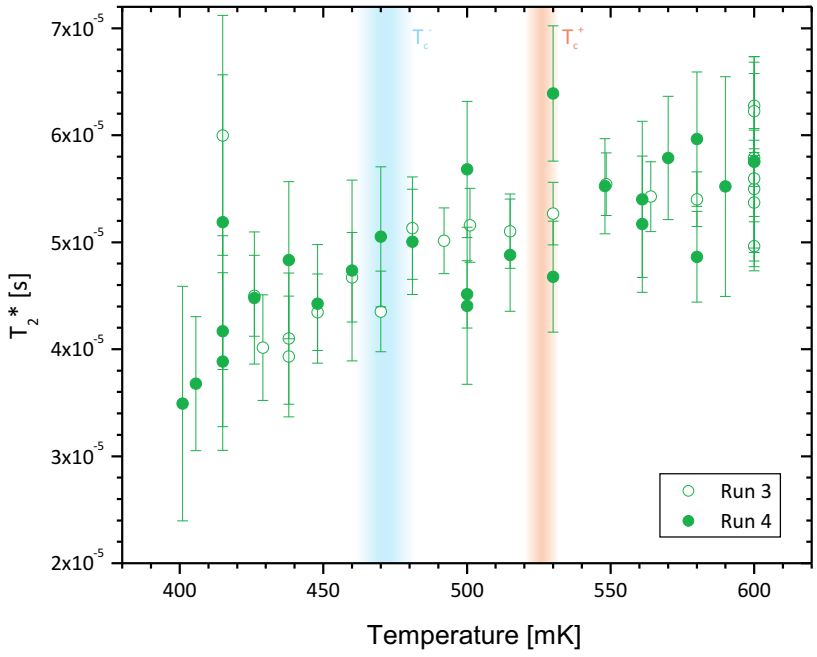

Figure 6.13: Temperature dependence of T_2^* in a field of 71.5 mT. T_c^+ and T_c^- as inferred from the mutual inductance measurement are shown.

Figure 6.13 shows the measured spin-spin relaxation times of the UPt_3 NMR signals as a function of temperature in a field of 71.5 mT. The upper transition temperature T_c^+ in the figure has been obtained by approximating to first order, a linear relationship between T_c^+ and field, using the mutual inductance measure-

ments in Section 6.1.3 for zero field and 84.6 mT. The lower transition temperature T_c^- was then approximated to lie 55 mK lower, giving $T_c^+(71.5\text{ mT}) \simeq 526$ mK and $T_c^-(71.5\text{ mT}) \simeq 471$ mK. The width of these lines reflect the uncertainty in the critical temperatures. From the data, we can infer an average $T_{2\,\mathrm{N}}^* = (55.7 \pm 3.7)$ μs in the normal state. This corresponds to a linewidth of 5.7 kHz in the frequency domain. This is much lower than the typical linewidth of 50 kHz measured at 4.94 K by Lee *et al.* in a field of 1.25 T (B $\perp$ *c*) [56]. This narrowing in linewidth can be attributed to the improvement in the relative homogeneity of the magnet as the measurement field is decreased, as discussed in the room temperature experiment in Section 3.5.5. However, it is comparable to the 5.3 kHz linewidth obtained by Tou in a field of $\sim$ 180 mT with the field along the basal plane [62], which should be a factor of about 2 broader than that measured with the field along the *c*-axis. Also, the linewidths obtained by Körber with the field along the *c*-axis for a different single crystal wafer were much lower at 2.6 kHz in a field of 85 mT [2]. The reason for the broad linewidth for the sample used in this thesis is uncertain; it is unlikely to be due to the experimental setup as this has not changed significantly. It may be due to surface defects as NMR is a surface sensitive probe. Nevertheless, the linewidth was accepted as measured.

The data seem to show a gentle decrease of T_2^* below T_c^+ and continuing below T_c^- although it is difficult to say whether there is a change in slope at T_c^-. At the lowest temperatures, there is an increased scatter that is likely due to the small signal size and low SNR. To see if this decrease in T_2^* is due to the formation of the Abrikosov lattice, we can calculate the relaxation due to the vortex lattice in the following way. The linewidth associated with the vortex lattice given in Section 4.1.5, δB is estimated by

$$\delta B \approx \frac{\Phi_0}{\lambda^2\sqrt{16\pi^3}}, \tag{6.7}$$

where Φ_0 is the flux quantum and λ is the London penetration depth. For $B \parallel c$, we take the penetration depth in the basal plane $\lambda_\perp = 6600$ Å [73, 74] and obtain

$\delta B = 213$ μT. The relaxation time associated with the vortex lattice is given by

$$T_{2\,\mathrm{VL}}^{*} = \frac{2}{\gamma \delta B}. \tag{6.8}$$

If we take the Knight shift as measured in the superconducting state at 400 mK as -1.35 % (see later section), then $\gamma = 5.637 \times 10^7$ Hz/T and $T_{2\,\mathrm{VL}}^{*} = 166$ μs. This gives a contribution to the measured linewidth in the superconducting mixed state of the form

$$\frac{1}{T_{2\,\mathrm{SC}}^{*}} = \frac{1}{T_{2\,\mathrm{N}}^{*}} + \frac{1}{T_{2\,\mathrm{VL}}^{*}}. \tag{6.9}$$

We obtain from this, $T_{2\,\mathrm{SC}}^{*} \simeq 42$ μs in the superconducting mixed state, which is in very good agreement with the measured values at the lowest temperatures of Figure 6.13. Thus we can conclude that the broadening of the UPt_3 NMR line to lower temperatures can be accounted for by the formation of the Abrikosov vortex lattice in the superconducting mixed state.

6.3.3 Temperature dependence of the signal size

The lower dataset of Figure 6.14 shows the temperature dependence of the measured signal size A in the time domain, obtained from the Python fit to the real and imaginary parts of the Fourier transform of the FID given by Equation 2.20. As can be seen from the figure, it was found that the signal size decreased with decreasing temperature into the superconducting state. This determined a lower temperature limit of 400 mK, below which it was not possible to detect the NMR signal from UPt_3 above the noise. This decrease in signal size could be due to a combination of two factors - the first being a decrease in the initial magnetisation of the sample, which was found to be the case for previous measurements on different single crystals on this dilution fridge [2]. This was attributed to a reduction in penetration of the rf pulse into the sample due to the impurity of the sample as discussed in Section 4.6.3. The second factor is due to the broadening of the NMR line through formation of the Abrikosov vortex lattice when in the superconducting mixed state, as evident from the decrease in T_2^* seen in the previous section. In order to determine the relative contributions of these two factors, it is necessary to

compare the height of the FID extrapolated back to the middle of the rf pulse, H_0. This takes into account the different T_2^* relaxation times for each signal and so is a measure of the initial magnetisation. The upper dataset of Figure 6.14 shows H_0 as a function of temperature. It is apparent that H_0 assumes a steady value down to the lowest temperatures, within the uncertainty of the measurement. From this, we can conclude that the decrease in signal size down into the superconducting state is due to the linewidth broadening from the formation of the vortex lattice as the initial magnetisation of the sample is $\sim$ constant with temperature.

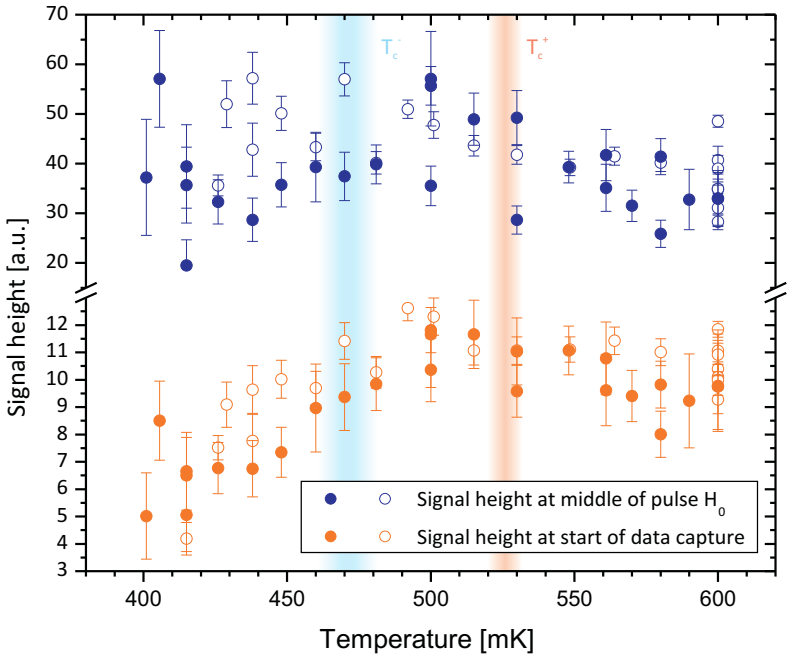

Figure 6.14: Temperature dependence of the measured signal size in the time domain (orange), and extrapolated to the middle of the tipping pulse (blue) in a field of 71.5 mT. T_c^+ and T_c^- as inferred from the mutual inductance measurement are shown.

The thermal equilibrium magnetisation is expected to grow at lower temperatures according to the Curie law: $M \propto 1/T$. However, this effect was difficult to observe in Figure 6.14 due to the uncertainty in the data. An attempt was made to try to observe an NMR signal close to the base temperature of the fridge at 30 mK but no signal could be seen.

6.3.4 Temperature dependence of the Knight shift

Finally, we are in a position to interpret the Knight shift measurements that were the aim of this part of the thesis. Figure 6.15 shows the temperature dependence of the Knight shift, K for $B \parallel c$ in a static field of 71.5 mT. Note that the y-axis has been reversed (as is the convention), to show the Knight shift approaching zero in a clearer way. The Knight shift was determined by fitting to both the UPt_3 and ^{3}He NMR lines with the Python fitting routine (see Section 5.7.1 for a description) to determine the resonance frequency for each signal. Equation 2.1 was used to calculate the local field using the known gyromagnetic ratio of ^{3}He and its measured resonance frequency. Equation 4.2 was then used to determine the Knight shift. Data from runs 3 and 4 of the fridge are shown. The fridge had

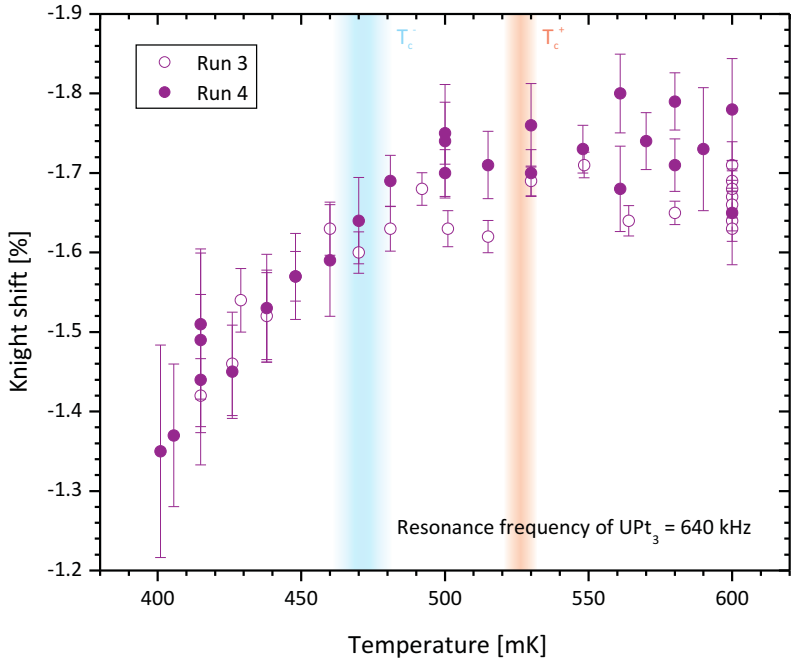

Figure 6.15: Temperature dependence of the Knight shift for $B \parallel c$ in a field of 71.5 mT. T_c^+ and T_c^- as inferred from the mutual inductance measurement are shown. The diamagnetic contribution is not included.

to be warmed up in between these runs as the IVC had developed a leak at the solder joint of its pumping line as well as at the indium seal, that prevented the fridge from remaining cold for extended periods of time. The IVC was opened and

the indium was replaced, the pumping line solder joint was re-run until leak-tight and the fridge was restarted, with no further changes made to the experimental setup. From the plot, it seems that the spread in the data for the normal state was smaller in run 3; the reason for this is not clear as there were no known differences between the two runs.

The local field at the sample for each case was measured by the ^{3}He marker and so any change in the field trapped upon cooldown would be taken into account in calculating the Knight shift. Thus, the trend for both runs is a definite reduction of K as UPt_3 enters the superconducting state. We cannot comment on the Knight shift in the A phase and the B phase independently as there are not a statistically significant number of points in the A phase. If we take the value of the Knight shift in the normal state as the average for both runs above $T = 540$ mK, we obtain $K_N = (-1.70 \pm 0.05)$ %. This value is comfortably in the same region as that measured by previous authors: -1.8 % (Lee), -1.4 % (Kohori) and -1.9 % (Tou) for fields along the c-axis.

Diamagnetic correction

As we have shown in the previous sections, we have seen evidence of the formation of a vortex lattice in the superconducting state in fields of 71.5 mT. This will generate a diamagnetic contribution to the Knight shift as described in Section 4.1.4. Recall Figure 4.3 which gives the estimated temperature dependence of this diamagnetic correction. This is a negative shift, meaning a decrease in the resonance frequency from the Larmor frequency, so it will only accentuate the drop in the Knight shift if this is taken into account. Figure 6.16 shows the Knight shift data before and after the diamagnetic correction to illustrate this. However, to find the true field dependence of the diamagnetic contribution, it would be necessary to take Knight shift measurements in different static fields.

As it has not been possible with the current sample to measure the Knight shift deeper into the superconducting state for temperatures approaching 0 K, one can only extrapolate with uncertainty whether the Knight shift approaches the orbital shift for lower temperatures. However, if we take $K^{dia}(410 \text{ mK}) = -1.75$ % from

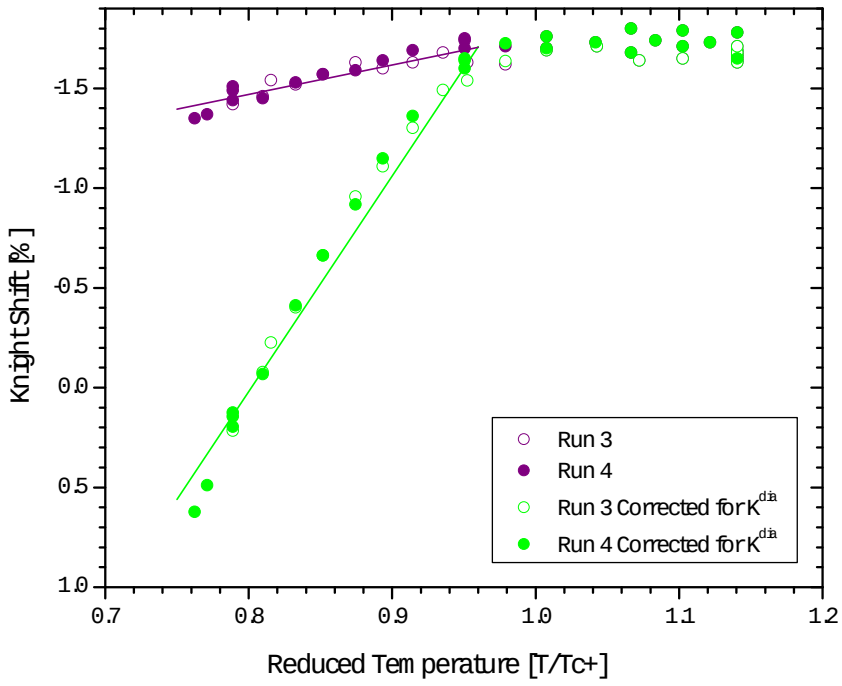

Figure 6.16: Temperature dependence of the Knight shift for $B \parallel c$ in a field of 71.5 mT with and without the diamagnetic correction. The fit below T_c is a linear approximation valid for $T \sim T_c$.

the temperature dependence estimated in Section 4.1.4 and the average Knight shift at ~ 410 mK to be (-1.43 ± 0.06) %, then taking into account the diamagnetic contribution, the actual Knight shift at 410 mK is $K_{SC} \simeq 0.32$ %. Thus we see a drop in the Knight shift of magnitude $\delta K \simeq 2.02$ % down to 0.75 T/T_c. This is in contrast with the measurements of Tou *et al.* [106] who measured a fractional change of $\delta K \simeq 0.08$ % down to 25 mK for $B \parallel c$. Even when taking into account their small diamagnetic contribution of $K^{dia} \sim -0.08$ %, this leaves a fractional change of only $\delta K \simeq 0.16$ %.

In the 1998 paper [106], Tou used the same expression as in this work (Equation 4.8) to calculate the diamagnetic field. However, he uses a constant lower critical field of 1 mT. This value is subjective as the transition temperatures and other properties vary from crystal to crystal and so only an estimate of B_{c1} can be obtained from results such as Figure 4.10. With this taken into account, Tou's diamagnetic treatment of the a-axis measurement is reasonable although no explicit temperature dependence of the diamagnetic correction was taken into considera-

tion. Similarly, as many estimations for various parameters are required, although his treatment for the diamagnetic correction was inconsistent for his two publications [62, 106], the same result can be obtained with just a slight alteration of an estimated parameter.

Discussion of the Körber experiment in light of this work

Figure 6.17 shows the results from the previous UPt_3 Knight shift experiment on this dilution fridge, performed by Körber [2] along with the Knight shift measurements taken in this thesis. It would be beneficial to be able to conduct a quantitative comparison between these data. In order to do this, the temperature axis is normalised to a reduced temperature, T/T_c^+ to take into account the differences in transition temperatures. The diamagnetic correction has not been included for both sets of data.

Due to the 30° misalignment of the c-axis with respect to the static field, the normal state Knight shift is larger at -3.33 % compared with -1.70 % for $B \parallel c$. A change in the Knight shift of $\delta K \sim 0.21$ % is observed in the Körber experiment, from the normal state to 0.75 T/T_{onset}. For the measurements in this thesis, the change in the Knight shift is $\delta K \sim 0.27$ % down to 0.75 T/T_c^+. From this information, it may be possible to say that this difference can be explained simply by resolving angles. If we make the hypothesis that there is no change in the Knight shift for orientations $B \perp c$ (as is the case for the E_{2u} scenario), then the change in Knight shift that was measured by Körber would be approximately $\cos 30$ of what is measured for $B \parallel c$ i.e. ~ 0.23 %. Within the uncertainty of the measurements, this is possible but difficult to conclude with precision, as the temperature range of the measurements was limited. Also, as evidence for the formation of the Abrikosov lattice was observed in one crystal but not the other, it is difficult to know whether the treatment for the diamagnetic correction is consistent between the two datasets.

Recall from Section 4.4.2 that in the E_{1g} and E_{2u} models, K is expected to reduce to the orbital shift deep into the superconducting state for $B \parallel c$. The revised Spin triplet model also predicts a decrease in the Knight shift for $B \parallel c, b$

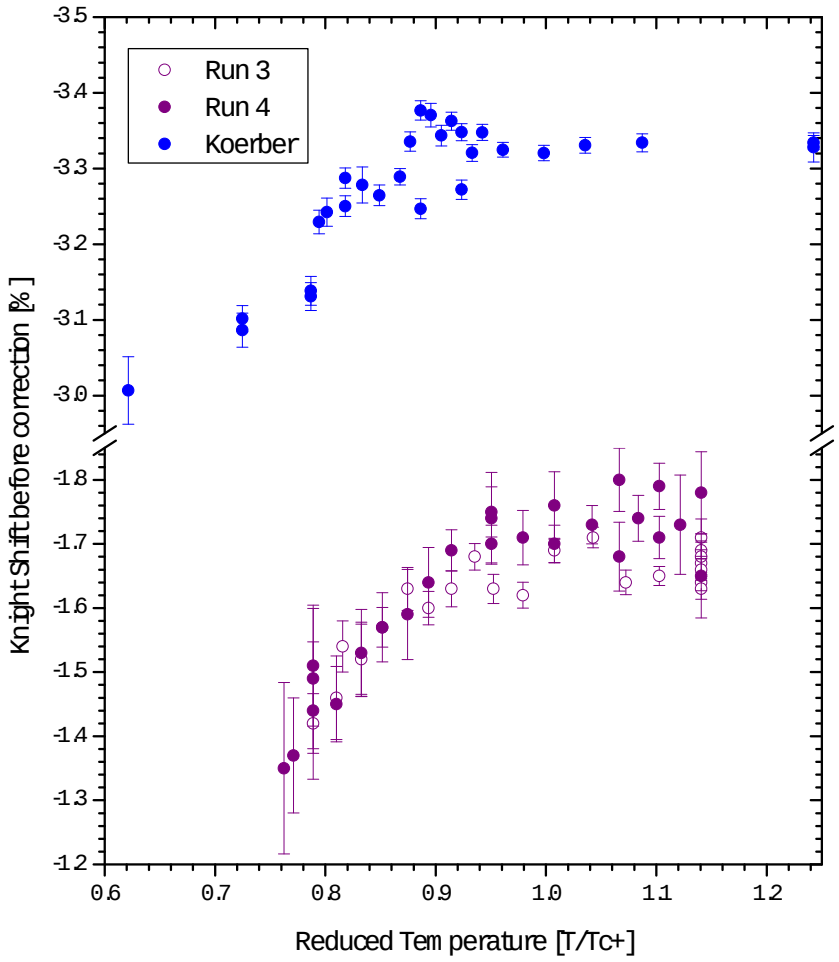

Figure 6.17: Comparison of previous Knight shift measurements (Körber) with those of this work. Körber's crystal was aligned at 30° to the c-axis and the static field was 85.3 mT. In this work, the field was 71.5 mT and $B \parallel c$. No diamagnetic correction has been applied.

at low fields but a constant K for $B \parallel a$. This experiment alone therefore remains consistent with all three theories and so cannot discriminate between them. However, with the results of this Knight shift experiment together with the previous experiment by Körber [2], it may be possible to draw the conclusion that a drop in the Knight shift is seen for fields parallel to the c-axis into the superconducting state, but not for fields perpendicular to the c-axis. This conclusion, if it were the case, would be supportive of the E_{2u} theory.

The following section now continues this analysis by looking at the signal to noise ratios for the two experiments with a view to improving future experiments

on measuring the Knight shift of UPt_3.

6.4 SNR calculations

In this final section, a comparison is made between the SNR in this experiment and the previous experiment by Körber, in order to determine whether further measurements on this dilution fridge to measure the Knight shift of UPt_3 will be more successful. The most notable improvement that has been made in the current setup to increase the SNR is the upgrade of the SQUID to a two-stage sensor, which is also operated at a lower temperature. This modification led to a decrease in the white noise level at the frequencies of interest by an order of magnitude. However, due to the misalignment of the crystal used in the previous experiment, a new crystal is used here that unfortunately has smaller dimensions. Despite this, the calculations below show that there should be an increase in the SNR by ∼7.5 with the new setup at a resonance frequency of 640 kHz. In reality, the NMR signals from the current crystal had linewidths that were twice as wide as for the previous wafer sample, leading to only a ∼ 50% increase in the SNR.

6.4.1 Expected signal size in the normal state

In the signal size calculations in his PhD thesis [2], Körber calculated the signal size for an effective volume where due to the skin effect, only spins from within half the skin depth of the surface contributed to the signal. This was shown to be a valid approximation in previous NMR experiments on metals [26]. However, it was found that the actual signal size was approximately a factor of 5.7 smaller than this, which was attributed to the loss of signal from the planes of the wafer, due to the geometry of the sample within the NMR coilset. The ratio of the volume in the planes to that in the edges is ∼4.8, supporting this hypothesis. As the sample used in this thesis has the same geometrical alignment as the previous wafer, I will calculate the expected signal size in the frequency domain using an effective volume which only includes spins within half the skin depth around the edge of the crystal and not those in the planes perpendicular to the receiver coil.

The following calculation is performed using the conditions for a known signal measured at 640 kHz from the current UPt_3 crystal in the normal state at 600 mK. (Figure 6.10 shows the signal magnitude in the frequency domain.)

The effective volume

In order to estimate the effective volume, we must know the resistivity of the sample to calculate the skin depth δ. To first approximation, the resistivity of the UPt_3 sample is calculated using the same coefficients assumed by Körber. These are $\rho_0 = 0.4$ μΩcm and A= 1.55 μΩcm/K^2 for currents parallel to the a-axis, as we are interested in δ_a. These give a resistivity of $\rho_a = 9.58 \times 10^{-9}$ Ωm.

The skin depth is the characteristic length scale over which an RF field penetrates a metallic substance. It is given by

$$\delta = \sqrt{\frac{2\rho}{\omega\mu_0}}, \tag{6.10}$$

where $\omega = 2\pi f$ where f is the frequency of the field and $\mu_0 = 4\pi \times 10^{-7}$ Tm/A. At 640 kHz, this gives a skin depth of $\delta_a = 61.6$ μm.

The orientation of the sample in the NMR coilset is shown in Figure 6.18, along with a schematic of the effective volume. The crystal shape is approximated by a cuboid of size $l = 5.2$ mm, $w = 2.3$ mm, $h = 0.2$ mm, with volume $V = 2.39 \times 10^{-9}$ m^3. The dead volume that does not contribute to the signal is $V_{dead} =$

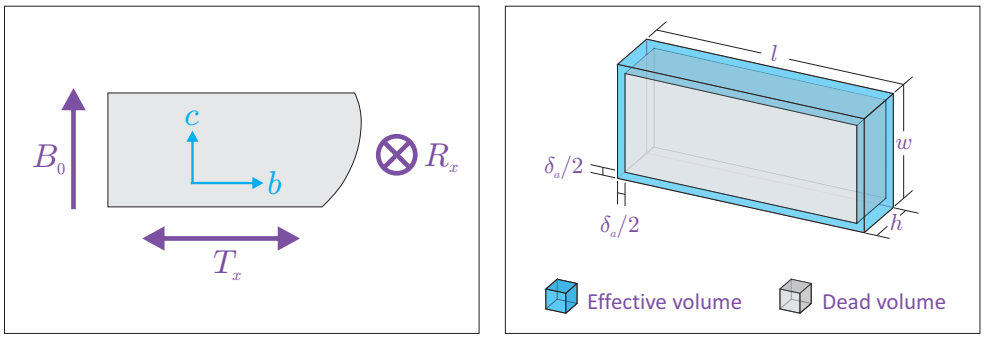

Figure 6.18: Left: Orientation of UPt_3 crystal in the NMR coilset. Right: Schematic showing the effective volume that contains the excited spins (not to scale).

$(l - \delta_a)(w - \delta_a)h = 2.30 \times 10^{-9}$ m^3. This leaves an effective volume of $V_{eff} = V - V_{dead} = 9.16 \times 10^{-11}$ m^3 which contains 1.32×10^{18} spins.

Signal size in the frequency domain

To calculate the signal size in the frequency domain, we need to know the flux coupled into the SQUID from the precessing spins in the sample. Firstly, the magnetisation of a spin $\frac{1}{2}$ nucleus is given by

$$M_0 = \frac{N_v \hbar^2 \gamma}{4 k_B T} \omega_0, \tag{6.11}$$

where $N_v = 1.444 \times 10^{28}$ m^{-3} is the spin density in UPt_3, $\hbar = 1.055 \times 10^{-34}$ Js, γ is the gyromagnetic ratio of UPt_3, $\omega_0 = 2\pi f_0$ where f_0 is the resonance frequency and $k_b = 1.381 \times 10^{-23}$ J/K. The measured Knight shift for this signal was -1.64 %, giving $\gamma_{\mathrm{UPt_3}} = 5.620 \times 10^7 \frac{1}{sT}$ (reference earlier equation). At $T = 600$ mK and $f_0 = 640$ kHz, we obtain

$$M_0 = 1.096 \times 10^{-9} \text{ A/m}.$$

Using the reciprocity theorem (see Section 3.5.4), we can determine the flux linkage in the receiver coil (pickup coil). It follows that the flux in the pickup coil is given by

$$\Phi_p = B_{1p} M_0 V_{eff}. \tag{6.12}$$

The magnetic field at the centre of the pickup coil per unit current is calculated using Equation 3.1 for a saddle coil to be $B_{1p} = 1.47$ mA/T. Using this,

$$\Phi_p = 1.48 \times 10^{-16} \text{ Wb} = 71.4 \text{ m}\Phi_0,$$

where Φ_0 is the flux quantum $= 2.0678 \times 10^{-15}$ Wb.

The flux coupled to the SQUID is given by

$$\Phi_{SQ} = \frac{\Phi_p M_i}{(L_i + L_p)}. \tag{6.13}$$

For the two-stage SQUID C506-G24, the mutual inductance between the input coil and the SQUID $M_i = 9$ nH, the SQUID input coil inductance $L_i = 1.8$ μH and the pickup coil inductance $L_p = 2.07$ μH. This gives:

$$\Phi_{SQ} = 166\ \mu\Phi_0.$$

For the FFT routine used by LabVIEW, the expected signal size in the frequency domain is related to the initial voltage in the time domain by

$$H_0 = \frac{\Phi_{SQ} G_{FLL} T_2^*}{2\Delta}. \tag{6.14}$$

Although I am analysing the time transients using the Python FFT routine and the signal sizes I obtain in the Fourier transform are not the same as the LabVIEW FFT, nevertheless they are directly proportional to each other. This justifies the use of the above formula as an aid to comparing signals even if the exact values are out by a constant. In particular, it is useful for estimating the SNR and comparing ratios of signal heights. Using this formula, the gain of the SQUID in flux locked loop mode is $G_{FLL} = 300$ mV/Φ_0. The sampling frequency used was 100 MHz, so the time between points is $\Delta = 10$ ns. The relaxation time T_2^* was measured for the signal in question to be 50 μs. As a T_2^* filter (with $T_{fil} = 300$ μs) was used to enhance the signal which has the effect of broadening the linewidth, the actual $T_2^* = 59$ μs. These values give a height of

$$H_0 = 147\ \text{mV}.$$

However, this signal size is the extrapolated height as if data capture began at the middle of the tipping pulse. Taking into account the exponential T_2^* decay until data is captured, we obtain the following equation:

$$H_{decayed} = H_0 \exp\left(\frac{-\tau_1}{T_2^*}\right), \tag{6.15}$$

where τ_1 is the time from the middle of the tipping pulse to the start of data capture = 70 μs. This gives

$$H_{decayed} = 44.8\ \text{mV}.$$

Finally, taking into account the low input impedance of the PXI card used to capture the signal and the shorter tipping pulse of 53°, the final height in the frequency domain is given by:

$$H_{final} = \frac{1}{2} H_{decayed} \text{ Sin } 53° \tag{6.16}$$

$$H_{final} = 17.9 \text{ mV}.$$

Carrying out analogous calculations for the previous sample at a frequency of 570 kHz, taking into account the different sample and setup conditions, the final signal height in the frequency domain is 71.2 mV. The larger signal size is mainly due to the longer T_2^* of 124 µs obtained but also the larger crystal (approximated as elliptical with axes 5.2 mm and 4.1 mm, thickness 0.46 mm, with $V_{eff} = 2.06 \times 10^{-10}$ m^3 containing 2.97×10^{18} spins). This gives a theoretical ratio of ~ 4.1 for the signal heights for the two samples. Figure 6.19 is a plot of the actual signal magnitude of the two signals in question. From this figure, we can

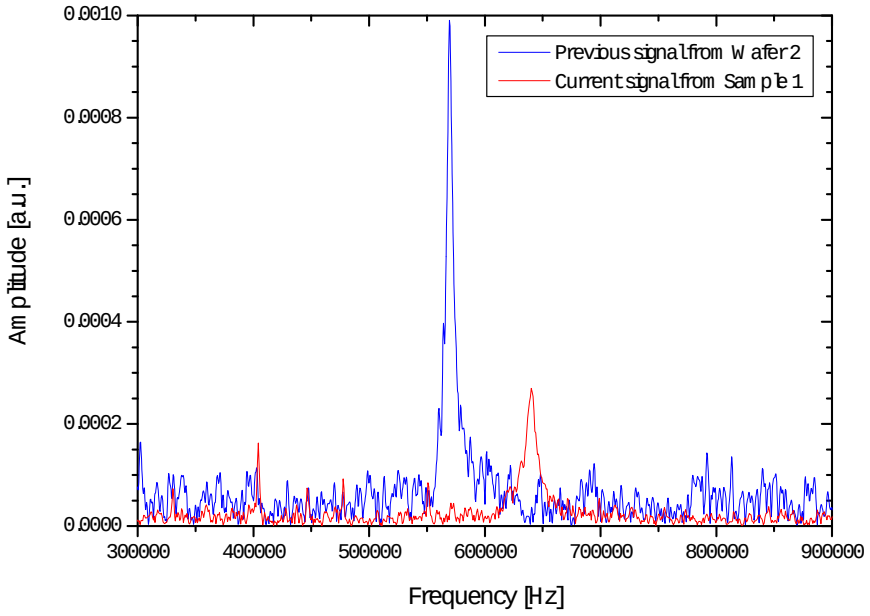

Figure 6.19: Comparison of signal from previous experiment and UPt_3 wafer 2 with the current experimental setup with UPt_3 Sample 1. Both time traces were Fourier transformed using the Python FFT routine.

see that the ratio of signal heights is ~ 3.7, thus we can conclude that the signal sizes make sense i.e. the effective volume being only in the edge of the crystal to within half the skin depth gives a good estimate of the signal height, taking the different experimental setups into consideration.

6.4.2 Expected noise

In this section, the expected noise level in the frequency domain is estimated and the SNR compared with that for the previous experimental setup on the cryostat.

Noise from the current experiment

The peak noise in the frequency domain can be calculated with the following equation:

$$N_p = \frac{K_N^f}{\Delta}\sqrt{\frac{T_{cap}}{2}\langle S_V\rangle}, \tag{6.17}$$

where K_N^f is the ratio between the peak noise in the frequency domain to the RMS value of the noise and is ~ 2.5. T_{cap} is the capture time = 850 μs. S_V is the square of the total RMS voltage noise. At $\sim$ 600 kHz, the SQUID noise was measured with a spectrum analyser to be $\langle\Phi_N\rangle = 195\ \mathrm{n}\Phi_0/\sqrt{\mathrm{Hz}}$. Using the gain of $G_{FLL} = 300\ \mathrm{mV}/\Phi_0$, this gives a peak noise level of $N_p = 302$ mV. Taking into account the averaging of 40,000 signals, this brings down this noise by a factor of $\sqrt{N_{av}} = 200$. The noise level in the frequency domain for the current setup is therefore

$$N_p = 1.51\ \mathrm{mV}.$$

This gives a SNR of 11.9 in the frequency domain. From Figure 6.19, the actual peak signal to peak noise ratio can be estimated and is approximately 10, in good agreement with calculations.

Noise from the previous experiment

Similarly, the peak noise level from the previous experiment can be calculated as the parameters are known. These are $\langle P_N\rangle^{\frac{1}{2}} = 2.24\ \mu\Phi_0/\sqrt{\mathrm{Hz}}$ at $\sim$ 600 kHz,

$G_{FLL} = 440$ mV/Φ_0, $T_{cap} = 301$ µs and $\Delta = 20$ ns. After 40,000 averages, the peak noise level is

$$N_p = 10.7 \text{ mV}.$$

This gives a SNR of 6.7 in the frequency domain. The actual SNR from Figure 6.19 is ~ 9.2, again in reasonable agreement, considering the approximations made in the estimate. A point to keep in mind is that in the above calculations, the subtraction of magneto acoustic resonances has not been taken into consideration. This is obviously an important part of signal processing as the amplitude of the magneto acoustics is many times the noise level. By using background subtraction, these can be reduced to about ~ 2 %, or at least as low as the noise level after 40,000 averages if taken close together in time.

6.4.3 Comparison of setups and crystals

Now that the signal to noise ratios make sense, we are in a position to directly compare the SNR for the two experimental setups. Now we can ask the question, "What if?" Below is a table showing the calculated signal to noise ratios for various scenarios. The Knight shift has been fixed at -1.64 % and the capture time at 850 µs for all scenarios.

Scenario	**Previous setup**	**Present setup**
Sample 1	0.5	12
Sample 1 if $T_2^* = 100$ µs	2	32
Sample 1 if $T_2^* = 124$ µs	3	45
Sample 2	0.9	21
Wafer 2	6	100

Table 6.1: Calculated signal to noise ratios with 40 000 averages for various scenarios, comparing the current setup with the previous setup. Samples 1 and 2 refer to my crystal, Wafer 2 to Körber's misaligned crystal.

It seems clear that with the combination of the present low noise experimental setup and a crystal with a narrower linewidth and/or a larger crystal, we are in an excellent position to measure the Knight shift of UPt_3 deeper into the superconducting state and hopefully with much smaller error bars owing to the better

SNR. As the effective volume contributing to the signal size can be approximated by the perimeter perpendicular to the receiver coil, Sample 2 is seen to give a 75 % larger signal size being twice as thick as Sample 1. If the heat sinking of Sample 2 can be resolved, it seems like a promising sample to measure in the immediate future for fields along the c-axis down to lower temperatures. In order to verify the hypothesis that the Knight shift only decreases for fields parallel to the c-axis, it remains an open assignment for Knight shift measurements to be taken for $B \parallel a, b$. In Chapter 7 I propose dimensions for future crystals in order for the Knight shift measurements to be completed reliably.

Chapter 7

Conclusions

This thesis documents the research performed on NMR of room temperature samples and on the measurement of the Knight shift of single crystal UPt_3. Here we summarise the key findings of both experiments and propose directions for the future.

7.1 Summary of key findings

7.1.1 Room temperature NMR experiment

In the room temperature experiment, a compact dc SQUID NMR spectrometer was developed, which was optimised to measure signals from liquid samples in ultra low magnetic fields in the μT to nT range. The short term aim was to exploit the gain in frequency resolution of NMR lines at low fields to observe NMR spectra. The sensor used was a two-stage dc SQUID (C1c04-G25) which was operated with a broadband input coupling scheme for sensitivity across NMR frequencies up to the SQUID bandwidth. The NMR excitation was also broadband, realised by the application of a dc prepolarising field. The spectrometer was characterised using a water sample, with which an extremely narrow NMR linewidth of 0.16 Hz was observed in a field of 693 nT. Following this, a two component relaxation was observed directly in the FID of an oil-water mixture of 4:1 ratio by mass. This allowed the straightforward determination of the oil/water ratio, showing promise

as a technique for detecting relatively low levels of water contamination in oil samples.

Doubly carbonyl labelled glycine was assessed as a possible sample for measurement using the current spectrometer and SNR calculations showed an increase in signal size was necessary in order to observe the ^{13}C J-spectrum which as of yet has not been observed at low fields. The SNR was improved by a factor of ~ 3.5 by means of a Techron amplifier which increased the amplitude of the prepolarising pulse from 2 mT to 3.9 mT and from noise reduction through heat sinking of diodes in the prepolarising circuit. Various attempts were made to increase the prepolarising pulse further however, due to possible flux trapping in nearby superconducting elements, the application of larger prepolarising pulses was inhibited due to broadening of the NMR line.

7.1.2 UPt_3 Knight shift experiment

For the UPt_3 experiment on the dilution fridge, the aim was to perform measurements of the Knight shift into the superconducting state at low magnetic fields using a dc SQUID sensor. UPt_3 is a much studied unconventional heavy fermion superconductor and the reliable identification of the spin part of the order parameter through measurement of the Knight shift that agrees with existing experiments has been sought after for many years. The SQUID NMR spectrometer developed in this work has been optimised for measuring metals with fast relaxation times as the deadtime is on the order of μs and the low frequencies mean that more spins are excited. A two-stage SQUID sensor (C506-G24) was mounted onto the cryostat, heat sunk to the still at $\sim$ 700 mK, lowering the white noise level by a factor of ~ 3.4 from the previous experiment [2]. With the implementation of a ^{3}He marker, field calibrations at resonance frequencies away from that of UPt_3 have been possible with improved accuracy, whilst still being able to enjoy the benefits of the 5-layer inner overlapping Nb shield. Data acquisition and analysis methods were improved by introducing a PXI controlled waveform generator to provide the NMR tipping pulse and a new fitting routine which fit to both the real and imaginary parts of the NMR Fourier transform.

Two single crystal UPt_3 wafers were obtained from Andrew Huxley (Edinburgh) of which only one was measured on the dilution fridge (Sample 1) with the magnetic field parallel to the c-axis. The upper transition temperature T_c^+ was measured using mutual inductance to be (546 ± 4) mK in zero field, attesting to the high quality of the sample. Due to the dimensions and orientation of the sample as well as a broader linewidth, a reduced signal size was observed compared to the previous work on this spectrometer [2] by a factor of ~ 3.7. This made it difficult to accurately measure a good quality signal from UPt_3 deep into the superconducting state. Through measurements of the NMR line as a function of temperature, evidence of the formation of an Abrikosov flux lattice was observed in the broadening of the linewidth below the transition temperature. This resulted in the reduction of the signal height with decreasing temperature, such that NMR measurements were only possible down to 400 mK ($0.75\ T/T_c^+$). The Knight shift was measured in the normal state to be (-1.70 ± 0.05) % for $B \parallel c$, in accordance with other authors [56, 61, 106]. The temperature dependence of the diamagnetic correction was calculated, resulting in a significant decrease in the Knight shift below T_c of $\delta K \simeq 2.02$ % down to a temperature of $0.75\ T/T_c^+$. This is in contrast with the results of Tou *et al.* who measure a fractional change of $\delta K \simeq 0.16$ % down to much lower temperatures of 25 mK [106]. A decrease in the Knight shift of $\delta K \simeq 0.21$ % was measured for the previous experiment by Körber [2] down to the same reduced temperature as in this thesis. As a diamagnetic correction was considered unnecessary (due to no evidence of the formation of the Abrikosov lattice), and the crystal orientation resulting in the field being 30° to the c-axis, it is difficult to quantitatively compare his results with that of this thesis.

The results of this thesis alone remain consistent with all three theories (E_{1g}, E_{2u}, spin triplet) as they all predict a decrease of the Knight shift below T_c. However, as the change in the Knight shift was smaller in the previous experiment by Körber [2], it may be possible to draw the conclusion that a drop in the Knight shift is seen for fields parallel to the c-axis into the superconducting state, but not for fields perpendicular to the c-axis, as the δK measured in this thesis is larger. This conclusion, if it were the case, would be supportive of the E_{2u} theory.

7.2 Future prospects

7.2.1 Room temperature NMR experiment

For the room temperature experiment, there is the possibility of finding a material suitable for the superconducting receiver wire that would allow the amplitude of the prepolarising pulse to be increased further, increasing the SNR. For a longer term experiment, a magnetically shielded room has been purchased from Amuneal, which may be a solution that provides adequate shielding of environmental field gradients for low field measurements on larger room temperature samples outside of the cryostat. With this new design, the sample could be out of the cryogenic environment altogether, and be held against the base of the Dewar. The need for an inner overlapping shield would be eliminated, and is a promising step towards turning the benefits of low field NMR into a practical solution. A low noise Dewar for this purpose has been constructed and is currently being tested.

7.2.2 UPt_3 Knight shift experiment

For the UPt_3 experiment, the best way forward would be to obtain a larger, good quality single crystal in order to be able to perform Knight shift measurements down to much lower temperatures. It is the aim to be able to measure an NMR signal above the noise down to ~ 20 mK for all three axis orientations.

Assuming in the worst case scenario that the signal amplitude continues to shrink at the same rate with decreasing temperature as seen in Figure 6.14, it would be necessary to obtain an initial signal size of a factor 3.5 larger in the normal state for the orientation $B \parallel c$. The SNR calculations from Section 6.4 showed that the signal size seemed to originate from spins residing in an effective surface volume within half the skin depth around the edge of the crystal (see Figure 6.18) but not from the faces perpendicular to the receiver coil. Following this, in order to increase the SNR in the normal state by a factor of 3.5 (assuming the crystal properties are identical to Sample 1 and the spectrometer setup and noise remains unchanged), an effective volume of 3.21×10^{-10} m^3 is necessary. This

can be achieved by simply increasing the thickness of the crystal from 0.2 mm to 0.7 mm, thus a crystal with dimensions 2.3 $\times$ 5.2 $\times$ 0.7 mm^3 would give a clear signal down to low temperatures for $B \parallel c$. However, as the linewidth is seen to double when the orientation is changed to $B \perp c$ [56], to be able to see a signal for all orientations down to low temperatures, it would be necessary to double the effective volume again. This would be possible in a crystal with dimensions 6 $\times$ 6 $\times$ 0.9 mm^3 for the a or b axes aligned in the plane. The 6 mm size restriction is placed by the dimensions of the receiver coil.

However, the reason for the linewidth broadening by a factor of two in comparison to the crystal measured by Körber is not clear. If we obtained a linewidth comparable to that measured by Körber (124 µs in the normal state) then the effective volume of the crystal could be reduced by half, relaxing the conditions set on the size of the crystal.

In terms of possible improvements to the experimental technique, a PXI data acquisition card with higher voltage resolution would always be desirable due to the small UPt_3 signals. Perhaps heatsinking the SQUID sensor to the pot as opposed to the still will give it better temperature stability and thus reduce the need to frequently optimise the bias position as the still temperature is dependent on the mixing chamber and therefore sample temperature. This would however have to be weighed against the higher working temperature of the SQUID, which would increase the noise floor. For future crystals, it would also be extremely useful to be able to measure the two transition temperatures T_c^+ and T_c^- to help with the analysis of the Knight shift measurements. This could be performed using heat capacity measurements on a PPMS machine that operates down to $\sim$ dilution fridge temperatures such as the one in the Quantum Matter Group at the University of Cambridge.

All things considered, it seems we have taken one small step closer to achieving our goal of determining the spin part of the order parameter of this elusive heavy fermion superconductor that is UPt_3.

Bibliography

[1] Trabesinger, A. H., McDermott, R., Lee, S., Mulck, M., Clarke, J., and Pines, A. *J. Phys. Chem. A* **108**(6), 957–963 (2004).

[2] Reif, F. *Phys. Rev.* **106**(2), 208–220 (1957).

[3] Franse, J. J. M., de Visser, A., Menovsky, A., and Frings, P. H. *J. Magn. Magn. Mater.* **52**, 61–69 (1985).

[4] Adenwalla, S., Lin, S. W., Ran, Q. Z., Zhao, Z., Ketterson, J. B., Sauls, J. A., Taillefer, L., Hinks, D. G., Levy, M., and Sarma, B. K. *Phys. Rev. Lett.* **65**(18), 2298–2301 (1990).

[5] Strand, J. D., Harlingen, D. J. V., Kycia, J. B., and Halperin, W. P. *Phys. Rev. Lett.* **103**(19), 197002 (2009).

[6] Kohori, Y., Kohara, T., Shibai, H., Oda, Y., Kitaoka, Y., and Asayama, K. *J. Phys. Soc. Jpn.* **57**(2) (1988).

[7] Vincent, E., Hammann, J., Taillefer, L., Behnia, K., Keller, N., and Flouquet, J. *J. Phys.: Cond. Mat.* **3**(20), 3517 (1991).

[8] Kohori, Y., Kohara, T., Shibai, H., Oda, Y., Kaneko, T., Kitaoka, Y., and Asayama, K. *J. Phys. Soc. Jpn.* **56**(7) (1987).

[9] Tou, H., Kitaoka, Y., Ishida, K., Asayama, K., Kimura, N., Onuki, Y., Yamamoto, E., Haga, Y., and Maezawa, K. *Phys. Rev. Lett.* **80**(14) (1998).

[10] McDermott, R., Trabesinger, A. H., Mück, M., Hahn, E. L., Pines, A., and Clarke, J. *Science* **295**, 2247–2249 (2002).

[11] Burghoff, M., Hartwig, S., Trahms, L., and Bernarding, J. *Appl. Phys. Lett.* **87**(054103) (2005).

[12] Appelt, S., Kühn, H., Häsing, F. W., and Blümich, B. *Nature* **2**, 105–109 (2006).

[13] Stewart, G. R., Fisk, Z., Willis, J. O., and Smith, J. L. *Phys. Rev. Lett.* **52**(8) (1984).

[14] Körber, R. J. *Low Field DC SQUID Nuclear Magnetic Resonance on UPt_3 single crystals*. PhD thesis, Royal Holloway, University of London, (2005).

[15] Cowan, B. *Nuclear Magnetic Resonance and Relaxation*. Cambridge University Press, (2005).

[16] Clarke, J. and Braginski, A. I. *The SQUID Handbook Vol.I*. Wiley-VCH Verlag GmbH & Co. KGaA, (2004).

[17] Weinstock, H., editor. *SQUID sensors: fundamentals, fabrication, and applications*. Kluwer Academic Publishers, (1996).

[18] Gallop, J. C. *SQUIDs, the Josephson Effects and Superconducting Electronics*. Taylor & Francis, (1991).

[19] Friedman, L. J., Wennberg, A. K. M., Ytterboe, S. N., and Bozler, H. M. *Rev. Sci. Instrum.* **57**(3), 410–413 (1986).

[20] Drung, D. *SQUID sensors: fundamentals, fabrication, and applications*, chapter 2. Kluwer Academic Publishers (1996). (Edited by H. Weinstock).

[21] Drung, D., Aßmann, C., Beyer, J., Kirste, A., Peters, M., Rüde, F., and Schurig, T. In *ASC 2006*, (2007).

[22] XXF-1 electronics, Magnicon GbR, Lemsahler Landstraße 171, D-22397, Hamburg, Germany; www.magnicon.com.

[23] Vedrine, P., Aubert, G., Beaudet, F., Belorgey, J., Berriaud, C., Bredy, P., Donati, A., Dubois, O., Gilgrass, G., Juster, F., Meuris, C., Molinie, F.,

Nunio, F., Payn, A., Schild, T., Scola, L., and Sinanna, A. *Appl. Supercon. IEEE Trans.* **20**(3), 696–701 (2010).

[24] McRobbie, D. W., Moore, E. A., Graves, M. J., and Prince, M. R. *MRI from picture to proton.* Cambridge University Press, (2003).

[25] Miner, V. W. and Conover, W. W. *The Shimming of High Resolution NMR Magnets.* Acorn NMR Inc., (1997).

[26] Koenig, S. H. and III, R. D. B. *Prog. Nucl. Magn. Reson. Spec.* **22**(6), 487–567 (1990).

[27] Mößler, M. *Trans. App. Supercond.* **15**(2) (2005).

[28] Jardetzky, O. and Roberts, G. C. K. *NMR in Molecular Biology.* Academic Press, (1981).

[29] Akitt, J. W. *N.M.R. and Chemistry.* Chapman and Hall, (1973).

[30] Bernarding, J., Buntkowsky, G., Macholl, S., Hartwig, S., Burghoff, M., and Trahms, L. *J. Am. Chem. Soc.* **128**, 714–715 (2006).

[31] Guyton, A. C. *Textbook of Medical Physiology.* Saunders, 11th edition, (2005).

[32] Graf, V., Noack, F., and Béné, G. J. *J. Chem. Phys.* **72**(2), 861–863 (1980).

[33] TeachSpin Pulsed NMR Spectrometer, TeachSpin Inc., Buffalo, NY 14214-2153, USA.

[34] Kim, K., Bodart, J. R., and Sullivan, N. S. *Cryogenics* **36**, 311–312 (1996).

[35] Digby, M. *Broadband DC SQUID NMR Spectrometry on Metals.* PhD thesis, Royal Holloway, University of London, (1999).

[36] Casey, A. J. *Two Dimensional ^{3}He Adsorbed on Grafoil Plated with a Bilayer of HD.* PhD thesis, Royal Holloway, University of London, (2001).

[37] Ginsberg, D. M. and Melchner, M. J. *Rev. Sci. Instrum.* **41**(1), 122–123 (1970).

[38] Hoult, D. I. and Richards, R. E. *J. Magn. Reson.* **124**, 71–85 (1976).

[39] Grover, F. *Inductance Calculations.* Dover Publications Inc., (1946).

[40] Hechtfischer, D. *J. Phys. E: Sci. Instrum.* **20**, 143–146 (1987).

[41] Bachman, H. N. and Silvera, I. F. *J. Magn. Reson.* **162**, 417–422 (2003).

[42] Standard Curve 10, Lake Shore Cryotronics, Westerville, OH, 43082-8888, USA; www.lakeshore.com/pdf_files/sensors/AppNotes/Curve10.pdf.

[43] Stanford Research Systems Inc., 1290-D Reamwood Avenue, Sunnyvale, CA 94089, USA; www.thinksrs.com.

[44] Körber, R., Casey, A., Shibahara, A., Piscitelli, M., Cowan, B. P., Lusher, C., Saunders, J., Drung, D., and Schurig, T. *Appl. Phys. Lett.* **91**(142501) (2007).

[45] Lusher, C. P., Li, J., abd R. P. Reeds, M. E. D., Cowan, B., Saunders, J., Drung, D., and Schurig, T. *App. Supercon.* **6**, 591–601 (1998).

[46] Coates, G. R., Xiao, L., and Prammer, M. G. *NMR Logging Principles and Applications.* Halliburton Energy Services, Houston, (1999).

[47] Sanders, J. K. M. and Hunter, B. K. *Modern NMR spectroscopy :a guide for chemists.* Oxford University Press, (1993).

[48] Cope, F. W. *Biophys. J* **9**(3), 303–319 (1969).

[49] Jacobsen, N. E. *NMR Spectroscopy Explained.* John Wiley & Sons, Inc., (2007).

[50] Material Safety Data Sheet, www.sciencelab.com.

[51] Lide, D. R. *CRC Handbook of Chemistry and Physics.* Taylor and Francis Group, (2009).

[52] Chris Lusher, Private communications.

[53] AE Techron 7782 Amplifier, AE Techron, Inc., Elkhart, IN 46516, USA; www.aetechron.com/7782.html.

[54] Arbitrary Waveform Composer (AWC) downloaded from Stanford Research Systems; www.thinksrs.com/downloads/soft.htm.

[55] National Instruments Corporation (U.K.) Ltd., Measurement House, Newbury Business Park, Newbury, Berkshire RG14 2PS, UK; www.ni.com.

[56] Finnemore, D. K., Stromberg, T. F., and Swenson, C. A. *Phys. Rev.* **149**, 231–243 (1966).

[57] Weber, H. W., Seidl, E., and Laa, C. *Phys. Rev. B* **44**, 7585–7600 (1991).

[58] Kerchner, H. R., Christen, D. K., and Sekula, S. T. *Phys. Rev. B* **21**, 86–101 (1980).

[59] Rose-Innes, A. C. and Rhoderick, E. H. *Introduction to Superconductivity.* Pergamon, (1994).

[60] Winter, J. *Magnetic Resonance in Metals.* Oxford University Press, (1971).

[61] Knight, W. D. *Phys. Rev.* **76**, 1259–1260 (1949).

[62] Abragam, A. *Principles of Nuclear Magnetism.* Clarendon Press, (1989).

[63] Townes, C. H., Herring, C., and Knight, W. D. *Phys. Rev.* **77**, 852–853 (1950).

[64] Lee, M., Moores, G. F., Song, Y. Q., Halperin, W. P., Kim, W. W., and Stewart, G. R. *Phys. Rev. B* **48**(10) (1993).

[65] Clogston, A. M. and Jaccarino, V. *Phys. Rev.* **121**(5), 1357–1362 (1961).

[66] Clogston, A. M., Jaccarino, V., and Yafet, Y. *Phys. Rev.* **134**(3A), A650–A661 (1964).

[67] Clogston, A. M., Gossard, A. C., Jaccarino, V., and Yafet, Y. *Rev. Mod. Phys.* **36**(1), 170–175 (1964).

[68] Heine, V. *Phys. Rev.* **107**(4), 1002–1003 (1957).

[69] Tou, H., Kitaoka, Y., Asayama, K., Kimura, N., Onuki, Y., Yamamoto, E., Haga, Y., and Maezawa, K. *Phys. Rev. Lett.* **77**(7) (1996).

[70] Annett, J. F. *Superconductivity, Superfluids and Condensates*. Oxford University Press, (2005).

[71] Takigawa, M., Hammel, P. C., Heffner, R. H., and Fisk, Z. *Phys. Rev. B* **39**(10), 7371–7374 (1989).

[72] Yosida, K. *Phys. Rev.* **110**(3), 769–770 (1958).

[73] Hammond, R. H. and Kelly, G. M. *Phys. Rev. Lett.* **18**(5), 156–158 (1967).

[74] Maeno, Y., Rice, T. M., and Sigrist, M. *Physics Today* **54**(1), 42–47 (2001).

[75] Leggett, A. J. *Rev. Mod. Phys.* **47**(2), 331–414 (1975).

[76] Huxley, A., Rodière, P., Paul, D. M., van Dijk, N., Cubitt, R., and Flouquet, J. *Nature* **406**, 160–164 (2000).

[77] de Gennes, P. G. *Superconductivity of Metals and Alloys*. Westview Press, (1999).

[78] Kleiman, R. N., Broholm, C., Aeppli, G., Bucher, E., Stucheli, N., Bishop, D. J., Clausen, K. N., Mortensen, K., Pedersen, J. S., and Howard, B. *Phys. Rev. Lett.* **69**(21), 3120–3124 (1992).

[79] Yaouanc, A., de Réotier, P. D., Huxley, A., Flouquet, J., Bonville, P., Gubbens, P. C. M., and Mulders, A. M. *J. Phys. Cond. Matt.* **10**, 9791–9798 (1998).

[80] Pincus, P., Gossard, A. C., Jaccarino, V., and Wernick, J. H. *Phys. Lett.* **13**(1), 21–22 (1964).

[81] Fazekas, P. *Lecture Notes on Electron Correlation and Magnetism.* World Scientific, (1999).

[82] de Visser, A., Menovsky, A., and Franse, J. J. M. *Physica B* **147**, 81–160 (1987).

[83] Walko, D. A., Hong, J. I., Rao, T. V. C., Wawrzak, Z., Seidman, D. N., Halperin, W. P., and Bedzyk, M. J. *Phys. Rev. B* **63**(054522) (2001).

[84] McMullan, G. J., Rourke, P. M. C., Norman, M. R., Huxley, A. D., Doiron-Leyraud, N., Flouquet, J., Lonzarich, G. G., McCollam, A., and Julian, S. R. *New J. Phys.* **10**(053029) (2008).

[85] Joynt, R. and Taillefer, L. *Rev. Mod. Phys.* **74**(1), 235–294 (2002).

[86] Park, K. A. and Joynt, R. *Phys. Rev. Lett.* **74**(23) (1995).

[87] Aeppli, G., Bucher, E., Broholm, C., Kjems, J. K., Baumann, J., and Hufnagl, J. *Phys. Rev. Lett.* **60**(7) (1988).

[88] Aeppli, G., Bishop, D., Broholm, C., Bucher, E., Siemensmeyer, K., Steiner, M., and Stüsser, N. *Phys. Rev. Lett.* **63**, 676–679 (1989).

[89] Isaacs, E. D., Zschack, P., Broholm, C. L., Burns, C., Aeppli, G., Ramirez, A. P., Palstra, T. T. M., Erwin, R. W., Stücheli, N., and Bucher, E. *Phys. Rev. Lett.* **75**(6) (1995).

[90] Fisher, R. A., Woodfield, B. F., Kim, S., Phillips, N. E., Taillefer, L., Giorgi, A. L., and Smith, J. L. *Sol. St. Comm.* **80**(4), 263–266 (1991).

[91] Frings, P. H., Franse, J. J. M., de Boera, F. R., and Menovsky, A. *J. Magn. Magn. Mater.* **31-34**, 240–242 (1983).

[92] de Réotier, P. D., Huxley, A., Yaouanc, A., Flouquet, J., Bonville, P., Imbert, P., Pari, P., Gubbens, P. C. M., and Mulders, A. M. *Phys. Lett. A* **205**, 239–243 (1995).

[93] Lippman, T. M., Choi, H., Davis, J. P., Pollanen, J., Gannon, W. J., and Halperin, W. P. *New J. Phys.* **10**(043006) (2008).

[94] Fisher, R. A., Kim, S., Woodfield, B. F., NE, N. E. P., Taillefer, L., Hasselbach, K., Flouquet, J., Giorgi, A. L., and Smith, J. L. *Phys. Rev. Lett.* **62**(12) (1989).

[95] Hayden, S. M., Taillefer, L., Vettier, C., and Flouquet, J. *Phys. Rev. B* **46**(13) (1992).

[96] Trappmann, T., v. Löhneysen, H., and Taillefer, L. *Phys. Rev. B* **43**(16) (1991).

[97] Bruls, G., Weber, D., Wolf, B., Thalmeier, P., Lüthi, B., de Visser, A., and Menovsky, A. *Phys. Rev. Lett.* **65**(18) (1990).

[98] Choi, C. H. and Sauls, J. A. *Phys. Rev. Lett.* **66**(4) (1991).

[99] Buckel, W. and Kleiner, R. *Superconductivity: Fundamentals and Applications*. Wiley-VCH Verlag GmbH & Co. KGaA, (2004).

[100] Graf, M. J., Yip, S. K., and Sauls, J. A. *Phys. Rev. B* **62**(21) (2000).

[101] Machida, K., Nishira, T., and Ohmi, T. *J. Phys. Soc. Jpn* **68**(10) (1999).

[102] Anderson, P. W. *Phys. Rev. B* **30**(7) (1984).

[103] Micklitz, T. and Norman, M. R. *Phys. Rev. B* **80**, 100506 (2009).

[104] Sauls, J. A. and Rainer, D. *Czech. J. Phys.* (1996).

[105] Suderow, H., Brison, J. P., Huxley, A., and Flouquet, J. *Phys. Rev. Lett.* **80**(1) (1998).

[106] *Physica B: Cond. Mat.* **280**(1-4), 172 – 173 (2000).

[107] Tou, H., Ishida, K., and Kitaoka, Y. *Physica C* **408-410**, 305–308 (2004).

[108] Machida, K. and Ohmi, T. *J. Phys. Soc. Jpn* **67**(4), 1122–1125 (1998).

[109] Sigrist, M. and Ueda, K. *Rev. Mod. Phys.* **63**(2) (1991).

[110] Lussier, B., Ellman, B., and Taillefer, L. *Phys. Rev. B* **53**(9) (1996).

[111] Shivaram, B. S., Jeong, Y. H., and Rosenbaum, T. F. *Phys. Rev. Lett.* **56**(10) (1986).

[112] Ellman, B., Taillefer, L., and Poirier, M. *Phys. Rev. B* **54**, 13 (1996).

[113] Shivaram, B. S., Gannon, J. J., and Hinks, D. G. *Phys. Rev. Lett.* **63**(16), 1723–1726 Oct (1989).

[114] Zhao, Z., Behroozi, F., Adenwalla, S., Guan, Y., Ketterson, J. B., Sarma, B. K., and Hinks, D. G. *Phys. Rev. B* **43**(16), 13720–13723 Jun (1991).

[115] Strand, J. D., Bahr, D. J., Harlingen, D. J. V., Davis, J. P., Gannon, W. J., and Halperin, W. P. *Science* **328**, 1368–1369 (2010).

[116] Schuberth, E., Hofmann, G., Gross, F., Andres, K., and Hufnagl, J. *Europhys. Lett.* **11**(3) (1990).

[117] Strongin, M., Maxwell, E., and Reed, T. B. *Rev. Mod. Phys.* **36**(1), 164–168 Jan (1964).

[118] Pobell, F. *Matter and Methods at Low Temperatures.* Springer-Verlag, (2007).

[119] Richardson, R. C. and Smith, E. N. *Experimental Techniques in Condensed Matter Physics at Low Temperatures.* Perseus Books, (1998).

[120] Oxford Instruments, Tubney Woods, Abingdon, Oxfordshire OX13 5QX, UK; www.oxinst.com.

[121] Cryogenic Limited, Acton Park Industrial Estate, London W3 7QE, UK; www.cryogenic.co.uk.

[122] High Pressure Equipment Company, Erie, PA 16505, USA; www.highpressure.com.

[123] Picowatt, Veromiehentie 14, FI-01510 Vantaa, Finland; www.picowatt.fi.

[124] Agilent Technologies UK, 610 Wharfedale Road, Winnersh Triangle, Wokingham, Berkshire RG41 5TP, UK; www.home.agilent.com.

[125] Amplifier Research (AR, acquired Kalmus), 160 School House Road, Souderton, PA 18964-9990, USA; www.ar-worldwide.com.

[126] Pickering Interfaces Ltd., Stephenson Road, Clacton On Sea, Essex CO15 4NL, UK; www.pickeringtest.com.

[127] Shvarts, D., Adams, A., Lusher, C. P., Körber, R., Cowan, B. P., Noonan, P., Saunders, J., and Mikheev, V. A. *Physica B: Condensed Matter* **329-333**, 1566 – 1567 (2003).

[128] Andrew Huxley, Private communications.

[129] Schöttl, S. *Magnetische Untersuchungen am Schwer-Fermion-Supraleiter UPt_3.* PhD thesis, Technische Universität München, (2000).

[130] Aronson, M., Clarke, R., Demczyk, B., Coles, B., Smith, J., de Visser, A., Vorenkamp, T., and Franse, J. *Physica B: Cond. Matt.* **186-188**, 788 – 791 (1993).

[131] Signal Recovery (formerly EG&G), AMETEK Advanced Measurement Technology, Spectrum House, Wokingham, RG41 2TZ, UK; www.signalrecovery.com/7265page.htm.

[132] Löhneysen, H. *Physica B: Cond. Mat.* **197**(1-4), 551–562 (1994).

[133] Mehring, M., Kotzur, D., and Kanert, O. *Phys. Stat. Sol. B* **53**(K25) (1972).

[134] Wilks, J. *Liquid and Solid Helium.* Clarendon Press, (1967).